Novel X-ray Instrumentation for Astronomy

Adrian Martindale

April 10, 2008

Thesis submitted to the University of Leicester
for the degree of Doctor of Philosophy.

Space Research Centre
Department of Physics and Astronomy
University of Leicester
UK.

Abstract

This thesis describes experimental and theoretical work and technology development directed towards the next generation of X-ray astronomical instrumentation. A great heritage exists of instruments which are sensitive to X-rays which operate on board space based observatories. The next generation of such telescopes will take advantage of the rapid technology advancement of the last four decades to more accurately observe the universe and give greater insight into the objects within it, how they formed and how they will evolve.

Chapters 2 and 3 describe the investigation of extremely high speed microchannel plate detectors capable of counting individual photons with a timing accuracy of a few tens of picoseconds (1 ps = 10^{-12} s) at extremely high spatial resolution. Although many early X-ray astronomical instruments were based on MCP detectors, it is only recent manufacturing improvements which have enabled the production of such small pore diameters, enabling the unparalleled temporal and spatial resolution. Prospects for future application exist in fields as diverse as X-ray and ultraviolet astronomy and the life sciences.

Chapters 4 and 5 report the testing of Microchannel plates as low mass X-ray optics where the development of square pore geometries has made true imaging MCP telescopes possible. Two flight programs are identified as areas where such optics will provide tangible scientific benefits: These are *BepiColombo*, a European mission to the planet Mercury which will contain the first ever imaging X-ray telescope on a planetary science mission and *Lobster-ISS*, a wide field of view telescope for X-ray astronomy which will provide coverage of, almost, the whole sky every 90 minute orbit. Testing reported herein finds that the manufacturing techniques are maturing to a point where they can exceed the ≤ 5 arcmin resolution required for these missions.

Chapters 6 and 7 comprise a description of a completely novel X-ray polarimeter. For the past three decades, little or no progress has been made in the field of X-ray astrophysical polarimetry owing to the lack of suitable instrumentation, this is despite intense scientific interest in such measurements. A very simple optical design for a polarimeter is made possible using highly ordered materials which exhibit dichroism at fixed, narrow energy bands, for the first time allowing simultaneous measurement of ALL astronomically pertinent observables.

The areas of science influenced by these three areas of instrument development are shown to be very broad, including; astrophysics and cosmology, planetary science, life sciences, nano-science and even fundamental chemistry.

Declaration

I hereby declare that no part of this thesis has previously been submitted to this or any other university as part of the requirement for a higher degree. The work described herein was conducted solely by the undersigned except for those colleagues and other workers acknowledged in the text.

Adrian Martindale

April 10, 2008

Dedication

For Mum and Dad.

My love always.

Acknowledgments

There are a huge number of people without whom this thesis would have been impossible.

To everyone at the Space Research Centre for making the last three years so enjoyable and providing such a fun and lively environment in which to work my thanks and greatest respect. Special thanks to Jim Pearson, John Lees and Jon Lapington who conspired to provide the best education in experimental work I could have hoped for.

In no particular order, Tony Crawford, Baden Favil, Dave Vernon, Duncan Ross, Chris Bicknell, Rob Limpenny and Dave Bassford; all of whom have provided huge amounts of help during my PhD. Their relentless banter kept me sane when I felt like I was loosing it! Thank you to Craig Brown and Helen Yates for providing data for chapter 5. Also, thanks to everyone in the X-ray polarimetry consortium and to everyone at Photonis for their fantastic channel plates, in particular, Emile Schyns and Ray Fairbend for the outstanding hospitality in Brive. Thanks to Dick Willingale for all his help with the ray tracing software and interpretation of MCP imaging results. Also thanks to Dick and my external examiner Alan Smith for their insightful and helpful comments and suggested revisions to the thesis which have greatly improved it. Thank you to George Fraser who offered many helpful discussions and a great deal of advice that was very much appreciated.

For the help and support of my supervisors Martin Barstow and Nigel Banister I will always be grateful. Their comments and guidance whilst writing this thesis saved me many days of struggling with my results and with the English language! Special thanks to Nige for listening to all of my spleen-venting, for his constant help and good humor and of course for advice on how not to kill my fish! I'm less grateful to him for introducing me to the "prairie-oyster" but that's another story.

Thanks to the members of Aylestone Athletic rugby club for providing an outlet for my frustrations both on the pitch and in the pub after a game. To Mum and Dad, thank you for a lifetime of love and encouragement and for always being there when I needed you. Thanks to my brother and sister-in-law, Richard and Rebecca, for housing me when I found myself homeless and my grandparents for always believing in me. Particular thanks to my Grandad, Dougie, who's love of tools I have inherited and who schooled me in the art of "tinkering". Finally, thanks to Charlotte - for everything.

Publications

N. P. Bannister, K. D. M. Harris, S. P. Collins, A. Martindale, P. S. Monks, G. Solan and G. W. Fraser. *Dichroic Filters For Astronomical X-Ray Polarimetry*, Experimental Astronomy, Vol. 21, 1-12, September 2006.

R.M. Ambrosi, R. Street, B. Feller, G.W. Fraser, J.I.W. Watterson, R.C. Lanza, J. Dowson, D. Ross, A. Martindale, A.F. Abbey and D. Vernon. *X-ray tests of a microchannel plate detector and amorphous silicon pixel array readout for neutron radiography*, Nuclear Instruments and Methods in Physics Research Section A, 572, 844-852, March 2007.

Martindale, A., Lapington, J. S. and Fraser, G. W. *Photon counting with small pore microchannel plates*, Nuclear Instruments and Methods in Physics Research A, 573, 111-114, April 2007.

A. Martindale, N.P. Bannister, K.D.M. Harris, S.P. Collins, G. Solan, Y. Champouret, V.K. Muppidi, G.W. Fraser, *Narrow-band X-ray polarizing filters*, Proc. SPIE, San Diego, August 2007 In Press.

A. Martindale, H. Yates, C. Brown, J.S. Lapington, J.F. Pearson, J.E. Lees, R. Fairbend, E. Shyns, N.P. Bannister, J.D. Carpenter, G.W. Fraser. *Improved imaging resolution of square pore, square packed microchannel plate X-ray optics*, Nuclear Instruments and Methods in Physics Research A. 2007 In-Prep.

Contents

Abstract **I**

Declaration **II**

Dedication **III**

Acknowledgements **IV**

Publications **V**

Table of contents **VI**

List of figures **XII**

1 Introduction **1**

1.1 Astrophysical X-ray generation 4

1.1.1 Thermal emission 4

1.1.2 Non Thermal emission 6

1.1.3 Astrophysically significant observables 8

1.2 Historical X-ray astrophysical observatories 10

1.2.1 Mature X-ray detector technologies 12

1.2.2 The current state of the art detectors . . . 14
1.2.3 Imaging and early optics . . . 16
1.2.4 Collimators . . . 16
1.2.5 Imaging optics . . . 17
1.3 Current observatories and instruments . . . 20
1.4 Future space missions . . . 21
1.4.1 XEUS . . . 23
1.4.2 WFT and BepiColombo . . . 25
1.5 The subject of the current thesis . . . 26
1.5.1 Small pore microchannel plate detectors . . . 26
1.5.2 Microchannel plate optics . . . 27
1.5.3 X-ray polarimetry . . . 28
1.6 Thesis outline . . . 29

2 Microchannel Plate X-ray Detectors **32**

2.1 Microchannel plates . . . 32
2.1.1 Microchannel plate manufacture . . . 34
2.2 MCPs as X-ray and charged particle detectors . . . 36
2.2.1 Control of detector response . . . 38
2.2.2 Diagnostics from MCP detectors . . . 39
2.3 Small pore sizes . . . 40
2.4 Applications . . . 41
2.4.1 Astronomy . . . 41

2.4.2 Terrestrial applications . . . 45

2.5 Summary . . . 46

3 Photon counting with small pore microchannel plates 47

3.1 Introduction . . . 47

3.2 Experimental characterisation . . . 47

3.2.1 The test facility . . . 48

3.2.2 Detector assembly . . . 50

3.2.3 Photon counting . . . 52

3.2.4 Timing . . . 56

3.2.5 Experimental issues . . . 61

3.3 Modifications and improvements . . . 63

3.3.1 Protection of electronics . . . 63

3.3.2 Unwanted contributions to the signal . . . 63

3.4 Conclusions . . . 65

3.5 Further work . . . 66

3.5.1 Increasing signal speed . . . 66

3.5.2 Excess noise . . . 67

4 An Introduction to Microchannel Plate X-ray Optics 68

4.1 MCP optics . . . 68

4.2 Applications . . . 73

4.2.1 Terrestrial applications . . . 73

4.2.2 Space missions . . . 73

4.3 X-ray testing . . . 79
4.3.1 The focal plane detector . . . 80
4.3.2 Point to point focusing . . . 82
4.3.3 Focusing with slumped plates . . . 87
4.4 Mechanical testing of MCP optics . . . 89
4.5 Summary . . . 89

5 Microchannel plate X-ray optics - Experiments and Modeling 91

5.1 Introduction . . . 91
5.2 Optic samples . . . 92
5.3 Simulations . . . 93
5.3.1 Simulating expected images . . . 93
5.3.2 Effective area . . . 101
5.4 X-ray testing . . . 105
5.4.1 Point to point focusing . . . 105
5.4.2 Imaging in the long beamline . . . 111
5.5 Mechanical testing . . . 116
5.6 Experimental issues . . . 119
5.6.1 Proposed solutions and further work . . . 120
5.7 Comparison of performance . . . 120
5.8 Summary . . . 121

6 X-ray polarimetry 123

6.1 Polarisation of light . . . 124

6.2 Polarisation of astrophysical X-ray emission . . . 127
6.2.1 Synchrotron emission . . . 128
6.2.2 Linear Bremsstrahlung . . . 129
6.2.3 Thermal radiation and scattering . . . 131
6.3 Measuring polarisation . . . 133
6.3.1 Polarimeters . . . 134
6.4 Bragg and Thompson polarimetry . . . 135
6.4.1 Results to date . . . 137
6.5 Novel polarimeters . . . 140
6.5.1 CCD split pixel events . . . 141
6.5.2 Micropattern Photoelectric Polarimeter - MPP . . . 141
6.5.3 Time projection chambers - TPCs . . . 143
6.5.4 Dichroic X-ray filters . . . 144
6.6 Summary . . . 147

7 Dichroic Filters for X-ray Polarimetry 148

7.1 Introduction . . . 148
7.2 Material design strategy . . . 149
7.2.1 Inclusion compounds . . . 150
7.2.2 Inorganic crystals . . . 151
7.3 Experimental characterisation . . . 151
7.3.1 Sample preparation . . . 154
7.3.2 Sample storage . . . 157

7.3.3 Sample characterisation . . . 157
7.4 Results . . . 158
7.4.1 Inclusion compounds . . . 158
7.4.2 Coordination compounds . . . 164
7.4.3 Vacuum stability . . . 166
7.5 Prototype Instrument Design . . . 166
7.6 Discussion . . . 167
7.6.1 Optimisation of the filters . . . 168
7.6.2 Future experiments . . . 171
7.7 Modeling instrument response . . . 172
7.7.1 *XEUS* . . . 172
7.7.2 Detector response . . . 174
7.7.3 Astrophysical sources . . . 175
7.8 The polarimeter model . . . 177
7.8.1 Sensitivity predictions . . . 179
7.9 Comparison and complementarity of MPPs and Dichroic filters . . . 181
7.10 Conclusions . . . 183
7.11 Summary . . . 184

8 Conclusions **185**

8.1 Thesis overview . . . 185
8.1.1 Small pore MCP detectors . . . 186
8.1.2 MCP optics . . . 187

8.1.3 X-ray polarimetry 188

8.2 Closing remarks 188

Bibliography **190**

List of Figures

1.1 Image of the moon taken by the ROSAT PSPC, showing the fluorescence X-rays from the sunlit side and no significant emission from the unilluminated side. The events present on the dark side of the moon are attributed to geocoronal emission in the Earth's atmosphere. 3

1.2 The shell picture of electron orbitals 6

1.3 Typical theoretical X-ray spectrum from an electron bombardment source, including transmission through an aluminised lexan filter to remove the low energy photons. The tube accelerating voltage was assumed to be 2 kV. The Bremsstrahlung continuum is seen to be significantly lower intensity than the L-shell fluorescence from the copper anode. 7

1.4 A selection of different detector technologies. Clockwise from the left; a selection of microchannel plates, the XMM - EPIC camera CCD focal plane, A channel electron multiplier and a schematic diagram of a superconducting tunnel junction. 13

1.5 Schematic diagram of the operation of a collimator. The blue rays are transmitted while the red rays are absorbed and the open angle of the channels (ie the ratio of length to diameter) defines the angle of acceptance. 17

1.6 The Wolter geometries (after Giacconi *et al.* (1969))panels a, b and c are respectively; the Wolter-I , Wolter-II and Wolter-III geometries 19

1.7 Photographs of the three operational observatories in their clean rooms prior to launch. From left to right *Swift*, *XMM* and *Chandra* (Photos courtesy of NASA (left and right) and ESA (center)). 20

2.1 Schematic diagram of the MCP parameters which govern detector/optic response. Note the difference in channel alignment between a slumped plate, where the channels point towards the radius of curvature (left) and a ground plate, where the channels are all parallel (center). L is the channel length, D is the channel diameter and β is the bias angle of the MCPs. 35

2.2 Schematic of the P5 detector with salient features marked. Note the chevron arrangement of the channels 37

3.1 Photograph of the detector end of the DTF The end flange is clearly visible and is where the detector sits on the translation stages. 49

3.2 Photograph of the SP1 detector mounted onto the test facility end flange 51

3.3 Modal gain (triangles, right hand scale) and pulse height FWHM (squares; left hand scale) as functions of total MCP voltage. 52

3.4 (left) Peaked X-ray pulse height distribution for C-K X-rays with a total detector bias of 1958 V. (Right) Noise pulse height distribution for the same voltage. 53

3.5 Analysis of the X-ray PHD shown in Figure 3.4. The green points are measured data, the red line an exponential fit to the first 15 and last 600 data points where the shape is thought to be dominated by the exponential function characteristic of MCPs, and the blue points the residual excess noise counts. The excess noise is shown to be peaked and is thought to be caused by radioactive decay in the detector body. It should be noted that the count rate in the residuals is in places negative, this is explained by the fact that in places the exponential fit overestimates the experimental results due mainly to statistical scatter. 55

3.6 Analysis of the noise PHD shown in Figure 3.4. The green points are measured X-ray data, the blue line measured noise counts and the red curve the X-ray data with the noise counts removed. 56

3.7 (Upper panel) Pulse width and rise time as a function of rear voltage in the original configuration. NB. $\sim$ 1 mm between the rear plates and the electrode. (Lower panel) Evolution of pulse shape with rear voltage. 59

3.8 Data from the most optimised detector configuration in the initial work. The rear voltage was 2021 V. The red line is a Gaussian fit to the the pulse and the + signs are the data points. The relatively poor sampling of the pulse is characteristic of the maximum resolution of the oscilloscope. 61

3.9 detector pulse with rear grid and 2.5 kV between the grid and rear plate (1900 V on the MCP stack). Note the secondary peak has been almost removed. 64

4.1 Schematic diagrams of the KB geometry (top) after http://astroa.physics.metu.edu.tr/-~emrah/lece/xtelescopes_systems.html and the MCP optic geometry where the square channels make the two reflecting surfaces of the KB geometry coincident in space - (bottom) 70

4.2 Schematic diagrams of the focusing mechanisms of planar (top) and slumped (bottom) MCP optics 71

4.3 Schematic diagram of the MIXS mechanical design. The Right hand element of the figure is the collimator channel which is described in Carpenter (2006). The Left hand part of the image shows MIXS-T (the telescope part of MIXS) where the mirror optic module (MOM) is shown at the top of the image. The three concentric rings of MCP tandems can be seen, the white ring contains six 57° tandems, the Green ring has twelve 30° tandems and the red outer ring has eighteen 20° tandems. Image courtesy of Magna Parva Ltd (Loughborough Innovation Centre, Epinal Way, Loughborough, Leicestershire, LE11 3EH). 78

4.4 The large area MCP detector in the long beamline facility with the two axis rotation stage used for mounting the optics 80

4.5 The effect of image linearisation on the image taken using the pinhole array. Left, the raw, distorted image. Right, the image after linearisation. Note the good regularity of the linearised image in the center and the degradation in linearity towards the edge of the field of view. 82

4.6 The cruciform focal structure of a planar square pore, square packed MCP optic. The central focus comprises photons reflected an odd number of times from orthogonal walls, the base of the pyramid is $2D$ resulting from the non-ellipsoid nature of the channel walls. The unreflected component has a base size of $2L_sD/L$, resulting from the maximum transmission angle of the channels being D/L. The cross arms result from odd-even reflections from orthogonal walls. After Price (2001) 83

4.7 The illumination geometry of radial plates under X-ray testing. The Blue lines represent the PSF for point to point investigation as described in Section 4.3.2 84

4.8 The radial cross arm structure of a radially packed MCP sector, (Left) an X-ray image with the illumination geometry of Figure 4.7. (Right) a ray trace image of a similar geometry with the optic rotated approximately 45° azimuthally. 84

4.9 (Left) photograph of the short (1.4m) beamline. (Right) the two axis rotation stage used to mount MCP optics. 85

4.10 Spectrum of an electron bombardment X-ray source with a 2 μm macrofol filter (top) and 4 μm aluminium filter (bottom) 86

4.11 Schematic showing the foreshortening of the X-ray source spot in the image plane . . 87

4.12 Schematic diagram of the Tunnel Test Facility (TTF). 88

5.1 Images of the test sample MCP optics. A − Square pore, square pack lobster optic. B − radially packed optic sector. 93

5.2 Ray traced simulations showing the effect of increasing deformations to the channel alignment for a planar, square pore, square pack MCP in point-to-point focusing mode. The detector pixels are 0.2 mm square. The inserts in the bottom right of each panel are zoomed in versions of the central 50 pixels of the point spread function magnified by a factor of 3. A) zero channel deformation B) 2 arcminute RMS channel deformation C) 3 arcminute RMS channel deformation D) 5 arcminute RMS channel deformation. The colour scale represents the effective area (in cm^2) per pixel in the image plane and should be interpreted as intensity in the X-ray image. The images have a common saturation level of 10^{-2} cm^2 per pixel in order to increase the contrast between the bright cental focus and the lower level structure. 94

5.3 Ray traced images showing the effect of increasing deformations to the channel alignment for a planar, square pore, square pack MCP focusing almost parallel X-rays in a 27 m beamline. The detector pixels are 0.045 mm square. The inserts in the bottom right of each panel are zoomed in versions of the central 200 pixels of the point spread function magnified by a factor of 3. A) zero channel deformation B) 2 arcminute RMS channel deformation C) 3 arcminute RMS channel deformation D) 5 arcminute RMS channel deformation. The colour scale is as described in Figure 5.2. 96

5.4 Images showing the modal average of the number of reflections undergone by rays in order to arrive at the focal plane in the given position. The colour scale represents the number of hits plus one, in order to differentiate between pixels with no events and those with an average of zero reflections. A) planar MCP in a 1.4 m beamline. B) MCP slumped to 750 mm spherical radius of curvature in a 27m beamline – the position of the focal plane is 370 mm from the optic in order to account for the finite length of the beamline. Both models assume 2 arcminute blurring of the channel axes. 97

5.5 Image showing the number of reflections vs the x/y position of the last reflection on the optic rear surface. The image is directly comparable with Figure 5.4 and shows, on average, where on the optic the features in the PSF originate from (the same colour scale is applied as Figure 5.4). 97

5.6 Ray trace images of a sector with the same parameters as the slumped optic to show the focal structure as the image moves off axis. A) 20 arcminutes off axis horizontally. B) 20 arcmins off axis vertically. C) 20 arcmins off axis vertically (in opposite direction to B). D) 10 arcmins off axis in both axes. The colour scale is as described in Figure 5.2.100

5.7 A) data from ray trace modeling showing the modal average of the number of reflections undergone by rays. The colour scale represents the number of hits plus one, in order to differentiate between pixels with no events and those with an average of zero reflections. B) As in A but the image positions represent the position of the ray in the optic plane (i.e. where the rays are reflected in the optic - for the final reflection if multiple reflections). The model assumes the MCP is slumped to 1333 mm spherical radius of curvature and is fitted in a 27m beamline – the position of the focal plane is 650 mm from the optic in order to account for the finite length of the beamline. Both models assume zero blurring due to random misalignment between channel axes (i.e. that all channels point towards the centre of curvature of the optic) and that the off axis angle is zero in both axes. No RMS blurring of the channel axes was included as I could not make the blur give physically reasonable deformations in the ray tracing software this will be included in the next phase of study. 102

5.8 Diagram to demonstrate the Abbe sine condition, both rays intersect at the focal point meaning that they have the same magnification. 102

5.9 Comparison of effective area as a function of energy for source distance u =27 m (red and light blue) and $u = \infty$ (green and dark blue) with either an unobstructed 40 mm by 40 mm field of view (green and red) or with a 35 mm $\times$ 35 mm aperture to represent the mounting structure (two blue curves). 104

5.10 A) Linearised image of the PSF from the flat plate point-to-point measurement. The elliptical central focus is a consequence of the elliptical source spot. The direction of the cut shown in panel B is from bottom left to top right. Each pixel is $\sim 76\mu$m and the colours indicate normalized intensity. Data from Brown & Yates (2006). B) Cut taken through Figure 5.10 as indicated by the black line. The FWHM indicates an optic resolution of 3.1 arcmins before source size correction. 106

5.11 A) cut taken through Figure 5.10 as indicated by the black line in Figure 5.10-A. The green "fit lines" represent the model profiles and the red points are measured data points from Figure 5.10-B. B) cut perpendicular to that in panel A. The black triangular line in both panels is the response when the source size is approximated by a delta function i.e. it is the limiting resolution as source size tends to zero. The fit lines represent (in order of increasing width) ratio of source size to optic FWZM of approximately 0.2, 0.3, 0.45, 0.55. The sharp change in gradient of the model curves towards the edge of the plots is simply the edge of the modeled region and is not a physical effect. 107

5.12 (right) is an X-ray image taken in point to point focusing mode in the 1.4 m beamline with a radially packed sector. A rectangular aperture was placed in front of the MCP to prevent stray X-rays reaching the focal plane. The axes are pixels (0.27 mm across) and the colour scale is counts per pixel. (Left) a ray trace model of the same configuration. In the model, the optic has an off-axis angle of $\sim 0.5^\circ$ in both axes of the rotation stage, and is 50 mm out of focus. 108

5.13 (Left) saturated ray trace image of a similar geometry to the test. (Right) X-ray image of the point spread function measured by point to point focusing. The FWHM resolution is ~ 7 arcmins. The components of this image are as reported in Figure 5.12. 110

5.14 Cut through Figure 5.13 in a direction tangential to the radial cross arm from top left to bottom right. 110

5.15 Variation in optic resolution as a function of position along the optical axis. Elliptical approximation is the square root of the product of the two axes shown in this figure (dashes). Axis 1: Squares, Axis 2: Triangles. The circled data points are considered anomalous and are excluded from the fitted curve. 112

5.16 Logarithmically scaled image of the cruciform PSF from the slumped plate. The axes are in pixels with 1 pixel = 38 μm. No colour bar is included as the shape is of primary interest in this case. 112

5.17 X-ray image formed by the (nominal) 1.33 m slumped radially packed optic KL001-2. The FWHM angular resolution is 8.9 arcmins in the vertical direction. The band of intensity at the bottom of the image is due to direct transmission around the mounting structure. The panels to the left of and below the main image are horizontal and vertical integrations of the image. Axes in (0.27 mm) pixels. The plot in the bottom left hand corner is the MCP detector pulse height distribution (units of channels). 115

5.18 (Left) image with detector ~ 3 cm behind the focus. (Right) image ~ 20 cm in front of the focus. The shape of the focus changes as the detector moves from behind the best focus to in front of it. The images are taken in the same way as Figure 5.17. 116

5.19 A true cut through the central focus shown in Figure 5.17. The cut is in the $y - axis$. 117

5.20 Surface height profile (blue) measured for the slumped optic, the radius of curvature was ~ 69 cm. Superimposed is the best fit model profile of the mounting jig which showed a radius of curvature of ~ 38 cm, half the required value. Therefore, mounting stresses are likely to be distorting the optic. 119

6.1 Diagram showing the effect of adding two electromagnetic waves. Top, the waves are in phase leading to linear polarised light. Bottom, The waves are $\pi/2$ radians out of phase leading to circular polarisation. Figure courtesy of www.scielo.br/img/fbpe/qn/-v25n5/11410f2.gif 125

6.2 Diagrams of the beaming effect of synchrotron emmission. Left panel, in the rest frame of the electron, the dipolar lines around the electron represents the intensity of the emission in that direction and is also characteristic of cyclotron radiation. Right pannel, demonstrating the effect of the Lorentz transform into the rest frame of the observer, the strong beaming effect is often called the headlight effect. Image from http://www.astro.utu.fi/∼cflynn/astroII/l4.html 130

6.3 Diagrams of Bragg crystal polarimeters (left - (A) is in non-focusing mode, (B) is focusing) and Thompson scattering polarimeters (right). 137

6.4 The 19% polarisation modulation curve reproduced from Weisskopf *et al.* (1978b), Figure 2. 138

6.5 Diagrams of Bragg crystal polarimeters Flown on the OSO 8 spacecraft (reproduced from Novick (1975) - Figure 9). 139

6.6 Shematic of the MPP design taken from Costa *et al.* (2001). 142

6.7 The X-ray absorption fine structure for a silicon wafer. The "ripples" after the main edge are a consequence of the electronic states close to the excited silicon atom. Image reproduced from http://pfwww.kek.jp/kitajima/sx/bl11b_e.html. 145

7.1 Transmission spectra from Collins *et al.* (2002) for a dibromoalkane/urea inclusion compound (left) and Chao *et al.* (2003) for a 1-Bromoadamantane/Thiourea inclusion compound (right) 151

7.2 Structure of YC19 showing the bond orientations and the position of the atoms. The copper atoms are shown in light blue and in between them lies a planar bridging ligand which, along with the ring structures either side of the copper atoms constrain the crystals to grow in a regular manner, forcing the electronic structure into a mono-axial configuration. 152

7.3 Photograph of the experimental arrangement for testing dichroic crystals at station 16.3 of the Daresbury SRS. The χ axis is a rotation around the green ring in the center of the image and ϕ is a rotation at 90° to this axis about the sample mounting structure. 155

7.4 Schematic diagram of the experimental arrangement for testing dichroic crystals at station 16.3 of the Daresbury SRS. Panel A shows the plan veiw with the plane of the synchrotron and therefore the X-ray polaratation in the page. The ion chambers used for detection are shown. Panel B is a view from ion chanber 2 towards the synchrotron such that the plane of polarisation is now horizontal on the page. The chi axis isa rotation around the optical axis of the beamline (i.e. around the green ring) the Phi axis is vertical in the Figure 7.3 and is represented as rotation around the sample in panel A. 156

7.5 Energy spectra for an inclusion compound of 1-Bromoadamantane/Thiourea. The red curve is for $\chi = 90°$ and the black curve for $\chi = 0°$ where χ is the angle between the axis of the crystal expected to be parallel to the bond which leads to the dichroism and the polarisation direction of the photons. 159

7.6 Surface showing absorption as a function of photon energy and crystal orientation for a 1-Bromoadamantane/Thiourea inclusion compound. 160

7.7 Transmission spectrum of a 1-Bromoadamantane/Thiourea inclusion compound, the extended energy range from Figure 7.5 demonstrating the narrow bandwidth of the dichroic response. The curves are as described in Figure 7.5 161

7.8 Energy spectra for an inclusion compound of a 1-Iodoadamantane guest in a Thiourea host. The curves are as described in Figure 7.5 162

7.9 Transmission spectra for a Ferrocine/Thiourea inclusion compound (left) and an inclusion compound of benzene chromium(0) Tricarbonyl in Thiourea. The significant dip in the plot for the chromium compound is not real. It is believed to be indicative of a monochromator glitch meaning that data from this compound is not as reliable as for the other materials. This and the poor signal to noise ratio of the data mean that the only realistic conclusion obtainable from this data set is that there is no significant dichroic effect. The curves are as described in Figure 7.5 162

7.10 Showing the broadband transmission properties (Henke *et. al.* 1993), for Thiourea (black) and urea (red). Left, arbitrary sample thickness = 0.5 mm. Right, sample thickness = 0.1 mm (as for Cr compound). 163

7.11 Diagrams of the unit cell of the coordination compounds (A) YC19 (B) YC31c. In YC19 the bonds pertinent to dichroism are parallel, for YC31c they are inclined with respect to each other. 164

7.12 Energy spectra for YC19. The curves are as described in Figure 7.5 165

7.13 Energy spectra for YC31c. The curves are as described in Figure 7.5 165

7.14 Engineering sketch of a potential filter wheel design for the dichroic filter polarimeter (courtesy of Baden Favill, University of Leicester). 168

7.15 Overplot of the difference in transmission change between the two axes of the polariser for all three useful dichroic materials. The results indicate that polarisation information is contained within a bandwidth of a few hundred eV of the absorption edge(I-K 33.17 keV, Br-K 13.47 keV, Cu-K 8.98 keV). 169

7.16 The modulation factor plotted as a function of filter thickness for the 1-Bromoadamantane/thiourea inclusion compound. 170

7.17 The figure of merit μ as a function of filter thickness for the 1-Bromoadamantane/-Thiourea inclusion compound (left) and YC19 (right). 171

7.18 The effective area of the *XEUS* mirrors based on the most recent optical configuration (June 2007) with a multilayer coating. No detector efficiency is included in the curve. (Data courtesy of Willingale (2007a)) 174

7.19 Fractional absorption in the filter calculated using the NIST web calculators (Chantler, 1995). The empirical formula for the molecule was used in the calculation and the data fitted to the absorption edge measured at the Daresbury SRS. 178

7.20 Theoretical X-ray spectrum of the crab nebula calculated using the parameters in Table 7.2. The absorption features are explained in Schattenburg & Canizares (1986), where the main feature is oxygen in the interstellar medium. Also present are Nitrogen, Iron, Magnesium and Silicon. 178

7.21 The detected spectrum from the Crab nebula assuming the *XEUS* effective area and transmission through a 1-Bromoadamantane/Thiourea inclusion compound filter with transmission given by experiments at the Daresbury SRS. It should be noted that a constant, 100% detector efficiency is assumed over the whole energy range – results should, therefore, be scaled according to detector efficiency. 179

Chapter 1

Introduction

X-ray astronomy is now a mature science. The "accidental" discovery of cosmic X-ray emission (Giacconi *et al.*, 1962) marked the beginning of a discipline which has provided new insights into the universe we live in and the objects within it. In particular, observing X-ray emission from celestial sources has allowed astronomers to probe the most exotic and energetic processes in the cosmos. These include: accretion power (the loss of gravitational energy as matter falls onto a compact object in an accretion disk, leading to intense heating of the disk to millions of degrees Kelvin), electrons accelerating in strong magnetic fields at speeds approaching the speed of light, and the afterglow from gamma ray bursts which are thought to be the birth of black holes by the collision of neutron stars or the collapse of supermassive systems.

X-ray astronomy began in the 1960s with sounding rocket experiments carrying Geiger counters above the atmosphere to look for high energy photons. Although Friedman *et al.* (1951) had observed the first example of X-ray emission from a celestial object (the sun), it was not until the 1960s that extra-solar X-ray emission was confirmed. Giacconi *et al.* (1962) reported a sounding rocket experiment, designed to detect the fluorescence X-rays from the surface of the moon. These were expected to

be induced by the impact of the solar wind on the lunar regolith. However, the experiment "failed" owing to a very high measurement background. This was shown to have a cosmic origin and was interpreted as a diffuse background radiation with a discrete source (or sources) superimposed on it. The discrete source was later resolved and found to be in the constellation Scorpio and was named Sco-X1, confirming the existence of extra-solar X-ray sources. Subsequent increases in optic performance have allowed much of this diffuse background to be resolved into known point sources. However, there is still a diffuse, unresolved component to cosmic X-ray emission.

It was not until the U.S. *Apollo* moon program in the late 1960s and 70's that Giacconi's lunar X-ray fluorescence measurements became possible (Adler & Trombka, 1977). This is because of the low signal from the moon and high sky background. The first X-ray image of the moon taken from Earth orbit was acquired by the *ROSAT* Position Sensitive Proportional Counter (PSPC) (Figure 1.1) and demonstrates the rather poor statistical discrimination between the sky background and fluorescence from the lunar surface, despite the significantly improved instruments onboard *ROSAT* (when compared to the early sounding rockets). Chapters 4 and 5 describe a new kind of X-ray optic which could enable the same observations to be made of the surface of the planet Mercury.

X-ray astronomy has remained the predominant observational probe of extreme astrophysical environments for over 40 years. Since the early rocket borne experiments, it has developed at a fast pace, enabled largely by the rapid improvements in instrumentation designed for such observations. Yet despite the major breakthroughs in X-ray astronomy in recent years, many fundamental questions remain unanswered. As we approach the second decade of the new millennium, several new and exciting missions are planned which will further our understanding of the X-ray universe.

This thesis describes new technologies for X-ray astronomical instrumentation. It can be broken down into three broad areas; high speed microchannel plate detectors, microchannel plate X-ray optics and new instrumentation for X-ray polarimetry. These will be considered with reference to the

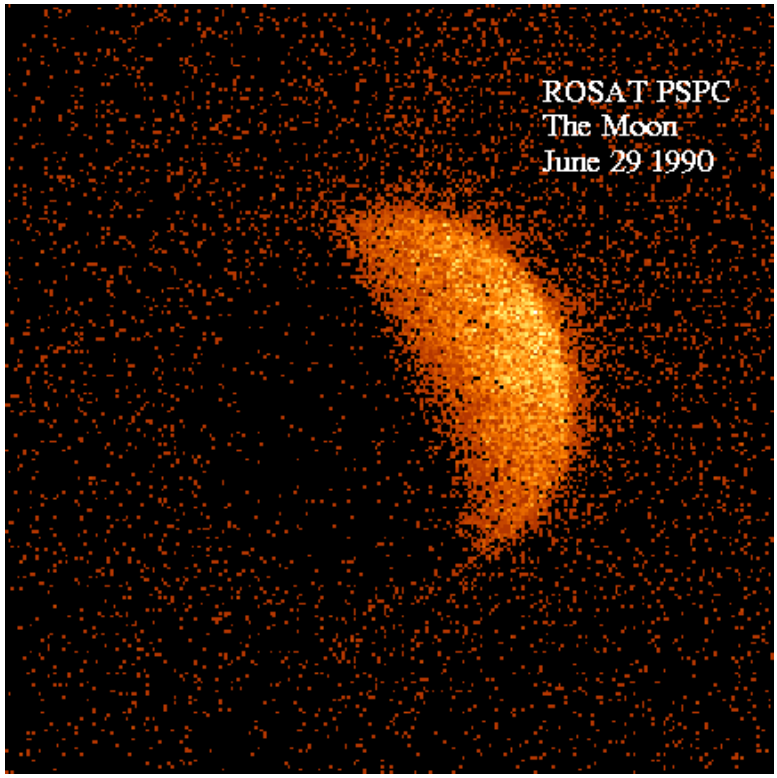

Figure 1.1: Image of the moon taken by the ROSAT PSPC, showing the fluorescence X-rays from the sunlit side and no significant emission from the unilluminated side. The events present on the dark side of the moon are attributed to geocoronal emission in the Earth's atmosphere.

technology development, scientific drivers and possible application in a number of space and terrestrial environments, while concentrating on their use in X-ray astronomy.

This chapter provides a broad overview of the science goals which motivate the work, introduces some of the technology necessary to pursue these scientific objectives, and finally provides a plan of the thesis.

1.1 Astrophysical X-ray generation

X-rays are high energy (~ 0.1 keV $\leq$ E$\leq$ 100 keV, 0.1Å$\leq \lambda \leq$ 100Å) electromagnetic photons. This large energy range and the variation in the behaviour (reflection, absorption etc.) of the photons within this range means that X-rays are further divided into "soft" (low energy) and "hard" (high energy). These definitions are somewhat arbitrary and depend on the context of the discussion. In this thesis, soft X-rays will be defined as those with energies below 10 keV, and hard X-rays those photons with E $\geq$ 10 keV. Any deviation from this convention will be explained in the text.

Many astrophysical processes can produce X-rays. These processes are often divided into two areas; "thermal" and "non-thermal" emission, and are explained in detail below.

1.1.1 Thermal emission

The main example of thermal emission is *black-body radiation*, where a source emits a spectrum of photons characteristic of its temperature. This spectrum is described by the Planck function (Equation 1.1), giving the proportion of the radiation emitted from a source of a given temperature as a function of wavelength (or energy),

$$I(\lambda, T) = \frac{2hc^2}{\lambda^5} \frac{1}{e^{\frac{hc}{\lambda kT}} - 1}, \tag{1.1}$$

with I the emitted intensity of radiation as a function of wavelength, λ (in metres) and temperature (T, in Kelvin), h is Planck's constant (6.63×10^{-34} Js), k is Boltzmann's constant (1.38×10^{-23} J/K) and c is the speed of light in a vacuum (3×10^{8} m/s). Wein's law relates the peak of the Planck function to a given wavelength, such that:

$$\lambda_{max} = \frac{b}{T}, \tag{1.2}$$

where λ_{max} is the peak wavelength (in nanometres), b is Wein's displacement constant (2.898×10^{-3} nm K) and T is temperature (in Kelvin). Therefore, Equation 1.2 gives the wavelength at which most photons are emitted from the source. For a thermal X-ray emission process, this wavelength is in the X-ray regime, and the source emits a significant fraction of the radiation in the X-ray band. Assuming the peak of the Planck function lies at an X-ray wavelength of 10 Å, Wein's law implies a characteristic temperature of $\sim 3 \times 10^6$ K. At these temperatures, thermal excitation of electrons from atoms can lead to multiple ionisation of the matter in the source, meaning that thermal X-ray sources often consist of highly ionised plasmas (explained in more detail in Section 2.4).

Another example of a thermal emission process is *thermal bremsstrahlung radiation*, where charged particles (usually electrons) are slowed when they scatter off other charged particles such as atomic nuclei. The Maxwell-Boltzmann distribution governs the velocities of the ions within a thermally excited plasma, and can be stated as

$$f(v) = \frac{4}{\sqrt{\pi}} \left(\frac{m}{2kT}\right)^{3/2} v^2 e^{-mv^2/2kT}, \tag{1.3}$$

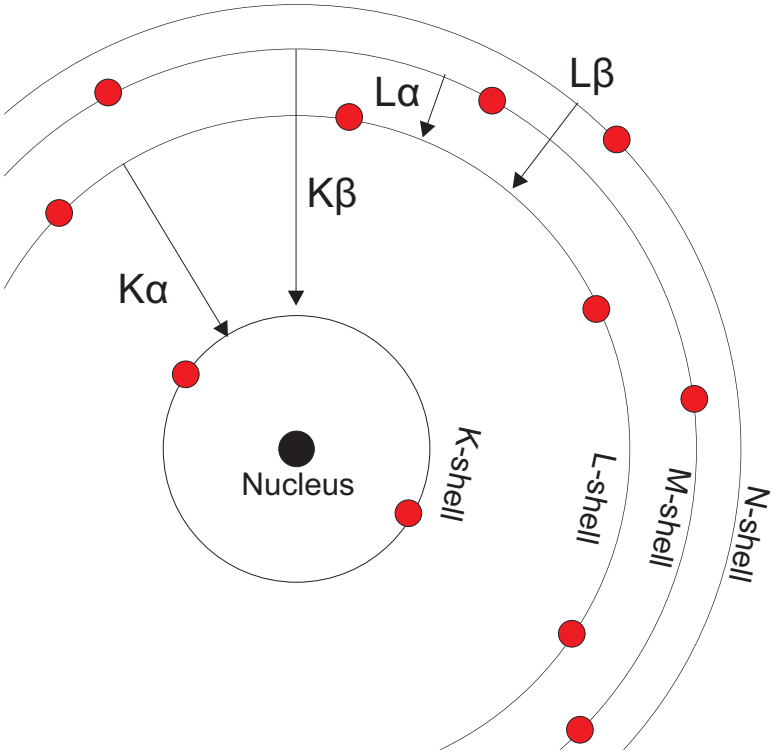

Figure 1.2: The shell picture of electron orbitals

where $f(v)$ is the fraction of particles having velocity v, and m is the particle mass. The other parameters are as defined in Equation 1.1. If we assume that the scattering is inelastic, the average velocity distribution is constant on a macroscopic scale, but continual changes in the direction of particles as they scatter off each other leads to the emission of X-ray radiation (here the cooling effect implied by the radiation of energy as X-rays is considered negligible).

1.1.2 Non Thermal emission

X-ray fluorescence is an example of a non-thermal process. As a photon or charged particle impinges on an atom, it deposits its energy and photo-ionises a core level electron. This creates an instability in the electronic structure of the ionised target anode material and electrons fall from higher energy electron orbitals (shells) into the lower energy states vacated by the ionised electron. The extra energy is released as an X-ray photon whose energy is given by the difference in the atomic energy

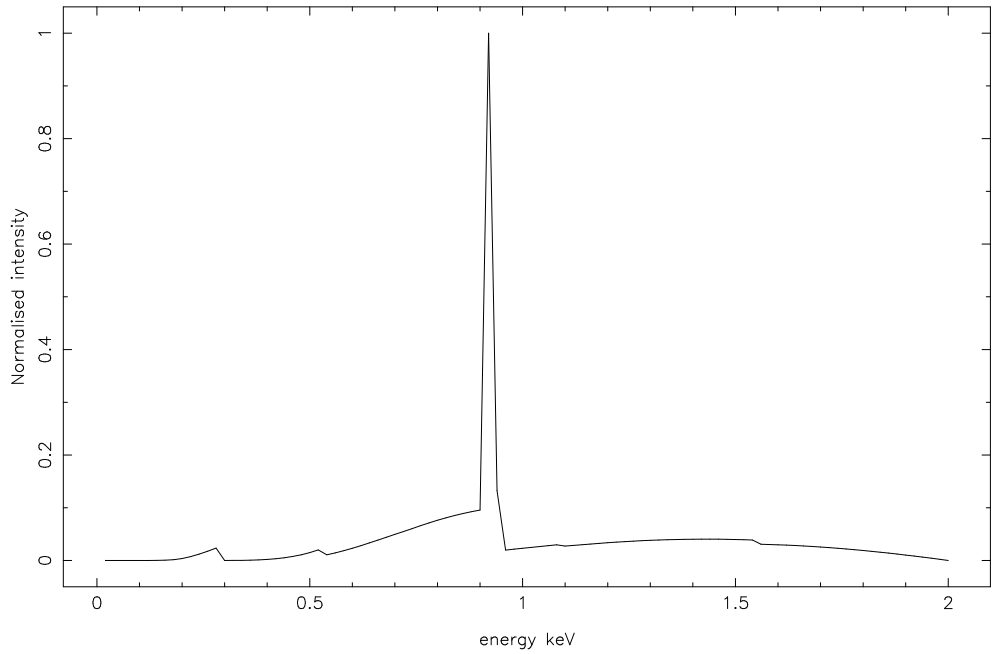

Figure 1.3: Typical theoretical X-ray spectrum from an electron bombardment source, including transmission through an aluminised lexan filter to remove the low energy photons. The tube accelerating voltage was assumed to be 2 kV. The Bremsstrahlung continuum is seen to be significantly lower intensity than the L-shell fluorescence from the copper anode.

levels involved. K-shell emission occurs when the excited electron comes from the innermost electron orbital (the K-shell) and an electron falls into the K-shell from the L- or M-shells, L-shell emission is when an electron is emitted from the L-orbital and electrons fall from the M- or N-shells (Figure 1.2). This process is used in the laboratory as a method for producing an approximately monochromatic beam of X-rays in an electron bombardment source (see Section 4.3.2 and Figure 1.3). In addition to this fluorescence line, a non-thermal Bremsstrahlung continuum will be present (Figure 1.3). This is caused by electrons being slowed as they impinge on the metal anode.

In a celestial context, excitation of a planetary surface by solar X-rays and solar wind particles leads to an X-ray fluorescence spectrum characteristic of the surface composition (see Section 4.2).

Other non-thermal processes include cyclotron and synchrotron emission, where X-rays are emitted owing to the acceleration of electrons in circular orbits within an intense magnetic field. These

processes will be considered further when the production of polarised X-rays is discussed in Chapter 6.

1.1.3 Astrophysically significant observables

X-ray emission processes all manifest themselves in terms of "observable parameters." To date the only extensively used observables are spectroscopy, photometry, imaging and timing, which are described below. They have provided extremely powerful diagnostics to constrain models proposed to explain the emission from celestial sources.

Spectroscopy is the study of the fraction of photons seen from a source at different energies. This can give information on the temperature, elemental composition, ionisation state and redshift (therefore distance) of matter where the photons are created. Spectroscopy also provides the only method of remotely measuring the magnetic field where the X-ray is emitted (at least in the absence of polarimetry, more later). This is done by observing the Zeeman effect where emission lines are split into discrete states by the presence of a magnetic field. In practice, it is usually the *inverse* Zeeman effect that is observed, where a similar splitting is observed for absorption edges (Kitchin, 1984). Therefore, emission and absorption features in the spectrum give a wealth of information about the nature of the environment in which they are created.

Photometry is the study of the number of photons emitted in all energy bands from a source. Spatially resolved photometry is often used, giving an image of the extended nature of a source (see *imaging* bullet). The nature of the bright and dim regions allow discrimination between different emission processes occurring at different positions in an extended source (e.g. supernova remnants).

Imaging a key data product from X-ray observatories is given by images of the morphology of

extended objects. These images allow us to recognise structures like the shells of some supernova remnants which give information about where the X-rays are created and the processes which are causing their emission.

Timing allows study of the evolution of the emission from a source as a function of time. Almost all X-ray sources exhibit variability at some temporal scale, a good example being X-ray pulsars. Pulsars can be described as astronomical lighthouses as they emit beamed radiation which passes into and out of our line of sight to the object as a function of time. The typically millisecond interval between the reception of consecutive pulses is interpreted as the rotation period of the source. If we observe pulsars for years or decades, pulsar spin periods are typically observed to be decreasing very slowly due to energy lost through radiation. Therefore, on timescales of hundreds to thousands of years the rate a pulsar spins at will change significantly, thus demonstrating the broad array of characteristic timescales even in a single astrophysical source.

Independently, all four measurements are powerful diagnostics of the behaviour of matter within the source, but by combining them, substantially more information is revealed. Consider an instrument that can measure the intensity and energy of the incident photons as a function of position and time. Such an instrument can record all three of these observables and give a much more comprehensive picture of a source than any of them individually. An obvious example of such a device is a CCD (described below), which can record the position (at an accuracy of approximately the pixel size of the device), the measured energy of the photon (limited by the Fano factor[1]) and, finally, the time of arrival of the photon (limited by the readout time or clocking frequency).

A number of unanswered questions exist in X-ray astronomy because of the degeneracy of predictions from competing models of certain emission processes when constrained solely by these three observ-

[1] This is a measure of the dispersion of the statistical distribution of the number of electron hole pairs created on absorption of a photon with a given energy. For silicon detectors such as CCDs, this number is ~ 0.12 (Michette, A., 1993).

ables. One example of this was the argument in the early 1970s as to whether the emission from the Crab nebula was governed by a complex thermal spectrum, or by emission via a synchrotron process. It was only with the direct measurement of polarisation of the X-rays that this degeneracy could be broken. Unfortunately, to date this remains the only conclusive measurement of polarisation in an astrophysical X-ray source (Chapter 6). The implied difficulty of polarisation measurements is real and means that the long-awaited addition of two new observable parameters (the degree (P) and direction (θ) of polarisation) released by X-ray polarimetry is yet to be achieved. This will be discussed further in Section 1.5.3 and Chapters 6 and 7.

Measurements of these observables must be extremely well understood in terms of the instrument characteristics in order to effectively constrain theories on astrophysical X-ray emission. Instrument effects must be distinguished from those occurring in the target object where typically, several emission processes will be occurring in any given source. Add to this the absorption of X-rays due to gas, dust, plasmas etc. along the line of sight to the object and it becomes very difficult to disentangle all of the processes which are occurring. Consequently, the instruments used to make these measurements must be extremely well calibrated and characterised. They must also have high efficiency in order to capture as much of the (intrinsically low) flux from celestial X-ray sources as possible. Therefore, highly complex space based telescope systems are needed to generate useful data in X-ray astronomy. Such observatories have existed for over 30 years, increasing in complexity over time but yielding new diagnostic power with every new instrument.

1.2 Historical X-ray astrophysical observatories

Instrumentation for X-ray astronomy has to be space based due to the attenuation of X-rays by the atmosphere. High altitude balloon flights and sub-orbital sounding rocket flights were used extensively in the early days of X-ray astronomy in order to overcome this attenuation and are still used today

(e.g. Cruddace *et al.* (2002) or Harrison *et al.* (2000)). However, the short exposure times, coupled with the typically weak signals from these sources makes such transient observations problematic.

A better way of observing X-ray sources is from a dedicated orbital platform where the observation time is not limited to the (∼few minute to few hour) duration of the rocket or balloon flight. The early *OSO* series of satellites[2], used mainly to observe the Sun, employed collimators to restrict the field of view and as such had little imaging capability (the only imaging being possible by rastering the field of view over an object). Nevertheless, these satellites provided a marked step forward in our understanding of the X-ray universe. For instance, OSO 8 detected the iron line signature in clusters of galaxies (Mushotzky *et al.*, 1978, Smith *et al.*, 1979), detected the black body nature of X-ray bursts (e.g. Swank *et al.* (1976)) and placed upper limits on the polarisation of a number of celestial X-ray sources (e.g. Long *et al.* (1980))[3]. These remain the latest results X-ray astronomical polarimetry, a topic which will be covered in more detail in Chapters 6 and 7.

Einstein was launched in November 1978 and was the first orbital platform to employ grazing incidence (Wolter 1) focusing optics (Giacconi, 1980). As such, its sensitivity was over 100 times greater than any previous X-ray instrumentation, reserving its place as the first of the great X-ray observatories. It performed the first high resolution spectroscopy on supernova remnants as well as being the first telescope to resolve numerous discrete X-ray sources (for instance in the Andromeda galaxy). *Einstein* was followed by *EXOSAT* which allowed imaging, photometry and medium resolution spectroscopy. The impressive array of instruments it carried allowed it to discover quasi-periodic oscillations (the periodic flaring of low mass X-ray binaries – e.g. Dieters *et al.* (2000)) and X-ray pulsars, as well as studying the variability of active galactic nuclei and the presence of iron lines in galactic and extra-galactic sources.

[2] http://en.wikipedia.org/wiki/Orbiting_Solar_Observatory
[3] http://imagine.gsfc.nasa.gov/docs/sats_n_data/missions/oso8.html

The launch of *ROSAT* in 1990 and the subsequent decade of its operational life saw yet another great leap forward for X-ray astronomy. The first 6 months of operation were dedicated to the first ever all sky surveys using imaging instruments. These were in the energy ranges $0.1 - 2.5$ keV, using the 2.4 m focal length telescope and imaging, Position Sensitive Proportional Counter (PSPC) detector and in the $\sim 60 - 200$ eV range using the wide field camera (WFC) which had a microchannel plate detector (Pounds *et al.*, 1993). Both of these telescopes employed Wolter-1 focusing optics, optimised for the energies of interest. Later, targeted observations with *ROSAT* showed the X-ray brightening of Jupiter's auroral zones after the impact of the comet Shoemaker-Levy 9 in 1994 (Waite *et al.*, 1995) and also discovered persistent X-ray emission from comets. The length of the mission allowed the first temporal studies of the emission from stars over the stellar magnetic cycle (11 years for the sun, typically 8-15 years in most solar-like stars).

1.2.1 Mature X-ray detector technologies

The first detectors used in X-ray astronomy were simply Geiger counters attached to sounding rockets, and possessed no imaging capabilities. However, there now exists a broad array of suitable equipment available for astrophysical X-ray detection (Figure 1.4).

1.2.1.1 Gas counters

Absorption of an X-ray in a gas leads to the generation of ions and electrons which can then be accelerated towards an electrode by the application of an electric potential. This acceleration leads to further excitation of secondary particles, inducing a signal on the electrodes. If this charge is "read" by grids of electrodes, the position of the incident charge can be reconstructed. Hence, the device is an imaging, photon counting detector. The advantage of these devices is that they can be made extremely large to cover a large focal plane. They also have a directly calculable efficiency making

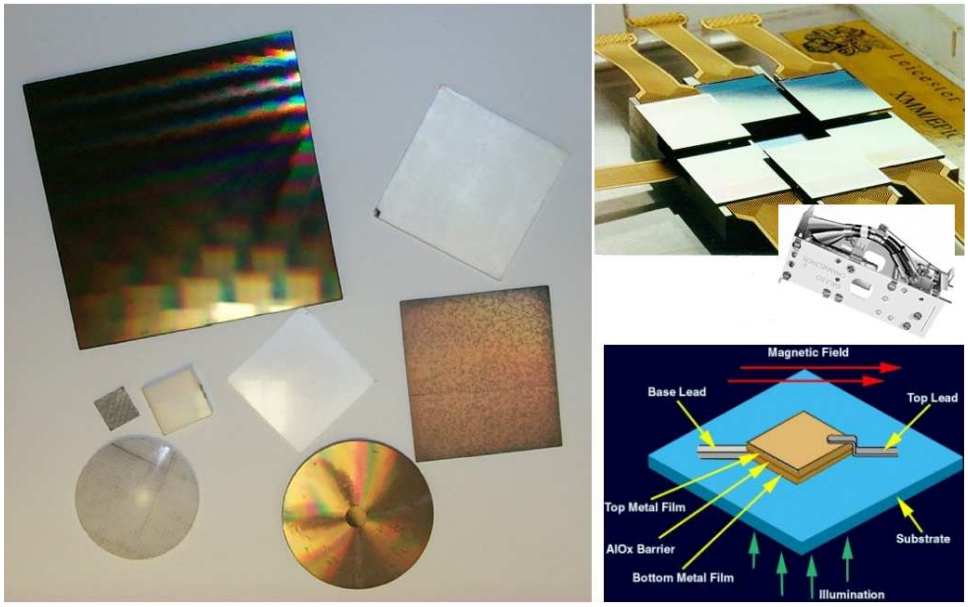

Figure 1.4: A selection of different detector technologies. Clockwise from the left; a selection of microchannel plates, the XMM - EPIC camera CCD focal plane, A channel electron multiplier and a schematic diagram of a superconducting tunnel junction.

them ideal as a reference standard detector for photometric calibration and possess limited energy resolution (e.g. $\sim 51/\mathrm{E}^{-0.5}\%$ for the medium energy detector array (MEDA - Turner *et al.* (1981)) and $\sim 27/\mathrm{E}^{-0.5}\%$ for the gas scintillation proportional counter (GSPC - Peacock *et al.* (1981, 1985)), both flown on *EXOSAT* and reviewed by Fraser (1989) further generations of this technology have flown on, for example, *beppoSAX* (e.g. Smith *et al.*, 1987)).

1.2.1.2 Electron mulitpliers

Although the first solid state X-ray multipliers were discrete dynode devices – where electrons were accelerated from one dynode to another by an electric potential, a better solution is achieved using a continuous dynode electron multiplier or channel electron multiplier (CEM). In such a device, X-rays incident on semiconducting glass tubes of diameter $\sim 0.1 - 1$ mm emit electrons and yield an exponential amplification (or avalanche) of charge when a high voltage is applied between the two ends of the tube. This gain of $\sim 10^6$ electrons is high enough to induce space charge saturation, meaning

that no more electrons can be excited from the glass near the channel exit. Therefore, the CEM can be used as a photon counting detector because the gain and efficiency is constant for small changes in bias voltage. The tubes are generally curved to prevent ions, created by ionisation of residual gas within the tube, from propagating to the input surface and initiating spurious noise counts in a process known as ion feedback.

An array of such devices could be used to provide an imaging capability, by stacking CEMs together. However, a much better way of doing this became available after the declassification of microchannel plate technology in the late 1960s. Microchannel plates (MCPs) offer the ideal solution to the need to stack many discrete CEMs to simulate an imaging detector. MCPs are lead glass disks with millions of closely stacked microscopic pores. Typical channel diameters are $\sim$ 10-20 μm with each pore working in a similar manner to a CEM channel. MCPs have a similar high gain, but with much more compact geometry and higher spatial resolution than possible with an array of CEMs.

1.2.2 The current state of the art detectors

The current great observatories have differing focal plane instruments, the chandra high resolution imager is based on MCP technology (section 1.2.2.1), whereas the principal instruments on *XMM* are solid state detectors (section 1.2.2.2).

1.2.2.1 Microchannel plates MCPs

The Chandra High Resolution Camera (HRC) (e.g. Lees & Pearson (1997)) is a large area microchannel plate detector. As this thesis is concerned primarily with X-ray instrumentation, it must be stated that the HRC is likely to be the last MCP detector ever flown on a large scale X-ray astronomy satellite. The reason for this fall in popularity of MCPs in X-ray astronomy can be explained by the growing desire for high resolution imaging spectroscopy. Devices optimised for such measurements

include CCDs and possibly in the future, arrays of cryogenic detectors (Saab *et al.*, 2004).

Despite this rather bleak outlook for the MCP, if we broaden the wavelength range of interest to include longer wavelengths between ultraviolet and X-rays, MCPs will retain their importance because of their unparalleled combination of spatial and temporal resolution. The future for these devices is likely to lie in two areas;

- Orbiting Ultraviolet observatories, where their high efficiency and high spatial resolution make them ideally suites to sit in the focal plane of dispersive spectrometers (Barstow *et al.*, 2003) or as the imaging detector for a wide field of view telescope for ultraviolet auroral imagery (Bannister *et al.*, 2007).
- Spin-out into terrestrial applications (Chapters 2 and 3).

A detailed description of MCPs is left until Chapter 2.

1.2.2.2 Charge coupled devices - CCDs

In simple terms, a CCD is an integrated circuit containing an array of coupled capacitors. These capacitors store charge excited by the arrival of a photon until it can be read out and can, therefore, be used as discrete pixels in an imager. A clocking mechanism is used to transfer charge form one pixel to the next and eventually into the readout electronics. An image can later be recreated during data analysis so long as the readout sequence is known.

The amount of charge deposited in the detector is directly proportional to the energy of the incident photon (so long as only one event falls in the pixel before it is read out) meaning that a CCD is intrinsically an imaging spectrometer. This makes them ideally suited to X-ray astronomy where numerous examples can be quoted (eg. Soltau *et al.* (1996), Ambrosi *et al.* (2002), Bautz *et al.* (2000)

or future proposed instruments reported by Short (2005) and Strüder (1999)).

1.2.3 Imaging and early optics

In selecting the best detector for a given application, it is necessary to consider the characteristics of the "optics" which are employed. For instance, a collimated device or wide field telescope will need an extremely large area detector, meaning that the most appropriate choice is probably a gas counter. Conversely, if a high resolution focusing optic is used, a detector with good imaging resolution is needed and the requirements on energy/timing resolution dictate which one is used (Section 1.3). This section summarises some of the most common X-ray optical designs used in X-ray astronomy missions.

1.2.4 Collimators

Instruments flown on the first sounding rocket flights had no collimation and hence viewed large areas of the X-ray sky providing little information on source distribution. To resolve sources from each other, it was necessary to add collimation to the detectors to help restrict the field of view and give a crude imaging capability. True imaging came later, using grazing incidence, focusing optics and allowed morphological studies of extended X-ray sources.

Collimators work by restricting the field of view to a given "open angle." Consider an array of parallel channels whose walls are made out of a strongly absorbing material. An X-ray which is incident at an angle such that it passes down the channel without intersecting the wall will be transmitted through the collimator, while a ray which impinges on the channel wall will be absorbed. This defines an angular field of view equal to the open aperture of the channel, i.e. twice the angle given by the ratio of the channel length to diameter (Figure 1.5).

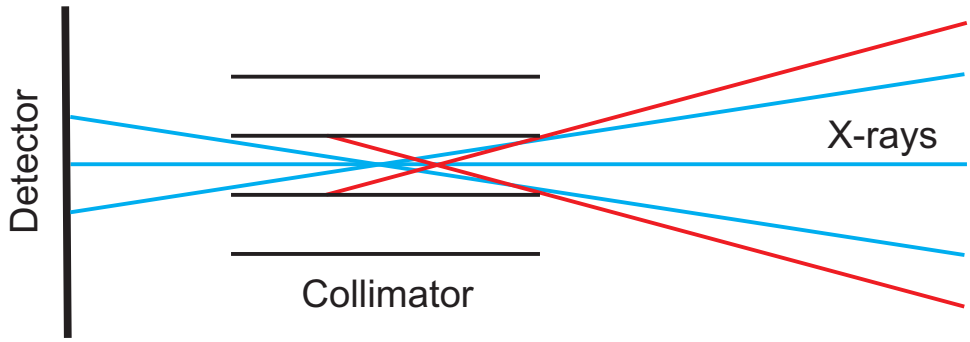

Figure 1.5: Schematic diagram of the operation of a collimator. The blue rays are transmitted while the red rays are absorbed and the open angle of the channels (ie the ratio of length to diameter) defines the angle of acceptance.

Restricting the field of view in this way means that rastering the instrument over an extended source gives a poor resolution "image" of that source. True imaging optics are required to achieve better resolution.

1.2.5 Imaging optics

At X-ray energies, photons are difficult to bring to a focus because of the low critical angle for X-ray reflection. At angles greater than $\sim 1 - 5°$, X-rays are absorbed by the medium on which they are incident rather being reflected by it. This means that the standard, normal incidence, telescope geometries used for optical light are inapplicable to high energy telescopes. To effectively focus X-rays, the photon incidence direction must form a shallow "grazing angle" to the surface from which it will reflect. Hence, the development of a number of grazing incidence geometries for focusing high energy photons (Figure 1.6).

A Kirkpatrick Baez (KB) optic uses two sequential ellipsoidal surfaces which are arranged in series and are set orthogonal to each other (Kirkpatrick & Baez, 1948). Each reflection brings the photon to a line focus in the direction perpendicular to the principal axis of the ellipse. As the axes of the successive ellipses are orthogonal, two successive reflections bring the photon to a point like focus.

Angel (1979) described a modification to the KB geometry in which the successive orthogonal reflectors are coincident in space, thus effectively forming square channel cross section pores. If the axes of the channels lie perpendicular to the surface of a sphere, photons from infinity are focused onto a spherical focal plane that is half the radius of this sphere. This is the focusing mechanism employed in the eyes of lobsters and other crustaceans and is, therefore, often called the *lobster eye* geometry. It is interesting to note that such an optic can theoretically give a 4π Sr field of view, making it ideally suited for application as a wide field telescope.

The final geometries I will consider (and the ones most commonly used in X-ray astronomy) are those proposed by Wolter (1952a,b) and reviewed in English by Aschenbach (1985). There are three types of Wolter telescope (types I, II and III), all of which are based on two successive reflections off paraboloids, hyperboloids or ellipsoids of revolution as shown in Figure 1.6. For a single reflection from a focusing mirror shell, severe coma distortion is expected for off axis sources (those where the wavefronts are not perpendicular to the optical axis). The double reflection in the Wolter geometries reduces the image distortion expected from a single grazing incidence reflection from photons which arrive at an off axis angle and as such, the Wolter-I geometry has been used extensively in X-ray astronomy satellites.

To simulate a large area telescope aperture, it is necessary to nest large numbers of mirror shells inside each other as the projection of a surface of revolution at the critical angle for X-ray reflection will be small. Mirrors are formed and polished to the required parabolic and hyperbolic surface for the Wolter I system then nested inside each other to fill the geometric open aperture of the telescope.

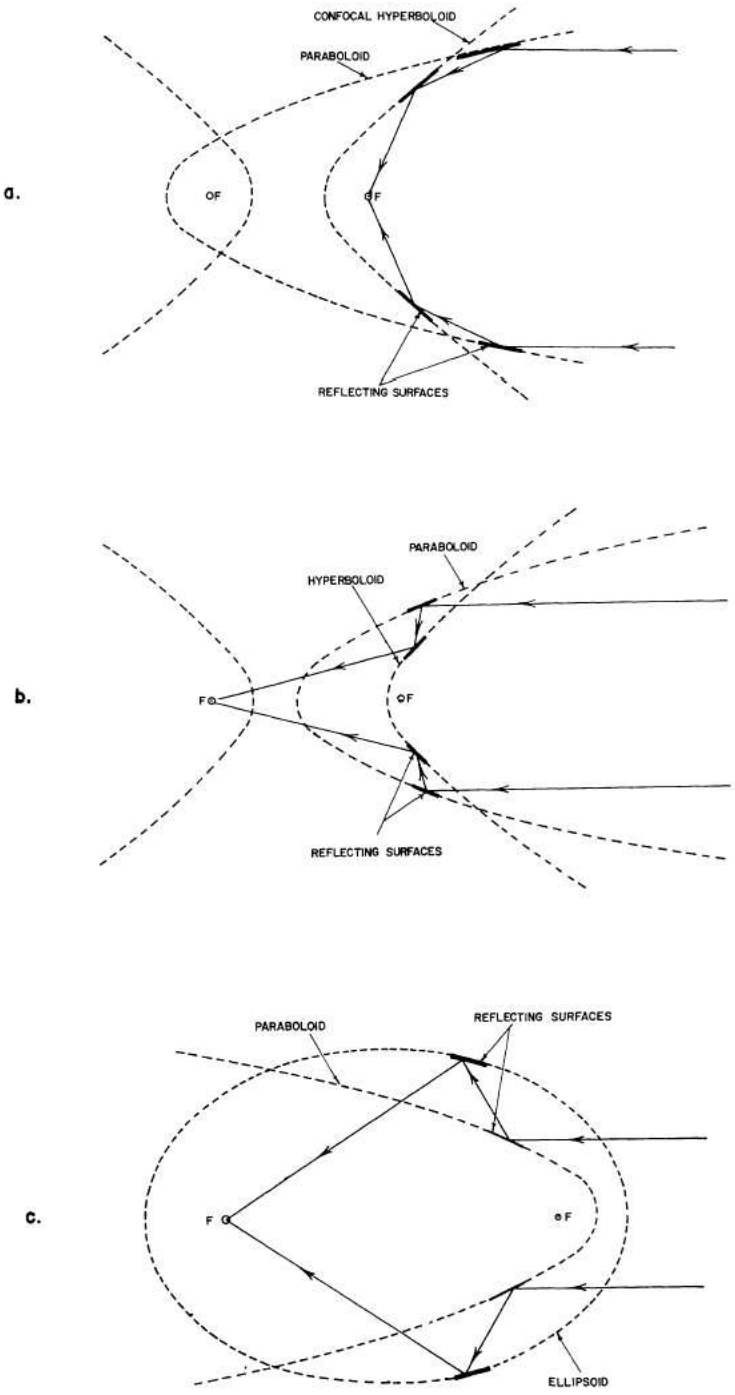

Figure 1.6: The Wolter geometries (after Giacconi *et al.* (1969))panels a, b and c are respectively; the Wolter-I , Wolter-II and Wolter-III geometries

Figure 1.7: Photographs of the three operational observatories in their clean rooms prior to launch. From left to right *Swift*, *XMM* and *Chandra* (Photos courtesy of NASA (left and right) and ESA (center)).

1.3 Current observatories and instruments

The current "great observatories," *Chandra* and *XMM Newton* and the *Swift* gamma ray burst observatory (described by Winkler *et al.* (1993), Janson & Murdin (2002) and Gehrels & Swift (2004) respectively) (Figure 1.7) have built on the experience gained from the early missions and the rapid advances in mirror and detector technologies mean that they have allowed the field of X-ray astronomy to flourish in recent years. These telescopes continue to yield a great deal of new science because of their unprecedented angular, energy and spatial resolutions. The capabilities of the three telescopes are complementary and by combining data from them, much greater insight into astronomical sources is possible as different mirror technologies and focal plane instrumentation optimise *XMM* for spectroscopy, while *Chandra* has better imaging capabilities (*Chandra* has a lower effective area, 400 cm^2 at 0.25 keV, but a much higher angular resolution, $\leq$ 1 arcsecond, compared *XMM*'s 1500 cm^2 and 6 arcsecond resolution).

Swift's, high speed slewing capabilities and the broad array of instruments it carries has enabled study of the most energetic events in the universe - the gamma-ray bursts. These events are thought to

be the birth of new black holes and the influx of data from *Swift* has helped to constrain models of how this occurs and increased our understanding of the fate of numerous stars. Such discoveries have fueled the desire for more powerful instruments to probe the X-ray sky.

All three of the current "great observatories" employ the Wolter-I geometry, with the nature of the nested shells differing for each of the three telescopes. *XMM* uses 58 lightweight metal-foil mirrors to generate a large effective area, *Chandra* uses more robust glass substrate mirror technology to give its high spatial resolution, and the XRT on *Swift* is a similar design to *XMM* but with fewer shells (12) because of its smaller size and mass.

1.4 Future space missions

The future of X-ray astronomy is bright as a wide variety of observatories have been proposed which have been concieved in order to answer the questions which remain unaddressed by today's operational observatories. The European and US flagship missions scheduled for launch in the next deccade are *XEUS* and *Constellation-X* which will combine much increased effective area and comparable angular resolution to *XMM* and *Chandra*. These characteristics will enable observations of much fainter, and therefore more distant sources, allowing astronomers to brobe previously unseen regions of the universe as well as improving our understanding of the objects we know of today. The Russian *Spectrum Roentgen Gamma (RG)* mission is intended to have carry a high energy resolution cryogenic spectrometer as well as the sky survey instruments *e-Rosita* and *WFT* which will over the course of the mission create the most detaild X-ray sky surveys to date (more later). *NEXT* is a Japanese mission dedicated to hard X-ray (> 10 keV) imaging spectroscopy opening up an area of science which is to date highly underdeveloped when compared to observations in the soft X-ray band (http://www.astro.isas.ac.jp/future/NeXT/).

As well as these missions led by the traditional "heavyweight countries" of X-ray astronomy, a number of other missions exist which are due for launch in a similar time scale. These include; *Astrosat* - the first Indian astronomical satellite, the Chinese Hard X-ray modulation telescope (HXMT) which will offer the most detailed hard X-ray (20-200 keV) sky survey to date (Li *et al.*, 2006), and *MIRAX*, a Brazillian X-ray astronomy mission to provide continuous broadband imaging spectroscopic observations of a large number of sources in the central Galactic plane region (Braga *et al.*, 2004).

I will now discuss a discrete number of these future space missions in X-ray astronomy (specifically those which are expected to employ the different instruments described in this thesis). These are listed in Table 1.1. In these missions, the higher effective area, spatial and spectral resolution and improved temporal coverage of objects in the sky will undoubtedly lead to more discoveries of new and exciting processes which are currently unobservable because of the limitations of existing technology.

The future instruments onboard *XEUS* (Parmar *et al.*, 2006) and the wide field telescope *WFT* on *Spectrum RG* (Pavlinsky *et al.*, 2006) will not only improve our knowledge of known phenomena, but will open up a new "discovery space" containing new and unforeseen science. They are described in more detail in Chapter 4 and Section 1.4.1.

As well as these advances in traditional X-ray astronomical instrumentation, a completely new field will be enabled by the ESA *BepiColombo* mission to the planet Mercury as it carries the first ever focusing X-ray telescope for planetary science applications. The telescope will perform a similar experiment for Mercury to that attempted by Giacconi *et al.* (1962) and Adler & Trombka (1977) for the moon, by measuring the solar wind induced X-ray fluorescence from the surface of the planet. This should yield the composition of the regolith and any influences thereon caused by the geological history of different regions of the surface. This will be discussed in Chapters 4 and 5 where the design and characterisation of the optics for the experiment are considered.

Name	Launch date	Agencies	Details
World Space Observatory	$\sim$ 2012	China, Russia + bilaterals	Orbital ultraviolet telescopes.
BepiColombo	$\sim$ 2012	ESA, JAXA	Mission to study the planet mercury. First X-ray telescope on a planetary science mission.
WFT[1]	$\sim$ 2012	Russia (IKI)	Wide field of view X-ray telescope. Extremely high temporal coverage, once per orbit.
XEUS	$\sim$ 2020	ESA, NASA	5 m^2 effective area. Unprecedented spectral resolution

Table 1.1: Detailing the future space missions towards which this work is directed. [1] on board *Spectrum RG*

1.4.1 XEUS

The European Space Agency (ESA) *XEUS* mission (Parmar *et al.*, 2006) and NASA's *Constellation-X (hereafter Con-X)* (Tananbaum *et al.*, 1999) are the successors to *XMM-Newton* and *Chandra*, scheduled for launch in the timeframe 2015-2025. They are ambitious telescopes offering several square metres of effective area ($\sim$5 m^2 at 1 keV for XEUS (Bavdaz *et al.*, 2006)) and incorporate instrumentation including cryogenic spectrometers capable of $\sim$eV energy resolution, at high spatial and temporal resolution. *XEUS* comprises two spacecraft, a mirror module and a detector module flown in formation to a precision of a few mm, the telescope focal length is 35 m with a field of view of $\sim$ 1 arcmin and angular resolution of $\sim$ 2-5 arcsec for the narrow field, high energy resolution detector and $\sim$ 7 arcmin for the wide field instrument giving CCD-type ($\sim$70-100 eV energy resolution). The energy bandpass is 0.5 keV $\leq$ E $\leq$ 50 keV.

Con-X has evolved from an original concept of a four-telescope constellation, to a mission with four telescopes on a single platform. It has an effective area of $\sim$ 1 m^2 at 1 keV and an energy bandpass of

0.25 keV $\leq$ E $\leq$ 80 keV, covered by different telescopes optimised for a particular energy range[4]. Most of the following discussion relates to *XEUS* and therefore further discussion of the *Con-X* design is omitted.

1.4.1.1 Cryogenic detectors

Improvement in spectral resolution is of key importance for the next generation of space telescopes. For CCDs, reducing the temperature of operation yields improved spectral resolution until the intrinsic limit (typically greater than $\sim$ 100 eV) set by the Fano factor is encountered. This limit is caused by dissipation of a finite amount of energy in processes which do not lead to the creation of electron-hole pairs in the silicon lattice (Janesick, 2001) and is achieved at temperatures of $\sim$ -50 °C. To achieve resolution in excess of this limit, cryogenic devices which operate at extremely low temperatures ($\sim$ mK to a few K depending on which type) are needed.

Cryogenic detectors are the future of X-ray spectroscopy. The low noise in these superconducting devices means that the intrinsic energy resolution is only a few eV, approximately 100 times better than a CCD at comparable photon energies. There are two main types of cryogenic detector. One is a superconducting tunnel junction (STJ), where electrons tunnel through a potential barrier into the electronic conduction band of the atomic lattice. The second is a transition edge sensor (TES). Here, a material is maintained at a temperature which lies on the transition between a superconducting and normal state. An incident photon raises the temperature of the absorber, leading to a large, measurable, change in the resistivity of the material and a measurable pulse which is proportional to the energy of the incident photon. Attempts to make large arrays of TESs capable of operating as a high resolution imaging spectrometer for *XEUS* are ongoing (e.g. Saab *et al.* (2004)).

[4] http://constellation.gsfc.nasa.gov/

1.4.1.2 The future of X-ray optics

The optics for *Con-X* are similar to those of Chandra but with more compact nesting to give increased effective area. It is proposed that *XEUS* will incorporate a new mirror technology manufactured from micro-machined silicon wafers (Bavdaz *et al.*, 2006). This micropore technology is expected to enable high effective area for a given mass. Both telescopes employ a Wolter-I geometry.

1.4.2 WFT and BepiColombo

Two other missions exist which could have a big role in future X-ray astronomy. These are ESAs *BepiColombo* mission to the planet Mercury, which will carry the first ever imaging X-ray telescope for planetary science applications, and the Russian *Spectrum RG* mission (Pavlinsky *et al.*, 2006) which could carry the British-led wide field telescope (*WFT*). This is a telescope offering almost full-sky coverage every orbit of its parent platform. This enormous temporal coverage of the sky will offer an exciting new perspective on the cosmos which will be described in more detail in Chapter 4.

1.4.2.1 Detectors

Gas counters are the proposed focal plane detector for *WFT*, where the need to cover a large focal plane makes competing technologies such as CCDs impractical (the need to cool such a large CCD focal plane would mean the power consumption would be too high).

BepiColombo will employ a radiation-hard type of silicon detector because the high radiation environment at Mercury would degrade the performance of a CCD too quickly. This device is known as a DEPFET active pixel sensor. However, the specific details of these devices are omitted as this thesis is concerned with the optics for these missions and not the detectors.

1.4.2.2 Novel microchannel plate optics

Both *WFT* and *BepiColombo* employ microchannel plate optics, a new technology of X-ray optic offering unsurpassed effective area for a given mass. They are particularly good for wide field telescopes, as they can be made to approximate to the lobster eye geometry described by Angel (1979) and for compact, low mass Wolter-type systems where the size and mass of traditional optics make them unsuitable. These optics have been described widely in the literature and will be described in detail in Chapters 4 and 5.

1.5 The subject of the current thesis

The preceding sections of this chapter have summarised a number of the advances made in X-ray astronomy. Progress in instrumentation has always led to improvements in our understanding of the X-ray Universe, providing the scientific driver for the current work and this thesis is concerned with efforts to develop technology in three areas, which are described briefly in this section.

1.5.1 Small pore microchannel plate detectors

As discussed in the previous sections, MCP detectors are a well established technology for current and future X-ray instrumentation (Section 1.2.1). Many examples of the use of microchannel plate detectors can be quoted in an astrophysical context (e.g. Barstow *et al.* (1985a), Fraser (1989), Lees & Pearson (1997) and future proposed applications e.g. Barstow *et al.* (2003) or Bannister *et al.* (2007)). Manufacturers have progressively reduced pore sizes to the current limit of ~ 2 μm (e.g. Laprade & Reinhart (1989), Laprade & Starcher (2001)) in order to improve the mass resolution for time of flight mass spectrometers and spatial resolution for single photon counting detectors. For photon counting detectors, the spatial resolution is limited by the pore diameter so long as the readout can achieve

better than this intrinsic limit (e.g. Lapington (2004)). However, MCP's high speed timing response is also limited by the pore diameter, where reduction in the size of the channels leads to improved temporal resolution (Fraser, 1990). This unique combination of $\sim \mu$m imaging resolution and 10s of picosecond time resolution makes the new small pore MCPs, designed for a space environment, ideally suited for terrestrial biological imaging solutions.

The desire to "spin out" these MCP detector technologies from astronomy into terrestrial applications has been pursued for a number of years by the University of Leicester's Bioimaging unit[5]. For instance the high resolution camera for the Chandra X-ray observatory has found a new use in biological imaging through the field of MCP-Beta Autoradiography (Lees & Pearson, 1997, Lees *et al.*, 1997). Chapters 2 and 3 describe preliminary work undertaken by the author to demonstrate the feasibility of using the exceptional temporal resolution of new small pore MCPs (Fraser, 1990) in a terrestrial context for a new technique to enable high speed imaging of biological samples (Section 2.4.2.1).

1.5.2 Microchannel plate optics

Section 1.2.3 describes the development of focusing geometries for X-ray radiation. Square pore microchannel plates can be used to approximate to the Wolter I geometry if the pores are arranged in a radial fashion. A tandem of MCPs slumped to different radii of curvature form a conic approximation to the paraboloid and hyperboloid surfaces in the Wolter-I geometry (Price *et al.*, 2002a). This conic approximation holds because of the short (few mm) length of the MCP channels and two successive reflections from the channel surfaces bring X-rays to a point focus.

If a cartesian (square packed) packing geometry is used, then MCPs approximate to the KB or Lobster eye geometries, depending on whether the optic is planar or slumped to a spherical radius of curvature (e.g. Brunton *et al.* (1995, 1997), Price *et al.* (2002b) and references therein). A planar, square pore,

[5] http://www.src.le.ac.uk/projects/bioimaging/

square packed MCP can be used as a point to point imaging device forming an unmagnified, image of the source with a cruciform point spread function if the image distance is equal to the object distance. The true lobster geometry is achieved if such a square pore, square packed optic is slumped to a spherical radius of curvature, enabling focusing of objects at infinity.

MCPs offer a moderate (arcminute) spatial resolution. However, they do so over a very large area, for a fraction of the mass required for more traditional mirror shell technologies, meaning that the effective area for a given mass is drastically increased. This will enable true X-ray imaging optics to form part of planetary science missions such as *BepiColombo*, where a conventional X-ray telescope would be prohibitively heavy. This will enable X-ray fluorescence spectroscopy of the planetary surface, in order to determine its composition from orbit.

MCP optics are described more comprehensively in Chapters 4 and 5 where the authors work to test and verify the performance of recent radial and cartesian-packed MCP samples is discussed. The aim of this work was to prove that the manufacturing process has matured since earlier work (e.g. Price (2001) or Nussey (2005)) and that it is approaching the requirements for *WFT* and *BepiColombo*.

1.5.3 X-ray polarimetry

To date, the only observable parameters used extensively in X-ray astronomy have been imaging, spectroscopy, photometry and (to a lesser extent) timing (Section 1.1.3). However, there exist another two observational parameters, routinely used in astronomy in other wavelength bands, which are both accessed by observing the linear polarisation of light from the source.

Photons consist of perpendicular electric and magnetic fields oriented at 90° to the velocity vector of the photon, where linear polarisation is a measure of the orientation of the electric field in space. A 100% polarised beam has all photons with their electric field vectors parallel, and an unpolarised

beam has random orientation of the electric field (Section 6.1). Different emission mechanisms for the photons give differing degrees of linear polarisation. Therefore, measuring the degree (P) and angle (θ) of polarisation allows direct diagnosis of the emission mechanism and geometry of the emitting region.

To date the instrumentation used to measure linear polarisation at X-ray wavelengths has remained insensitive to all but the Crab nebula. This is because of its seemingly unique combination of high brightness and relatively large polarisation at X-ray wavelengths. However, the expected arrival of the next generation of X-ray telescopes *XEUS* and *Constellation-X* (Section 1.4.1) have reopened the possibility of flying a highly sensitive X-ray polarimeter. A number of attempts have been made to provide such a device using a multitude of differing technologies, these will be discussed in detail in Chapters 6 and 7 where particular reference will be made to the author's contribution to producing narrow bandwidth polarising filters and how these devices could impact on the science questions addressed by studying celestial X-ray polarimetry.

1.6 Thesis outline

The following chapters describe the author's work in the three areas described in Sections 1.5.1 to 1.5.3. The thesis chapters are arranged as follows:

MCP detector technology

Chapter 2 introduces microchannel plates and their use as X-ray and charged particle detectors. It goes on to describe the technological and experimental factors which govern their behaviour and finally discusses the potential future application of MCP detectors in a number of contexts. Chapter 3 describes a number of experiments to validate the operation a set of new small pore (3.2 μm pore diameter) MCPs as high speed, imaging, photon counting detectors and discusses the potential

advantages of using these new, smaller pore sizes. It concludes that ultra fast timing resolution is possible with these new MCPs but further work is proposed to optimise their response both in the temporal and spatial domains.

MCP optics

Chapter 4 introduces the use of square pore MCPs as focusing X-ray optics, describing the differences between MCPs for application as detectors and optics. Future applications are discussed in the context of both terrestrial use in the laboratory and in two space missions *WFT* onboard *Spectrum RG* and *BepiColombo*. The differences between different focusing mechanisms (Wolter and "Lobster eye") are described, along with different methods of testing slumped and planar optic samples both mechanically and optically at X-ray wavelengths[6]. Chapter 5 describes experimental testing of a number of optics along with theoretical Ray trace modeling to explain and interpret the experimental data. Comparisons are drawn between theoretical and experimental results.

X-ray polarimetry

Chapter 6 forms a summary of the work so far completed in astrophysical X-ray polarimetry. First, the chapter describes the polarisation of light, the mechanisms which can cause it and techniques for measuring it. Future proposals for making sensitive polarimetry measurements are reviewed in terms of a number of new detection technologies. Finally, a polarisation analyser based on narrow band dichroic transmission filters is proposed as a potential instrument for future X-ray observatories. Chapter 7 describes theoretical and experimental investigation of the dichroic filter concept outlined in Chapter 6. Experimental charaterisation leads to a theoretical instrument response model which is used to predict the sensitivity of the potential instrument to X-ray polarisation in the context of the *XEUS* X-ray telescope.

[6]NB. as a convention, all description of "optical measurements" reported herein should be considered to refer to the optical properties at X-ray wavelengths. Any deviation from this convention will be explained in the text.

Finally, Chapter 8 concludes the work in this thesis, bringing together the experimental and theoretical work in all three areas and proposing a number of improvements or directions for future work to follow.

Chapter 2

Microchannel Plate X-ray Detectors

2.1 Microchannel plates

Microchannel plates (MCPs) are lead-glass disks with millions of microscopic pores etched out of them during manufacture (Wiza, 1979). They have been used extensively in astronomy and planetary science instrumentation as imaging, photon counting X-ray detectors (or single ion counting detectors) as well as in more traditional, terrestrial, applications as photomultipliers or mass spectrometers (eg. Wilken *et al.* (1987) or Lees & Pearson (1997)).

MCPs were originally classified technology due to their application in low light imaging devices for military applications. However, after declassification in the late 1960s, they quickly established a reputation as the detector of choice for many astronomical and terrestrial applications, this reputation has remained until the present day (eg. Wiza (1979), Barstow *et al.* (1985a), Wilken *et al.* (1987), Lees & Pearson (1997), Bannister *et al.* (2000) and Lapington *et al.* (2007)).

Parameter	**MCP**	**CCD**	**TES**[1]
Active area (mm)	$\leq$100×100	$\leq$25×25	$\leq$2.5×2.5
Δx (μm)	Pore size	10's (pixel size)	10's (pixel size)
ΔT (μs)	$\sim 10^{-5} - 10^{-6}$	1-2500	10-50
ΔE (eV at 5.9keV)	none	$\sim$140	$\sim$2
Curvature?	Grind/slump	Stack devices	None demonstrated

Table 2.1: Comparison of detector technologies, Δx is spatial resolution, ΔT is temporal resolution and ΔE is energy resolution. These values are for a typical (X-ray sensitive) device. It should be noted that sub pixel imaging is possible with CCDs (and presumably with TESs). However, the pixel size is indicative of spatial resolution without clever processing techniques.

The development of the charge coupled device (CCD), active pixel sensors and cryogenic detectors such as transition edge sensors (TESs) or superconducting tunnel junctions (STJs) has progressively reduced the impact of the MCP in many areas. MCPs do, however, still offer advantages over these technologies in terms of their large area, photon counting operation (a significant advantage over CCDs) and improved quantum efficiency in the ultraviolet and extreme ultraviolet regions of the electromagnetic spectrum. This chapter addresses the unparalleled combination of high spatial and temporal resolution for microchannel plates where Table 2.1 compares the operating characteristics of MCPs with CCDs and TESs.

MCP's are no longer solely used as detectors, a new, growing, area of MCP application is in the field of micropore X-ray optics. This thesis describes MCPs as both detectors (this chapter and Chapter 3) and optics (Chapters 4 & 5), showing how recent advances in manufacturing techniques have initiated significant progress for both of these applications. The rest of this chapter describes the operation of MCPs as X-ray and charged particle detectors, concentrating specifically on astronomical applications and the benefits of going to smaller pore sizes (higher spatial and temporal resolution - see section 2.3). Chapter 3 describes experimental work to characterise the behaviour of a new generation of small pore MCPs.

2.1.1 Microchannel plate manufacture

Many people have described the manufacturing process used to make MCPs; eg. Fraser (1989), Martin (2000), Nussey (2005), who show that the manufacturing process of an optic is remarkably similar to that of a standard electron multiplier MCP. First, a number of fibres of the required cross section are stacked and fused together with a different kind of (cladding) glass. This is then drawn out under heat and pressure to form what is known as primary (or first draw) fibre. These fibres are then stacked into an array of the required dimensions and are drawn again to form a bundle of microscopic channels, known as a multi-fibre. These are then in turn, stacked and fused to form a "block" which has a very large number of parallel glass rods which are housed in a matrix of the cladding glass. Finally, plates are cut from the block and etched (with either acid or alkali, depending on the type of glass) to remove the central glass rods, leaving the more robust glass matrix, which forms the MCP. At this point, the optics are complete. However, for detector MCPs, one final stage remains where the glass is reduced in a hydrogen atmosphere to provide an electron emitting surface on the pore walls.

As part of this manufacturing process, a number of geometrical aspects of the MCP can be altered (Figure 2.1):

Slump radius, the plates can be slumped to a given radius of curvature. Initially this was done by pressing the optics over a steel mandrel using a spring (eg. Price (2001) and references therein). This has been superseded by a technique which uses a convex and concave section of an appropriate spherical surface to effectively sandwich the MCP, applying equal pressure all over the surface to reduce the effect of shearing channels with respect to each other. This spherical profile is used to either match the curvature of the focal plane of a given instrument (e.g. The Auroral imager - Bannister *et al.* (2007)), or, in the case of micropore optics, to define the focal length of the optic (half the slump radius Price (2001)). In the past, to get an MCP

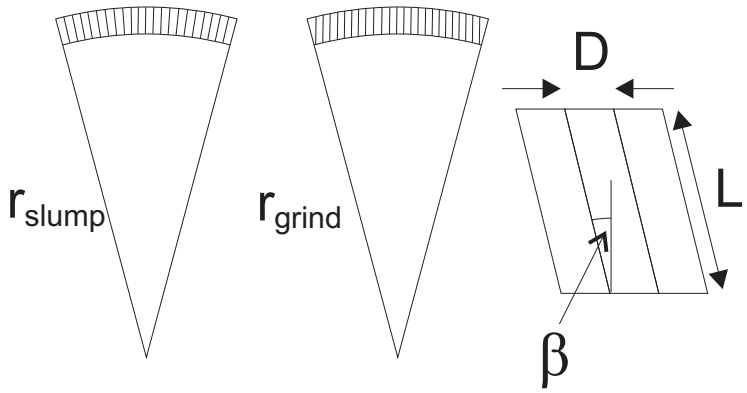

Figure 2.1: Schematic diagram of the MCP parameters which govern detector/optic response. Note the difference in channel alignment between a slumped plate, where the channels point towards the radius of curvature (left) and a ground plate, where the channels are all parallel (center). L is the channel length, D is the channel diameter and β is the bias angle of the MCPs.

to match the curved focal plane of an instrument they would be manufactured as a thick plate and then ground to match the focal plane (Barstow *et al.*, 1985a). This is an expensive process which is wasteful of MCP material and hence, the ability to slump an MCP to match the focal plane would offer a big technological and financial advantage as long as the performance of the detector was not compromised. Hamilton (2005) concludes that a slumped MCP detector can certainly meet the requirements of the wide field auroral imager described by Bannister *et al.* (2007).

The bias angle, is the angle between the axes of the channels and the normal to the MCP surface. It is varied by altering the angle at which the plates are cut from the block and can be controlled to an accuracy of a few arcminutes. For detectors, this is of paramount importance because of the quantum efficiency advantage gained when the X-rays strike the pore walls at an angle approximately equal to the critical angle for the incident photon energy in MCP glass (Pearson, 1984). The bias angle can be matched to a specific detector/telescope geometry to maximise overall efficiency. For optics, the bias angle of the plate should be as close to zero as possible, to ensure that all channels point to a common (on axis) center of focus after slumping.

Channel geometry, the size and length of the channels can be altered during manufacture, where improvements to the MCP manufacturing techniques allow the pores to be made with a much wider range of sizes and even with square channel cross sections. While this square geometry was reported to give much improved quantum efficiency at soft X-ray and extreme ultraviolet (EUV) energies (Fraser *et al.*, 1991a), it has remained relatively unused in detector systems due to conflicting reports of quantum efficiency performance (Siegmund *et al.*, 1992). The new geometry did however, open up a new and exciting application of MCPs in the field of micro-pore X-ray optics which are discussed in Chapters 4 & 5.

2.2 MCPs as X-ray and charged particle detectors

MCP detectors work by an avalanche effect where incident photons excite a small number of electrons into the channels via either the photoelectric or Auger effect. These electrons are then accelerated down the channels by a large electric field where any subsequent collisions with the walls excite further (secondary) electrons. An exponential multiplication in the size of the charge cloud propagating through the MCP ensues, this is known as an electron avalanche (eg. Wiza (1979) or Fraser (1989)).

Comparison of the avalanche in an MCP channel to a standard "discrete dynode" electron multiplier implies that the continuous nature of the channel walls can be approximated as a large number of dynodes (Fraser *et al.* (1988) and Fraser (1990)). After this amplification, the electron cloud emerges from the rear aperture of the channel and diverges towards a readout anode where it is detected. As the electrons are confined in space by the channel walls during amplification, space charge saturation leads to a discrete charge pulse on the anode for each (high gain) avalanche, where the centroid of this charge footprint represents the incident position of the photon.

The gain of the MCP is defined as the number of electrons which escape the pores onto the readout

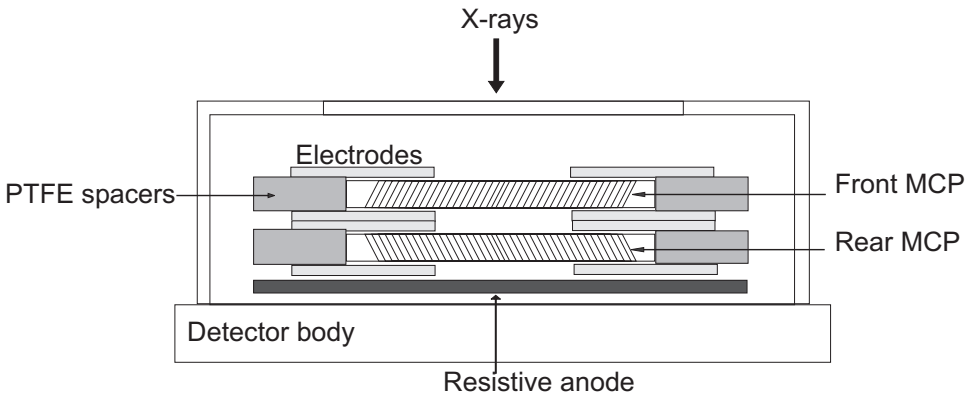

Figure 2.2: Schematic of the P5 detector with salient features marked. Note the chevron arrangement of the channels

at the back of the plate per primary excitation of the input surface. It is determined by the voltage applied to the plate, the secondary electron emission properties of the MCP glass and the pore geometry. For efficient photon counting operation, the gain must be high enough to induce space charge saturation of the avalanche (typically $\sim 10^6 - 10^7$) such that each pulse contains a well defined amount of charge and the quantum efficiency of the detector does not change as a function of bias voltage. In normal circumstances, it is not possible to operate a single MCP at a high enough gain to produce the saturated pulses needed for photon counting operation. This is because, the high potential allows positive ions created by ionisation of residual gas in the channels to propagate back up the channel, gaining sufficient energy to initiate a (spurious) high gain avalanche (Fraser *et al.*, 1987).

A number of methods of preventing ion feedback have been developed, but the most commonly used is the two plate *chevron*. Creating a plate with a bias to the channel orientation allows operation of a pair of MCPs in chevron format, where the bias angles of the two plates are arranged such that they are oppositely oriented in the detector, see Figure 2.2. As ions are preferentially created in the second MCP (because of the greatly increased electron density in the avalanche), this means that there is a discontinuity in the path an ion travels from where it is created to the input surface of the plate.

This effectively confines the ion to the rear plate of the stack, meaning that the pulse that it initiates contains a much reduced amount of charge and falls below the electronic low level discriminator. Other methods of reducing ion feedback include *Z−stacks* and introducing curvature to the MCP channels[2].

2.2.1 Control of detector response

Applying voltages across the MCP faces gives rise to the acceleration of the electrons and, therefore, to the multiplication process. Control of these voltages is extremely important in understanding and optimising the performance of the detector. It is preferable to have total control of the voltage on each face of either MCP in the chevron. Such flexibility allows manipulation of the voltage across each plate individually, across the inter-plate gap and between the rear of the MCP stack and the readout. For flight instruments, deployed in a space environment, it is often necessary to sacrifice some of this control for experimental and logistical reasons. This is sometimes also the case in a lab environment when practicalities such as the fragility of the MCPs dictate a different approach (more in Chapter 3).

Grids can be used in a number of places within the detector to optimise its response to a particular application. It is possible to have a *repeller grid* in front of the MCPs at high negative potential to repel electrons emitted from the surface of the plate back down into the channels. This increases detector efficiency at the cost of reduced spatial resolution because the electrons redirected into the MCP by the grid are collected in adjacent channels (eg. Barstow *et al.* (1985b)). Another place where a grid is commonly used is behind the MCP stack. This grid is held at ground potential to decouple the readout from any electronic signal induced on the rear surface of the MCP. As the electron avalanche

[2]Z−stacks are like a chevron but with three plates in the stack, this geometry more effectively reduces ion feedback and increases the achievable gain, however, it degrades the ultimate spatial resolution of the detector because of an extra interface between MCPs. Curved channel configurations reduce the chances of the ion reaching the input surface of the plate by increasing the chance that it collides with the wall a significant distance along the channel, meaning that it does not produce a detectable pulse.

excites a significant number of electrons from the pore walls, the MCP becomes highly positively charged near its exit surface until currents within the glass matrix neutralise this charge build up. The high resistivity of the MCP glass means that this neutralisation can take a significant amount of time to occur[3], meaning that the rear edge of the electron cloud could potentially be slowed by the induced potential. The inclusion of a grounded mesh after the MCP exit surface means that after the electrons have transited this mesh, they are effectively shielded from this induced potential, allowing the cloud to propagate onto the readout without being slowed down (more in Chapter 3).

2.2.2 Diagnostics from MCP detectors

The overall MCP performance is characterised by a pulse height distribution (PHD) and the event pulse shape measured directly on a high bandwidth oscilloscope.

A PHD is a frequency distribution of the amount of charge contained within each detector pulse, recorded on a multi-channel analyser (MCA). The channels of the MCA represent discrete charge bins and the absolute charge contained within each bin therefore needs to be calibrated. Dividing the channel number where a test pulse appears on the MCA by the (known) amount of charge within the test pulse, gives the conversion gain of the electronics in channels per pico-Coulomb (pC). The capacitor on the test input of the Preamp used here was known to be 1 pF. Therefore, given that the charge, Q, is equal to the capacitance, C, multiplied by the voltage applied, V, it was possible to calculate the amount of charge going through the preamp from a test pulse of known voltage. Two test pulses with different voltages were used to calculate the conversion gain as this allows the removal of any DC offsets in the electronics during data analysis.

There are two characteristic shapes to PHDs from MCP detectors. One is an exponential decay of

[3]The recharge time is governed by the RC time constant for recharging a single channel. Equation 1 in Fraser *et al.* (1991b) predicts a recharge time for a single channel of 2.5 ms taking the appropriate values given therein and assuming that the channel is fully recharged after 5 time constants.

the frequency with increasing charge. This is indicative of a lack of pulse saturation when X-rays are incident on the detector and is also expected from noise counts, on account of the noise source being evenly distributed along the channel length (Fraser *et al.* (1987) – more in Chapter 3). Second is a peaked (saturated) distribution which shows a *most likely* charge from a detector pulse. This type of distribution indicates that the electron avalanche has saturated, meaning no further amplification of the electron cloud will occur. Saturation is induced when the electron cloud gets sufficiently large that it effectively shields electrons towards the rear of the avalanche from part of the potential applied across the MCPs (space charge saturation). For a detector to operate in photon counting mode, a saturated PHD is needed as it ensures that the quantum efficiency of the detector is maximised and is not a function of the bias voltages. The width and position of the peak of the PHD can be manipulated by changing the fields within (and hence the potentials applied across) the MCP. Ideally, a detector would have a low peak gain to reduce the amount of charge lost from the MCPs per avalanche, (prolonging their life) and narrow width so that the output charge pulses are very regular and consistent. Unfortunately, these two conditions are mutually exclusive. Hence, subtle manipulation of the voltages are required to bring the width of the distribution down for a practical peak gain.

2.3 Small pore sizes

The Microchannel plate (MCP) electron multipliers used in most X-ray detectors typically have pore diameters of order $10 - 12\mu m$. MCPs with smaller pore size ($2 - 6\mu m$ pore diameter) have been shown to promise major improvements in the time resolution, count rate capability, dark noise and spatial resolution of imaging microchannel plate detectors. These improvements arise because the performance characteristics are fundamentally determined by the MCP channel array geometry; pore diameter, D, channel length, L, and pitch, p. Modeling of the propagation of the electron cloud is

described by Fraser *et al.* (1988) and Fraser (1990), where the transit time is shown to be proportional to $\frac{L^2}{D}$. Hence, for a given aspect ratio (channel $L:D$) it is proportional to the channel diameter, D. Transit time variance (or pulse width) is shown to be proportional to the channel length, L. Therefore, reducing the pore size of the active MCP reduces the transit time and transit time spread for a given aspect ratio.

Developing MCPs with such small pore diameters has been a major technological challenge, requiring new manufacturing techniques which have progressively reduced D from 25 μm to the present limit of 2-4 μm (Laprade & Reinhart (1989), Laprade & Starcher (2001)). These improvements were driven mainly by applications in night vision intensification and mass spectrometry, where any improvement in temporal resolution (Δt) translates into better mass resolution, particularly for ion analysers for space plasmas (Wilken *et al.*, 1987). A fortunate coincidence of all this development work is a potentially major improvement for scientific fields such as; X-ray, EUV and FUV astronomy as well as new, terrestrial, applications such as biological imaging, where the detector parameter space around $\Delta t \leq 1$ ns, $\Delta x \leq 10$ μm is of fundamental interest. MCPs remain the only class of detector capable of operating in this regime (Table 2.1).

2.4 Applications

2.4.1 Astronomy

To date, MCPs remain an important class of detectors for X-ray astronomy missions, for instance, the high resolution imager on the *Chandra* observatory is a large area microchannel plate detector (Lees & Pearson, 1997). However, due to technological improvements in other areas of detector technology and the drive towards high resolution imaging spectrometers for the focal plane of *XEUS* or *Con-X*, no MCP detector is proposed as part of their payload. The combination of imaging and spectroscopy

(eg. CCDs/TESs) is a much more attractive option for the future X-ray astronomical observatories.

However, MCPs remain in use in astrophysics because of their unparalleled performance at ultraviolet (UV) wavelengths. The open window, *solar blind* response of MCPs makes them ideal for detecting ultraviolet and extreme ultraviolet (EUV) light. Detectors with a significant response to visible radiation require comprehensive shielding in order to minimize the background for UV/EUV measurements. This shielding is often achieved using thin aluminium films which can be made of two layers such that the coincidence of pinholes in each layer is unlikely, thus reducing the optical transmission of the filter (e.g Mitrofanov (1998)). Having a detector which is inherently insensitive to photons outside the band of interest is of value to reduce the shielding requirement and hence reduce the constraints on the filter. The efficiency of an MCP falls almost exponentially with increasing wavelength from $\sim 2\%$ at 200 nm to $\sim 10^{-9}\%$ at 260 nm (Wiza, 1979). However, it is important to note that while MCPs are intrinsically *blind* to optical photons, they still sometimes require shielding from these wavelengths as the enormous flux from the Sun causes a statistically significant number to excite the MCP. An elegant way of performing this shielding is to use a high efficiency, solar blind (opaque) photocathode, which not only blocks visible light, but also provides an increase in the EUV efficiency of the detector (Tremsin & Siegmund, 2000). However, some filtering is still often required but it needs to be much less comprehensive than for a detector which is inherently sensitive to visible wavelengths.

EUV spectrometers have been flown on sounding rockets to investigate the emission from astrophysical plasmas, such as the atmospheres of white dwarf stars (Bannister *et al.*, 2000). In order to obtain spectra of sufficiently high energy resolution to resolve the features (absorption lines) in the spectrum within the $5 - 10$ minute observation period of a sub-orbital sounding rocket flight, a detector with both high quantum efficiency (QE) and high spatial resolution is required. For a dispersive grating spectrometer, photon position in the focal plane is a function of photon energy with high spatial resolution leading to high energy resolution. However, there must be a statistically significant number

of events in each energy *bin* of the spectrum, and hence the detector must have good *QE* to prevent observations being photon limited (i.e. limited by the Poisson statistics of the number of detected photons).

To date, the resolution of sounding rocket borne, EUV spectrometers has not been sufficient to unequivocally resolve the Helium lines of interest in the atmospheres of these stars (eg. Cruddace *et al.* (2002)). Therefore, a reduction in MCP pore size could potentially have a drastic impact in this field because of the higher spatial (and energy) resolution enabled by small pore MCPs and new readout technologies. A number of readouts are capable of achieving MCP pore-limited resolution; delay lines, vernier anodes and cross strip anodes, these are reviewed by Lapington (2004).

The World Space observatory (WSO – Barstow *et al.* (2003)) is the future successor to the UV instruments onboard *The Hubble Space Telescope* (HST). A number of the potential detectors for WSO are based on MCPs, their imaging capabilities are used either to provide high resolution images of the sky directly or as the imaging element in the dispersive spectrometers. Barstow *et al.* (2003) proposed the use of the high resolution *J-PEX* MCP detector for both the imager and the long slit spectrometer as its spatial resolution lends itself ideally to this purpose.

The generic detector, originally proposed for all three of the spectrographs on WSO is a Z-stack detector already demonstrated in the ORFEUS instrument flown form the Space Shuttle in 1993 and 1996 (Barstow *et al.*, 2003). This detector has dimensions of 30×40 mm, ideally suited for the UVES and VUVES instruments, yet the dispersion from the long slit (LSS) instrument is 80 mm, requiring two detectors to cover the necessary area. The *J-PEX* detector consists of a chevron of 6 μm pore MCPs read out by a vernier anode and has been demonstrated successfully onboard a sounding rocket flight (eg. Bannister *et al.* (2000) or Cruddace *et al.* (2002)). Such a detector could compress the LSS field onto a single detector and also offers the best option for the focal plane imagers, despite being limited by the 6 μm pore diameters. The validation of the operation of smaller pore size MCP detectors

would therefore offer improved imaging resolution assuming the readout is capable of achieving pore limited images.

The WSO would be in an ideal place to build on the science gained from HST, investigating a highly important region in the electromagnetic spectrum. Pagano *et al.* (2006) point out that the resonance lines of most atoms/ions/molecules of astrophysical significance lie in the UV waveband, making it a highly significant area of research. UV absorption spectroscopy can yield much information about the matter which lies in the line of sight to a bright object (Stellar/planetary atmospheres, inter stellar medium, etc.). For instance, by observing the absorption lines in the atmospheres of white dwarf stars, the interstellar medium and even the atmospheres of extrasolar planets, the chemical composition of these plasmas can be determined.

As an example: By analysing the absorption spectra both in and out of the transit phase of the orbit, exoplanet HD209458b has been shown by Vidal-Madjar *et al.* (2003, 2004) to have an atmosphere which contains hydrogen, carbon and oxygen. Although this in itself is a remarkable result, these papers take the analysis one stage further, allowing interpretation of the motion and behaviour of the atmosphere as well as its composition. In this case, the material is found to be escaping from the planetary atmosphere as it extends beyond the Roche-lobe, (the boundary of a stable atmosphere) forming a comet like tail behind the planet. WSO would offer much more precise investigation of such phenomena and could extend the analysis to other exo-planets.

Although I have restricted my discussion of the astrophysical importance of the UV region to discussion of one application, Gómez de Castro *et al.* (2006) review a great number of other areas where these kind of observations would be of fundamental interest. The great diagnostic power of the UV region of the electromagnetic spectrum for astrophysical targets is evident, indicating the fundamental importance of detector development for high resolution UV imaging and spectroscopy.

2.4.2 Terrestrial applications

Detectors optimised for particle physics, space science and astronomy are ideally suited for use in diverse areas of science from biological and chemical research to surface analysis and synchrotron physics. Therefore, new developments in MCP technology should be targeted at as broad a range of potential applications as possible. A number of applications exist which would benefit from a generic technology with large effective area, high spatial and temporal resolution and which is capable of handling a high event rate. Such a program has been funded by the RCUK−Basic technology research program and is led by Jon Lapington at the University of Leicester. This research aims to push MCPs beyond their current performance by developing new MCPs made from Bulk conductive glass (to increase the dynamic range in timing), develop new, high resolution, high speed readout technologies based on ASIC electronics and finally to investigate the new breed of small pore size MCPs and how they behave when operated as single photon/particle counting detectors (Lapington *et al.*, 2007). Chapter 3 reports experimental validation of the operation of small pore MCPs as high gain detectors and represents the first stage in the design of a detector geometry suitable for these fragile plates.

2.4.2.1 Biological imaging

The recent success of the human genome project, and more generally, the enormous field of genetics have been driven, in part, by technological advancements in fluorescence measurements. However, these methods are not strictly quantitative and cannot be used for the study of proteins in living cells. This study of complex proteins *in vivo,* (within a living cell) is in its infancy and the advent of new, ultra-fast, small pore MCPs could, conceivably, provide the technology driver for this area of research by drastically reducing the cost and complexity of such measurements. The multiplexing of a large number of observations simulaneously, as enabled by large area MCPs, would greatly increase the speed of data collection and allow even faster timing response than with a standard photomultiplier

tube. This arises because of the minaturisation of the multiplier leads to a shorter transit time and transit time spread for the electron avalanche.

High time resolution imaging of the fluorescence from a biological sample would allow the determination of the behaviour of proteins as they interact, drastically improving the diagnostic power of the technique. The $\sim$ ps resolution which is theoretically possible with small pore MCPs makes them the ideal detector for this type of application.

2.5 Summary

This chapter describes the operation of MCPs as imaging, photon/single-ion counting detectors of X-rays and charged particles. The potential improvements in detector response enabled by the new, smaller pore size MCPs are reviewed and placed in the context of a number of possible future applications both in space and in a terrestrial environment. Here, the combination of high quantum efficiency, good imaging resolution and extremely high temporal resolution means that MCPs will remain a crucial detector technology with scientific areas as diverse as X-ray/ultraviolet astronomy and the life sciences identified as areas where this superb combination of temporal and imaging resolution could have a significant impact.

Chapter 3 reports recent experiments which validate the operation of these new MCPs and provide a good platform for developing extremely high speed detectors out of them.

Chapter 3

Photon counting with small pore microchannel plates

3.1 Introduction

Chapter 2 has described the operation of MCPs as imaging, photon counting detectors and the potential scientific benefits of using smaller pore diameter MCPs. This chapter describes experimental investigation of a set of 3.2μm diameter pore MCPs produced by Photonis SAS (Brive, France).

3.2 Experimental characterisation

The small pore plates under investigation here represent extremely new technology. Therefore, a number of questions needed to be answered regarding their operation before they could be considered for practical use as X-ray detectors in a new generation of scientific instrumentation.

The handling and manipulation of these plates was complicated by their extreme fragility. Hence, the

practicality of successfully assembling a detector with such fragile plates needed to be demonstrated. Furthermore, it was not certain that a saturated gain could be achieved before ion feedback became significant, dictating whether these MCPs could be used as photon counting X-ray detectors.

By characterisation of the field needed to induce pulse saturation, and assessing the practicality of such a field by demonstrating long duration operation without electronic breakdown, these questions could be answered. Subsequently, the more pertinent scientific questions about the detector signal speed and dark noise were addressed. Future work will need to be undertaken to address issues such as the intrinsic quantum efficiency and limiting spatial resolution of these new plates as this has not been considered in this preliminary investigation.

3.2.1 The test facility

The Facility used in this work was originally developed for the calibration campaign of the *ROSAT* wide field camera and is known as the detector test facility (DTF - See Figure 3.1). It is an ultra high vacuum (UHV) beamline which typically operates at pressures $\sim 1 \times 10^{-6}$ mbar and below. The reason for using such low barometric pressures is twofold: One, the detectors must be kept extremely clean; free from dust, moisture and contaminants which can cause noise hotspots on the detector. Secondly, low pressures mean that the detector can be operated with less probability of electronic breakdown. Voltages needed for standard (10 μm pore size) plates are $\sim$1 kV, dictating a field of $\sim$2.5 kVmm^{-1}. Such high fields will cause breakdown events at atmospheric pressure, where a spark jumps through the air and could damage (or destroy) the detector or the expensive electronics used to read it out. For this reason, high voltages were not applied to the plates until the system reached pressures of $\leq 2 \times 10^{-6}$ mbar.

Effects such as outgassing of the MCP pore walls can lead to local increases in pressure and an increased potential for breakdown. The detectors were therefore baked out before use and powered up

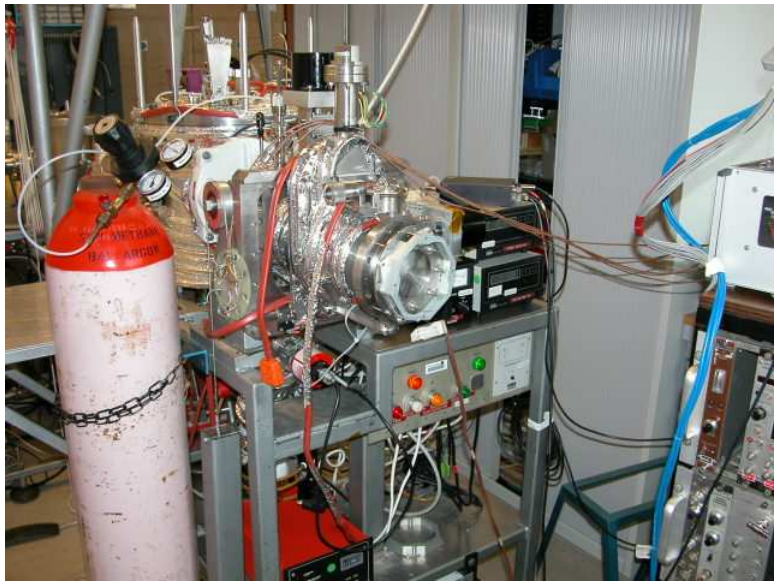

Figure 3.1: Photograph of the detector end of the DTF The end flange is clearly visible and is where the detector sits on the translation stages.

very slowly at first to remove much of the outgassing products. A pumping time of several hours after the system reached its base pressure was considered good practice before powering up the detector to allow for the local pressure increases caused by outgassing to dissipate.

Such an event was noticed when using a Lecroy oscilloscope and it damaged the input electronics of the device. However, despite apparent burn marks on the front of the MCP, the detector still worked after this event (more later).

To produce the photons needed for testing the detectors, a number of sources could be used. A Penning discharge source or a deuterium lamp, coupled with a grating monochromator gives low energy (Extreme (EUV) and Far (FUV) ultraviolet) photons and an electron bombardment source with anode and filter combinations produces the more energetic (soft X-ray) photons. All data reported in this chapter used the soft X-ray source alone with a macrofol ($2\mu m$ aluminised lexan) filter. A silicon carbide (SiC) coated copper anode was bombarded with electrons to produce carbon-K ($0.28keV$) X-rays. To optimise the emission line to brehmssrahlung background ratio an accelerating voltage of

0.7 kV (just over twice the line energy) was used.

The detector was assembled as detailed in section 3.2.2 and was mounted at the opposite end of the beamline to the X-ray source, on an $X - Y$ translation stage so that the beam could be accurately positioned at the centre of the detector. The flange also had a rotational degree of freedom about a vertical axis at the centre of the detector flange. This allowed the detector to be accurately positioned so that its face was perpendicular to the X-ray beam.

3.2.2 Detector assembly

The extreme fragility of the small pore plates becomes apparent when considering that they are, very simply, plates of glass $\sim 150\mu$m thick with $\sim 70\%$ of their bulk etched away during manufacture. It became immediately apparent that the standard detector design extensively used within the group (the P-series detectors, shown schematically in Figure 2.2) was wholly inappropriate for these new plates. This was due to the need to manipulate relatively large and cumbersome components in very close proximity to the fragile plates. It was also extremely difficult to make a good electrical contact onto the surfaces of the plates using the compression spring without putting undue pressure onto the plates, risking shattering them. After an incident where one of the plates was damaged in a P-type detector, a decision was taken to use a standard photomultiplier body to house the MCPs. This widely used, much simpler mechanical design allowed electrical contact to be made using a circlip and proved to be a much better solution than a spring for such fragile plates. This detector was designated the SP1 detector (Figure 3.2).

The SP1 detector configuration consisted of two solid edge, 18 mm diameter active area MCPs produced by Photonis SAS (Brive, France), mounted in direct contact. The channel aspect ratio L:D was 55 : 1, the channel bias angle 6° and the open area fraction was 66%. The total thickness of the MCP pair was only 0.35 mm, so despite changing the mechanical design of the detector, the plates

Figure 3.2: Photograph of the SP1 detector mounted onto the test facility end flange

still required great care during detector assembly.

A circular copper disc, 20 mm in diameter, was used as the non-imaging readout electrode. This conducting plane was held at ground potential behind the MCP stack, and connected through a 50Ω impedance matched transmission line (Laprade & Reinhart, 1989) to either a LeCroy Wavemaster 8600A (6 GHz bandwidth) oscilloscope for fast timing measurements, or a charge sensitive preamplifier (Ortec 109PC) for measurements of gain and dark noise. The preamp had the facility to connect a high voltage (HV) to the detector. This is needed, for example, when operating gas proportional counters or channel electron multipliers (CEMs) as it provides the electric field, required for the electron multiplication in these devices. In the present arrangement, this facility was superfluous. Hence, the high voltage connector was shorted to the preamp ground using a cap on the HV connector, removing a possible aerial from the system and reducing the electronic noise. Carbon-K (0.28 keV) X-rays from an electron bombardment source were used to illuminate an $\sim$ 2 mm diameter spot on the input MCP at normal incidence, dictating an effective incident angle of 6° to the channel axes.

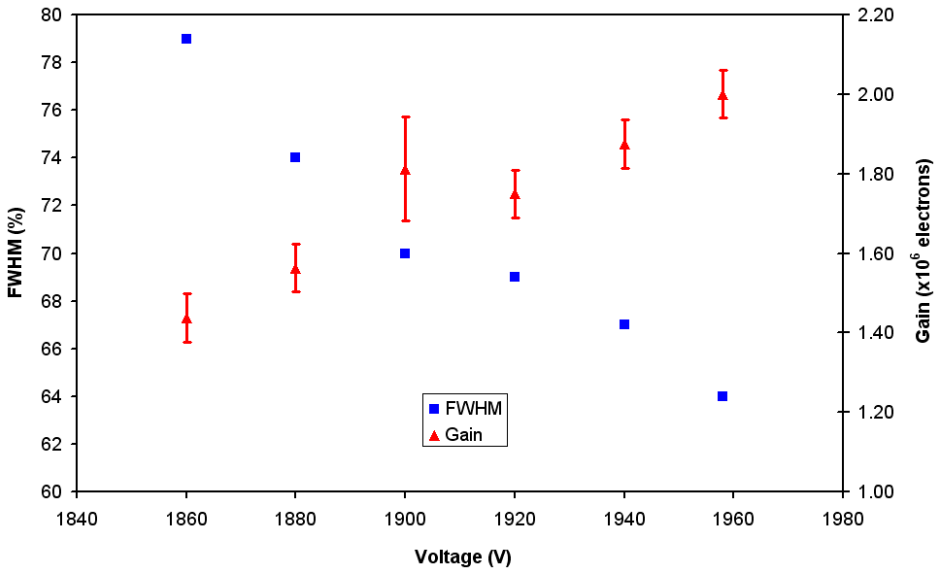

Figure 3.3: Modal gain (triangles, right hand scale) and pulse height FWHM (squares; left hand scale) as functions of total MCP voltage.

3.2.3 Photon counting

In order for these plates to be operated as saturated gain X-ray detectors, their optimum operating conditions required investigation. The photon counting behavior of these plates was assessed using pulse height distributions for C-K (0.28 keV) X-rays, and also for the unilluminated detector (to establish noise characteristics).

3.2.3.1 Voltage optimization

The first phase of testing was to perform voltage optimisation. Taking a number of pulse height distributions for different applied voltages (across the MCP stack) allows the optimum voltage for the detector to be deduced. Figure 3.3 shows how the gain and full width at half maximum (FWHM) of the pulse height distribution vary as a function of detector voltage. Section 2.2.2 states that the *ideal detector* is one with a low FWHM and low gain[1] and therefore, optimisation between FWHM

[1] Paradoxically, high gain is what gives us a measurable signal but the plates should be operated at as low gain as is practical to reduce the amount of charge removed from the glass by each event. This is because the lifetime of the

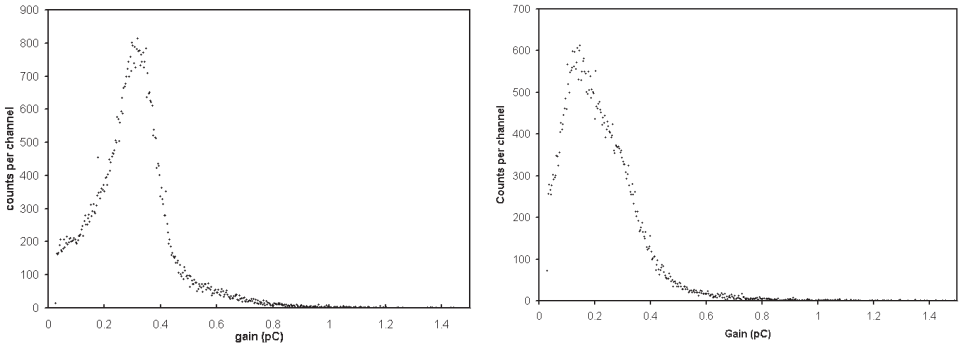

Figure 3.4: (left) Peaked X-ray pulse height distribution for C-K X-rays with a total detector bias of 1958 V. (Right) Noise pulse height distribution for the same voltage.

and gain is required (see Figure 3.3). To zeroth order, this can be taken to be the point at which the two curves in Figure 3.3 cross. However, it is sometimes better to choose a slightly different voltage to increase the detector gain or reduce the FWHM as required. This is chosen by careful analysis of the shape of the PHD and the number of counts within a given range of the peak gain. The optimum voltage setting was found to be $\sim$ 1920 V, dictating a field across the $\sim$ 0.35 mm detector stack of ~ 5.5 kVmm^{-1}. This is an extremely high field for MCP operation; by comparison, a standard $40:1$ 10μ m pore MCP is typically operated with a field of ~ 2.5 kVmm^{-1}.

3.2.3.2 X-ray and noise counting

Figure 3.4 (left) shows the peaked soft X-ray (C-K, 0.28 keV) pulse height distribution measured at a total MCP bias of 1958 V (the highest voltage used). Figure 3.4 (right) shows a deep (long duration - overnight) noise pulse height distribution, taken at the same bias voltage, from which, the assessment of dark noise was made. The noise above 10% of the modal gain should scale with plate thickness for a given aspect ratio (Fraser *et al.*, 1987). The sum of counts above this threshold gives the detector dark noise for the whole detector. The two PHDs shown in Figure 3.4 indicate a specific problem with the SP1 detector design. The expected exponentially decaying PHD, indicative of detector dark noise, is

plate before it undergoes gain decay is strongly linked to the amount of charge which has been removed from the glass during operation.

in fact a peaked distribution. This is believed to be caused by excess ^{40}K in the ceramic components of the photomultiplier body which degrades the X-ray PHD (Figure 3.4 (left)) by increasing the number of counts below the X-ray peak, broadening the FWHM.

The dark noise of the detector is 0.9 $s^{-1}cm^{-2}$, compared to ~ 0.4 $s^{-1}cm^{-2}$ for larger pore size plates (Fraser *et al.* (1987)). The intrinsic background rate due to ^{40}K in the glass is expected to be much reduced, owing to the reduction in MCP mass of a factor ~ 2.25 over a single thickness MCP with 10μm diameter pores. However, this expected reduction in MCP dark noise has not been demonstrated. It is believed that the noise pulse height distribution is composed of two discrete populations of events:

First, the exponentially decaying (as a function of gain) noise count rate expected from MCP detectors (Fraser *et al.*, 1987) owing to the distribution of radioactive elements in the glass. This exponential decay is a consequence of the even distribution of radioisotopes along the channel length and the reduction in gain for events which are initiated down the length of the channel.

Second is an excess noise contribution which is due to external radioactive decay of ^{40}K in the ceramic components of the detector housing. Fraser *et al.* (1987) shows that of the two decay processes for ^{40}K, only the contribution from the 1.31 MeV beta decay is significant for MCP noise and therefore I will neglect the 1.46 MeV gamma ray from my discussion. The beta particles incident onto the detector can initiate an electron avalanche in the same manner as the X-ray events, yet the distribution looks rather different to the X-ray pulse height distribution (even after the removal of the internal MCP noise - see Figure 3.5. This difference is not believed to be unreasonable as the precise pulse height distribution for electrons will depend strongly on the electrical and magnetic environment around the detector. These will control how far into the channels electrons travel before interacting with the glass, initiating the avalanche. It should be noted that the bias field is such that it will accelerate any electron which gets into a pore towards the back of the MCP, increasing the likelihood of interaction down the channel - hence the broader pulse height distribution for electrons than X-rays.

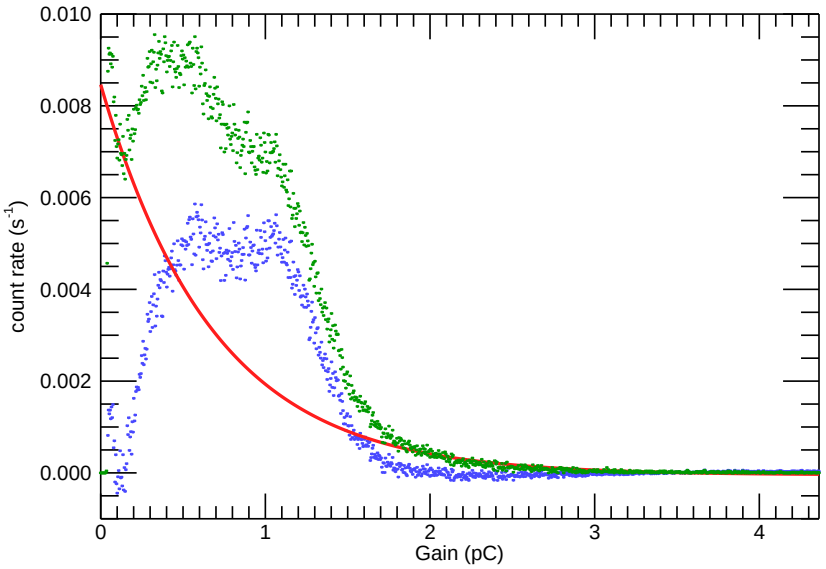

Figure 3.5: Analysis of the X-ray PHD shown in Figure 3.4. The green points are measured data, the red line an exponential fit to the first 15 and last 600 data points where the shape is thought to be dominated by the exponential function characteristic of MCPs, and the blue points the residual excess noise counts. The excess noise is shown to be peaked and is thought to be caused by radioactive decay in the detector body. It should be noted that the count rate in the residuals is in places negative, this is explained by the fact that in places the exponential fit overestimates the experimental results due mainly to statistical scatter.

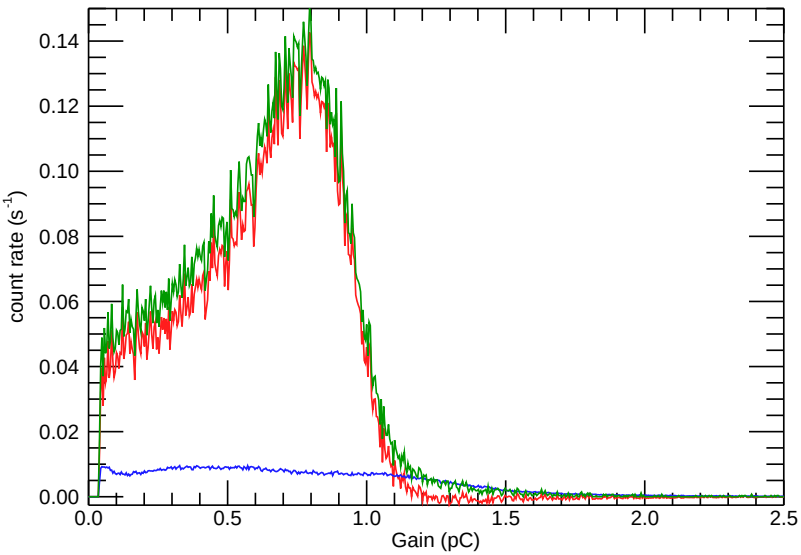

Figure 3.6: Analysis of the noise PHD shown in Figure 3.4. The green points are measured X-ray data, the blue line measured noise counts and the red curve the X-ray data with the noise counts removed.

Figure 3.6 shows that the high gain tail can be explained by the total noise observed from the MCP, meaning that the X-ray events do not lead to the high gain tail. However, at low charge, the pulse height distribution is only weakly influenced by the noise count rate. The asymmetry and non-zero baseline of the PHD is therefore believed to be real. My experience of optimising these kind of detectors suggests that the ability to manipulate the fields independently within the plates and in the gap between them would allow this low charge tail to be significantly reduced by increasing the bias on the front MCP in the chevron with respect to the rear plate.

3.2.4 Timing

Many applications, including time of flight (TOF) mass spectrometers, cavity ring down spectrometers and fluorescence lifetime imagers require extremely high temporal resolution ($\leq$ 1 ns). One of the

major potential advantages of smaller pore MCPs is the improvement in temporal resolution gained through the reduced transit time, and transit time variance, for the electron avalanche within the channels (Fraser *et al.*, 1988). Therefore, characterisation of the pulse rise time and pulse width was performed in order to assess the performance of the new plates and compare them to theoretical values derived in the literature.

3.2.4.1 Models from the literature

Fraser *et al.* (1988) consider a single 4 μm, 80:1 MCP at 1 kV and calculate a transit time[2] of 180 ps for an electron avalanche, with a 35 ps transit time spread[3]. Using the scaling laws and calculations in Fraser (1990) and Fraser *et al.* (1988) to scale to the current 55 : 1, two MCP chevron design allows comparison of the theory and experimental results. Using equation 7a in Fraser (1990), the transit time (t_f), and transit time spread (Δt_f) scale as:-

$$t_f^{new} = t_f^{old} \frac{\left(L^2/D\right)_{old}}{\left(L^2/D\right)_{new}}, \tag{3.1}$$

and,

$$\Delta t_f^{new} = \Delta t_f^{old} \frac{L_{new}}{L_{old}}, \tag{3.2}$$

where *new* indicates the plates of interest, *old* the calculated values, L is the length, and D is the pore diameter of the plates.

Equation 3.1 predicts a transit time of 68 ps and equation 3.2, a transit time spread (equivalent to the

[2]Transit time is the delay between pulse initiation and its exit from the MCP.

[3]The transit time spread is the FWHM width of the avalanche which is caused by the complex propagation of the avalanche through the channels - this can be compared with experimental pulse widths and rise times, both of which are a measure of the spread in transit times for electrons in the avalanche.

pulse width) of 19 ps for a single plate. To convert this "single-plate" value into a number representing a chevron pair of MCPs, the transit times add directly and the transit time spreads add quadratically. These calculations lead to expected values of 136 ps and 27 ps respectively for transit time and transit time spread for the detector under investigation here.

3.2.4.2 Timing results

The mean pulse width (FWHM) and rise time ($10-90\%$ of the pulse maximum) were recorded as a function of the field between the rear of the stack and the readout (Figure 3.7 (Top)). Acceleration of the pulses on to the readout by the rear field reduces any further pulse broadening (after broadening within the pores). When the pulse exits the MCP, the electrons have an energy (and therefore velocity) characteristic of where along the channel axis they were emitted, this variation in output electron energy may give rise to further pulse broadening in the output stage of the detector.

There is a clear change in the gradient of the pulse width curve (Figure 3.7 top) at a potential difference of ~ 740 V, this is justified by comparing the statistical significance of different fits, an exponential (green line) and a two component linear fit (blue line). Visually, it is clear that the broken linear fit gave a much improved correlation with the data with a break point at 740 V, this is supported mathematically by the inclusion of the *coefficient of determination*, R^2, which is a measure of the difference between the measured values and those predicted by the model, it approaches unity for a perfect fit. It is expected that at a certain voltage, the improvement in the speed of the detector pulses with increasing voltage would cease, evidence for tailing off of the gradient is seen in the plot, explaining the lack of perfect correlation for the linear model.

The data points (pulse widths and rise times) consist of the mean of a statistical sample of many thousand individual events, error bars are measured in hardware and are plotted as one standard deviation of the statistical distribution of measured pulses. A better estimate of the width of this

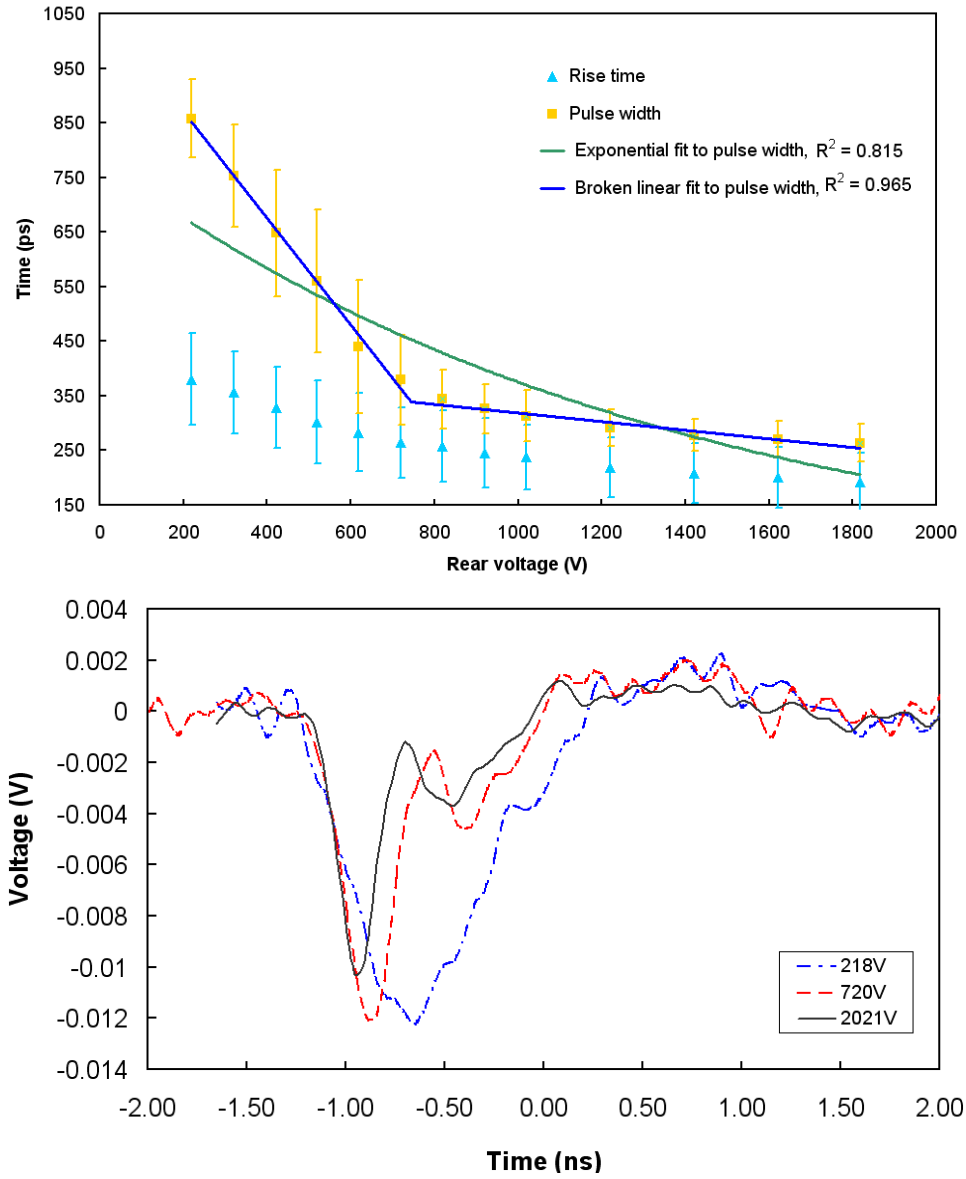

Figure 3.7: (Upper panel) Pulse width and rise time as a function of rear voltage in the original configuration. NB. $\sim$ 1 mm between the rear plates and the electrode. (Lower panel) Evolution of pulse shape with rear voltage.

distribution would be the full width at half maximum (FWHM), which for a Gaussian, would equal 2.36 times the standard deviation. However, this would mask the fact that there is a genuine downward trend in the curves as voltage is increased. The size of the error bars are also believed to be questionable as they appear too large. This is believed to be caused by imperfect triggering of the oscilloscope where a small number of extremely long pulses bias the average and standard deviation of pulse width and rise time to larger values. This is explained in more detail in Section 3.2.5, along with a way to reduce its effect.

The change in temporal pulse shape which gives rise to the gradient change in Figure 3.7 (top) is evident in the lower panel of the figure. At low voltages and hence weaker field strength, the pulses are single peaked and wide, whereas at higher voltages, the double-peaked nature of the pulse becomes apparent. This double peaked nature is less evident at low fields because it is smeared out by pulse broadening. The second peak is not expected in the output signal and is likely to be indicative of the electrical problems (ringing and coupling) within the system mentioned in section 3.2.4. These problems will be discussed in more detail later when experimental modifications are discussed (section 3.3). Once the dip between the two peaks exceeds 50% of the peak amplitude, the calculation of pulse width by the LeCroy oscilloscope no longer takes account of the second peak. This explains the apparent discontinuity in the curve of pulse width as a function of rear output voltage shown in Figure 3.7 (top).

The average pulse rise time $(10-90\%)$ of the fastest detector configuration was found to be 189 ps. After removal of the oscilloscope rise time by the method outlined in Laprade & Reinhart (1989), the pulse width was found to be 284 ps. Figure 3.8 shows a typical oscilloscope trace for a single event, the Gaussian fit (red) implies an uncorrected FWHM and rise time of 174 and 125 ps respectively. This is, therefore, a pulse towards the "fast end" of the statistical distribution sampled and demonstrates that the oscilloscope is not the limiting factor in the measurements. These values compare well with the

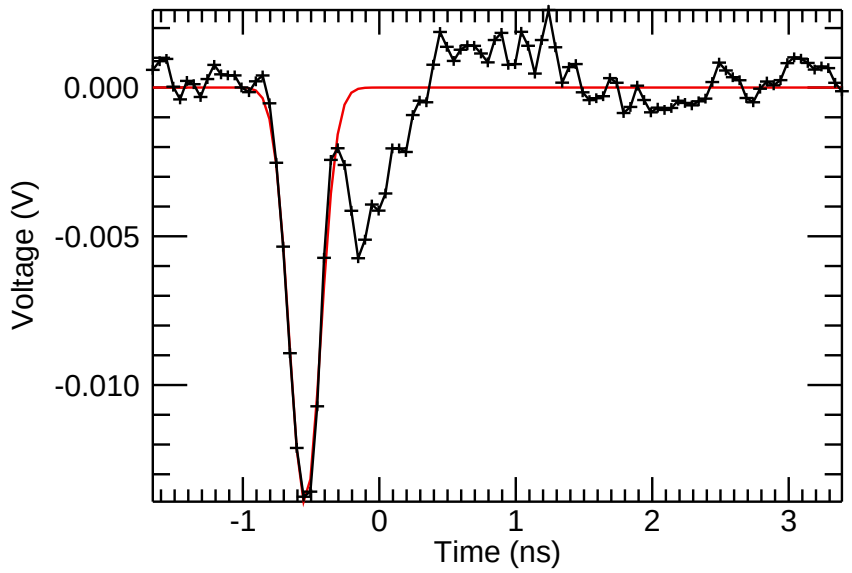

Figure 3.8: Data from the most optimised detector configuration in the initial work. The rear voltage was 2021 V. The red line is a Gaussian fit to the the pulse and the + signs are the data points. The relatively poor sampling of the pulse is characteristic of the maximum resolution of the oscilloscope.

122 ps rise times reported by Photek (Milnes & Howorth (2005)) for a number of MCP photomultiplier tubes.

3.2.5 Experimental issues

Several modifications were necessary in order to improve the timing response of the electronics and to screen out slow decaying signals induced on the MCP rear surface.

The first modification was in the triggering of the oscilloscope. Initially, it was believed that a "width trigger" would effectively constrain the detected pulses to true detector output-pulses and reject electronic noise. The width trigger forced the oscilloscope to trigger on a pulse as the voltage crossed the mean background level on the trailing edge of the pulse. As the pulse shape should, in theory, be consistent and triangular, this should have given a very stable triggering scheme, removing unwanted

noise signals. Gross changes in the standard deviation of the pulse width and rise time were observed when the trigger level was changed, confirming that the width trigger was very sensitive to the trigger level, precisely what it was being used to avoid.

Discussions with Martin Dinmore[4] made it clear that it would be much more successful to use a simple edge trigger (i.e. trigger on the leading edge of the pulse) and constrain a gate, or region of interest for the trigger. This effectively constrained the oscilloscope to disregard noise pulses and make the measurements less sensitive to the experimental setup of the trigger level and made the readings more robust and repeatable. Using the edge trigger and region of interest proved extremely successful, reducing both the absolute value and the standard deviation on the pulse width and rise time[5].

Investigation into the double peaked nature of detector pulses and slower than expected rise times revealed a number of possible causes for these effects (Martindale *et al.*, 2007b).

- Impedance mismatch in the electrical connection between anode and 50Ω feedthrough could have caused ringing in the electronics chain. The baseline overshoot, apparent after the pulse, is indicative of some level of reflection within the transmission line.
- Secondary electrons, emitted from the anode as a result of the impact of the primary charge cloud. Their later recollection on the anode would give rise to the after pulse.
- A double peaked electron energy distribution in the MCP output pulse giving rise to two distinct charge collection times on the anode, resulting from the collection of a fast electron component initially, followed later by a slow electron component.
- The net positive charge left on the MCP pore walls close to the charge exit aperture, could

[4] LeCroy sales and support engineer

[5] Although this may appear to be artificially influencing the data collection by disregarding "unwanted" signals, it is justified because of the effect of a single, extremely long, slow pulse on the statistics of the data. A pulse lasting many ns is unphysical and must be an electrical artifact, yet even a small number of these signals would significantly change the mean and standard deviation of the true detector pulses if they were accepted in the data analysis.

couple onto the MCP output and readout electrodes. This would induce a positive signal with a slow decay, reducing the anode electron signal amplitude and increasing its rise time.

3.3 Modifications and improvements

3.3.1 Protection of electronics

During operation of the detector, a breakdown event was noticed which was attributed to simultaneous firing of many channels by the impact of a cosmic ray. This event caused serious damage to the input stage of the oscilloscope. Unfortunately, it is not possible to protect the input in any comprehensive way as to do so would degrade the impedance matching within the signal cable. This impedance matching is necessary for high speed readings as any mismatches would cause reflections within the signal line and reduce the apparent speed of the MCP pulses. The only possible mechanism for input protection is a high frequency attenuator which would cut the magnitude of the input signal. Although this would reduce the possibility of driving the input over its upper voltage limit, these high charge events may still damage the electronics.

3.3.2 Unwanted contributions to the signal

It could be argued that the dispersion of electrons within the avalanche (which is implied by the calculation of the expected transit time and transit time spread in Section 3.2.4.1), could be used to deduce the temporal broadening after exiting the MCP. However, it should be noted that the dispersion relation inside the MCP is very different from that after the avalanche has exited the channel plate. In the first region, the avalanche is perturbed by the confinement within the channel, the random emission direction of secondary electrons, the wall charge left after excitation of the secondary electrons and finally the effect of the other electrons in the avalanche. Outside the plate

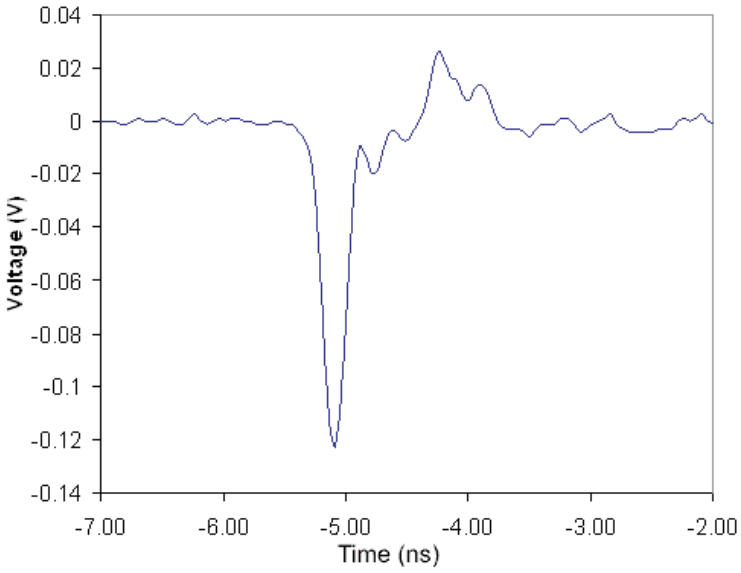

Figure 3.9: detector pulse with rear grid and 2.5 kV between the grid and rear plate (1900 V on the MCP stack). Note the secondary peak has been almost removed.

the electrons simply follow ballistic trajectories within the electric field. It is true that the field is still perturbed by the wall charge on the channel exit aperture and the presence of the other electrons. However, the lack of confinement within the channel means that the dispersion relation is so different for the two regions that no further pulse broadening can be removed in the data analysis.

A possible solution to the problem of double peaked detector pulses and slow rise times is to couple the MCP output electrode to ground using a high voltage capacitor with very high frequency response. This gave rise to minor improvements in the signal speed; however, it was believed that introducing this component significantly increased the possibility of breakdown events damaging the MCPs. Therefore, it was removed.

Another solution, used for commercial high speed microchannel plate detectors, is to place a grid between MCP and anode to pre-accelerate the output electrons before they are detected by the anode. This serves to decouple the anode from induced signals on the MCP by shielding it electrically.

Preliminary tests with the grid between the rear of the MCP and counting electrode showed a marked

reduction in the secondary peak, and a significant improvement in the rise time. This implies that the cause of the double peak and non-optimised rise time was coupling between the rear plate and the electrode. In preliminary tests, the grid was ~ 5 mm from the rear of the MCP stack, dictated by the ease of making a grid mount to fit within the detector. This allows significant time for further pulse broadening in the output stage of the detector and can certainly be improved upon.

The improvement to the pulse shape occurs despite the lower field between the rear of the MCP and electrode (2.5 kV were placed across a gap of ~ 5 mm compared to 2 kV across ~ 1 mm previously). Lower fields are extremely advantageous for practical detectors as it reduces the probability of electrical breakdown and increases the lifetime of the detector. Figure 3.9 shows a pulse from a detector configuration with mean pulse rise time of < 150 ps with the grid 5 mm from the rear MCP face.

Evidence of baseline overshoot after the pulse in Figure 3.9 is indicative of a problem with ringing in the signal chain which could also be limiting the aparent speed of the detector pulses. However, decoupling the anode from the rear MCP surface using the grid seems to have been successful. Lapington *et al.* (2007) has shown that with a different readout technique (with true 50Ω impedance matching) faster rise times of order 80 ps are certainly possible. This data was achieved with an inductive readout known as "image charge" where the effect of coupling the rear electric potential onto the detector is completely removed from the data by the inductive readout scheme. A better electrical arrangement, of the grid mounting to allow a reduction in the grid/MCP-stack distance is therefore likely to lead to additional improvements in signal speed for the SP1 detector.

3.4 Conclusions

3.2μm Photonis MCPs have been operated for the first time in X-ray photon counting mode. The pulse height distributions are well saturated and the MCPs operate stably at gains in excess of 10^6

electrons. Operation in this mode requires a remarkably high internal electric field, 5.6 $kVmm^{-1}$, but the system has been shown to behave stably over long periods (∼weeks) with relatively low noise and without electrical breakdown. This is clearly a significant result for future small pore, high speed MCP detectors.

Initially, a rise time of ~ 190 ps, measured at low gain, was observed with a relatively large accelerating voltage (2 kV across 1 mm) between the stack and the anode. The observed rise time did not vary significantly with MCP gain. Experimental results published elsewhere (Lapington *et al.* (2007)) and theoretical predictions (Fraser (1990) and Fraser *et al.* (1988)) indicate that the plates should achieve rise times significantly shorter than 190 ps under optimum conditions.

Modifications to the experimental arrangement led to much improved pulse shapes and increased signal speeds. With the grid 5mm behind the MCP stack, and with relatively moderate fields after the pulse exits the plates (~ 0.5 $kVmm^{-1}$), the pulse rise time was improved to < 150 ps.

3.5 Further work

3.5.1 Increasing signal speed

Improving the position of the rear grid and the readout plane could further improve the temporal resolution of the device by removing pulse broadening after exiting the MCP surface. A better design of anode which has improved impedance matching throughout the signal line would also be expected to improve pulse shape and timing characteristics, removing the baseline overshoot noted in this chapter.

3.5.2 Excess noise

To test the hypothesis that the excess noise was caused by increased ^{40}K within the detector body, a new detector housing needs to be designed which does not incorporate radioactive materials. This new design could provide greater control over the fields within the stack if a controllable inter-plate voltage was introduced. Such control may significantly reduce the field needed to achieve pulse saturation.

Chapter 4

An Introduction to Microchannel Plate X-ray Optics

4.1 MCP optics

As described in Chapters 2 and 3, microchannel plates have been used extensively in terrestrial and space based detectors of high energy photons and charged particles. It may seem odd, therefore, that a device which was originally designed to maximise the number of detected, and hence absorbed, events should be ideally suited to application as an X-ray optic where the number of reflected photons needs to be maximised.

Despite this apparent contradiction, clues as to the behaviour of MCPs as focusing optics are present in analysis of MCP detector response. When detector efficiency is plotted as a function of the X-ray angle of incidence, efficiency is poor at low grazing angle because the X-rays are reflected down the channel rather than being absorbed. At higher angles, the X-ray penetrates the glass before being absorbed and hence the photoelectron has to transit a finite barrier of glass to reach the channel

surface and initiate the electron avalanche. The peak in detector efficiency therefore occurs at an angle of incidence equal to the critical angle for X-ray reflection in MCP glass. For the lead glass used in MCP optics, the critical angle is given empirically by Willingale *et al.* (1998) as,

$$\theta_c\left(E\right) = aE^{-1.04}. \tag{4.1}$$

Here, E is the photon energy, $a = 2.4$ for θ_c in degrees and E in keV. At angles smaller than the critical angle, θ_c, X-rays are reflected - precisely the behaviour needed for focusing X-ray optics. As Equation 4.1 shows the critical angle is a function of the X-ray energy, these optics have a reducing efficiency and field of view as energy increases.

Early investigation of MCPs concentrated on the use of circular pore geometries e.g. Wilkins *et al.* (1989), Chapman *et al.* (1993a) and Chapman *et al.* (1993b). Wilkins *et al.* (1989) note that moving to a square pore geometry would increase the flux in the reflected images by at least one order of magnitude. The subsequent development of square-section channel geometries for microchannel plates, has enabled the practical realisation of micro-pore X-ray optics (Chapman *et al.* (1991), Fraser *et al.* (1993), Brunton *et al.* (1995), Peele *et al.* (1996), Brunton *et al.* (1997)). Square section MCPs approximate the Kirkpatrick-Baez (KB) geometry (Kirkpatrick & Baez, 1948), where small diameter channels lead to an increase in the area of the reflecting surface visible to the source for a fixed length reflector (Wilkins *et al.*, 1989). This design enables point-to-point focusing with planar MCPs where a large number of parallel channels behave as an array of KB collimators working in tandem (Figures 4.1 and 4.2).

Slumping such an optic to a spherical figure allows a square-pore, square-packed MCP optic to approximate the *Lobster-eye* geometry described by Angel (1979), enabling parallel beams of radiation to be focused with a characteristic cruciform point spread function. This development allows imaging

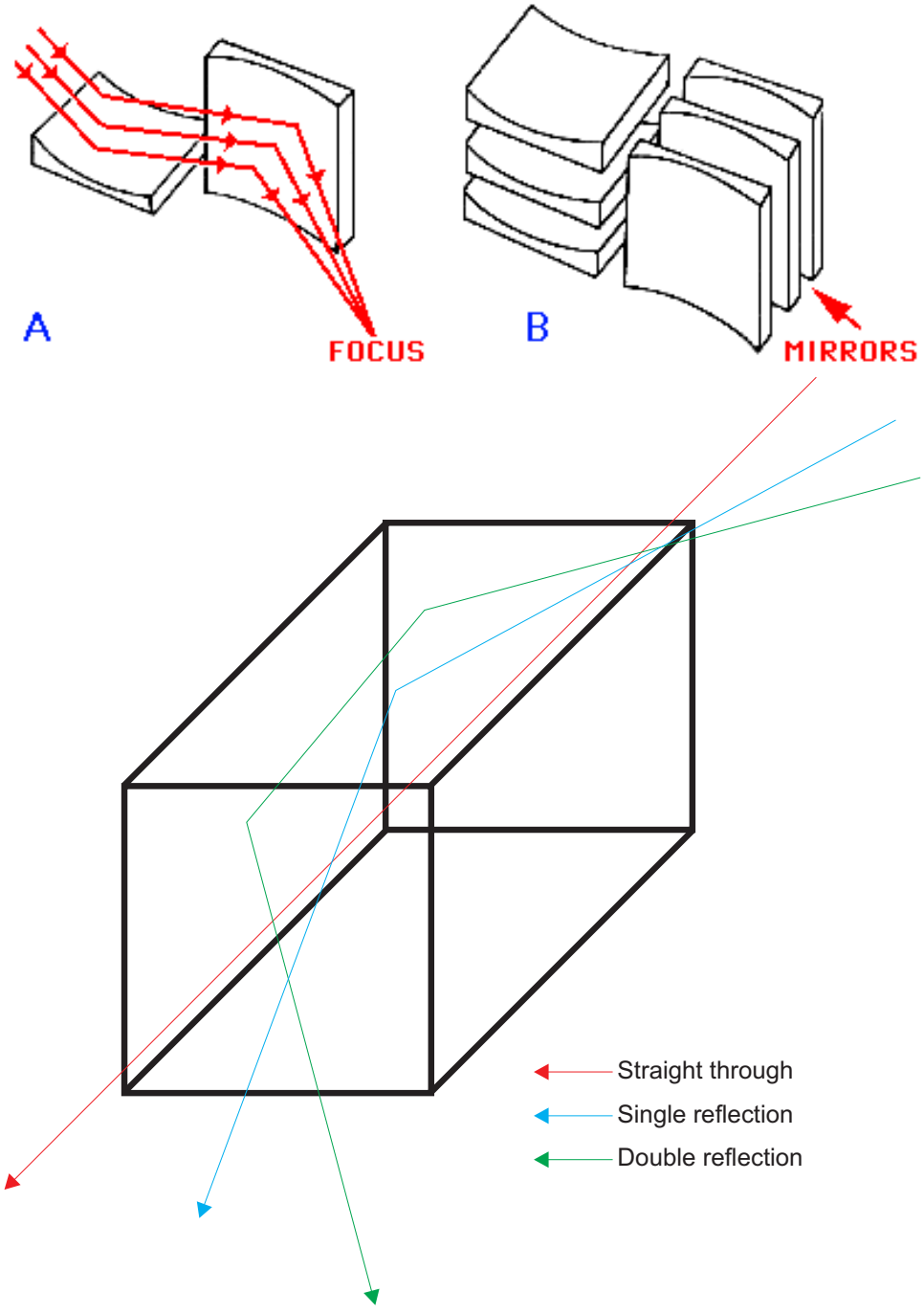

Figure 4.1: Schematic diagrams of the KB geometry (top) after http://astroa.physics.metu.edu.tr/-~emrah/lece/xtelescopes_systems.html and the MCP optic geometry where the square channels make the two reflecting surfaces of the KB geometry coincident in space (bottom)

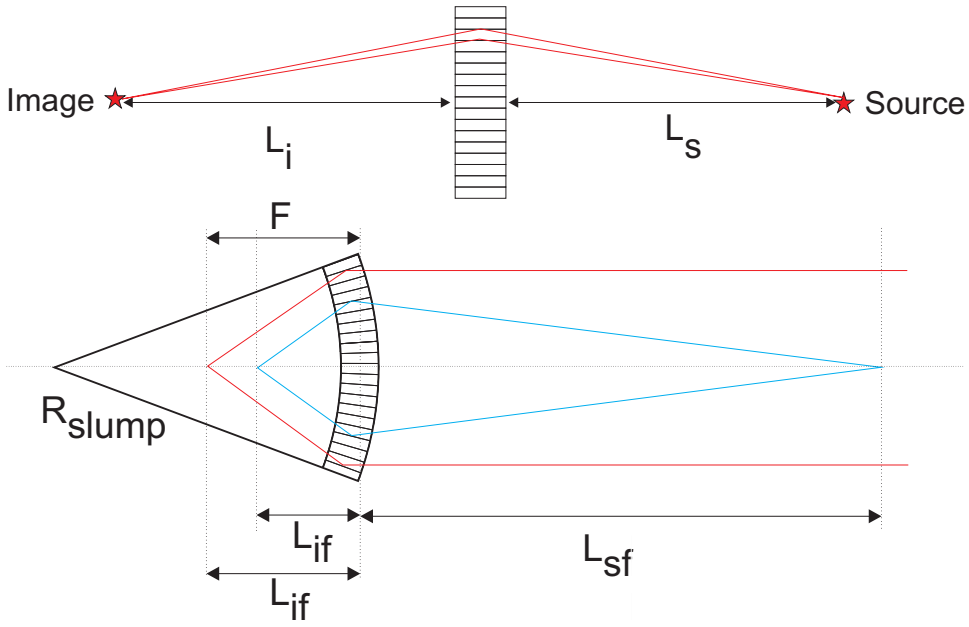

Figure 4.2: Schematic diagrams of the focusing mechanisms of planar (top) and slumped (bottom) MCP optics

of sources at infinity and theoretically enables an almost 4π Sr field of view (Figure 4.2).

The fundamental optical performance of MCP optics is governed by the parameters reported in table 4.1, which shows the best performance characteristics demonstrated in previous experimental characterisation of square pore, square pack format optics. This table demonstrates that the manufacturing process is mature enough to produce prototype optics of the required format for the *WFT* onboard the *Spectrum RG* mission. However, the angular resolution has, so far, remained below the 4 arcmin requirement for the flight optics. Data reported in Chapter 5 can be compared to the values in this table to demonstrate the improvement in performance of the most recent optic samples.

Recent developments in MCP manufacturing techniques, funded by a number of ESA technology research programmes (TRPs) have enabled production of radially packed, square pore MCPs as well as greatly improved performance of standard square packed optics. Packing square channels in a radial fashion may appear to offer little benefit for MCP optics as the azimuthal rotation of the reflecting channel surfaces around the optic removes the possibility of operating as a KB collimator. However,

Parameter	Values
Channel diameter (D)	8.5 − 200 μm
Channel aspect ratio (L/D)	50:1 500:1
Format	$\leq$ 54×54 mm^2
Slump radius (RMCP)	0.07 1.0 m
Channel surface roughness	1.1 nm RMS
Angular resolution	7 arcmins FHWM
Metallisation for enhanced reflectivity	Ni, Ir, or Ru

Table 4.1: The demonstrated performance of MCP optics before work reported herein

focusing from a slumped MCP with a radial geometry would offer an approximation to the nested mirror shell approach used in traditional X-ray optics in space science. Willingale *et al.* (1998) shows that a tandem of two differently slumped MCPs will form a conic approximation to the Wolter I geometry (Figure 1.6) used to eradicate the comatic distortion prevalent in optics employing a single reflection from a cylindrical mirror. The short channel length ensures that a conic approximation to the true Wolter geometry is appropriate because the deviation from the true parabolic and hyperbolic surfaces is small over practical channel lengths of a few mm.

Modern MCP optics are made by stacking small ($\sim$ 0.9 mm) 'multifibres' of square pore, square packed channels in the appropriate geometry and then slumping the optic over a mandrel to the required radius of curvature. For a Lobster eye optic the multifibres are stacked in a cartesian geometry, whereas for a Wolter system they are arranged in concentric rings to achieve the radial packing geometry. These MCP optics are the key technology for a number of proposed space missions in X-ray astronomy and planetary science which are discussed in more detail below. Chapter 5 describes testing of the latest square pore, square packed and radially packed optics at X-ray wavelengths.

4.2 Applications

4.2.1 Terrestrial applications

An imaging X-ray spectrometer has been reported by Martin *et al.* (2001), Price *et al.* (2004) and Su (in prep). This device is a laboratory instrument which can map the elemental composition of a sample by focusing fluorescence X-rays, emitted by the sample under excitation by a higher energy X-ray source, onto a charge-coupled device (CCD) imaging X-ray detector. Analysis of the X-ray spectrum as a function of position gives an elemental composition map of the sample at a spatial resolution better than 1 mm (Price *et al.*, 2004). The IXRF spectrometer uses a single, planar, square pore, square packed MCP optic to achieve point to point imaging (Figure 4.2) of fluorescent X-rays from the sample, meaning that there is no need to raster over the sample to build up the composition map, a time consuming process which is used in competing technologies.

4.2.2 Space missions

A vast array of space missions exist which have been proposed to include an X-ray telescope based on MCP optics technology. This thesis is concerned mainly with the two described in the subsections below; *WFT* and *BepiColombo*. However, I will briefly outline a number of other potential uses.

The baseline *XEUS* optics are to be made from high precision silicon pore optics (most recently described by Collon *et al.*, 2007). However, the extremely demanding constraints on mass, effective area and angular resolution have not been demonstrated and therefore there is an outside chance that another optics technology could be used on *XEUS* (Willingale, 2008). MCPs are identified as an outside chance for *XEUS*. However, to meet the requirements, a drastic improvement in angular resolution would be needed. More realistic proposals have been made to use MCPs: The US *X-Nav* program, a project led by Los Alamos National Laboratory to use the X-ray signals from pulsars

to measure a satellite's position in space without the need for intervention from earth, would use a large number of MCPs as the focusing technology. *Mag-X* is a mission concept led by Steve Sembay (University of Leicester) to put a lobster type telescope on the surface of The Moon to look back at Earth and see the X-rays produced by processes occurring within its magnetosphere. The Wide Field Auroral Imager proposed to fly on *KuaFu* (a Chinese magnetospheric satellite) uses highly slumped MCP optics to image the Earth's aurora at ultraviolet wavelengths (Bannister *et al.*, 2007). Finally, a number of concepts exist to use either the *BepiColombo* or *KuaFu* design for new missions, for example the ESA cosmic visions mission to the outer planets *Tandem/Laplace*.

4.2.2.1 *Spectrum RG - WFT*

Priedhorsky *et al.* (1996) describes a lobster telescope for a small satellite mission, while Fraser *et al.* (2002) describes a similar payload for the International Space Station (ISS)[1], both using the Angel (1979) optical design. The combination of wide field of view (up to 180°) and the orbital motion of the platform enables the instrument to image almost the entire X-ray sky every 90 minutes, producing, over a period of several years, the most comprehensive catalogue of X-ray variability to date for a wide variety of astrophysical sources.

Such an instrument is expected to survey the sky to the sensitivity of the 6 month ROSAT All Sky Survey once per week and with a 6 month integration time, approximately 10^6 discrete sources are expected to be detected (Priedhorsky *et al.*, 1996). Therefore, *WFT* will, over the lifetime of the mission, develop a deep survey of X-ray sources and also allow monitoring of photometric changes on time scales of about one week in any source bright enough to appear in the ROSAT All Sky Survey. Bright sources can be monitored for much shorter time period fluctuations limited by the number of orbital passes required to build up a statistically significant number of counts from the source.

[1] The design proposed by Fraser *et al.* (2002) has now been proposed for flight as the *Wide Field Telescope - WFT* onboard the Russian Spectrum RG mission

So what kind of sources can *WFT* detect? All classical X-ray binaries in our own galaxy can be monitored, and at much greater distances, for example in the Large Magellanic Cloud and the Andromeda galaxy, the *WFT* telescope would be capable of resolving and monitoring a large number of these binary sources, giving insight into matter in the most extreme temperatures, pressures and magnetic/gravitational fields. Fainter, non-traditional X-ray binaries will also be visible, and the first monitoring of extragalactic binaries over long periods of time will be possible.

The fact that fast X-ray transients have been captured in many narrow field of view instruments, implies that they are common. Statistics from current observations suggest that many thousands of these events occur in the sky per year and the wide field of view, temporal coverage and sensitivity of *WFT* allows it to detect a significant fraction of these events. Fraser *et al.* (2002) estimate that $\sim$ 4000 fast transients will be seen by *Lobster-ISS* per year at a brightness of 10^{-10}ergs cm^{-2} s^{-1} and $\sim$ 36000 at 10^{-11} ergs cm^{-2} s^{-1}. Most of these will have an associated positional accuracy on the sky which will allow identification of the source (star, galaxy, binary system) of the transient X-ray signal. This unprecedented temporal coverage and large statistical sample of observations with time-resolved photometry would allow identification of the driving processes, and host objects for fast X-ray transient events. Priedhorsky *et al.* (1996) provides a comprehensive description of the types of object which exhibit fast X-ray variability and the capabilities of a *Lobster* telescope to detect them. Flaring stars, cataclysmic variables (CVs) and active galactic nuclei (AGN) are all identified as targets that the telescope could detect and monitor over the duration of the mission.

Study of the afterglow of gamma ray bursts (GRBs) has come to the forefront of modern X-ray astronomy because of the *Swift* mission launched in November 2004. The capabilities of *WFT* are complementary to *Swift* and future GRB missions, as the wide field of view permits the detection of multiple bursts each day ($1000 - 2000$yr^{-1} – Fraser *et al.* (2002)), these could be located on the sky to $\sim$ 1 arcmin, allowing identification of probable counterparts in other wavelength bands. The (almost)

full sky coverage per orbit means that good temporal monitoring of a large number of GRB afterglows will also be possible, showing the change in flux in the X-ray band during and after the burst. Indeed, it can be shown that almost all GRBs could be detected by *WFT* as the timescale of the afterglow means that even if the GRB doesn't go off in the field of view, the increase in brightness will still be visible when the field of view scans over the relevant region of sky in the subsequent orbit. *WFT* would therefore be in an ideal position to alert other ground and space based facilities for follow up investigations of the most interesting bursts over a range of energies/wavelengths.

4.2.2.2 Planetary IXRF and *BepiColombo*

The technique of "planetary" XRF spectroscopy was first employed by the non-imaging X-ray spectrometer onboard *Apollo* 15 and 16, confirming the possibility of resolving X-ray fluorescence from the surface of a planetary body under excitation by the solar X-ray spectrum and particles in the solar wind (Adler & Trombka, 1977). The fluorescent X-ray spectrum contains emission lines characteristic of the elemental composition of the regolith, allowing remote sensing of surface composition from orbit.

NASA's *Messenger* spacecraft is due to arrive at Mercury in 2011 and contains a collimated X-ray fluorescence spectrometer. The highly elliptical orbit and poor resolution of this instrument conspires to give resolution between 40 km at periherm and 3000 km at apoherm, meaning that good (better than 120 km) resolution images will only be possible for a small fraction of the 12 hour orbit (Carpenter, 2006). Imaging resolution better than 120 km allows discrimination between different surface features such as impact craters, where compositional studies at this resolution reveal possible variations in mineralogy between areas with differing histories (impacts, tectonic or volcanic activity, etc.).

An imaging XRF spectrometer would allow significantly better resolution of these surface features. Consequently, such an instrument has been proposed as a payload for future planetary orbiters (e.g.

Martin *et al.* (1999), Price (2001), Owens *et al.* (2001) and Carpenter (2006)). The first generation of this technology will fly on *BepiColombo*, the ESA cornerstone mission to Mercury which is due for launch in $\sim$ 2013. The spectrometer onboard this mission is called "The Mercury Imaging X-ray spectrometer" (MIXS) and will image fluorescent X-rays from the regolith with a spatial resolution of a as little as a few hundred meters per surface pixel (Carpenter, 2006). Point to point focusing is impossible from an orbital platform because it requires that the object distance is equal to the image distance, MIXS therefore employs a more complex optical design than the laboratory IXRF. A true Wolter I telescope geometry is therefore required and thirty six tandems of slumped, radially packed MCPs will be used to approximate to it. These are arranged in three concentric rings containing 6, 12 and 18 tandems (Figure 4.3).

The *BepiColombo* spacecraft will enter an ellipical polar orbit around Mercury in roughly 2019. At periherm, it will be a distance of $\sim$ 400 km above the planetary surface ($\sim$ 1500 km at apoherm), which dictates a footprint size (field of view) on the surface of between 7 and 28 km around the orbit. The imaging nature of the telescope allows this to be subdivided to the number of pixels on the detector. However, in this context, the effective pixel size is limited by the amount of flux reaching the focal plane as the image has to binned up until a statistically significant number of counts are seen in each pixel. The surface resolution is however, expected to be $\sim$ 200 m at periherm (Carpenter, 2006), assuming no binning is required. This resolution allows inter-crater imaging, where differing surface composition can be resolved over spatial scales relevant to surface topological features such as craters, valleys and mountains. The comparatively poor spatial resolution of the spectrometer onboard *Messenger* means that inter-crater imaging will only be possible for a small fraction of the 12 hour orbit (Carpenter, 2006), rendering it insensitive to discrimination between the surface composition as a function of surface topology and impact history.

MIXS will perform the first ever *imaging* X-ray fluorescence spectrometry from orbit above a planetary

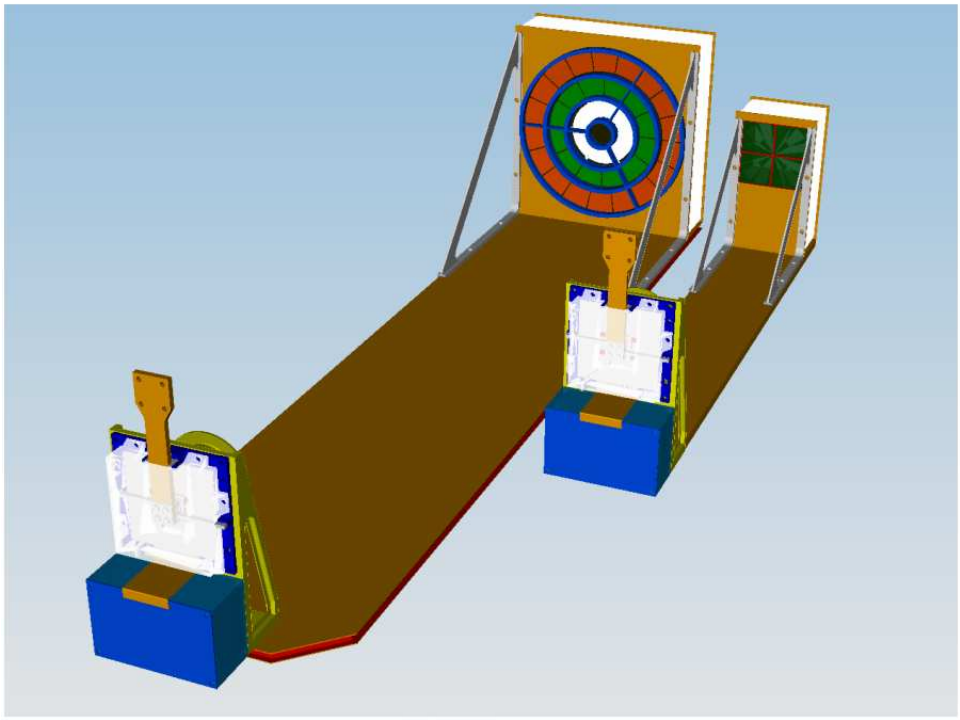

Figure 4.3: Schematic diagram of the MIXS mechanical design. The Right hand element of the figure is the collimator channel which is described in Carpenter (2006). The Left hand part of the image shows MIXS-T (the telescope part of MIXS) where the mirror optic module (MOM) is shown at the top of the image. The three concentric rings of MCP tandems can be seen, the white ring contains six 57° tandems, the Green ring has twelve 30° tandems and the red outer ring has eighteen 20° tandems. Image courtesy of Magna Parva Ltd (Loughborough Innovation Centre, Epinal Way, Loughborough, Leicestershire, LE11 3EH).

surface and hopes to answer key questions about both the origin and evolution of Mercury's surface. These observations will place new constraints on planetary formation models and will reveal much about the birth and evolution of planets in our solar system.

Knowledge of the incident spectrum of X-rays and particles is essential in the analysis of fluorescence data as the intensity of the fluorescence signal is a function of both the absolute and spectral form the incident X-ray and particle spectra. Different illumination conditions can result in different excitation of fluorescence lines, meaning that the source spectrum must be monitored if comparison of the intensity of surface fluorescence features is required. Therefore, MIXS has a sister experiment on the spacecraft known as SIXS (Solar Intensity and particle X-ray Spectrometer) which monitors the solar activity, giving context to the data collected by MIXS from the planetary surface.

4.3 X-ray testing

To aide development of MCP optics in general, and more specifically for the applications described above, it is necessary to test and feed back information to the manufacturer as to how they behave under X-ray and mechanical testing. To aid in this development, the manufacturer, Photonis SAS, (Brive, France) have provided a number of planar and slumped prototype optics for mechanical and X-ray tests. These tests included profilometry, to determine the surface figure of the optics before and after the slumping process and full field illumination of the plates to determine the point spread function of the optics as well as their effective area and behaviour as illumination moves off axis. Monte Carlo ray tracing software was used to predict the behaviour of the optics and diagnose unexpected features within the images, to help optimise the focal position, off-axis angles and source geometries during extended testing.

In the remainder of this chapter I will describe the experimental setup employed for testing MCP

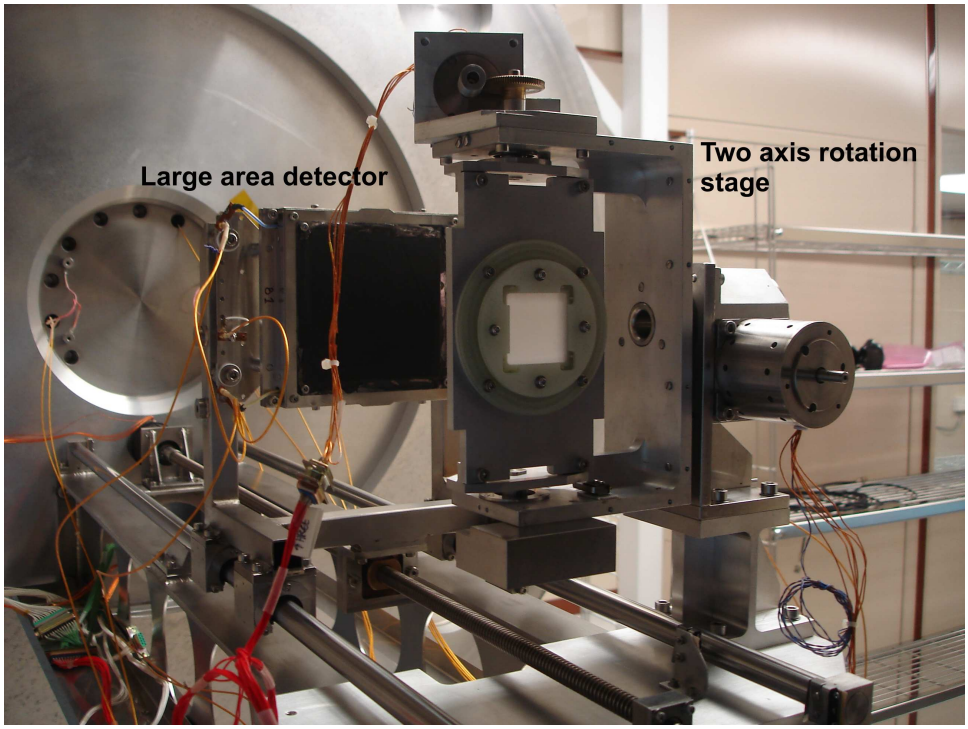

Figure 4.4: The large area MCP detector in the long beamline facility with the two axis rotation stage used for mounting the optics

optics, while in Chapter 5 experimental investigation of a set of prototype MCPs for the *WFT* and *BepiColombo* projects will be discussed.

4.3.1 The focal plane detector

A large area microchannel plate detector was used for all measurements reported herein and is pictured in Figure 4.4. The detector was a laboratory prototype of the High Resolution Imager developed for the *Chandra* X-ray observatory (Lees & Pearson, 1997), and consists of a pair of MCPs with channel bias angles of 6° (measured with respect to the normal to the MCP surface) mounted in a chevron arrangement. The geometric area of the detector presented to the beam was approximately 9.3cm × 9.3cm. Image readout was achieved by means of a charge division resistive anode where the charge passing through each corner of the anode is amplified by four preamplifiers and subsequently enters two parallel (Nuclear Instrumentation Module - NIM) counting and imaging chains.

The imaging electronics chain consists of a four-channel shaping amplifier and an ADC (analog to digital converter) unit which connects to a PC via a USB interface, digitising each readout channel separately. The output from the ADC is read and converted into an image using in-house software; a standard imaging algorithm converts the signals generated at each corner of the anode by an incident charge packet into to an $x - y$ coordinate on the readout plane (Lees *et al.*, 2005) where

$$X = \frac{Sx_1}{x_1 + x_2} \quad and \quad Y = \frac{Sy_1}{y_1 + y_2}. \tag{4.2}$$

Here x_1, y_1 and x_2, y_2 are the maximum electrode voltages and S is a scaling factor which gives the absolute size of the image (Lees & Pearson, 1997).

A characteristic of this type of resistive anode is the presence of "pincushion distortion" in the image, due the charge division technique (Fraser & Mathieson, 1981). This results in the need for image linearisation (Lees & Pearson, 1997), achieved by measuring the imaged position of a regular, square array of pinholes in a mask. The pinholes are ~ 200 μm in diameter and are separated by 4 mm in either axis. Correlating the displacement of pinholes in the image from their known positions on the mask allows subsequent images to be corrected for image non-linearity (Figure 4.5).

Saturation of the ADCs causes events to be lost from areas where the signal on any one of the ADCs exceeds a maximum value (currently $4V$, dictated by the dynamic range of the ADCs). Position-dependent efficiency variations must also be minimised by ensuring that the amplifier gain is set low enough to avoid saturation of the ADCs irrespective of where the pulse arrives in the image plane. A consequence of the charge division technique is that events which arrive close to one of the readout electrodes produce a large amplitude on the closest ADC. Hence, events are lost from the corners of the anode if the detector gain is set too high. A good rule of thumb is that the peak gain should be below approximately one third of the dynamic range of the ADCs.

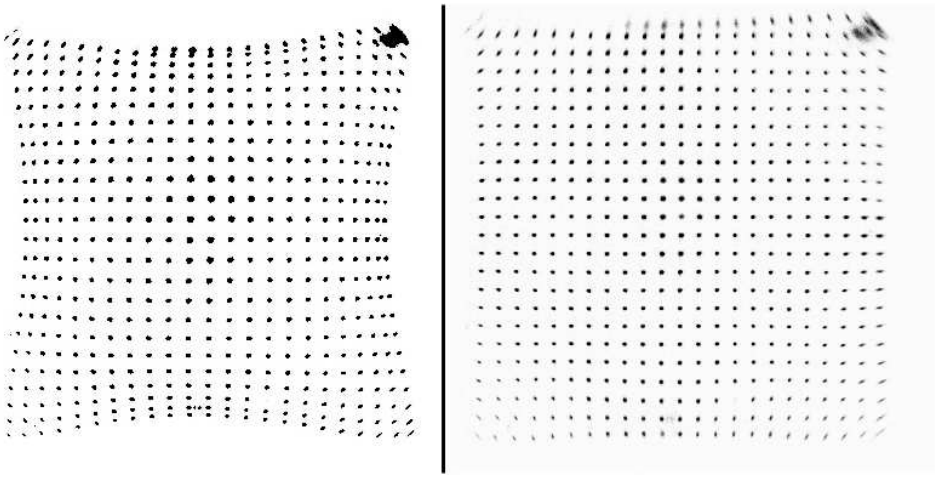

Figure 4.5: The effect of image linearisation on the image taken using the pinhole array. Left, the raw, distorted image. Right, the image after linearisation. Note the good regularity of the linearised image in the center and the degradation in linearity towards the edge of the field of view.

It should be noted that no background subtraction has been performed in the current work. Since the detector MCPs are manufactured from low noise glass, they are expected to generate negligible background; typically ~ 0.1 cm^{-2} s^{-1} (Garcia *et al.*, 1989).

4.3.2 Point to point focusing

Point to point focusing is achieved by placing a planar MCP at the midpoint between a source and detector. Under full field illumination, the reflective channel walls produce a focused (unmagnified) image of the source on the focal plane; this image is broadened by the point spread function which is characteristic of the channel packing geometry. A cruciform point spread function, first observed by Fraser *et al.* (1993), is characteristic of the square pore, square packed channel geometry (Figure 4.6). With a radial packing geometry, the point spread function (PSF) changes, one cross arm is bent into a circular form if the optical axis of the test facility is not congruent with the center of the concentric rings of channels in the radial packing structure (Figure 4.7).

When a planar, radially packed optic sector is illuminated with the optical axis through the centre

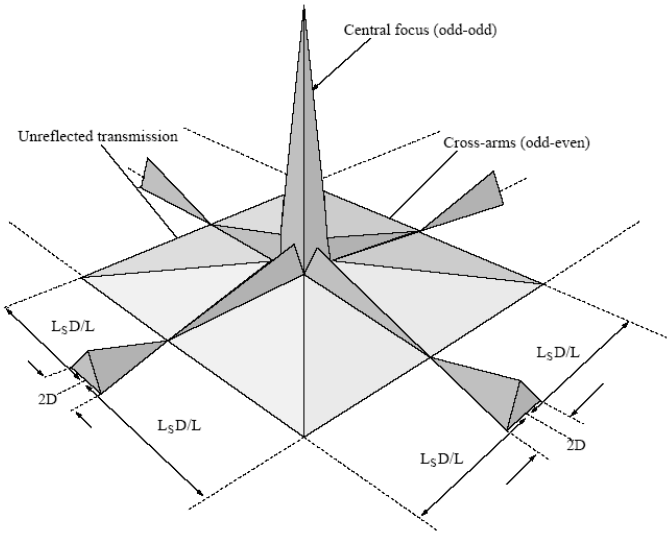

Figure 4.6: The cruciform focal structure of a planar square pore, square packed MCP optic. The central focus comprises photons reflected an odd number of times from orthogonal walls, the base of the pyramid is $2D$ resulting from the non-ellipsoid nature of the channel walls. The unreflected component has a base size of $2L_sD/L$, resulting from the maximum transmission angle of the channels being D/L. The cross arms result from odd-even reflections from orthogonal walls. After Price (2001)

of the sector, one extreme of the circular arm intersects the point of best focus and the other passes through the center of curvature of the radial shells of channels (Figure 4.7). The diameter of the circle is therefore equal to the "off axis distance". The other arm, caused by reflection from the radial channel walls is broadened over an angle equal to the azimuthal open angle of the sector (in these tests, 57°). Figure 4.8 shows experimental and theoretical verification of the distortions to the cruciform PSF of a square packing geometry in the presence of radially packed channels. These distortions were predicted from the conjecture which gave rise to Figure 4.7.

Figure 4.9 shows the 1.4 m beamline used for all point to point investigations. It is fitted with a microfocus X-ray source (ELS 5000 - PSP Vacuum technology) at one end, and the large area detector described above in the focal plane for X-ray detection. The MCP optic is located at the midpoint of the beamline in a holder which has two rotational degrees of freedom controlled via manual vacuum rotation drives (Figure 4.9). Translation of the optic along the axis of the beamline is also possible,

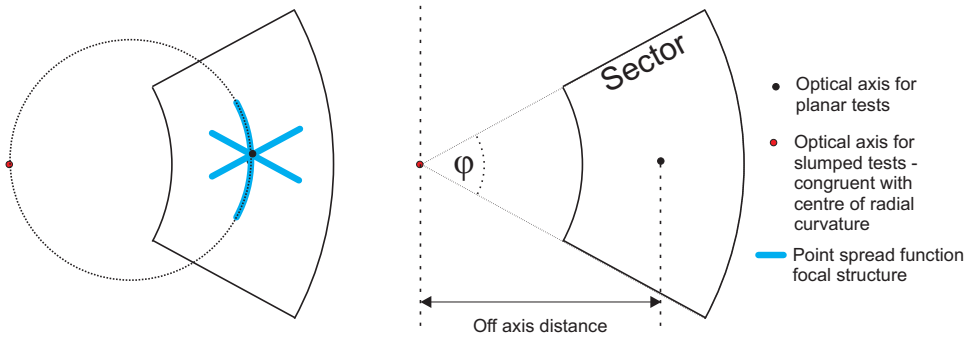

Figure 4.7: The illumination geometry of radial plates under X-ray testing. The Blue lines represent the PSF for point to point investigation as described in Section 4.3.2

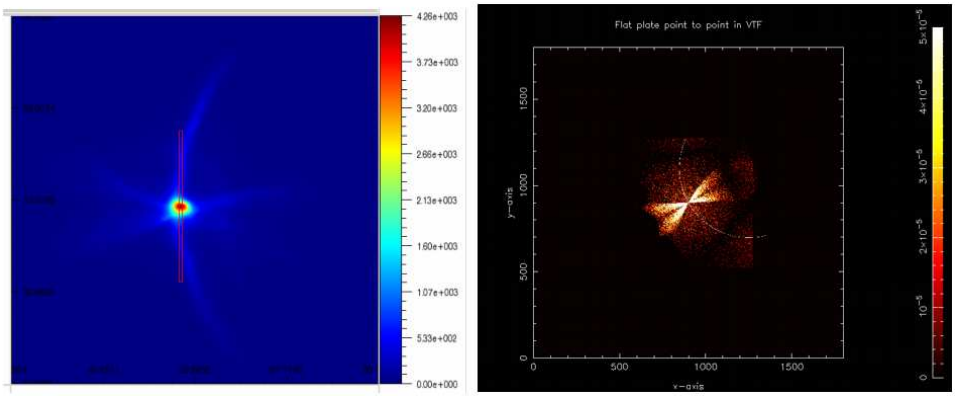

Figure 4.8: The radial cross arm structure of a radially packed MCP sector, (Left) an X-ray image with the illumination geometry of Figure 4.7. (Right) a ray trace image of a similar geometry with the optic rotated approximately 45° azimuthally.

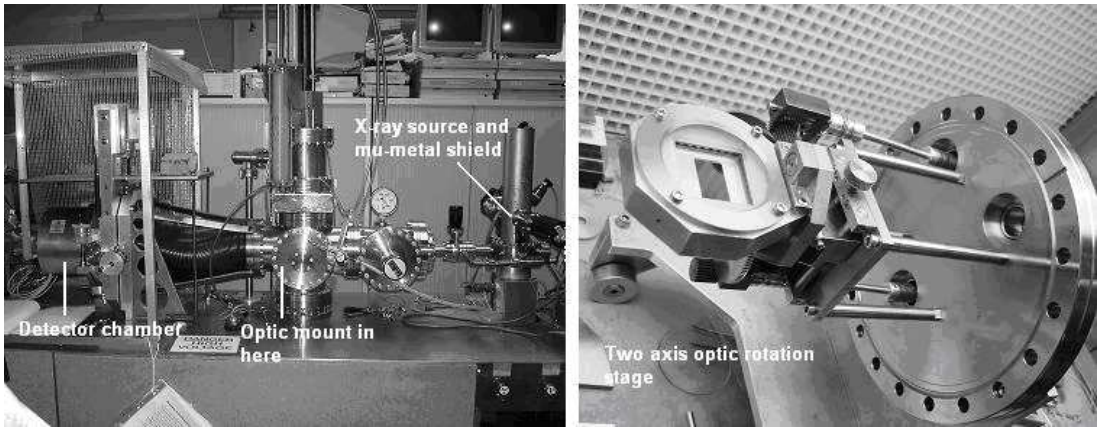

Figure 4.9: (Left) photograph of the short (1.4m) beamline. (Right) the two axis rotation stage used to mount MCP optics.

allowing adjustment of the position of the optic and therefore scanning through the depth of focus.

The microfocus source was fitted with a copper anode operating at ~ 2 kV to excite the Cu-L (0.98 keV) emission line. A 2 μm macrofol (aluminised lexan) filter was used to exclude low energy photons. However, a Brehmsstrahlung component is likely to be weakly contaminating the line emission from the source (Figure 4.10). This source should be capable of producing a spot size of approximately 50 μm diameter at low current (≤ 10 μA). However, the high (~mA) current used in this work to increase the X-ray flux, as well as other environmental effects (such as stray magnetic fields penetrating the mu-metal magnetic shield which surrounds the source) increase the spot size to a diameter of ~ 400 μm, measured experimentally using a pinhole camera technique. A small (1 mm) diameter pinhole was placed 444.5 mm from the source and 946 mm from the detector. Using simple geometry, the image of the pinhole on the detector is related to the X-ray source by

$$d_s = \frac{l_s}{l_i}\left(d_i - d_{pin}\right) - d_{pin}, \tag{4.3}$$

where, d_s is the diameter of source, d_i is the FWHM diameter of image, d_{pin} is the diameter of the pinhole (1 mm), l_s is the source to pinhole distance (444.5 mm) and l_i is the pinhole to detector

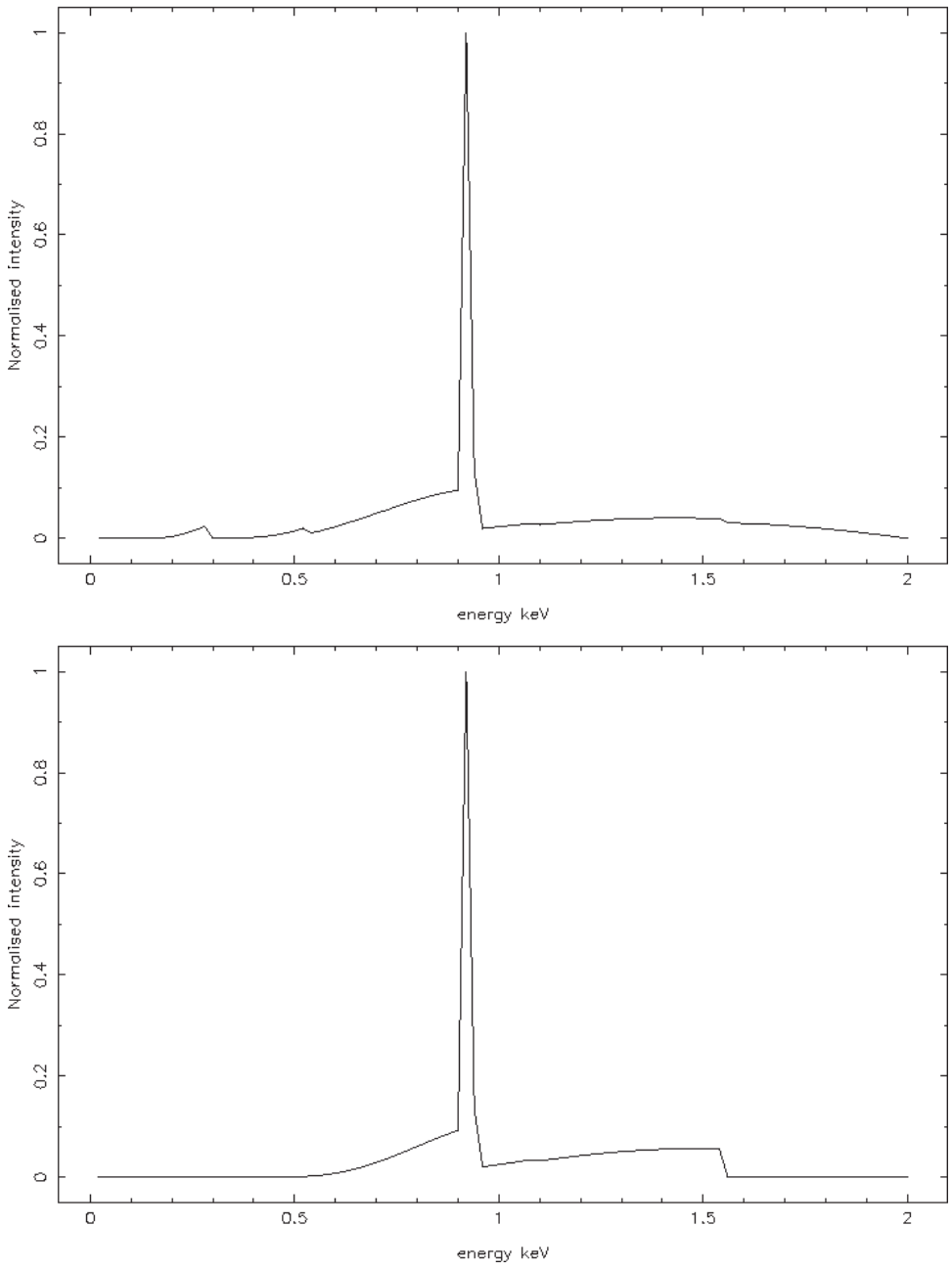

Figure 4.10: Spectrum of an electron bombardment X-ray source with a 2 μm macrofol filter (top) and 4 μm aluminium filter (bottom)

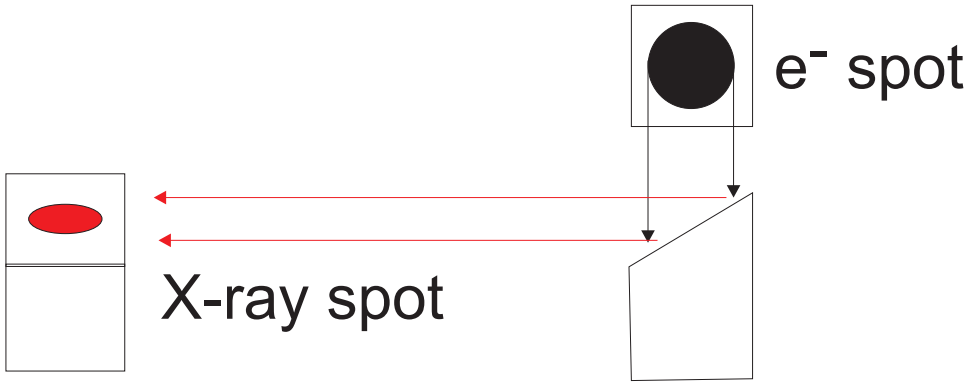

Figure 4.11: Schematic showing the foreshortening of the X-ray source spot in the image plane

distance (946 mm). The source was found to be elliptical in nature with minor and major axes of ~ 400 μm by ~ 800 μm respectively, which is expected because the electron gun illuminates a circular area of the anode, foreshortened in one axis in the detector field of view as the X-ray anode is cut at an angle of $\sim 30°$ to the axis of the beamline (Figure 4.11).

The angle of the optic was optimised in the two rotational degrees of freedom to co-align the MCP channels with the optical axis of the beamline. This was achieved by tilting the optic through a range of *off-axis* angles until the count rate on the detector was maximised. The detector was then moved in the plane perpendicular to the optical axis, centering the image in the detector field of view (the position of optimum image linearity - Figure 4.5). The position of best focus was found by scanning the optic along the optical axis of the system and locating the position of minimum FWHM. Source size and depth of focus effects are considered later during data analysis (Section 5.4.1.1).

4.3.3 Focusing with slumped plates

A long, 27 m, beamline was used to produce full field illumination of the slumped optics (Figure 4.12). It has an electron bombardment source at one end and the same large area detector in the focal plane as used in the short beamline. The optic mount has two rotational degrees of freedom and was fixed in the main tank at the detector end of the beamline. The position of optimum focus was located by

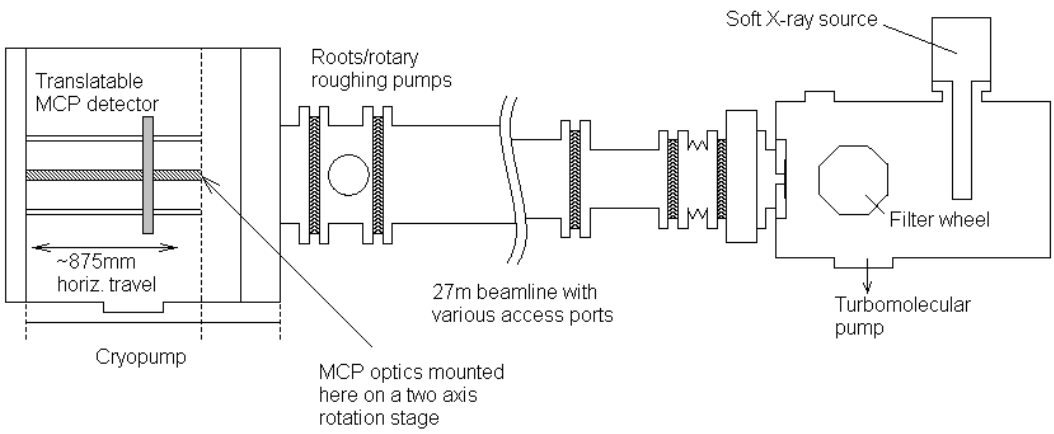

Figure 4.12: Schematic diagram of the Tunnel Test Facility (TTF).

driving the detector along the optical axis to locate the minimum in the FWHM of the PSF. Motion in all of these axes can be controlled under vacuum using stepper motor drives with an accuracy of ~ 1.6 arcmin in the rotation axes and ~ 15 μm in the linear axis.

Although the focusing mechanism for MCPs is reflection, they behave analogously to lenses and hence the MCP radius of curvature R, the image distance v and the object distance u are given by the thin lens formula (Chapman *et al.*, 1991), i.e.

$$\frac{2}{R} = \frac{1}{v} + \frac{1}{u}. \tag{4.4}$$

Note that R will be positive if the source is on the convex side of the lens. From equation 4.4, the nominal optic to detector distance was therefore ~ 370 mm for best focus, 5 mm less than the distance for $u = \infty$ (in which case, $\frac{2}{R} = \frac{1}{F}$ where F is the focal length of the optic).

The only effects of note in terms of broadening of the X-ray focal spot, other than the intrinsic misalignment of channels, are source size and depth of focus. The depth of focus broadening will be negligible because of the short channel length. The source size is estimated to be equal to the size of

the first collimating hole (2 mm) at a distance approximately equal to the length of the beamline. This gives a broadening due to source size of ~ 20 arcsecs. Since the core optic resolution is of order arcmin, the effects of source size are minimal and the measured width of the cruciform image is, therefore, a direct measure of the PSF without the need for source size correction as outlined in Section 5.4.1.1.

4.4 Mechanical testing of MCP optics

Mechnical measurements of MCPs can be made by surface profilometry. A Rank-Taylor Hobson, Form-2 talysurf profilometer was used to measure the surface figure of the MCP optics both in the mounting used for X-ray testing and also on unmounted MCPs. Assessment of the deformation induced into the optic's surface figure by the mounting structure and can therefore be used to inform X-ray image analysis, and can identify degradation in optical performance introduced by errors in the MCP figure, or by distortions introduced by the mounting structure.

The Talysurf works by dragging a stylus over the surface under test, recording the flexion of the stylus arm as a function of distance along the scan. The surface height is recovered using proprietary data processing routines, the details of which are omitted. Raw and processed data were compared in order to verify that the data processing was being used in the correct way. The raw data was analysed manually, fitting a surface gradient and circular profile yielded strikingly similar results to the automated data analysis package which is built into the talysurf software. More details of this are included in Section 5.5.

4.5 Summary

This chapter describes current and proposed uses of MCP optics in a variety of different contexts, explaining the science goals of such applications. It goes on to discuss optical and mechanical testing

of prototype optics, the test setup employed, and any significant limitations. Techniques to minimise the effects of these limitations are described, as successful analysis of the performance of the optics is dependent on fully understanding and optimising the experimental procedure. Chapter 5 describes the testing of these prototypes and what influence these results had on the manufacturing process, future experimental work and the consequences for the eventual applications in space.

Chapter 5

Microchannel plate X-ray optics - Experiments and Modeling

5.1 Introduction

This chapter presents results of recent theoretical studies and experimental X-ray focusing trials on planar and slumped versions of the square pore, square packed and radially packed MCP optics introduced in Chapter 4. This work demonstrates that the intrinsic quality of microchannel plate optics is significantly better than has been found previously. The planar lobster-optic has a resolution limited by the misalignments of multifibres within it, but the slumped version shows a degradation in performance from that intrinsic to the plate as measured from the planar sample. This is explained in terms of errors introduced in the slumping process but experimental issues are identified as a problem in these measurements and work is currently under way to fix this problem. The testing of planar and slumped sectors of radially packed MCPs shows that the performance is as expected from theoretical ray trace simulations and that the optics have been manufactured successfully and have a resolution

of roughly 8 arcminutes.

5.2 Optic samples

Two types of MCP optics are considered in this work: the square pore, square pack "lobster-eye" format and radially packed sectors which will eventually be used in a tandem structure to approximate the Wolter-I focusing geometry (Figure 5.1). All of these optics were produced by Photonis SAS (Brive, France). Both types are produced in much the same way as standard multiplier MCPs (Section 2.1.1). Square "multifibres" (0.9 mm in diameter) are produced and then stacked into the required geometry (cartesian of radial packing) then fused into a block by the application of heat and pressure. The MCPs are then made by slicing the appropriate thickness from the block and etching away the unwanted glass.

The "lobster-eye" MCPs were square tiles measuring 4 cm $\times$ 4 cm, containing square packed arrays of square channels. The optic had 20 μm width channels on a 26 μm pitch with a channel aspect ratio (L:D) of 50:1 (Figure 5.1-A). Two samples are discussed: one planar optic, and one slumped to a nominal (spherical) radius of curvature of 75 cm. Performance comparisons for these two optics allow assessment of the intrinsic performance of the MCP before and after the slumping process in terms of angular resolution and effective area.

The radial sectors under test have a 57° azimuthal extent with internal and external radii of 20 mm and 49 mm respectively (Figure 5.1-B). The channels are square, 20 μm in diameter on a 26 μm pitch. The planar sector is missing a small portion of one corner which was broken off during manufacture and has 0.9 mm length channels. The slumped sector is similar but the channels are 5 mm in length, producing a much more robust optic but complicating the testing geometry (see Sections 5.3.1.2 and 5.4.2.3).

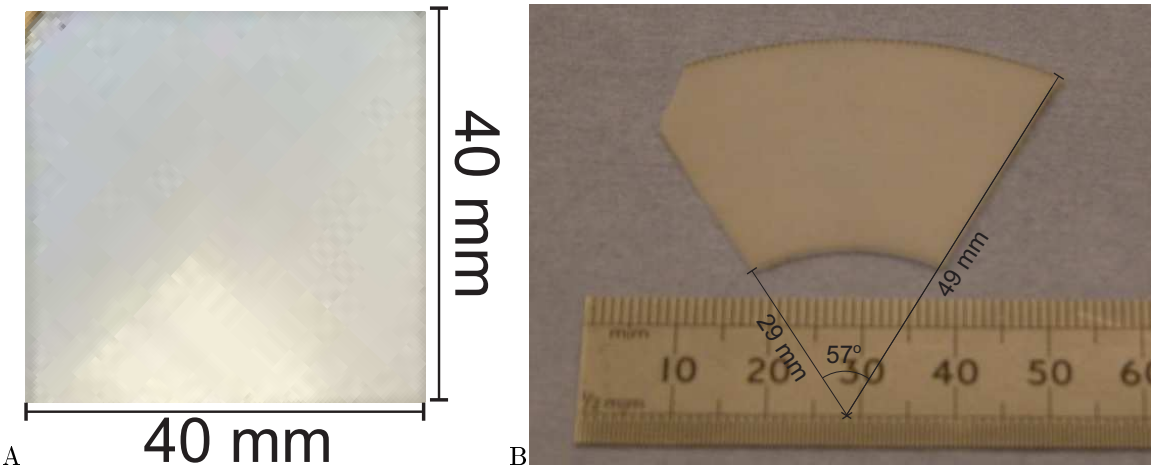

Figure 5.1: Images of the test sample MCP optics. A – Square pore, square pack lobster optic. B – radially packed optic sector.

5.3 Simulations

A Monte-Carlo sequential ray tracing code, developed by Willingale (2007b) is used to investigate MCP optics at X-ray energies. The code assumes Fresnel reflection of X-rays at the MCP pore walls, and traces rays from where they are generated in the source, through the optic and onto a detector. Models of the test facilities described in Section 4.3 were set up in order to investigate the imaging performance of the optics. The output of this ray tracing system provides valuable information about the testing geometry and what features are expected in the experimental images.

5.3.1 Simulating expected images

5.3.1.1 Cartesian optic geometry

Figure 5.2 shows the effect of increasing channel misalignments on the point spread function of a planar, square pore, square pack MCP in point-to-point focusing mode. As the RMS channel misalignment increases, the point spread function blurs from the pyramidal distribution expected for a perfect optic into a broader, more gaussian profile.

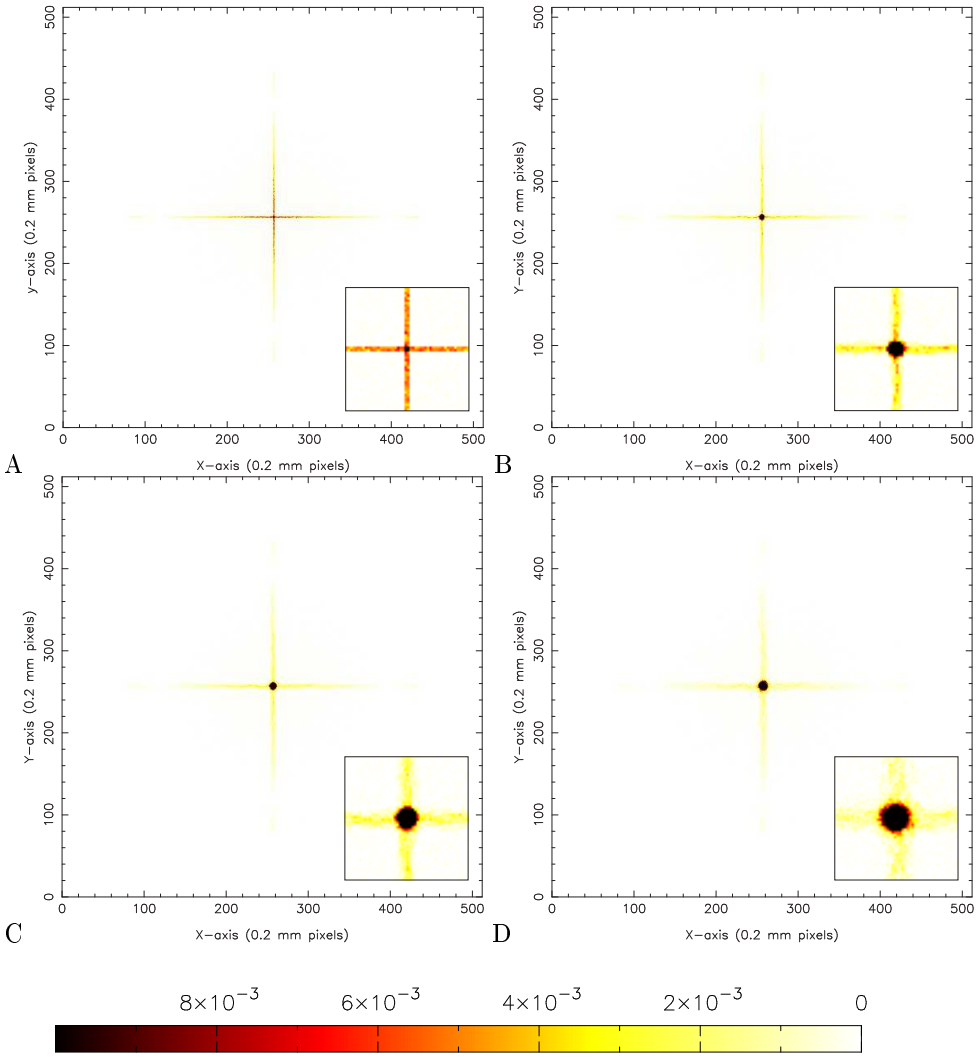

Figure 5.2: Ray traced simulations showing the effect of increasing deformations to the channel alignment for a planar, square pore, square pack MCP in point-to-point focusing mode. The detector pixels are 0.2 mm square. The inserts in the bottom right of each panel are zoomed in versions of the central 50 pixels of the point spread function magnified by a factor of 3. A) zero channel deformation B) 2 arcminute RMS channel deformation C) 3 arcminute RMS channel deformation D) 5 arcminute RMS channel deformation. The colour scale represents the effective area (in cm^2) per pixel in the image plane and should be interpreted as intensity in the X-ray image. The images have a common saturation level of 10^{-2} cm^2 per pixel in order to increase the contrast between the bright cental focus and the lower level structure.

Figure 5.3 is similar to Figure 5.2 but represents a slumped optic operating as a "lobster-eye" X-ray lens in the long (27 m) beam line test facility (Section 4.3) and with a higher spatial resolution in the focal plane (0.045 mm pixels). The extent of the cross arms and direct transmission region is a consequence of the illumination geometry. For point-to-point focusing mode, the characteristic size of the cruciform PSF is twice the side length of the illuminated area of the optic (Price, 2001), whereas, for focusing of parallel X-rays with a slumped optic the size of the region of direct transmission is roughly equal to the size of the illuminated area. The divergence of the X-rays due to the finite (27 m) length of the test facility will broaden this square of direct transmission by a small amount (similar triangles gives a negligible broadening of 0.5 mm for this geometry).

The increasing channel misalignment error leads to a broader PSF allowing us to measure the characteristic channel misalignment of the MCP under full aperture illumination by comparing the experimental PSF with one generated by the ray-trace software.

Figure 5.4 shows the number of reflections each ray has undergone to reach a specific position in the focal plane. The model used to generate the data assumed 2 arcmin RMS channel misalignments, and as such it is directly comparable with Figure 5.2 (B). The colour scale is shifted such that 1 on the colour scale represents zero reflections, 2 represents a single reflection etc. and white is a pixel containing no events. This shift is used to differentiate between pixels with no events in them and those pixels with rays which arrive at the focal plane unreflected.

The structure in Figure 5.4 (A and B) is explained in Section 4.3.2. The doubly reflected central focus is shown (Figure 5.5) to originate primarily from the corners of the optic (as expected because of the geometry involved). The centre of the optic allows rays through mostly unreflected, and the center of each edge contributes predominantly to the singly reflected cross arms. A consequence of this modeling is that for a future instrument design, it may be preferable to mount the optics by fixing in the center of each edge rather than at the corners to maintain the high effective area in the double

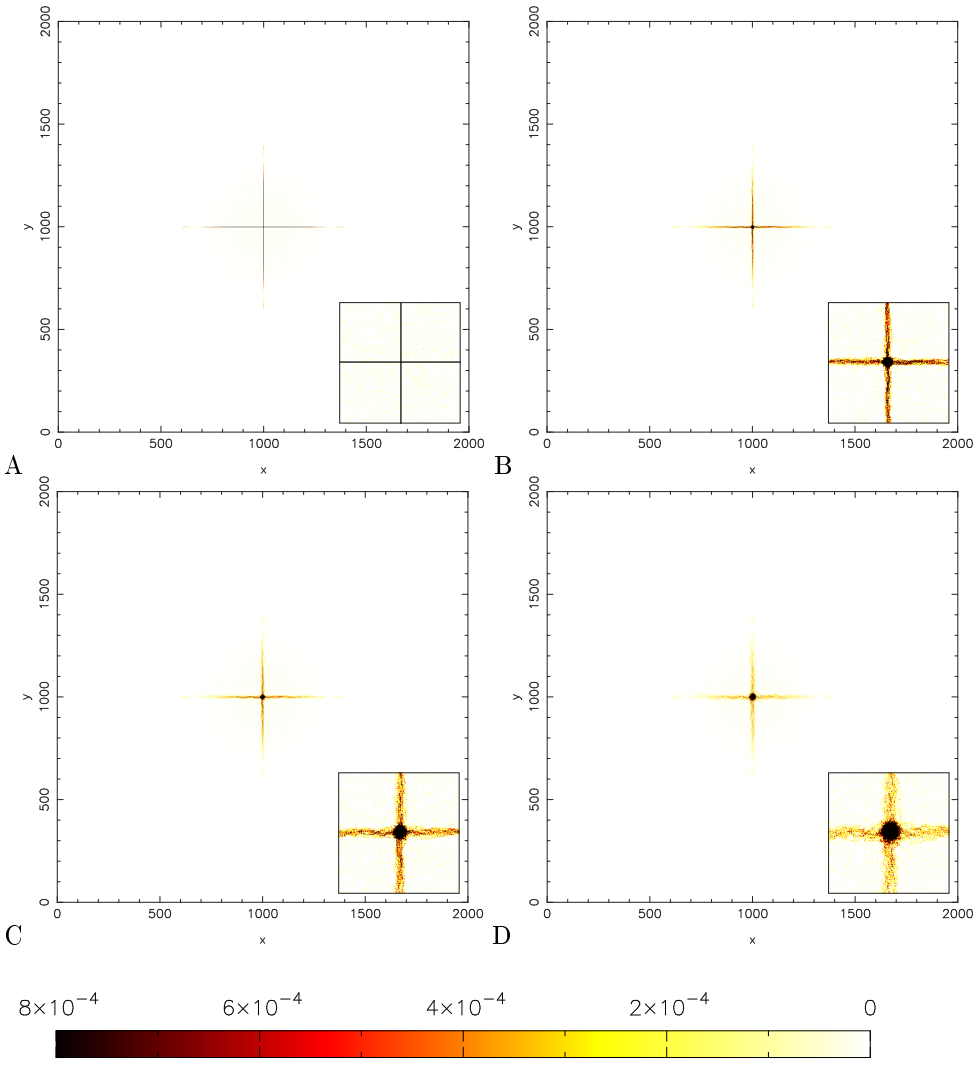

Figure 5.3: Ray traced images showing the effect of increasing deformations to the channel alignment for a planar, square pore, square pack MCP focusing almost parallel X-rays in a 27 m beamline. The detector pixels are 0.045 mm square. The inserts in the bottom right of each panel are zoomed in versions of the central 200 pixels of the point spread function magnified by a factor of 3. A) zero channel deformation B) 2 arcminute RMS channel deformation C) 3 arcminute RMS channel deformation D) 5 arcminute RMS channel deformation. The colour scale is as described in Figure 5.2.

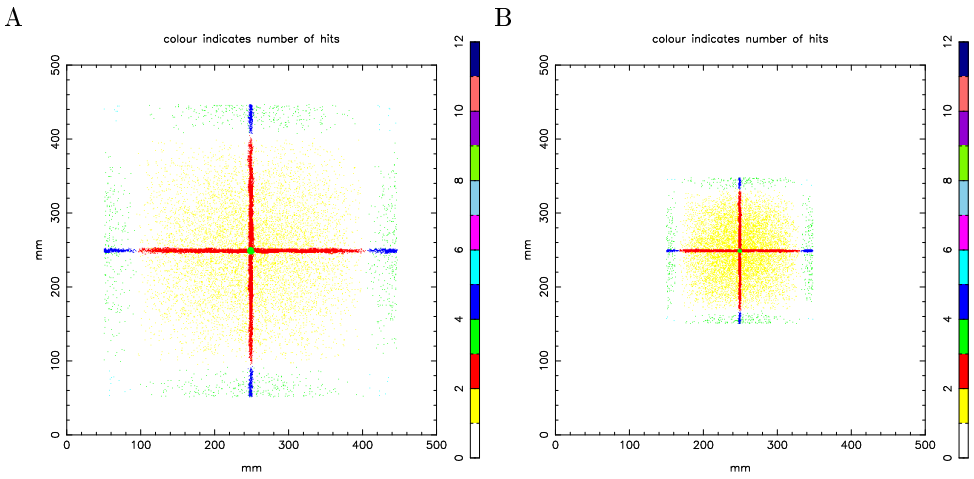

Figure 5.4: Images showing the modal average of the number of reflections undergone by rays in order to arrive at the focal plane in the given position. The colour scale represents the number of hits plus one, in order to differentiate between pixels with no events and those with an average of zero reflections. A) planar MCP in a 1.4 m beamline. B) MCP slumped to 750 mm spherical radius of curvature in a 27m beamline – the position of the focal plane is 370 mm from the optic in order to account for the finite length of the beamline. Both models assume 2 arcminute blurring of the channel axes.

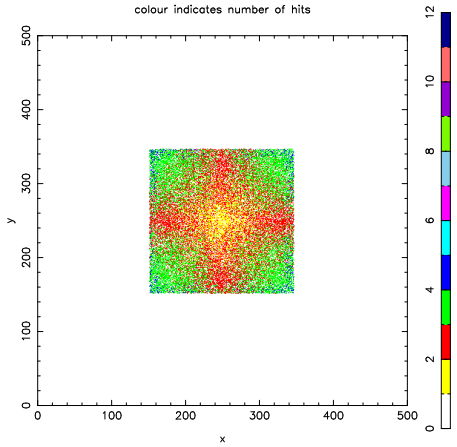

Figure 5.5: Image showing the number of reflections vs the x/y position of the last reflection on the optic rear surface. The image is directly comparable with Figure 5.4 and shows, on average, where on the optic the features in the PSF originate from (the same colour scale is applied as Figure 5.4).

reflected central focus.

5.3.1.2 Radial optic geometry

To interpret the images which will be produced during the radial packed optic alignment process, and inform adjustment of the assembly to achieve best focus, a series of ray trace images were produced (Figure 5.6). This figure shows the effect of moving the optic off axis in two cartesian axes (one parallel to either axis of the images). It is clear that as the optic is moved off axis, the image blurs into a section of a circle, the orientation of which indicates the off axis angles. Moving the detector into and out of focus has a similar effect and iteration is needed to find the true focus. The bands of events (rays) above the focus are a consequence of rays which undergo an even number of reflections from opposite walls in the channels.

Figure 5.6 shows the extreme complexity of the point spread function as the optic moves off axis. This is because of the coma distortion expected from a single focusing element and will not be present in the MCP Wolter telescope. However, in order to assess the quality of the MCPs themselves, testing of individual optics is needed. For this reason Ray trace analysis was performed prior to experimental testing in order to show what should be expected in the images. Let us take each panel (from Figure 5.6) in turn:

Panel A shows what happens to the focus when the optic 20 arcminutes off axis, rotated about the x-axis of the figure. The focus is observed to be centred on the optical axis, but it has blurred in the vertical axis into a section of a circle. Not shown in this figure is what happens for negative angles in this axis. However, this produces precisely the same behaviour but with the central focus curve in the opposite sense (i.e. it is like a mirror image of panel A about y-axis at x=1000). The bands of intensity at the top of the figure are difficult to see but they represent bands of X-rays which undergo an even number of reflections from opposite walls in the channels and are therefore undeviated by the

optic.

Panels B and C show the effect of rotating 20 arcminutes off axis by rotating about the y-axis of the figure. Panel B shows what happens as the grazing angles onto the channels are increased because of the off axis rotation. It is clear that the increased grazing angles reduce the intensity of the rays which pass through the optic (those at the top of the figure). This was expected as the reflectivity is reduced at higher grazing angle and as these bands are composed of multiple reflections, the intensity falls rapidly with increasing angle as it scales as one over the reflectivity raised to the power N where N is the number of reflections. The central focus is observed to be a section of a circle which is centred on the on axis point. Precisely the opposite effects are observed if the rotation is such that the grazing angles are reduced (as is the case in panel C), here the intensity in the bands of undeflected rays are increased and the central focus is above the on-axis point. Here, the central focus in panel C is a mirror image of panel B about the x-axis at y=1000.

Panel D shows that things become even more complicated at off-axis angles in both directions. Here the optic is 10 arcminutes off in both axes and the symmetry of the central focus is much more difficult to decipher. Experimental data should therefore always be analysed with theoretical ray tracing to support it as the morphology of the image may not be simply explained if the optic is off-axis in both axes. Yet more complications are present with the addition of the final experimental degree of freedom, the detector position along the optical axis.

Figure 5.7 shows that each zone of the PSF consists of events undergoing a particular number of reflections. Rays which undergo an even number of reflections (from parallel walls) pass straight through the optic and arrive on the focal plane in discrete bands towards the edge of the field of view. However, rays undergoing an odd number of reflections (from parallel walls) are focused by the optic, and arrive in the central focus. The optic is essentially a spherical reflector and therefore does not obey the Abbe sine condition (Michette, A., 1993). This condition requires that all geometrical paths

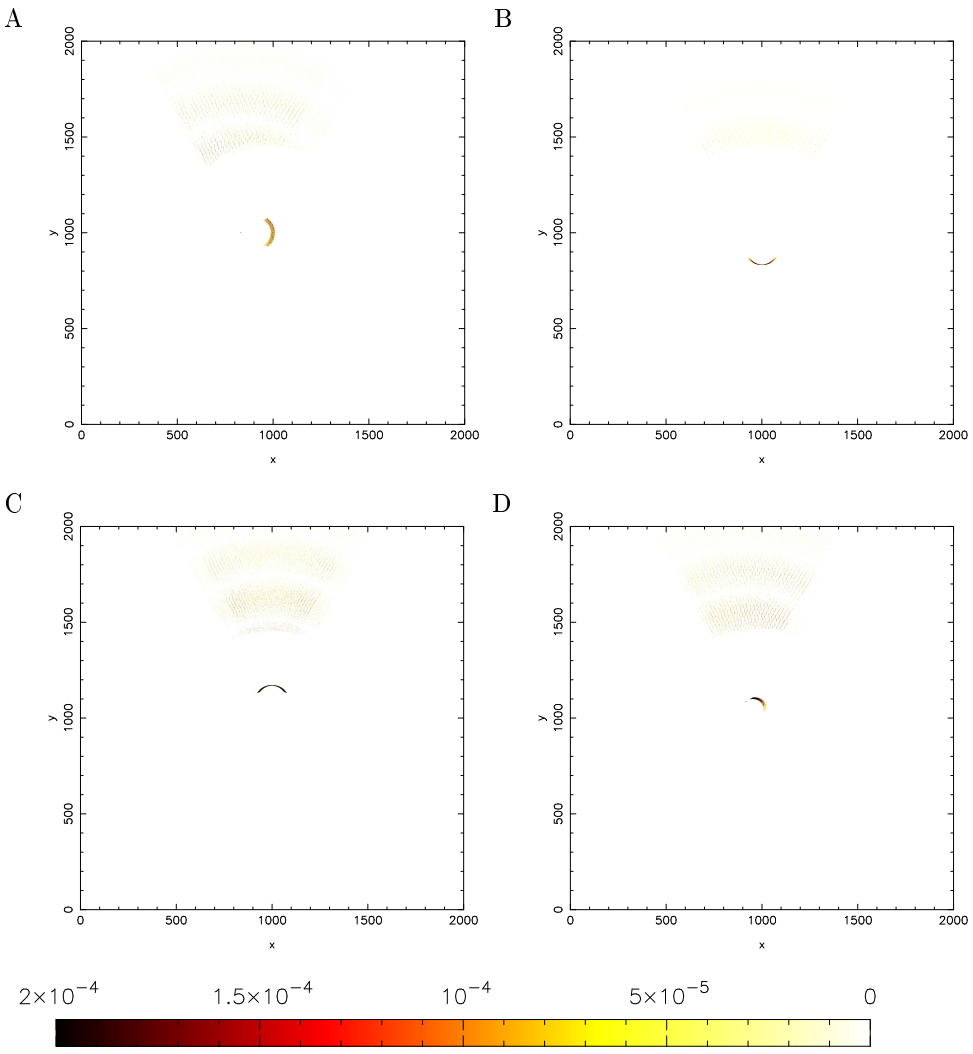

Figure 5.6: Ray trace images of a sector with the same parameters as the slumped optic to show the focal structure as the image moves off axis. A) 20 arcminutes off axis horizontally. B) 20 arcmins off axis vertically. C) 20 arcmins off axis vertically (in opposite direction to B). D) 10 arcmins off axis in both axes. The colour scale is as described in Figure 5.2.

through an optical system must produce the same magnification. In other words, for an optical system to produce sharp images, both on and off-axis, the sine of the output angle must be proportional to the sine of the input angle:

$$\frac{\sin u'}{\sin U'} = \frac{\sin u}{\sin U}, \tag{5.1}$$

where the variables u, U are the angles that the rays make with respect to the optical axis as they leave the object, and u, U are the angles of the same rays where they reach the image plane (Figure 5.8). The two reflections which occur in the Wolter geometries are arranged such that the Abbe sine condition is met over the whole optic. Therefore, spherical aberration and astigmatism will be observed when the optic is tested as a single MCP (rather than the tandem approximation to the Wolter geometry).

The ray trace simulations described above will be used to aid in the interpretation of experimental work later in the chapter. Further simulations will be shown alongside experimental data where appropriate to demonstrate the effectiveness of the model to aid later analysis.

5.3.2 Effective area

The effective area of an MCP optic is defined as; the area of the beam which contains the same number of counts as lie within the central focus of the image in a fixed exposure time. By selecting a region of interest in the point spread function within which to accept rays, the ray tracing software can be used to generate effective area curves based on the reflectivity model used in the simulation.

The reflectivity model used to produce Figure 5.9 assumed reflection from a surface made of silica, (SiO_2) with zero surface roughness. Measurements of the reflectivity of the channels made at the Daresbury synchrotron radiation source indicated that SiO_2 was a better assumption than the bulk

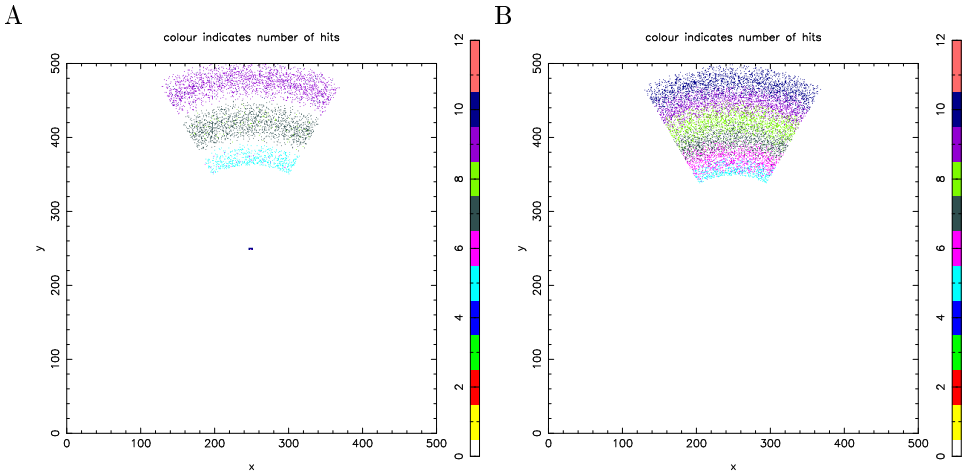

Figure 5.7: A) data from ray trace modeling showing the modal average of the number of reflections undergone by rays. The colour scale represents the number of hits plus one, in order to differentiate between pixels with no events and those with an average of zero reflections. B) As in A but the image positions represent the position of the ray in the optic plane (i.e. where the rays are reflected in the optic - for the final reflection if multiple reflections). The model assumes the MCP is slumped to 1333 mm spherical radius of curvature and is fitted in a 27m beamline – the position of the focal plane is 650 mm from the optic in order to account for the finite length of the beamline. Both models assume zero blurring due to random misalignment between channel axes (i.e. that all channels point towards the centre of curvature of the optic) and that the off axis angle is zero in both axes. No RMS blurring of the channel axes was included as I could not make the blur give physically reasonable deformations in the ray tracing software this will be included in the next phase of study.

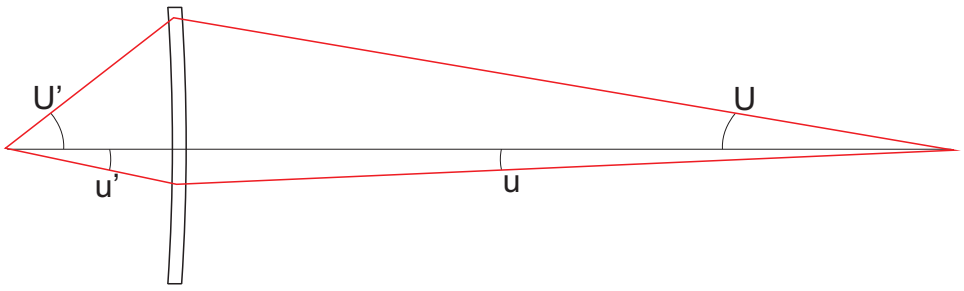

Figure 5.8: Diagram to demonstrate the Abbe sine condition, both rays intersect at the focal point meaning that they have the same magnification.

composition of MCP glass (Price *et al.*, 2002b). Perfect channel alignment and perfect square pore, square packing are also assumed in order to generate the effective area curves.

The surface figure errors and channel misalignments are expected to make little or no difference to the effective area, as changing the angles of incidence by $\sim$ arc minutes will not significantly change the reflection probabilities. However, future models should incorporate the reduction in reflectivity of a rough surface as a function of increasing X-ray energy. The assumption of zero surface roughness is valid at the energies of interest here (Cu-L, 0.93 keV) as the wavelength (13.3Å) is close to the ~ 15 Åsurface roughness measured for previous MCP optics (eg. Price *et al.* (2002b) or Price *et al.* (2002a) and references therein). However, this model is expected to overestimate the effective area at high energies because of the same assumption of zero surface roughness. This is because good specular reflection at grazing incidence is expected if the surface is smooth at spatial scales approximately equal to the wavelength of the incident radiation (Price (2001) and Michette, A. (1993)).

The upper (green and red) curves in Figure 5.9 represent an optic with an unobstructed (40 mm $\times$ 40 mm) geometric area, red is for a source distance of ∞ and green for a source distance of 27 m (as in the long beamline facility). For comparison, the blue curves show the effective area for the same optic with the geometric area reduced to 35 mm $\times$ 35 mm, owing to the mounting structure of the optic. Again, for these curves, the increased angles of incidence caused by the finite length of the beamline do not lead to a significant change in effective area. It is clear that the mounting structure causes a significant ($\sim 20\%$) reduction in MCP effective area at low energy ($\leq$1.5 keV). However, the hard X-ray response is dominated by the inner sections of the plate owing to the reduced angles of incidence there and the falling critical angle at higher energies. It can therefore be seen that at an energy of $\sim$ 1.7 keV, there is no degradation in effective area caused by the mounting structure. Using Equation 4.1, the critical angle for reflection at 1.7 keV is 1.38°, which compares to an angle of incidence implied by reflection from a pore at the edge of the MCP of 1.34°. Therefore, any photon with energy less

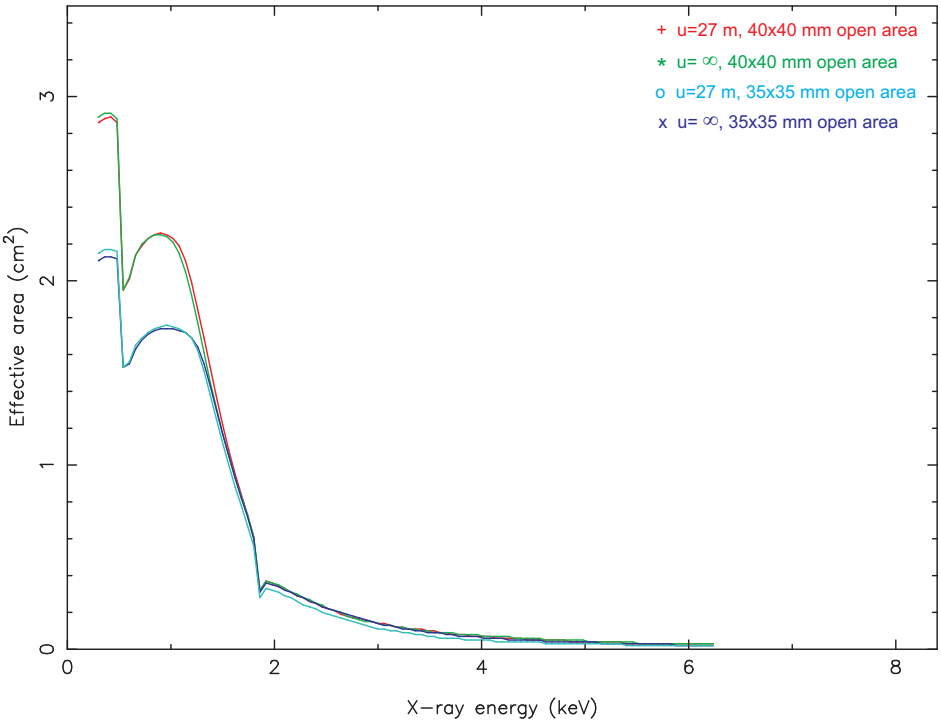

Figure 5.9: Comparison of effective area as a function of energy for source distance u =27 m (red and light blue) and $u = \infty$ (green and dark blue) with either an unobstructed 40 mm by 40 mm field of view (green and red) or with a 35 mm $\times$ 35 mm aperture to represent the mounting structure (two blue curves).

than 1.7 keV incident anywhere on the MCP can be focused. Photons with energy higher than 1.7 keV cannot be reflected from the extreme edges of the plate and, therefore, the effective area is reduced at high energy. This is an important validation of the effective area model.

5.4 X-ray testing

5.4.1 Point to point focusing

The planar optics were placed at the position of optimum focus (nominally half way between the source and detector plane) in the 1.4 m beamline by minimising the width, specifically the full width at half maximum height - FWHM, of the point spread function (PSF) as a function of detector position.

The imaged spot was expected to be elliptical in nature because of the geometry of the source. The electron beam illuminated an approximately circular area of the anode, which projected an ellipse along the axis of the beamline owing to the anode's inclination at angle of $\sim 30^{\circ}$ to the optical axis. The size of the ellipse was found by Brown & Yates (2006) to be 0.4 ± 0.05 mm in the vertical (semi-minor) axis and 0.8 ± 0.05 mm in the horizontal (semi-major) axis. This was achieved using a pinhole camera technique, described in Section 4.3.2.

5.4.1.1 Cartesian MCP geometry

Figure 5.10-A shows a linearised image produced by a 24 hour exposure at low count rate (< 500 cps) for 0.93 keV X-rays; Figure 5.10-B shows a cut taken through the focal spot in the best focus axis (indicated in panel A of the figure). The FWHM of the intensity profile is 3.1 arcmins before removing the non-zero size of the X-ray source spot (Section 5.4.1).

Removal of the source size by subtracting it in quadrature from the size of the image of the central

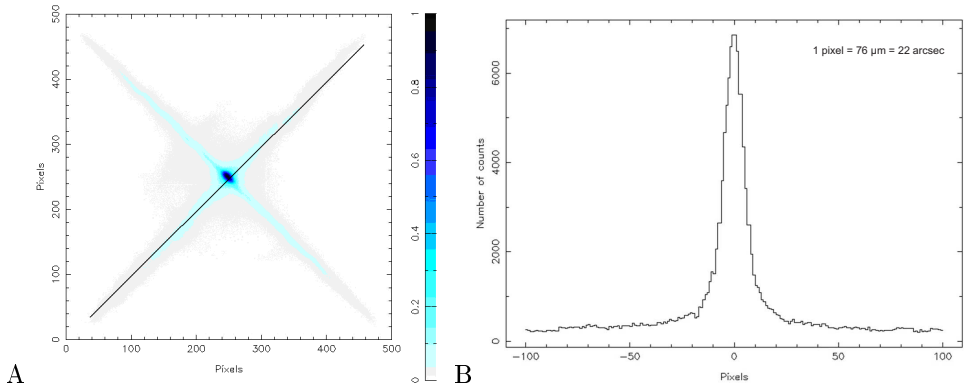

Figure 5.10: A) Linearised image of the PSF from the flat plate point-to-point measurement. The elliptical central focus is a consequence of the elliptical source spot. The direction of the cut shown in panel B is from bottom left to top right. Each pixel is $\sim 76\mu$m and the colours indicate normalized intensity. Data from Brown & Yates (2006). B) Cut taken through Figure 5.10 as indicated by the black line. The FWHM indicates an optic resolution of 3.1 arcmins before source size correction.

focus results in an optic resolution of 2.3 ± 0.2 arcmins. This intrinsic resolution is limited by channel misalignments and represents a significant improvement over the performance of MCPs characterised in previous work. Price (2001) and Nussey (2005) report a best resolution of $\sim 6-8$ arcmins FWHM. These latest results also exceed the ~ 4 arcmins optic resolution requirement for *WFT* which arises from the need to perform source position centroiding to an accuracy of < 2 arcmins (Black *et al.* (2003) and Bannister & Fraser (2003)).

The quadratic subtraction of source size reported by Brown & Yates (2006) is strictly only valid for overlapping gaussian profiles (as it is based on the central limit theorem). This assumption has held in previous optic tests (e.g. Price (2001) or Nussey (2005)) because the channel misalignments blur the PSF to a broader, approximately gaussian figure. MCP quality is now reaching the point where the true, triangular, nature of the PSF dominates and, therefore, a better model is needed for removal of source size effects.

Estimation of the contribution due to source size was achieved by convolving a triangular point spread function with a top hat function, used to represent the source. The relative contributions of

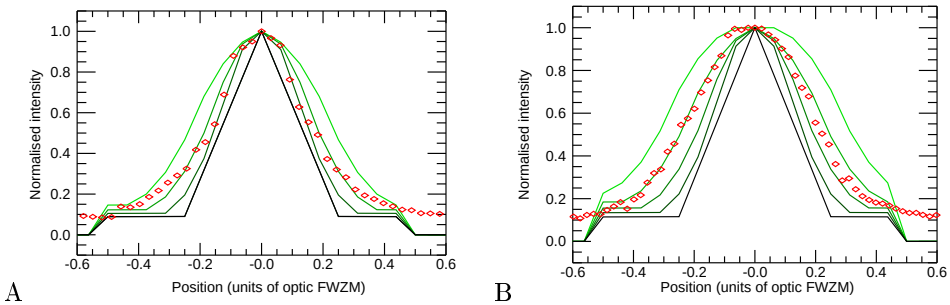

Figure 5.11: A) cut taken through Figure 5.10 as indicated by the black line in Figure 5.10-A. The green "fit lines" represent the model profiles and the red points are measured data points from Figure 5.10-B. B) cut perpendicular to that in panel A. The black triangular line in both panels is the response when the source size is approximated by a delta function i.e. it is the limiting resolution as source size tends to zero. The fit lines represent (in order of increasing width) ratio of source size to optic FWZM of approximately 0.2, 0.3, 0.45, 0.55. The sharp change in gradient of the model curves towards the edge of the plots is simply the edge of the modeled region and is not a physical effect.

the source and optic can be deconvolved by plotting the model in units of optic full width at zero maximum (FWZM) and comparing the size of the source with the width of the PSF. Figure 5.11 shows intensity histograms in orthogonal directions through Figure 5.10-A, giving a ratio of source size to optic FWZM of $25-50\%$ for the best focus axis, implying an optic resolution, after removal of source size, of $1.5-2$ arcmins FWHM (with a known source size of 400 μmin this axis) (Figure 5.11, A). Figure 5.11 B, shows the same type of fit for the PSF in the orthogonal direction. This implies a best fit ratio of $40-50\%$, or $\sim 3-4$ arcmins (with a known source size of 800 μmin this axis), supporting the observation of Brown & Yates (2006) that the optic had different focal positions in the two axes and hence that it had some apparent curvature in one of these axes. Such a curvature is not inherent to the optic and it is believed that it is due to mounting stresses introduced by the optic holder. A more detailed description of this issue is given in Section 5.4.2.1 where a similar effect is seen in the slumped plates.

A more rigorous model which convolved a gaussian source intensity profile with the triangular PSF led to a reduction in the significance of the fits and is therefore not included. The behaviour of the

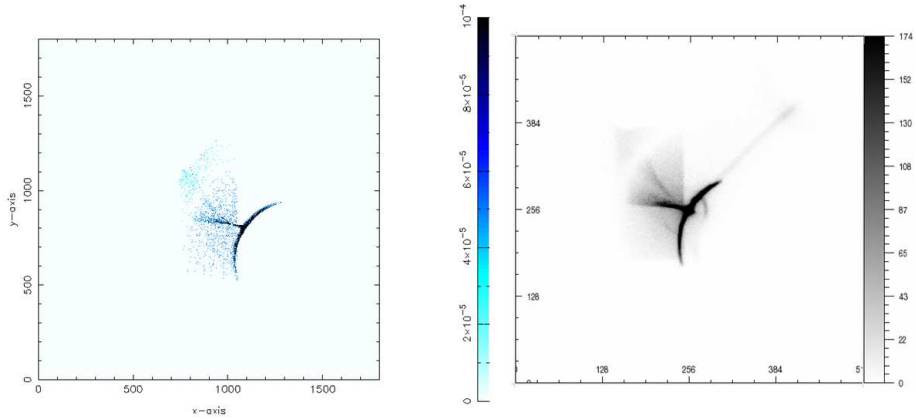

Figure 5.12: (right) is an X-ray image taken in point to point focusing mode in the 1.4 m beamline with a radially packed sector. A rectangular aperture was placed in front of the MCP to prevent stray X-rays reaching the focal plane. The axes are pixels (0.27 mm across) and the colour scale is counts per pixel. (Left) a ray trace model of the same configuration. In the model, the optic has an off-axis angle of $\sim 0.5°$ in both axes of the rotation stage, and is 50 mm out of focus.

source is believed to be best approximated by the top hat function as the intensity from the source spot is a function of the number of electrons incident on the anode at a given position. The lack of improvement in the fit seems to imply that a uniform beam of electrons is generated by the electron gun. This is not unreasonable as the gun is capable of achieving an extremely small and high intensity X-ray source spot (Section 4.3.2) and therefore a highly collimated, uniform beam is to be expected.

5.4.1.2 Radial MCP geometry

Initial "quick look" studies were made with a rectangular aperture mask measuring $\sim$ 15 mm $\times$ 35 mm. These studies produced the image shown in Figure 5.12. Analysis of this image and comparison with ray trace modeling indicates that the FWHM angular resolution is approximately 8 arcmins. However, the model also shows that the optic is 0.5° off axis in both axes of the rotation stage and also that it could be as much as 50 mm out of focus. It should be noted that the model assumes perfect channel coalignment and therefore the prediction of 50 mm out of focus is an upper limit.

Next, an improved optical arrangement was set up with almost the full aperture of the sector illuminated. The tip and tilt of the optic was optimised such that the focal spot arrived in the centre of the directly transmitted component of the PSF (as indicated by ray trace studies). It was then moved along the optical axis of the test facility to find the position of best focus. Unfortunately, the travel of the linear motion drive was insufficient to find this position, meaning that Figure 5.13 is still slightly out of focus. This is evident from the asymmetry of the cuts through the image. Previous experimental work shows that true optimisation of the focal position can give a significant improvement in the apparent angular resolution of these devices. Unfortunately, for experimental reasons the position of best focus could not be found as significant extension of the travel of the optic adjustment (or relocation of the optic) was not possible without significant, time consuming and expensive modifications to the test facility. The fact that the optic does not focus in the position expected implies that there is some residual curvature of the optic that was not expected. This is thought to be introduced by the mounting structure as the compression spring used to clamp the optic was square, implying uneven pressure onto the optic and therefore the likelihood is that the MCP was being deformed. Production of an improved mount for the optic was thought to be more comprehensively addressed using slumped plates in the long beamline as these results would be more representative of how the plates would be used in a real telescope and more adjustment and experimental flexibility was possible using the long beam facility (see Section 5.4.2.1).

Figure 5.14 shows a cut through the peak of the PSF from top left to bottom right in a direction tangential to the radial cross arm. The cut demonstrates the good signal to noise ratio of the data and also the steepness of the peak. The shoulders on the peak are caused by the radial cross arm and are, therefore, a consequence of the measurement geometry.

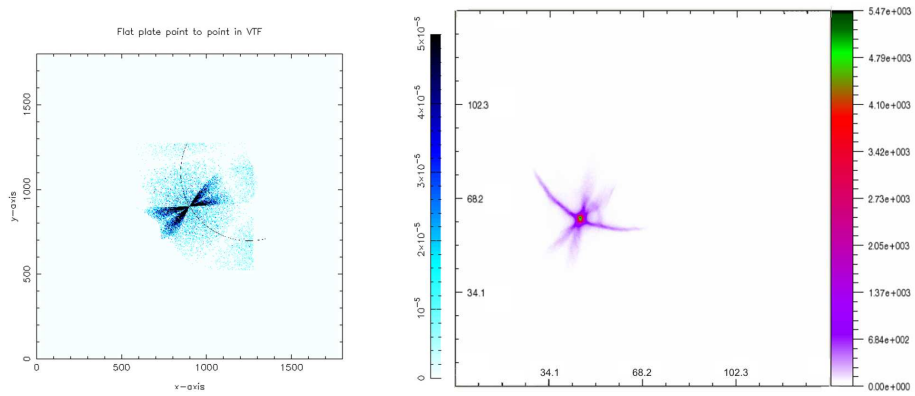

Figure 5.13: (Left) saturated ray trace image of a similar geometry to the test. (Right) X-ray image of the point spread function measured by point to point focusing. The FWHM resolution is ~ 7 arcmins. The components of this image are as reported in Figure 5.12.

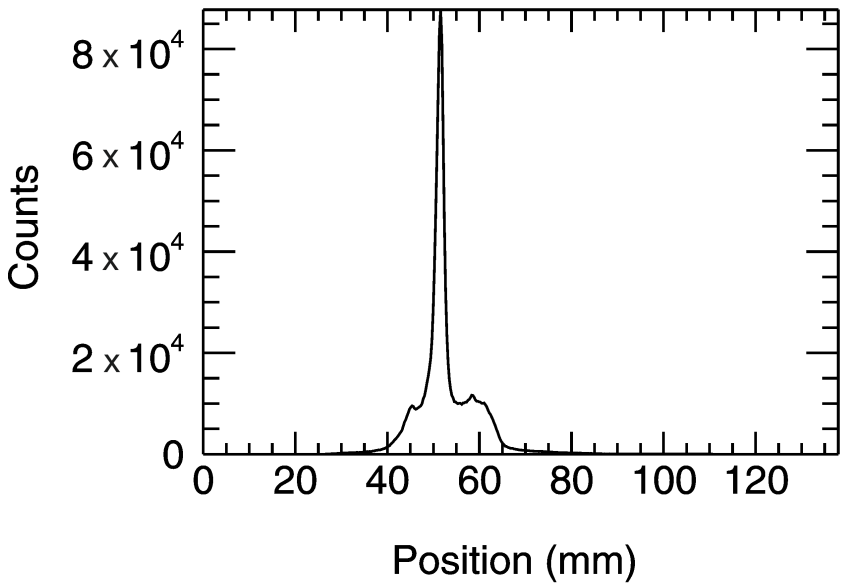

Figure 5.14: Cut through Figure 5.13 in a direction tangential to the radial cross arm from top left to bottom right.

5.4.2 Imaging in the long beamline

5.4.2.1 Cartesian MCP geometry

The image produced by the slumped MCP was taken in the long beamline facility (see Section 4.3.3 or Pearson & Martindale (2007)). It was optimised using the same procedure applied to the flat plate, and the FWHM of the focus at 0.93 keV was plotted as a function of detector distance from the MCP (Figure 5.15). A significant astigmatism is evident in Figure 5.15 since the position of the best focus in the two principal axes of the MCP differs by ~ 25 mm, indicating a ~ 50 mm apparent difference in the radius of curvature of the two axes.

The resolution in the best axis is shown to be ~ 5.5 arcmins (Figure 5.15) where the errors will be of a similar magnitude as for the flat plate. The broadened focus of the slumped MCP, compared to the $\sim 1.5 - 2$ arcmins performance of a flat plate in point to point focusing mode, is likely to be caused by departures from the ideal spherical figure of the optic, i.e. the astigmatism noted above. This conclusion is supported by further evidence of profile errors in Figure 5.16, where the flaring and bifurcation of the cross arms at their extremities is observed. The overall optic resolution, found to be ~ 10 arcmins, is defined as the position where the resolution in either axis is equal and, therefore, minimised for the optic as a whole.

The deviation of the MCP slump profile from the ideal spherical figure could be due to either (a) manufacturing error, (b) degradation of the slump profile during storage (an effect noted in earlier work (Nussey, 2005)), or (c) distortion of the figure introduced by uneven application of pressure in the mounting structure. Identifying the precise origin of this distortion was crucial to the optimisation of optic performance. The most likely cause of this degradation in performance was thought to be the optic mounting structure and further X-ray testing was used to confirm this suspicion.

The optic was removed from the mount and refitted in exactly the same manner as before. This

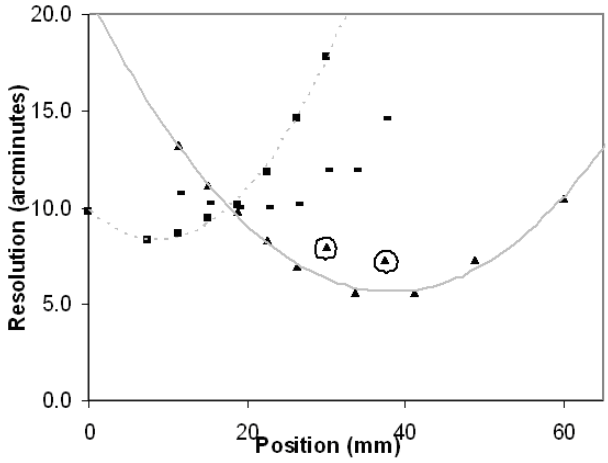

Figure 5.15: Variation in optic resolution as a function of position along the optical axis. Elliptical approximation is the square root of the product of the two axes shown in this figure (dashes). Axis 1: Squares, Axis 2: Triangles. The circled data points are considered anomalous and are excluded from the fitted curve.

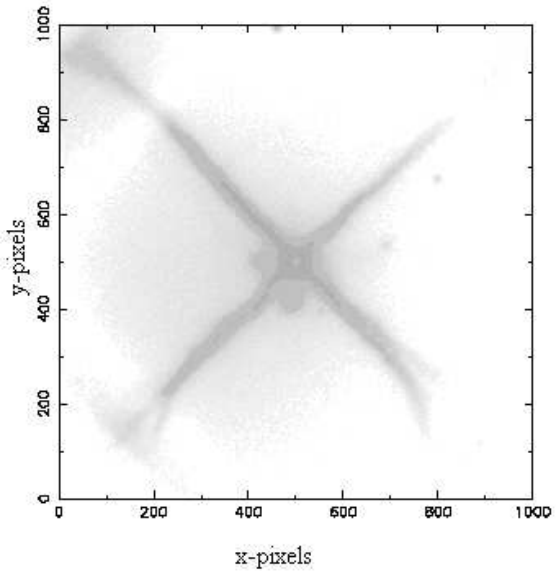

Figure 5.16: Logarithmically scaled image of the cruciform PSF from the slumped plate. The axes are in pixels with 1 pixel = 38 μm. No colour bar is included as the shape is of primary interest in this case.

produced a marked difference in the focal position measured under X-ray illumination, indicating that the mounting structure was significantly altering X-ray performance. The process was repeated, but this time with two of the four locking bolts removed and minimal pressure applied to the optic, and still no repeatable performance could be found.

Therefore, the mounting structure was clearly implicated in the degradation of X-ray performance and further investigation was necessary. This took the form of talysurf profilometry and is reported in Section 5.5.

5.4.2.2 Experimental effective area

After locating the position of best focus, it was possible to establish the imaging gain of the system, which is a direct measure of effective area. The measurement is made by rotating the optic out of the beam and comparing the intensity of the focal spot with the intensity of the unfocused beam.

The intrinsic variation in efficiency of the MCP detector as a function of incident angle (Lees & Pearson, 1997) can be seen in the images as the dimming of one cross arm with respect to the other. This effect is a consequence of the converging cone of rays generated by the optic, which introduces a position-dependence in the angle of X-rays incident on the detector. The dependence of MCP Quantum Efficiency (QE) on angle is a well documented effect (e.g. Pearson (1984)). This has implications for the apparent gain of a system containing an MCP optic and MCP detector as the focused X-rays arrive at a different angle to the unfocused ones, and therefore are detected with a different efficiency.

Comparison of calculated and experimental effective areas is complicated by the elliptical nature of the focused spot. Using the FWHM in either axis of the optic to define the major and minor axes, the imaging gain can be estimated based on the number of counts within the ellipse. Assuming all

counts within this ellipse then fall within a circle with the diameter of the best measured FWHM, a concentration factor, C, of ~ 240 is achieved, implying an effective area of $A_m \times C$ of ~ 0.8 cm^2 where A_m is the area of the circle.

This implies that the experimentally determined effective area is within a factor of two of the theoretical ray trace simulations (Figure 5.9). Because of the significant problems associated with the varying quantum efficiency of the detector across the converging cone of rays from the optic, this should only be taken as a lower limit because of severe degradation in detector performance at low grazing angles. However, it is difficult to determine how big this effect is without a much more complicated experiment or inclusion of a detector with no variation in efficiency as a function of angle of incidence. It is intended that a CCD detector will be added to the facility in the relatively near future. This device will aid the measurement of a reliable effective area. The distorted optic profile discussed above is also not accounted for and could further reduce the measured effective area. Investigating the varying quantum efficiency of the detector for different angles of incidence and the influence of the Bremsstrahlung component of the incident X-ray spectrum is the subject of the next phase of study.

5.4.2.3 Radial MCP geometry

Figure 5.17 shows an X-ray image (containing ~ 4 million events) with the plate in best alignment in both axes of the rotation stage and in its nominal best focus position along the optical axis. The angular resolution in the vertical axis is ~ 9 arcmins FWHM and in the horizontal axis, ~ 12 arcmins. The image contains a number of secondary features - the three concentric rings to the right of the focus are probably caused by an even number of reflections arising from the 5 mm length of the channels (Figure 5.7). The unexpected curved feature which comes out of the focal spot appears in all images and may be related to the MCP's angular orientation in the beamline (see Figure 5.6). However, repeated attempts to eliminate this feature by tilting the optic have been unsuccessful.

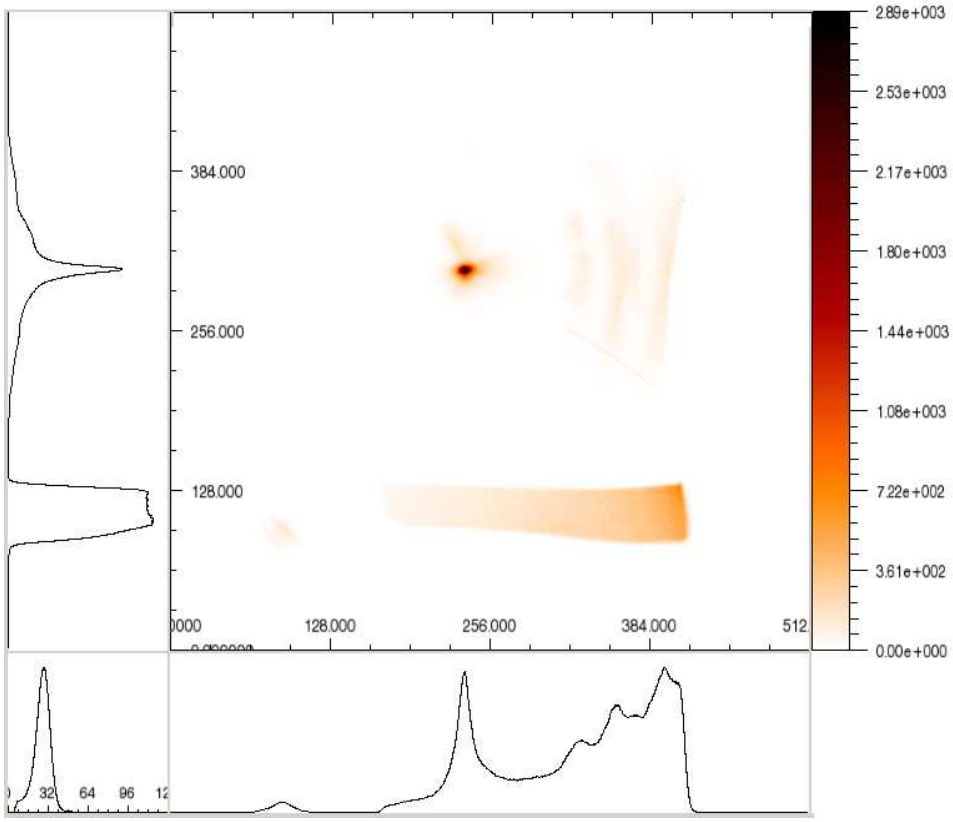

Figure 5.17: X-ray image formed by the (nominal) 1.33 m slumped radially packed optic KL001-2. The FWHM angular resolution is 8.9 arcmins in the vertical direction. The band of intensity at the bottom of the image is due to direct transmission around the mounting structure. The panels to the left of and below the main image are horizontal and vertical integrations of the image. Axes in (0.27 mm) pixels. The plot in the bottom left hand corner is the MCP detector pulse height distribution (units of channels).

Further testing and modeling is proposed to resolve the origin of this feature.

Figure 5.18 shows the effect of moving into and out of the best focus position. The blurring of the short "cross arms" noted above is significantly worsened as the detector moves out of the best focus.

The integration of the image to give the histograms in Figures 5.17 and 5.18 can be misleading as features appear blurred by the summing across rows and columns in detector space. Therefore, a true cut, taken in the $y - axis$ from bottom to top, is included in Figure 5.19 to show the "sharpness" of the true focus. The small feature at $x \sim 30$ mm in Figure 5.19 is indicative of direct transmission

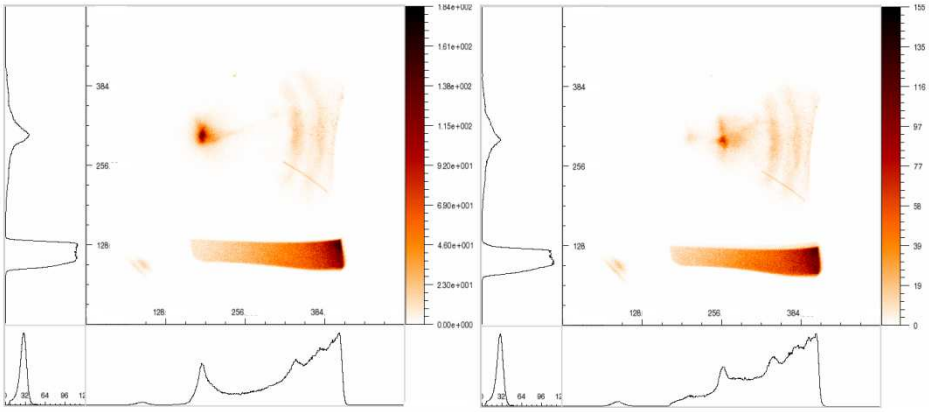

Figure 5.18: (Left) image with detector $\sim$ 3 cm behind the focus. (Right) image $\sim$ 20 cm in front of the focus. The shape of the focus changes as the detector moves from behind the best focus to in front of it. The images are taken in the same way as Figure 5.17.

about the mounting structure. All images and plots presented here remain unlinearised and the true plate scale of the detector has therefore not yet been measured. The pixel size is calculated to be 0.27 mm pixel^{-1} by measuring a known distance on the detector.

5.5 Mechanical testing

Results from Section 5.4.2.1 pertaining to the square pore, square pack "lobster-eye" optic imply a marked astigmatism in its performance. This manifests itself in a degradation in focal performance and shift in the focal position for the PSF in the two principal axes of the MCP. This was believed to be indicative of either a distortion in the optic caused during manufacture, a similar distortion caused by the mounting scheme of the optic, a systematic problem with the test facility (eg. an elliptical source spot) or deviation from the nominal, 0°, bias angle in the two axes of the MCP. Consequently, it was decided to test the sphericity of the optic using a Rank-Taylor-Hobson talysurf profilometer. The slumping technique (see section 2.1.1) was believed to be robust as it has been developed specifically to ensure that a highly accurate spherical surface is achieved. Also the results imply that the form of the optic changes significantly whenever it is disturbed in the mounting structure. This dictated the

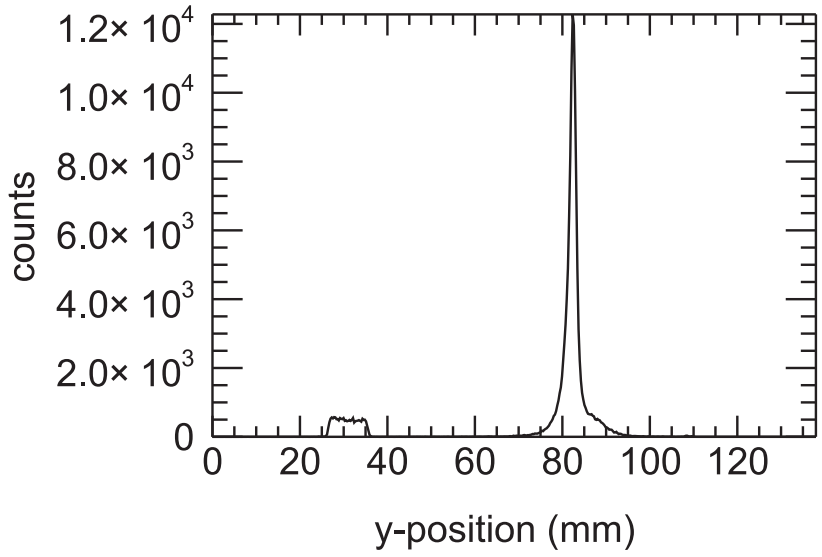

Figure 5.19: A true cut through the central focus shown in Figure 5.17. The cut is in the $y - axis$.

following mechanical tests to home in on the cause of the astigmatism:

Initially, the inbuilt software package was used to generate the radius of the optic profile whilst the optic was undisturbed from the mounting structure used for X-ray tests. The deviation of the surface from the *best fit* circle of $\sim$ 69 cm was only 2 μm. This remarkably accurate profile was initially thought to be suspect as it implied that any stresses on the optic as a result of the mounting structure were not causing a significant deviation from a spherical figure.

Insufficient information could be found about the software and it was decided that it was necessary to validate the results. To this end, a "raw" profile was recorded which simply contained the surface height as a function of position. A manual recreation of the talysurf analysis was then performed by fitting a surface gradient and circular profile to the data. The radii and deviations from that circle were found to have the same functional form and numerical magnitude for the two methods. This, and the reproduction of data from a calibration ball used to evaluate the talysurf performance, gave great

confidence that the data analysis package was being used correctly. Therefore, the remarkable accuracy of the optic surface is believed to be real and is testament to the reliability of the manufacturing process in which the MCP is optically polished and then slumped to the desired radius of curvature.

Comprehensive data were then taken on the surface profile of the optic. These showed that although the MCP was indeed spherical, the radius of curvarture of that sphere was less than specified in the manufacturing process. The optic was designed to have a radius of curvature of 75 cm. The MCP was then removed from the mounting jig and remeasured. A nominal radius of curvature of 73 cm was observed, implying that the mounting structure was severely distorting the optic. Although the optic is distorted, it maintains the "circularity" of the 1-D profiles. The deviations from the best fit circle are small and any degradation in the surface figure as a function of position on the optic lie beyond the resolution of this measurement technique.

The radii of the two spherical faces of the mounting holder were then measured and found to be approximately 38 cm, roughly half of the expected radius of 75 cm (Figure 5.20). It is believed that these surfaces were manufactured to the wrong specification, and hence a new mounting structure was sought. The errors in the measurement process have been shown (Martindale & Yates, 2007) to translate into an error on the measured radii of curvature of $\pm \sim 2$ cm indicating that the deviations between the mounted and unmounted profiles are statistically significant. However, this optic is likely to have been inelastically deformed by the mounting structure and so more testing is needed on a fresh sample. No evidence could be found for the apparent 50 mm difference in the radius of curvature of the optic noted in Section 5.4.2.1, further testing is needed to resolve the origin of this experimentally observed astigmatism.

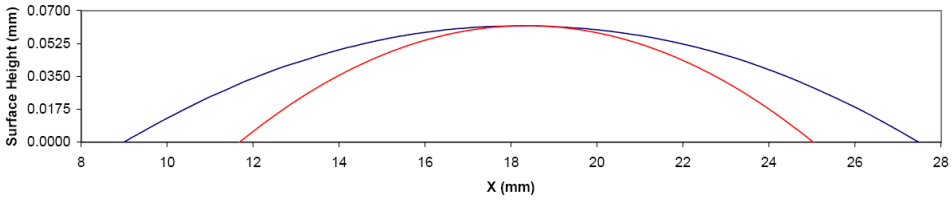

Figure 5.20: Surface height profile (blue) measured for the slumped optic, the radius of curvature was $\sim$ 69 cm. Superimposed is the best fit model profile of the mounting jig which showed a radius of curvature of $\sim$ 38 cm, half the required value. Therefore, mounting stresses are likely to be distorting the optic.

5.6 Experimental issues

During the course of the experiments a number of issues have arisen which need to be addressed before the apparent improvement in optic quality can be quantified. These are:

- Detector quantum efficiency variation.
- Optic mounting problems.
- Electronic problems in the detector wiring.

The first two of these have been discussed above and so I will leave further discussion until Section 5.6.1. The third is a problem that was noted during efforts to linearise the detector. The pinhole mask used for detector linearisation contained a square grid of $\sim$100 μm pinholes on a 4 mm pitch. The images taken of this mask showed the pinholes to be $\sim$600 μm wide, and noise within the signal wiring was identified as the cause of this. Such noise would lead to an intrinsic limit on the smallest feature visible on the detector and would undoubtedly blur the measured PSF. This noise was only present in the long beamline and was traced to the cable and vacuum feedthroughs. These are being replaced and it is expected that the reduction in noise will significantly improve the measured point spread function.

5.6.1 Proposed solutions and further work

To resolve the problems associated with the bias angle of the detector MCPs, a new set of 100 mm square MCPs with 12.5 μm pores and 13° bias angle have been procured from Photonis. These have been installed into a detector which has been optimised for best imaging performance. This detector is expected to give much improved imaging and counting performance, allowing more reliable effective area values to be calculated.

The mounting problems associated with the optics were initially addressed by securing the optic to a metal plate using vacuum compatible wax. This proved extremely difficult as the wax was too viscous to form a bond onto the plate without applying undue pressure to the MCP and distorting the surface figure. The proposed solution for the next phase of laboratory tests is to stick the MCPs onto a metal carrier using an adhesive such as superglue. The low viscosity of superglue means that it will require no mechanical pressure to form the bond, indicating that the surface figures should remain unaltered (so long as stress is not introduced into the optic as the adhesive cures). Should this approach prove successful, a more suitable "flight qualified" adhesive will be sought.

Finally, new low-noise cables and feedthroughs are being installed into the long beamline facility to address the detector noise issue. The whole system is being rewired both in the unamplified side under vacuum, and the external amplifiers, counting and imaging electronics chains. Retesting of the optics will take place once the rewiring work is completed and is expected to lead to an improvement in the understanding of the latest generation of MCP optics.

5.7 Comparison of performance

In order to compare the performance of the MCPs tested herein with past measurements Table 5.1 reproduces Table 4.1 but shows the performance of the plates tested herein. It is clear that the

Parameter	Previous values	Current work
Channel diameter (D)	8.5 – 200 μm	20 μm
Channel aspect ratio (L/D)	50:1500:1	50:1 and 250:1
Format	$\leq$ 54×54 mm^2	40×40 mm^2 and radial sectors
Slump radius (RMCP)	0.07-1.0 m	0.75-1.33 m
Channel surface roughness	1.1 nm RMS	N/A
Angular resolution	7 arcmins FHWM	1.5[1], 5.5[2], $\sim$8[3] arcmins FHWM
Metallisation for enhanced reflectivity	Ni, Ir, or Ru	N/A

Table 5.1: Comparison of performance of MCP optics reported herein with past technology reported in Table 4.1. [1] for cartesian pack MCPs in point to point focusing mode [2] for cartesian packed MCPs which are slumped and tested with almost parallel X-rays [3] for radial packed optic sectors in both point to point and slumped focusing modes.

manufacturing process is now good enough to produce MCPs with highly aligned and uniform channels, leading to a marked improvement in the imaging resolution of these new optics. This work also represents the first comprehensive experimental study of radially packed optic sectors in point to point and parallel focusing modes and shows that the true packing geometry has been successfully realised and that the optics focus X-rays despite the difficulties of testing such samples as described in Section 5.3.1.2.

5.8 Summary

The results reported here represent a significant improvement in the spatial resolution of MCP optics operating in the $\sim$ 1 keV region, made possible by improved channel alignment which can be achieved in the manufacturing process (Table 5.1). Tests on the flat plate probe the intrinsic optic resolution, which is limited by the misalignment of channels at the multifibre level. The results show that a channel-limited resolution of better than $\sim$ 2 arcmins is possible, exceeding the resolution required for the *WFT* mission.

The slumped lobster-optic discussed above has an elliptical focus. However, the best resolution has

been shown to be ~ 5.6 arcmins with a concentration factor of 240. This corresponds to an estimated effective area of 0.8 cm^2. Hence, the experimental results appear to be less than a factor of two below the predicted performance, and this deficit could be explained by the variation of detector efficiency with the incident angle of the incoming beam. This problem could be alleviated by replacing the 6° bias detector plates previously used with the new pair of 13° plates which have been installed in chevron format. The detector will have a lower but more uniform efficiency over the converging cone from the optic meaning that the difference in QE between unreflected and reflected rays should be reduced. A significantly improved method of finding the effective area will be available in the relatively near future when a CCD detector will be added to the system, allowing discrimination in energy space and also removing the angular dependence of the detector. Further studies to investigate methods of reducing the deviation in the spherical figure of the MCP optic are currently in progress.

A radial MCP sector has been tested to determine its angular resolution, which is found to be better than 7 arcmin from point to point focusing investigation of the plate. This data is still considered a worst case estimate as the detector position is not believed to be optimised. Ray trace modeling of the optical arrangement shows that the point spread function is of the expected shape, indicating the successful realisation of a true radial packing geometry. The results reported herein show that the sector with 1.33 m radius of curvature has been successfully slumped and a best focus of ~ 9 arcmins at the nominal focal length of the sector is obtained. The detector resolution appears to be noise limited, implying that the optic could be performing significantly better than this measurement implies. This is backed up by a scan through the depth of focus which yields a flat bottomed curve implying that the resolution is limited to the level of ~ 9 arcmins by some physical mechanism. The presence of this effect in the results for the radial sectors means that they should be considered a worst case estimate (or an upper limit). Section 5.6 proposes solutions to these problems and identifies future work which is necessary to fully characterise optic performance.

Chapter 6

X-ray polarimetry

In recent years, almost all areas of X-ray instrumentation have seen rapid development, allowing astronomers to gain an improved understanding of celestial X-ray sources and the processes involved in driving them. Three particular areas of technology development promise a step change in how we observe cosmic X-ray sources. These are: wide field-of-view telescopes, allowing unprecedented temporal coverage of a wide variety of sources, and X-ray interferometry, providing telescopes with a spatial resolution capable of imaging the event horizon of a black hole. Thirdly, X-ray polarimetry will allow the study of the state of matter from which X-rays are emitted. All these techniques will offer insight into the most extreme environments in the cosmos.

In the preceeding chapters I have described techniques to achieve an unparalleled combination of temporal and spatial resolution for X-ray/UV/charged particle detectors which promise a drastic improvement in instrumentation for ultraviolet astronomy (Section 2.4.1) and also, how to generate $\sim$ arcminute resolution, lightweight, large effective area X-ray optics with either wide or narrow field of view, depending on geometry. These developments are targeted at a broad array of applications; from the life sciences, to space-based planetary science and astrophysics missions.

This chapter will introduce X-ray polarimetry (XRP) by comparing it with polarimetric measurements at other wavelengths, considering the mechanisms which lead to polarisation and a review of efforts made to investigare X-ray polarimetry to date. Chapter 7 will describe experimental work to develop a novel polarimeter based on narrow bandwidth dichroic filters which could provide the next generation of observatories with focal plane instruments capable of simultaneously measuring all astrophysically pertinent parameters.

The degeneracy of predictions from some competing astrophysical models, when constrained only by photometric and spectroscopic observations, can be broken by measuring the degree (P) and angle (θ) of polarisation. Despite similar predictions for the current observables, the models often predict differences in P and θ and also, how they evolve as a function of time and/or photon energy. X-ray polarimetry, therefore, promises the realisation of the next milestone in X-ray astronomy. Section 6.4.1 describes how measurement of the polarisation of the source at one fixed energy (19.2% polarisation at 2.6 keV) was able to break the degeneracy between two competing theories for the power law spectrum observed from the Crab nebula. Addition of these two new observables is therefore expected to aid modeling of the behaviour of sources, constrained by data from future observatories.

6.1 Polarisation of light

Electromagnetic theory tells us that light is described as a transverse wave. In the wave model, light can be considered as if it were made up of two perpendicular electromagnetic wave components which are mutually perpendicular to the wavevector (or photon direction). Note that this is not an attempt to describe the perpendicular magnetic and electric fields present in an individual electromagnetic wave, but is used to explain the behaviour of its polarisation (Figure 6.1). Consider the general case of two perpendicular waves with $\underline{E}$ fields in the planes $\hat{x}$ and $\hat{y}$ and the wavevector, k, in the $\hat{z}$ direction. These waves can be described, respectively, by the expressions;

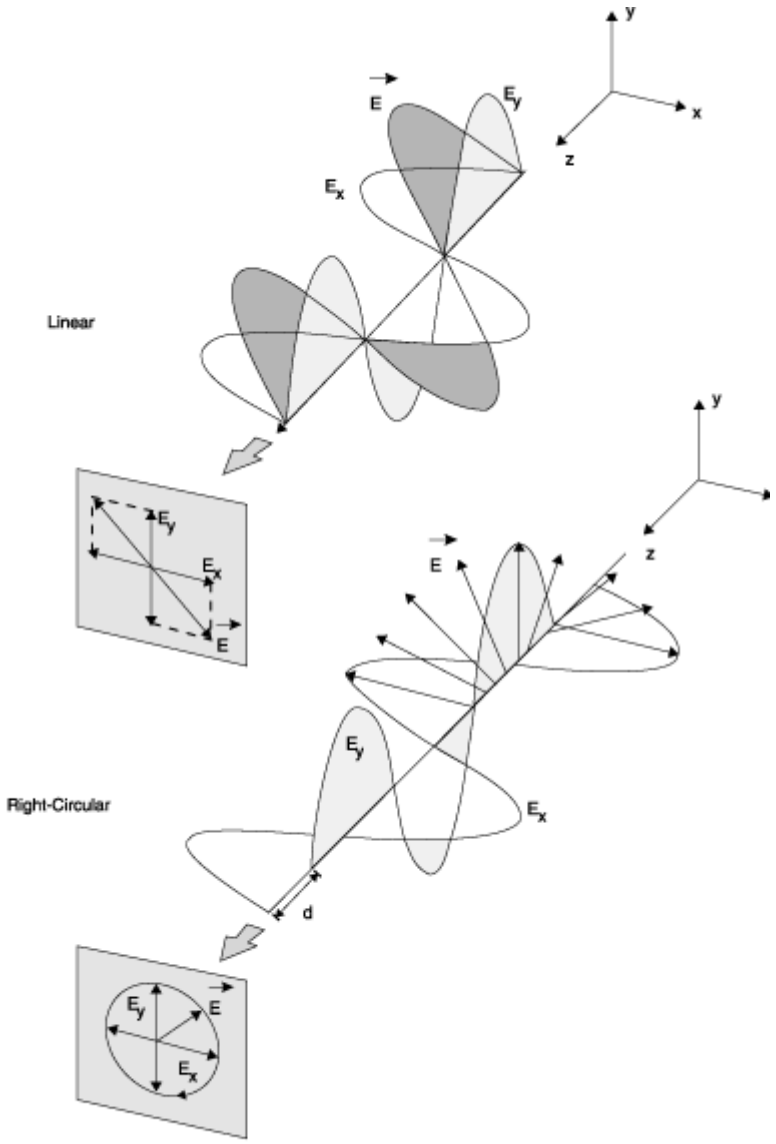

Figure 6.1: Diagram showing the effect of adding two electromagnetic waves. Top, the waves are in phase leading to linear polarised light. Bottom, The waves are $\pi/2$ radians out of phase leading to circular polarisation. Figure courtesy of www.scielo.br/img/fbpe/qn/v25n5/11410f2.gif

$$E_x = \hat{x} E_{ox} cos\left(\omega t - kz\right), \tag{6.1}$$

$$E_y = \hat{y} E_{oy} cos\left(\omega t - kz + \phi\right). \tag{6.2}$$

Here $\hat{x}$ and $\hat{y}$ are unit vectors, ω is the angular frequency, t is time, ϕ is a phase shift and E_{ox}, E_{oy} are the amplitudes of the electric fields. These equations can be solved for four inital conditions leading to the four possibilities for wave polarisations; linear polarisation, circular polarisation, elliptical polarisation and unpolarised light.

Unpolarised light occurs when the phase shift, ϕ, varies randomly with time and across the wavefront, leading to no preferred polarisation. Linear and circular polarisation are both special cases of the more general elliptical polarisation state, where linear polarisation occurs when ϕ is any integer multiple of 2π radians; in this case,

$$\mathbf{E} = \left(\hat{x} E_{ox} + \hat{y} E_{oy}\right) cos\left(\omega t - kz\right). \tag{6.3}$$

Where $\theta = tan^{-1}\left(E_{oy}/E_{ox}\right)$ is the angle of polarisation with respect to the $x-axis$ (Figure 6.1 [top]).

If $\phi = 2\pi n + \pi/2$, the amplitude of the wave is constant because $sin^2 A + cos^2 A = 1$ for all values of A, leading to;

$$\mathbf{E} = E_o \left(cos\left(\omega t - kz\right) \hat{x} + sin\left(\omega t - kz\right) \hat{y}\right) \tag{6.4}$$

$$\text{and} \quad \theta = tan^{-1}\left(\frac{sin\left(\omega t - kz\right)}{cos\left(\omega t - kz\right)}\right) = \omega t - kz, \tag{6.5}$$

for a fixed position in space z, the vector rotates as a function of time at a frequency $\omega/2\pi$. This is an R-state or right hand polarised wave. If $\phi = 2\pi n - \pi/2$, the same arguments give an L-state or left hand polarised wave (Figure 6.1 [bottom]).

Finally if ϕ is fixed at an arbitrary value and the amplitude components are not equal, an elliptically polarised wave (ϵ-state), is produced in which the vector rotates as for circular polarisation, but such that the amplitude changes to describe an ellipse rather than a circle. A more complete description of these effects is available in any optics textbook (e.g. Hecht (1987)).

6.2 Polarisation of astrophysical X-ray emission

Measuring the degree and angle of polarisation of photons from an astrophysical source gives information on the state of the matter from which the photons are emitted. These measurements are made routinely at many wavelengths. However, in the X-ray and gamma-ray regimes, the lack of suitable instrumentation to measure polarisation has frustrated astronomers for over three decades. Measurements of X-ray polarisation in astrophysical sources would provide a powerful probe of emission processes; thermal, synchrotron, bremsstrahlung etc. Hence, considerable scientific interest remains to this day because of the dearth of information regarding the polarisation of X-ray astrophysical sources. In this section I review a discrete sample of the many emission mechanisms which can be constrained by X-ray polarisation measurements.

If emitted in a thermal process, photons will be unpolarised (assuming they do not undergo any polarisation dependent process along the light path - eg. scattering or transiting a region of intense magnetic field). Conversely, if photons are produced in a non-thermal process, they will have some intrinsic polarisation. The degree and direction of this polarisation can be used to identify the responsible emission process, because each has a different polarisation signature. Therefore, polarisation measurements are a powerful diagnostic between astrophysical models, identifying the predominant driving process for the X-ray emission.

A variety of processes can cause polarisation of photons. Weisskopf *et al.* (2006) review a number

of such emission mechanisms, concentrating on the use of polarimetry to understand neutron star systems; identifying the variation in polarisation as a function of pulsar phase as a prime example of where X-ray polarimetric data could distinguish between competing astrophysical models. The authors also describe a method of obtaining possible observational evidence for vacuum birefringence - an exotic effect of quantum electrodynamics (QED). This theory predicts that in the presence of a strong magnetic field, the refractive index of a vacuum is different for orthogonally polarised photons. Consequently, certain models of pulsar emission predict variation in the polarisation dependence as a function of pulsar phase and photon energy. Weisskopf *et. al.* predict a $\sim 10^{\circ}$ phase lag between optical and X-ray polarisation angle as a function of pulsar period for the Crab pulsar owing to this effect.

A number of other authors have reviewed the possible impact of X-ray polarimetry (e.g. Novick (1974), Meszaros *et al.* (1988), Blandford *et al.* (2002), Kallman (2004) and others). Here I will consider a small subset of the extremely broad areas of interest for astrophysical X-ray polarimetry in an attempt to highlight a number of key concepts and mechanisms for production of polarised photons.

6.2.1 Synchrotron emission

If a charged particle is confined to move in a circular orbit by a magnetic field, the centripetal acceleration leads to the emission of electromagnetic radiation. This radiation will be characteristic of the mass and velocity of the particle and the magnetic field in which it is confined. For non-relativistic particle speeds, the emission is termed *cyclotron emission*, with an equation of motion;

$$m\frac{d\mathbf{v}}{dt} = q\mathbf{v} \wedge \mathbf{B}. \tag{6.6}$$

Here m represents the mass of a particle of charge q and velocity $\mathbf{v}$ moving in magnetic field $\mathbf{B}$. Cy-

clotron emission produces a dipolar emission pattern with no radiation emitted along the acceleration vector of the particle, and with maximum intensity emission perpendicular to it (Figure 6.2 , Left).

For the relativistic case where particles are accelerated to a significant fraction of the speed of light, this distribution changes such that in the observer's rest frame, the emission is highly beamed towards the direction of motion of the accelerating charges. This effect is sometimes called the *headlight effect* and is a consequence of the Lorentz transform from the rest frame of the emitting particle into the rest frame of the observer. The equation of motion then becomes;

$$\frac{d}{dt}(\gamma m\mathbf{v}) = \frac{q}{c}\mathbf{v} \wedge \mathbf{B}, \tag{6.7}$$

where γ is the standard Lorentz factor used in relativistic equations, and is defined as $\frac{1}{\sqrt{1-\frac{v^2}{c^2}}}$, and c is the speed of light. Figure 6.2 shows the effect of the Lorentz transform, the left hand image is in the rest frame of the particle, where the lobes to the left and right of the electron represent the angular intensity distibution (the distribution for cyclotron emission also takes this dipolar form). The right hand panel represents the headlight effect, showing strong beaming in the direction of motion caused by the Lorentz transform into the rest frame of the observer. X-rays emitted in this manner will be linearly polarised with the photon electric field oriented perpendicular to the magnetic field vector of the external field. The polarisation becomes elliptical at emission angles out of the plane of the moving electrons.

6.2.2 Linear Bremsstrahlung

A Bremsstrahlung continuum is created by the acceleration of an electron in the coulomb field of a charged particle or collection of charged particles. This accelerating charge radiates linearly polarised X-rays with the electric field of the photon parallel to the acceleration vector of the particle. The

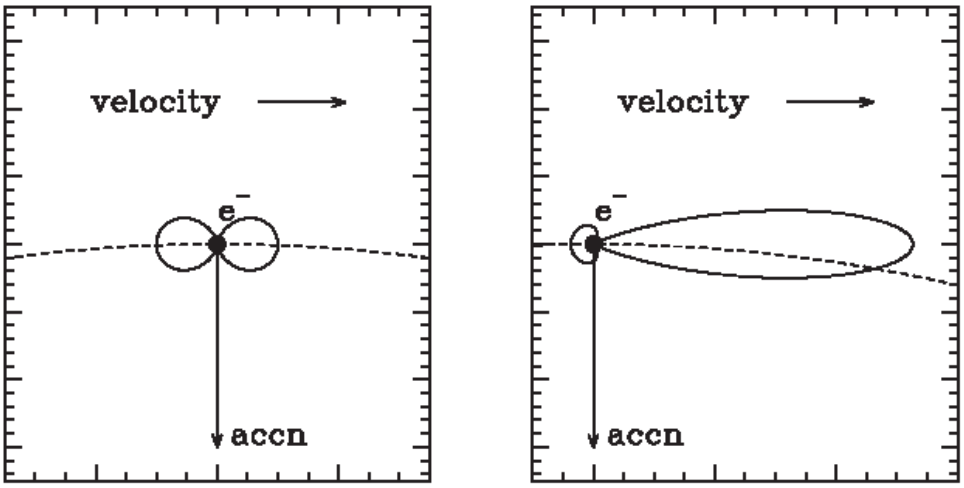

Figure 6.2: Diagrams of the beaming effect of synchrotron emmission. Left panel, in the rest frame of the electron, the dipolar lines around the electron represents the intensity of the emission in that direction and is also characteristic of cyclotron radiation. Right pannel, demonstrating the effect of the Lorentz transform into the rest frame of the observer, the strong beaming effect is often called the headlight effect. Image from http://www.astro.utu.fi/~cflynn/astroII/l4.html

polarisation of such an X-ray spectrum is shown by Dolan (1967) to be a strong function of energy because of the different position of the interaction between the electrons and the charged particles at different energies. At low photon energy, the electrons interact with the coulomb field at a large distance, meaning that the predominant force (and therefore acceleration) on the electron is in the plane perpendicular to the electron momentum vector. This produces a photon polarised in the direction perpendicular to the plane created by the electron momentum vector and the line of sight (or photon direction vector). For higher energy photons created by close collisions with the coulomb field, the main component of force is along the electron momentum vector, and the polarisation direction therefore lies in the electron momentum and observer plane. Detection of this 90° change in polarisation direction would provide indisputable evidence of linear Bremsstrahlung X-ray production as no other emission process is expected to show this effect (Novick, 1975).

6.2.3 Thermal radiation and scattering

Any spherically symmetric plasma which emits X-rays by a thermal process will generate an unpolarised X-ray beam. However, if the plasma is non-spherically symmetric and the optical depth[1] is large enough for significant scattering to occur, a significant polarised fraction may be introduced. This mechanism is predicted by the standard accretion disk model for a galactic black hole (e.g. Blandford *et al.* (2002)).

An accretion disk is a planar structure where scattering, either by dust grains or free electrons in the disk, determine its opacity. This kind of scattering process can introduce significant polarisation in the X-ray beam, encoding the orientation and inclination of the disk and the location of the continuum source into the emission. As disks are often also associated with jets and outflows, observations may also reveal the projected rotation axis. As an example of the kind of effects which could be detected by polarimety, let us consider what happens within a disk on small spatial scales, inaccessible to even an interferometric imager:

Warping of the disk at small radii leads to a change in the orientation of the rotation axis and as such, the polarisation direction and degree may change as a function of the position of emission within the disk. A temperature gradient also exists in the disk since particles gain kinetic energy as they fall down the gravitational potential towards the central black hole. This temperature gradient leads to a hardening of the X-ray spectrum towards the centre of the disk, so that any warping of the disk at small radii will translate into a change in polarisation angle at higher energies. Blandford *et al.* (2002) propose spectro-polarimetry (polarisation measurements as a function of photon energy) to resolve the complex geometries of disk structures around compact objects. They argue that such measurements of the polarisation of X-rays produced in close proximity to the event horizon of a Kerr

[1] optical depth is a measure of the transparency of a medium or probability that a photon is absorbed or scattered within it.

(rotating) black hole would provide a useful probe on the Kerr metric, a mathematical space that has been shown to explain a rotating black hole but has never been investigated observationally.

Laor *et al.* (1990) show calculations of the polarisation degree and direction of optical and UV radiation from an accreting system, showing typical polarisation fractions of $< 5\%$. This model purports to explain the discrepancy between the observed polarisation fractions and the results of previous models which predicted higher degrees of polarisation. Relativistic effects are identified as the cause for this discrepancy. For X-ray polarimetry to be useful in this context, minimum detectable polarisations (MDP) must be better than the $\sim few\%$ levels seen in this and other wavelength bands and 1% MDP is assumed throughout the recent literature as a good indication of a useful polarimeter (e.g. Costa *et al.* (2001), Bellazzini *et al.* (2003), Jahoda *et al.* (2007)). Demonstration of such performance in a realistic (10^5 s) observing time with the instrument is essential for a successful proposal to fly a polarimeter on a future X-ray observatory.

Connors *et al.* (1980) report a similar set of calculations for a standard accretion disk model in the soft X-ray band and compare them to geometrically thick clouds surrounding a black hole. They find that polarisation measurements at a number of energies could give information about the strong gravitational fields in a source. They assert that;

> *"detection of a non-90° rotation in the angle of polarisation (either due to temporal variations or due to observing at different energies) is a good indicator of strong-field general-relativistic effects."*

The variation in polarisation direction at different energies corresponds to the different positions within the disk at which these energies are preferentially emitted. Detection of this signature would simultaneously confirm the existence of a black hole within the system and that the driving mechanism for the X-ray emission is an accretion disk. Candidate objects could be chosen to maximise the effect since the degree of polarisation increases as the observer approaches the equatorial plane (P = 0.12 for zero inclination and P = 0.02 for 60° inclination – Blandford *et al.* (2002)), indicating that edge-on

disks are the most promising place to look for these effects.

In this section I have described a number of mechanisms which can lead to polarisation of X-rays emitted from astrophysical sources. Observing this polarisation is therefore a critical constraint for models used to explain the origin of the X-rays. The next sections will deal with past and future instrumentation used to measure the degree and angle of polarisation.

6.3 Measuring polarisation

Scientific interest in X-ray polarimetry remains strong, and there exists a strong drive to build new and improved polarisation analysers at X-ray wavelengths. To measure the polarisation of an incident beam of electromagnetic radiation, some measurable property of the photons must be correlated with a physical change in the response of the instrument to them. Taking simple optical polaroids as an example; the transmission of the Polaroid film changes as a function of the angle between the principal axis of the film and the mean polarisation direction of the incident photons. Hence, rotating the film leads to a measurable change in the intensity of the beam. Any polarisation analyser must exploit such a polarisation dependent effect.

Recent polarimeters have relied on the polarisation dependence of photoelectron emission to convert beam polarisation into a measurable quantity. When an X-ray is incident onto a material, an electron is emitted if the photon energy is greater than the work function of the material. This is the photoelectric effect, which states that;

$$hf = \phi + E_k. \tag{6.8}$$

Here hf is the photon energy (Planck's constant multiplied by the frequency of the incident radiation),

ϕ is the work function of the material and E_k is the kinetic energy of the emitted electron.

Electrons can also be excited into higher bound states in an atom or molecule. In this case the electronic structure around the molecule provides "allowed states" which the electron can be excited into. Therefore, the absorption probability of the photon can be a function of the polarisation of the photon and the local electronic structure. It should be noted that photoionisation is a special case of this more general description, where the free electron is excited into the infinite band of allowed states outside of the atomic potential. Both photoionisation and excitation to higher, bound states can potentially provide the active element of a practical X-ray polarimeter (Section 6.5)

6.3.1 Polarimeters

Polarimeters are characterised in terms of their modulation factor, M, defined by Novick (1974) and reviewed by e.g. Lees (1989) as;

$$M = \frac{(C_\perp - C_\parallel)}{(C_\perp + C_\parallel)}, \tag{6.9}$$

where $C_\perp$ and $C_\parallel$ are the count rates experienced by the detector with the polarimeters axis perpendicular and parallel to the beam polarisation vector for a 100% polarised beam.

The polarisation of a source is always positive as it is defined as the fraction of photons which have their electric field aligned in the same direction. Therefore, photon counting statistics imply that even a perfect polarimeter with 100% modulation between the tansmission axis and the absorption axis will measure a small positive polarisation even from a completely unpolarised source. For this reason, the efficiency of the polarimeter is defined in terms of the minimum detectable polarisation (MDP). This figure of merit is defined in Equation 6.10 and discussed in more detail in Chapter 7. Novick (1974) defines the 3σ or 99% confidence limit of a polarimeter as;

$$MDP = P\left(3\sigma\right) = \frac{3}{MS}\left(2\left(\frac{S+B}{T}\right)\right)^{1/2}. \tag{6.10}$$

In this expression, $P\left(3\sigma\right)$ is the 99% confidence limit of the measurement, defining the MDP for a source, S is the signal counting rate, B is the background count rate, T is the observing time and M is the modulation factor as defined above.

The polarisation P of a beam can then be deduced from the equation;

$$P = \frac{1}{M}\frac{\left(C_{max} - C_{min}\right)}{\left(C_{max} + C_{min}\right)}, \tag{6.11}$$

where C_{max} and C_{min} are the maximum and minimum count rates recorded as the principal axis of the polarimeter is rotated with respect to the polarisation direction of the incident beam. If a polarisation $P > P\left(3\sigma\right)$ is measured, it is 99% certain that it is real and not a statistical anomaly - or, in other words, the measurement can be quoted to an accuracy of 3 standard deviations (3σ).

6.4 Bragg and Thompson polarimetry

The science case for measuring polarisation at X-ray wavelengths is strong and such measurements have been attempted for many years. However, to date, no comprehensive data has been taken, largely because of the insensitivity of the techniques used. "Conventional" X-ray polarimetry uses the polarisation dependence of Bragg reflection from a crystal (e.g. Gowen *et al.* (1977)) or Thompson scattering (e.g. Lemen *et al.* (1982)) of photons within a low atomic number scattering material to determine the intrinsic polarisation of an incident X-ray beam.

Thompson scattering polarimeters rely on the angular dependence of the scattering efficiency of

photons within a low atomic number material which is highest in the direction of the photon electric field vector. Therefore, the scattered beam will be more intense in the direction of the photon electric field for a polarised incident beam of X-rays. To make the measurement, a homogeneous scattering block is surrounded by X-ray detectors and the whole instrument rotated about the line of sight to the object under investigation. Reconstruction of the intensity of the scattered X-rays as a function of angle then gives the preferred scattering angle, and consequently the angle of polarisation. The amplitude of the $sin^2(\phi)$ modulation gives the degree of polarisation. The effect operates over a broad range of energy, being limited by photon absorption in the material at the lower end (dictating a cut off of $\sim$ 4 keV) and by the falling incident flux from a source at higher energies. Thompson scatter polarimeters have only flown on rocket flights, with limited results e.g. Novick *et al.* (1972), Soffitta *et al.* (2003) (Figure 6.3 - Right).

Bragg crystal polarimeters are intrinsically narrow band devices which rely on satisfying the Bragg condition, $n\lambda = 2dsin\theta$, at an $\sim 45^\circ$ angle of incidence. Where, n is the diffraction order, λ is the wavelength of the incident radiation, d is the crystal plane spacing and theta is the angle of incidence. Such polarimeters typically consist of a graphite crystal (although other crystals have been used) oriented at relatively large angles to the incident direction. Only photons which meet the Bragg condition and have their electric field in the plane of the crystal are reflected onto the detector, while other photons are efficiently transmitted through the crystal. To satisfy the Bragg condition, the energy is constrained to be within $\sim$ 1 eV of the peak pass energy (2.6 keV and 5.2 keV for the first and second order peaks in a graphite crystal at 45°). This can be increased by using mosaic crystals where the angles of incidence vary slightly with respect to the crystal planes, efficiently reflecting photons which obey the above conditions in a slightly broadened energy band. These devices have flown on rocket flights as well as on the Ariel-5 and OSO-8 satellites (Griffiths *et al.*, 1976, Novick *et al.*, 1978) (Figure 6.3 - Left).

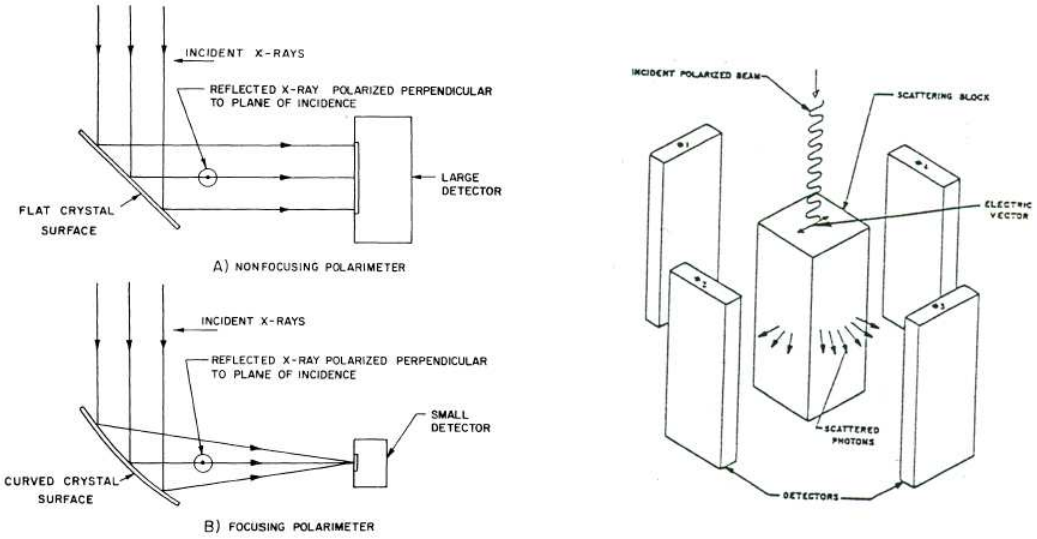

Figure 6.3: Diagrams of Bragg crystal polarimeters (left - (A) is in non-focusing mode, (B) is focusing) and Thompson scattering polarimeters (right).

Moving parts are required to rotate both of these types of polarimeter (or the spacecraft needs to be rotated) in order to normalise out any systematic effects and to sample all polarisation directions equally. This dictates a need for extensive characterisation and calibration of the instrument to avoid interpretation of spurious instrument effects as a polarisation signature.

6.4.1 Results to date

Only one unambiguous measurement of X-ray polarisation in a cosmological source has been reported - that of 19% linear polarisation for the Crab nebula at 2.6 keV (e.g. Weisskopf *et al.* (1978b) - Figure 6.4). This is shown to be in good agreement with measurements at other wavelengths and confirms the synchrotron hypothesis for the emission mechanism. Although long suspected because of the power law specrum of X-ray emission, in 1975 Novick (1975) and references therein showed that it was only with the direct measurement of the polarisation of the source that a complicated thermal model could be definitively excluded[2].

[2]Today, the thermal model could have been excluded by observation of the power law over a much broader energy range. However, the diagnostic power of polarimetry is clear.

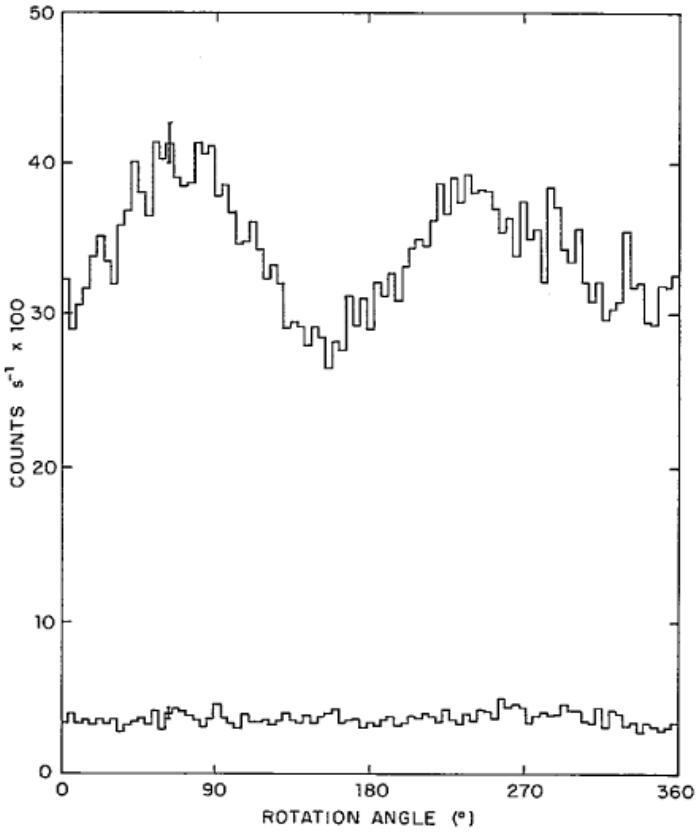

FIG. 2.—Average modulation curves obtained with both detectors at 2.6 keV during (*upper curve*) observations of the Crab Nebula and during (*lower curve*) observations of the Earth-occulted instrumental background.

Figure 6.4: The 19% polarisation modulation curve reproduced from Weisskopf *et al.* (1978b), Figure 2.

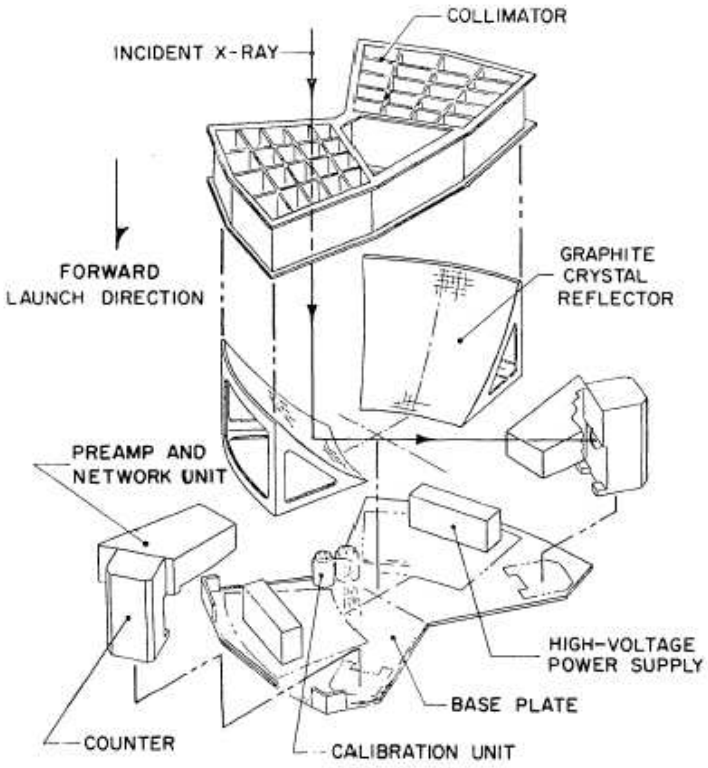

Fig. 9. Exploded view of OSO-I polarimeter assembly.

Figure 6.5: Diagrams of Bragg crystal polarimeters Flown on the OSO 8 spacecraft (reproduced from Novick (1975) - Figure 9).

Upper limits have been established for the degree of polarisation in other sources, primarily using the mosaic graphite (Bragg) crystal polarimeters on OSO 8 (Figure 6.5). For example, Silver *et al.* (1979) give 13.5% and 60% upper limits for the pulsars Cen X-3 and Her X-1 respectively at 2.6 keV, averaged over the pulsar phase cycle. The authors also report evidence, at "relatively low" statistical significance, for variation in the X-ray polarisation of Cen X-3 as a function of pulsar phase. Weisskopf *et al.* (1978a) report an upper limit to the polarisation of Sco X-1 as 2.7% at 2.6 keV. Long *et al.* (1980) report a number of marginally significant polarisation detections for Cygnus X-1, X-2 and X-3. However, the errors are rather large with respect to the measurements, and modulations due to the presence of other sources in the field of view are identified as a possible cause of contamination in the data from the weaker source, Cyg X-3.

This lack of a comprehensive data set for the polarisation of astrophysical sources, despite three decades of rapid progress in X-ray astronomical instrumentation since the first measurement, demonstrates the difficulty of designing an efficient and reliable polarimeter. To date, all measurements (other than that of the Crab) are very close to the detection threshold of the instruments, and are therefore difficult to interpret. These difficulties mean that although attempts have been made, no X-ray polarimeter has been successfully flown since OSO 8 some 30 years ago.

This section has described how the only successful measurement of astrophysical X-ray polarisation to date was used to verify the long suspected synchrotron origin of the power law X-ray spectrum from the Crab nebula (Novick, 1975). Synchroron emission will occur anywhere where high energy electrons move in a large magnetic field. Consequently, objects such as neutron stars are expected to have a highly significant synchrotron component to the spectrum and to show linear or elliptical polarisation depending on the inclination of the magnetic axis to our line of sight. These and many other targets are ideal for future attempts to measure X-ray polarisation where such data will yield valuable information about the geometry and emission mechanisms present in the target object.

6.5 Novel polarimeters

All recent attempts to produce an efficient polarisation analyser for X-rays have exploited the fact that the preferred emission direction of photoelectrons is correlated with the electric field vector of the incident photons. Therefore, measuring the mean direction of the emission of photoelectrons is a direct indication of the polarisation vector of the incident beam and a method of determining the emission direction of the electrons is needed to generate a polarisation analyser. A number of methods for performing such measurements have been proposed, and the principal designs are summarised in this section.

6.5.1 CCD split pixel events

Holland *et al.* (1995) reports the polarisation sensitivity of CCDs which arises because of the splitting of charge from an X-ray interaction over adjacent pixels. Elongated pixel events are observed when a polarised beam is incident onto the detector because the photoelectrons are preferentially emitted parallel to the electric field of the incident photon. However, the sensitivity of this technique is limited because of the reduced quantum efficiency of the detector for the high energy photons required to induce a significant number of the split pixel events. The authors show how the modulation factor and quantum efficiency vary as a function of photon energy, giving a modulation factor of 9% at 15 keV for a CCD with 4 μm square pixels. At this energy, the quantum efficiency of the CCD is predicted to be 15%.

The modulation factor varies approximately linearly in proportion to the photon energy, indicating that increasing the photon energy should improve the sensitivity of the instrument. Unfortunately, the quantum efficiency of the CCD falls rapidly with increasing energy, and as the polarisation response is governed by both the modulation factor and CCD efficiency, the possible increase in sensitivity implied by improved modulation is not observed. At 30 keV, the modulation has improved to over 20%, however, the quantum efficiency has fallen to $\sim$2%.

6.5.2 Micropattern Photoelectric Polarimeter - MPP

In this design, originally proposed by Costa *et al.* (2001), polarisation is measured by imaging the photoelectron tracks in a large area gas sensor. Broadly analogous to a cloud chamber, the device takes charge deposited over the finite length of a photoelectron track within the gas of the counter and images it using a gas electron multiplier (GEM). This distribution of charge can then be analysed to give the initial direction of the photoelectron (see Figure 6.6). Plotting a frequency distribution

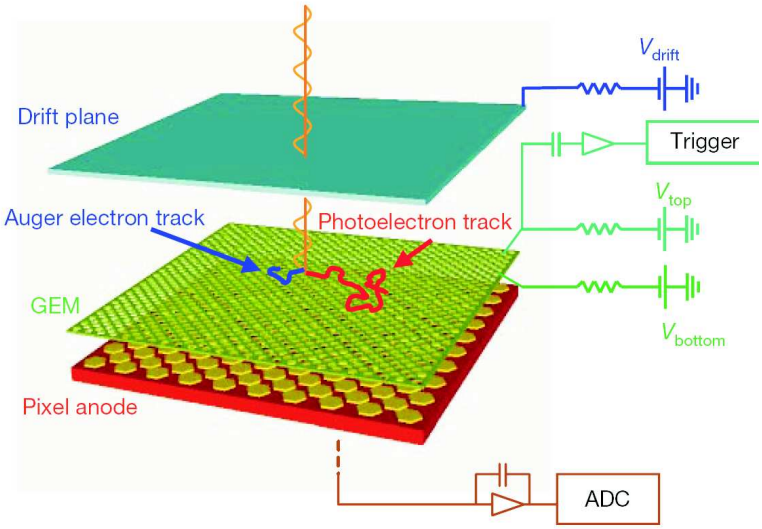

Figure 6.6: Shematic of the MPP design taken from Costa *et al.* (2001).

of the measured electron ejection directions in a statistical sample of X-ray events allows the mean polarisation direction of the X-ray beam to be deduced as it is correlated with the electric field vector of the photon (e.g. Bellazzini *et al.* (2003)).

6.5.2.1 The baseline polarimeter for XEUS

The MPP device has been proposed for inclusion on a number of future missions, including *XEUS* - the next generation X-ray observatory (Parmar *et al.*, 2006). Bellazzini *et al.* (2006) propose inclusion of a photoelectric polarimeter as a focal plane element, however, it does not form part of the current baseline payload. The authors show that with the expected *XEUS* performance in 2003 and an observation time of $10^5 s$ they could achieve minimum detectable polarisation fractions of below 1% for a variety of active galactic nuclei (AGN). These include; CENA, NGC4151 and IC4329A, along with a number of others, this kind of sensitivity would revolutionise astrophysical X-ray polarimetry allowing definitive measurement of the polarisation of tens of AGN as well as other bright objects.

The *XEUS* proposal (Turner & Hasinger, 2007) states that the instrument will weigh 23.3 Kg, have

a power budget of 34 W and must demonstrate a performance of 2% MDP (3σ) in 10^4 s. This document also states that interested parties will be invited to join the XPOL consortium, meaning that if dichroic filters can be shown to add to the capabilities of the baseline polarimeter, a route into the mission exists.

6.5.2.2 Other oppotunities for the MPP

A dedicated X-ray polarimetric observatory *POLARIX* has also been proposed by Costa *et al.* (2006), using existing *Jet-X*[3] mirrors and a photoelectric polarimeter in the focal plane to provide a pathfinder mission for polarimetry before the launch of *XEUS* and *Con-X*. This telescope would have an effective area of $\sim$160 cm^2 at 1.5 keV and would allow observation of a number of effects of high astrophysical significance. For instance, the authors show how *POLARIX* could, at last, measure the rotation of the polarisation vector as a function of energy for Cyg X1, confirming the presence of a rotating black hole (Stark & Connors, 1977).

To the author's knowledge, the final proposed mission for the MPP is the Chinese *HXMT* mission which is primarily going to be a hard X-ray sky survey. However, Costa *et al.* (2007) shows that the later pointed observations could make this satellite ideal as a host for a pair of X-ray telescopes designed for polarimetry. Despite the limited resources available on the *HXMT* mission, this paper shows a number of areas where the measurements would provide a breakthrough in polarimetry.

6.5.3 Time projection chambers - TPCs

Jahoda *et al.* (2007) propose a new evolution of the MPP design, using a time projection chamber to image the photoelectrons as a possible instrument for the next large NASA X-ray observatory - *Constellation-X* (e.g. White (2006) or Petre *et al.* (2006) further information is available at http://-

[3] Jet-X was an X-ray telescope built for the Russian Spectrum X mission which never flew

constellation.gsfc.nasa.gov/resources/papers/index.html). This instrument is proposed to go in front of the focal plane to allow simultaneous polarimetric and spectroscopic observations of a source.

The quantum efficiency of the TPC is independent of modulation factor and it can, in principle have 100% quantum efficiency. In practice, a trade off between the signal detected in the polarimeter and the spectroscopic focal plane instrumentation reduces the efficiency of each measurement as a significant number of photons must be detected in each instrument. However, the diagnostic power of such parallel observations would offer a huge improvement in the reliability of astrophysical models used to fit the data simultaneously. The authors claim *Con-X*, would offer the first ever simultaneous observations of all astronomically pertinent parameters (imaging, timing, spectroscopy and polarisation).

6.5.4 Dichroic X-ray filters

Auton (1967) showed that a wire grid of period d will effectively polarise light of wavelength λ if $d \leq \lambda/2$. At visible wavelengths, polarization can be detected using highly ordered materials such as Polaroid H-sheet, a commercially available polymer sheet which is used in LCD displays and sunglasses. H-sheet consists of long chain polyvinyl alcohol molecules which are stretched during manufacture to ensure that all polymer chains are uniformly aligned, doping these chains with iodine makes them conduct along their length, effectively forming a wire grid polariser. This imposes a preferred axis on the material and light polarised parallel to the chains is efficiently absorbed, while light polarised in a direction perpendicular to the chains is transmitted.

Collins (1997) reports the successful analysis of polarisation, for 33.17 keV X-rays using ordinary H-sheet material. However, the wavelength dependence of the wire grid dichroic polarisers should preclude the operation of materials such as H-sheet at X-ray wavelengths. Therefore, the underlying physics explaining this result must be very different from that which governs optical wavelength polarisation.

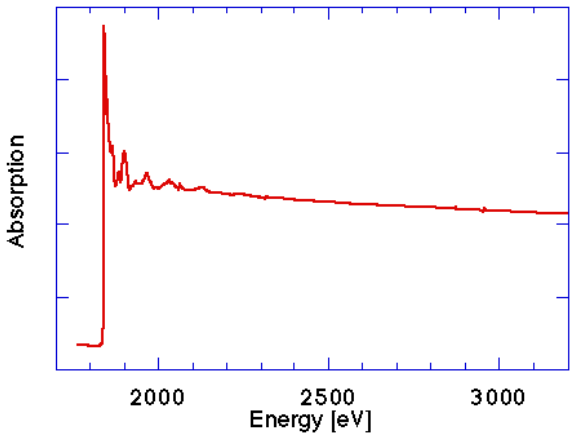

Figure 6.7: The X-ray absorption fine structure for a silicon wafer. The "ripples" after the main edge are a consequence of the electronic states close to the excited silicon atom. Image reproduced from http://pfwww.kek.jp/kitajima/sx/bl11b_e.html.

This dichroism is a consequence of structure in the X-ray absorption coefficient of a material within a few 10's of eV of an absorption edge. Such *X-ray absorption fine structure* (XAFS) is a consequence of the occupancy of electronic states close to the atom, and is shown for the case of a silicon wafer in Figure 6.7. In most materials this structure is independent of the polarisation angle of the incident X-ray photon. However, in the highly ordered materials which form the basis of the dichroic filter concept, the presence or absence of a vacant allowed state in either axis of the material leads to a polarisation dependency in the XAFS, and hence a polarisation-dependent absorption coefficient in a narrow energy band around the absorption edge.

We have already seen that the emission direction of photoelectrons is biased towards the direction of polarisation of a photon. Therefore, it must follow that the X-ray absorption coefficient of an absorber must be highest in the axis of polarisation. However, the measured X-ray absorption coefficient is the average over all polarisation directions, and for any isotropic absorbing material it is independent of the orientation of the absorber. In materials where the electronic structure around an atom is highly non-isotropic, the absorber will show a different absorption coefficient depending on the orientation

of the polarisation vector with respect to the axis of anisotropy of the electronic states. This only happens in narrow bands around an absorption edge, but results in a change in the transmission of the material as a function of angle for polarised incident beams. It is by this mechanism that such materials act as efficient polarisers for a narrow band of X-ray energies.

XEUS and *Con-X* are described more fully in section 1.4.1 and have, as part of their key science package, cryogenically cooled detector arrays with energy resolution capable of resolving the varying transmission of one of these filters. Hence, placing such a filter in the light path before the focal plane allows simultaneous exploitation of imaging, timing, spectroscopic and polarimetric measurements. These discrete energy polarisation measurements could be achieved with no added focal plane elements for a very marginl increase in the mass of the spacecraft. All that is needed is a filter wheel which can introduce and remove a filter from the light path as needed and rotate the filter to measure the modulation in intensity of the beam as a function of angle. The $\sim eV$ energy resolution of the cryogenic focal plane spectrometer can be used to measure polarisation.

A window for simultaneous science will also exist which is dependent on the broad band transmission of the filter. Here, the spectroscopic, imaging[4] and timing performance of the cryogenic focal plane can still be used.

Another potential advantage of this method, which is yet to be investigated, is the extension of the polarisation sensitive band for an observatory. Costa *et al.* (2006) and Bellazzini *et al.* (2006) show that the useful bandwidth of an MPP device is limited by the gas mixture and absorption gap thickness, this limits the bandwidth to ∼1.5 keV at low photon energy, with ∼11 keV as the upper spectral limit, although sensitivity falls rapidly below ∼ 2.5-3 keV. Addition of dicrete polarisation measurements at higher and lower energies could add significant diagnostic power to an observation. For instance,

[4]Note that the beam scatter from dichroic crystals has yet to be investigated and as such it is possible that the imaging resolution may be reduced from the intrinsic limit set by the optics and focal plane instruments.

adding more data points to the potential measurement of rotation of the plane of polarisation for Cyg X-1 which, it is hoped, would confirm the existence of a rotating black hole (Costa *et al.* (2006) Figure 3). A number of methods exist for making a number of discrete energy polarisation measurements with a dichroic filter, these will be discussed in Chapter 7.

6.6 Summary

This chapter has described the polarisation of electromagnetic radiation and methods of measuring it, the scientific case for measuring X-ray polarisation and finally historical and proposed future methods of making such measurements. Chapter 7 describes experimental and theoretical work to optimise the dichroic filters mentioned above for inclusion on the next generation of X-ray telescopes. An X-ray dichroic polariser would offer a low cost, compact, low mass method of performing X-ray polarimetry, so long as a detector with suitable energy resolution is used to detect the X-rays.

Chapter 7

Dichroic Filters for X-ray Polarimetry

7.1 Introduction

In Chapter 6 the scientific background to astrophysical X-ray polarimetry is reviewed along with historical results and future proposed instrumentation. The concept of dichroic X-ray filters was introduced in terms of the use of Polaroid H-sheet (a commercially available polariser for optical light) as a narrow band polariser of 33.17 keV X-rays. These filters are proposed as the basis of a possible polarimeter for the next generation of X-ray telescopes. As H-sheet has been shown to exhibit dichroic behaviour in close proximity to an X-ray absorption edge, the question arose: Could other such materials be designed to exhibit this effect?

The structure of H-sheet on nanometer scales is responsible for the difference in transmission of the filter as a function of the azimuthal angle between the beam polarisation and the principal axis of the polariser. The long chains of doped PVA molecules lead to an electronic structure which is different

in two perpendicular axes. This difference in structure leads to an apparent shift in the position of an absorption edge because of a polarisation-dependent EXAFS peak (present in one axis and not the other) which overlaps the edge. The peak is caused by the number of allowed molecular electronic states, which differs in these two directions. As the most probable direction of ejection of a photoelectron is parallel to the polarisation vector of the photon, the absorption probability (for a polarised incident beam) differs in these two principal axes because of a reduction in the absorption in the material in one axis than the other in a narrow energy band (i.e those energies that lie within the apparent energy shift of the absorption edge).

Consequently, a material designed to have highly ordered and different electronic structure in two perpendicular axes is expected to produce an efficient polariser in ~ 10 eV bands around the absorption edge of the ordered atomic species which provides the dichroism.

7.2 Material design strategy

The goal of this research is to produce single crystals with highly ordered and well-aligned bonding structure to act as transmissive filters. Initial attempts concentrated on inclusion compounds, where the guest molecules of interest were confined to a particular orientation within a tunnel-like host substance. The guest molecules are chosen to provide an atomic absorption edge of interest and a bonding structure and molecular shape which allows them to be oriented by the host. The molecular bonds and their directionality (imposed by the host) cause the dichroic response.

The host material acts to reduce the transmission of the filter without adding to the dichroic response and although this is not a problem for high energy photons where absorption in the host is small, at lower energies, absorption in the host dominates. Hence, a parallel development of materials was followed to achieve a similar structure by using coordination chemistry to constrain a molecule in a

particular orientation. This is achieved by designing a discrete molecule with a shape which leads to predictable interactions between molecules (Van der Waals, graphitic interaction, hydrogen bonding), resulting in highly ordered structure with the relevant molecular electronic states aligned in a single axis. The mechanism which leads to the dichroism is similar to that in the inclusion compound approach, i.e. the orientation of atomic bonds within the molecules.

These two approaches to the crystal engineering, and the related experimental work are discussed in the following sections.

7.2.1 Inclusion compounds

A host matrix is used to confine molecules of interest into a structure where their chemical bonds remain coaligned with the axes of the host tunnel. The hosts of interest in the current work are Urea and Thiourea, which crystalise into tunnel structures. These can be engineered to contain a guest molecule of interest which is used to introduce the dichroism.

Initial attempts to make X-ray polarising filters concentrated on a dibromoalkane/urea inclusion compound (Collins *et al.*, 2002, e.g.); this was shown to be an unoptimised material because the bonds in the guest molecule did not align perfectly with the tunnel axis. A 1-Bromoadamantane/Thiourea inclusion compound was shown to exhibit perfectly aligned bonding with the tunnel axis and the X-ray testing of Chao *et al.* (2003) showed that this was a much better polarisation analyser as the strength of the differential effect was increased by the improved bond alignment (Figure 7.1).

During the current work, a number of new compounds have been made and tested to investigate their possible use in an astrophysical instrument. The success of the bromine-based compound implies that elements in the same group of the periodic table should show a similar dichroic response, governed by their similar chemistry. Therefore, the iodide and chloride analogues of this material were synthesised

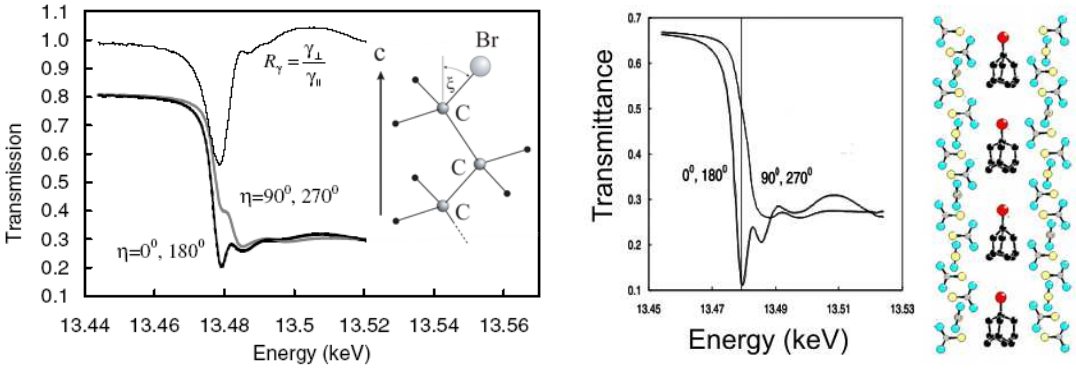

Figure 7.1: Transmission spectra from Collins *et al.* (2002) for a dibromoalkane/urea inclusion compound (left) and Chao *et al.* (2003) for a 1-Bromoadamantane/Thiourea inclusion compound (right)

along with some completely novel materials containing absorption edges within the astronomically important 0.2-10 keV region.

7.2.2 Inorganic crystals

An alternative approach to the production of polarising filters was the use of coordination chemistry to constrain a crystal in a repetitive unit cell containing different bonding structure in orthogonal directions. Such an array of coaligned bonds was expected to produce dichroic absorption as a function of beam polarisation direction, owing to the different electronic environment in the two axes. The presence of planar and ring-like ligands in the molecule confine crystal growth to ensure that the relevant bonds in the molecule are co-aligned and mono-axial. Figure 7.2 shows the structure of one particular inorganic crystal, labelled YC19, produced in this work.

7.3 Experimental characterisation

Following synthesis of a number of candidate filter crystals, a campaign of experimental performance characterisation was required. Two general approaches to this work were considered.

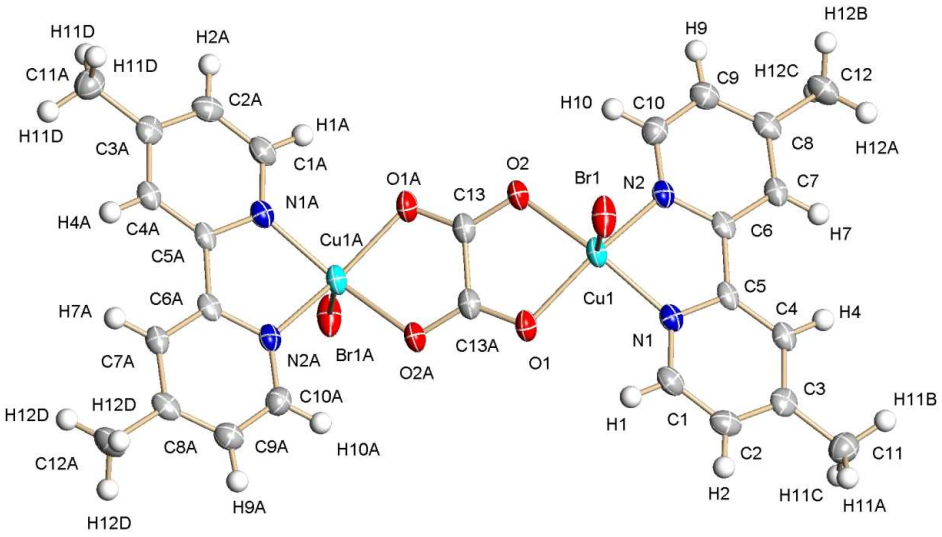

Figure 7.2: Structure of YC19 showing the bond orientations and the position of the atoms. The copper atoms are shown in light blue and in between them lies a planar bridging ligand which, along with the ring structures either side of the copper atoms constrain the crystals to grow in a regular manner, forcing the electronic structure into a mono-axial configuration.

First, a "flight-like" system in which a high energy resolution detector is placed behind one of the dichroic filters and a laboratory X-ray source is used as the illumination source. Rotation of the filter would then allow the intrinsic polarisation of the source to be measured experimentally. However, laboratory X-ray sources are not expected to show a significant polarisation so this kind of measurement may prove difficult. It is possible that a second filter could be introduced into the light-path to act as a polariser, producing a preferred polarisation direction to the beam. The bandwidth of the polariser and polarisation analyser are small but they are ideally matched because they are caused by the same electronic transition within the material. Talks are underway with the NASA - Goddard Spaceflight Center (GSFC) to conduct this experiment with one of the high energy resolution, transition edge sensors proposed for *Con-X* and *XEUS* (Kilbourne, 2007).

An easier method (and the one used in all previous experimental work) is to use the intrinsic linear polarisation of a synchrotron source to characterise the filters. Station 16.3 of the Daresbury SRS was chosen for this work because of the heritage of the facility for this kind of investigation (Collins,

1997). The beamline consists of a double crystal monochromataor capable of giving sub-eV energy resolution between $\sim$ 5 and 30 keV. A series of pre- and post-monochromator slits are used to control the size of the beam, which can be anywhere from $\sim$ mm to a few tens of μm, giving a uniform beam with a linear polarised fraction well above 90% in the plane of the synchrotron (Collins *et al.*, 1998). This is the approach to characterisation adopted in the current work.

Figure 7.3 shows the experimental arrangement. The beam emerges from the vacuum section of the beamline and traverses through an air gap which contains the relevant instrumentation. It first enters an ion chamber which is filled with an appropriate gas mixture to attenuate approximately 20% of the incident beam. The signal from this chamber serves as the beam monitor, measuring the incident flux onto the sample (I_0), allowing normalisation of the transmitted signal. The beam then continues until it reaches the sample which is mounted on a diffractometer with many degrees of freedom. For low energy edges it is useful to place an evacuated chamber between the I_0 monitor and the sample to reduce attenuation due to the air path. After transmission through the sample, the beam then traverses another air path en-route to the rear ion chamber (I_1) which is used to measure the absorption of the filter. A third detector measures the fluorescence signal generated as the excited atoms from the material decay back into the ground state. Any X-ray that is absorbed will give off a corresponding fluorescence X-ray providing another method of measuring the dichroic response. However, using the fluoresence signal is more troublesome as precise knowledge of the geometry of the sample is required to reconstruct the absorption of the beam from the fluorescence X-rays. For this reason, all analysis herein concerns the data from the I_1 ion chamber.

During data analysis, it is very important to normalise out the effect of the air path as attenuation here should not be confused with attenuation in the sample. A necessary and valid assumption is that over the energy range of the XAFS region ($\sim$ 200 eV), the attenuation due to the air path is achromatic. As part of the sample alignment procedure, the crystal is scanned through the X-ray

beam both horizontally and vertically such that the beam can be positioned in the center of the sample. The extremes of these scans represent beam transmission un-occulted by the sample and can be used to normalise the signals from the front and rear ion chambers. This normalisation removes two main effects; attenuation of the X-ray beam by the air path, and probably more importantly for high energy X-rays, the difference in gain and efficiency of the two ion chambers.

The experiment requires the sample to be moved in four degrees of freedom. The vertical and horizontal position adjustment is used for the alignment scans and χ and ϕ rotations (the azimuthal rotation about the optical axis and rotation of the sample holder perpendicular to the optical axis respectively - See Figure 7.4). χ is used to rotate the principal axis of the sample with respect to the polarisation vector of the synchrotron beam and ϕ is used for very fine optimisation of the position of the samples with respect to the beam.

7.3.1 Sample preparation

A detailed discussion of the manufacture of the samples lies beyond the scope of this thesis (Further information can be found in e.g. Champouret (2007), Chao *et al.* (2003) or Collins *et al.* (2002)). All samples tested here were single crystals of the relevant material. The inclusion compound crystals were produced by Kenneth Harris *et. al.* at the school of chemistry, University of Cardiff, and the coordination complexes produced by Greg Solan *et. al.* at the chemistry department in the University of Leicester. The pre-synchrotron characterisation by X-ray diffraction experiments, outlined below, was conducted by the chemists who manufactured the samples.

Preparing the samples for testing on the beamline involved securing the crystal to an appropriate sample stage for insertion into the goniometer. A number of methods were used, from attaching the crystal using a hot wax, using super glue and even using sticky tape; the particular morphology of the crystal dictated the preferred method of mounting it. The mount was a silicon wafer which was

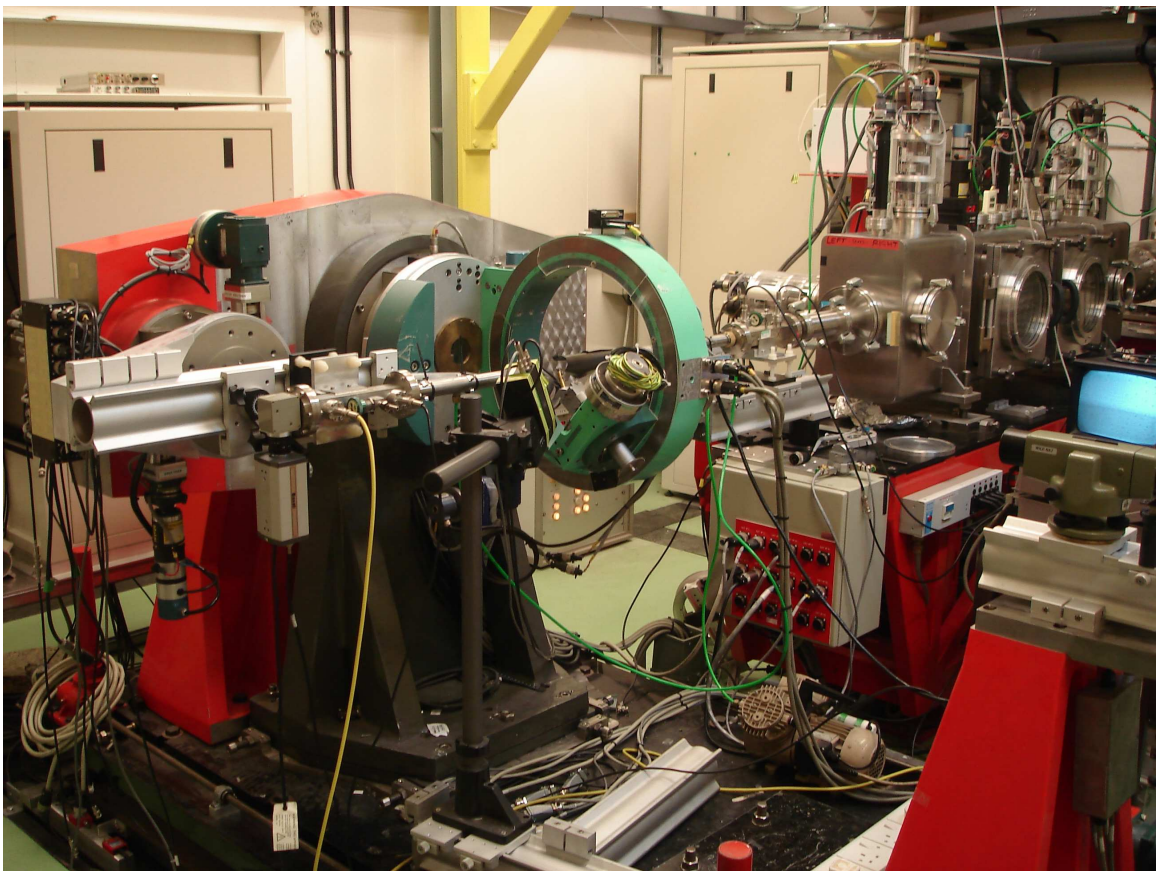

Figure 7.3: Photograph of the experimental arrangement for testing dichroic crystals at station 16.3 of the Daresbury SRS. The χ axis is a rotation around the green ring in the center of the image and ϕ is a rotation at 90° to this axis about the sample mounting structure.

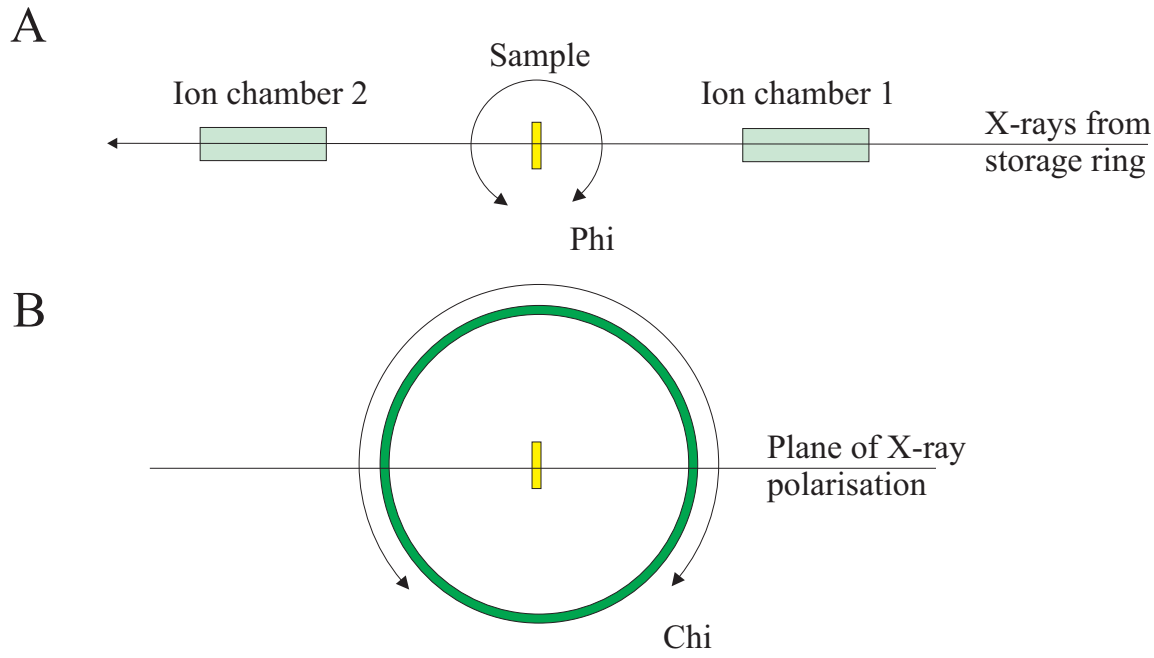

Figure 7.4: Schematic diagram of the experimental arrangement for testing dichroic crystals at station 16.3 of the Daresbury SRS. Panel A shows the plan veiw with the plane of the synchrotron and therefore the X-ray polaratation in the page. The ion chambers used for detection are shown. Panel B is a view from ion chanber 2 towards the synchrotron such that the plane of polarisation is now horizontal on the page. The chi axis isa rotation around the optical axis of the beamline (i.e. around the green ring) the Phi axis is vertical in the Figure 7.3 and is represented as rotation around the sample in panel A.

expected to reduce the amount of beam scatter by the sample holder.

7.3.2 Sample storage

The single crystals were stored either in solution or at atmospheric pressure until testing at the SRS commenced. The first run of beam time was used as a screening process to ascertain which of the samples were of interest as polarisers. The second run was then dedicated to testing the vacuum stability of these samples by comparing their response measured in the first run with the new data generated after the samples had been stored in a vacuum chamber at $\sim 10^{-6}$ mbar for approximately three months.

7.3.3 Sample characterisation

Before arrival at the SRS, the samples were characterised by single crystal X-ray diffraction in order to verify the chemical and structural composition of the crystal. This gives the unit cell of the crystal and shows where the bond directions lie. Consequently, it yields the expected axis of the dichroic behaviour. Unfortunately, some of the coordination compounds grew in a structure with little or no symmetry. Therefore, the macroscopic appearance of the crystal was not indicative of the bond orientation. However, our polarisation measurements showed that, in general, if the crystals grew in needle like shapes, the axis of the crystal was the same as the axis of the bond causing the dichroism. The needle-like crystals were therefore preferred for X-ray testing. The same is true for the inclusion compounds as the axis of the pertinent bong is parallel to the macroscopic "long-axis" of the needle crystals.

Sample	Active element	K-edge	Crystal type
			(I=incl., C=coord.)
1-Bromoadamantane/Thiourea	Br	13.47	I
2-Bromoadamantane/Thiourea	Br	13.47	I
1-Iodoadamantane/Thiourea	I	33.17	I
Ferrocine/Thiourea	Fe	7.11	I
Benzene Chromium(0) Tricarbonyl	Cr	5.99	I
YC19	Cu	8.98	C
YC31	Cu	8.98	C

Table 7.1: The samples subjected to X-ray testing at the Daresbury SRS.

7.4 Results

7.4.1 Inclusion compounds

The obvious place to begin experiments was to repeat work that had already been done (Chao *et al.*, 2003) and extend this analysis further to energies higher above the edge, in order to assess any dichroism in the extended X-ray absorption fine structure (EXAFS) region, and also to investigate in more detail the angular dependence of the response at different energies.

A single crystal of the 1-Bromoadamantane/Thiourea inclusion compound was attached to a sample stage using vacuum grease as it was believed that this grease would hold the very light crystals securely, yet enable them to be quickly interchanged. The stage was then inserted into the goniometer head and aligned using a telescope and theodolite mounted onto the diffractometer table. The alignment was then checked in both horizontal and vertical directions by scanning the sample through the X-ray beam. This was achieved by moving the diffractometer table and rotating the sample in the χ and ϕ directions.

Figure 7.5 shows the fractional absorption spectrum for polarisation parallel to the crystal (and tunnel) principal axis (red) and perpendicular to it (black). The level of dichroism is consistent

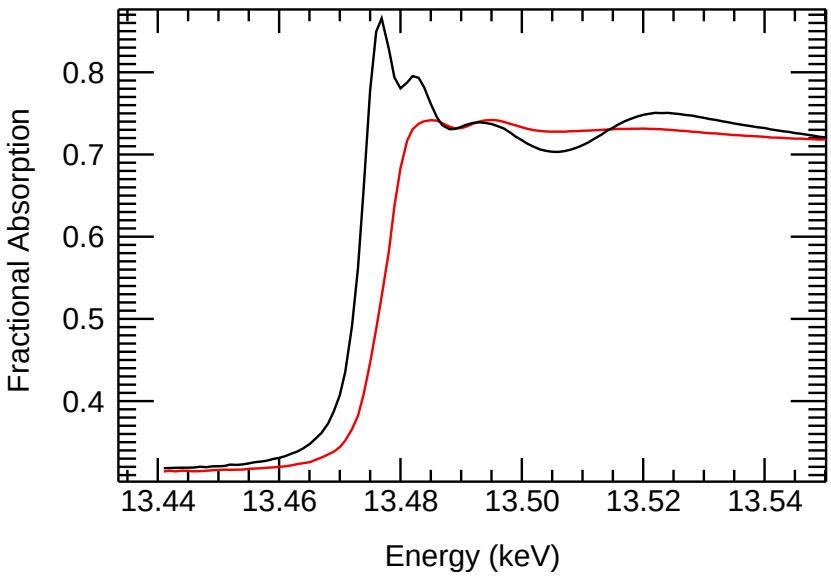

Figure 7.5: Energy spectra for an inclusion compound of 1-Bromoadamantane/Thiourea. The red curve is for $\chi = 90°$ and the black curve for $\chi = 0°$ where χ is the angle between the axis of the crystal expected to be parallel to the bond which leads to the dichroism and the polarisation direction of the photons.

with that reported in Chao *et al.* (2003) and has a similar functional form, thus confirming the correct experimental arrangement. This was an important result, as the complexity of the experiment is compounded if sample alignment is poor.

The well optimised setup was unfortunately compromised because the high temperature ($\sim 25-30°$C) in the experimental hutch reduced the grease viscosity and the sample moved. Therefore, it was decided that the samples would be attached to the stage using superglue. Another sample of 1-Bromoadamantane/Thiourea was installed and a *grid scan* taken, involving scanning energy from 13.45 keV to 13.51 keV in steps of 0.5 eV at all angles between 0° and 355° in steps of 5° (Figure 7.6).

The narrow bandwidth of the effect means that all data is self normalising if the absorption edge can be resolved in energy space. Any variation in transmission as a function of angle well above or below the edge is indicative of an experimental artifact as the driving mechanism of the polarisation

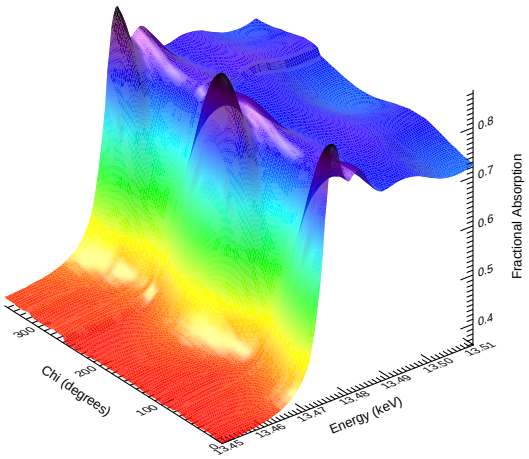

Figure 7.6: Surface showing absorption as a function of photon energy and crystal orientation for a 1-Bromoadamantane/Thiourea inclusion compound.

response is confined to a few tens of eV around the edge. Such variations have been seen and were correlated with poor sample alignment leading to a variation in beam position on the crystal as it was rotated. Inhomogeneity in the thickness of the crystal then led to variation in transmission at all energies during sample rotation. Figure 7.6 provides a data surface which describes the behavoiur of the sample as a function of energy and angle χ, and shows no such variation, implying that the response close to the edge is a real dichroism in the absorption spectra. This is highly significant as it demonstrates that the polarisation response is real, and not an artifact of the experimental conditions. The self normalisation offers a definite advantage for a dichroic filter over competing technology as in other techniques, a large number of effects could potentially contaminate the true modulation.

Since the dichroic response in the EXAFS region is still significant at the upper energy limit of Figures 7.5 and 7.6, a long energy scan was taken for parallel and perpendicular orientations of the crystal to determine at what energy below the edge the dichroism stops being significant (Figure 7.7); this was found to be $\sim$13.54 keV, although some weak differences extend out to 13.6$-$13.7 keV.

Testing then progressed to a screening process for materials with significant dichroism. The io-

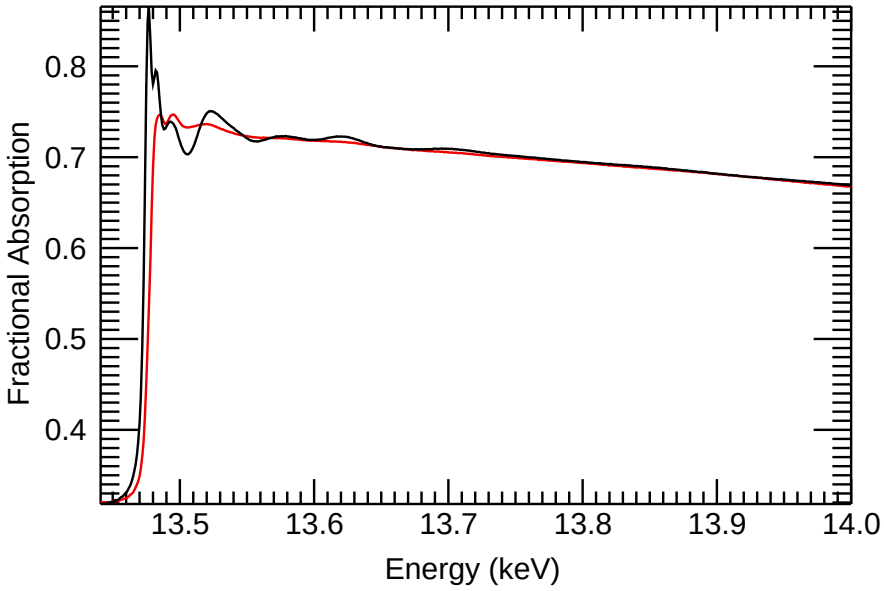

Figure 7.7: Transmission spectrum of a 1-Bromoadamantane/Thiourea inclusion compound, the extended energy range from Figure 7.5 demonstrating the narrow bandwidth of the dichroic response. The curves are as described in Figure 7.5

dide analogue of the compound investigated above (1-Iodoadamantane/Thiourea), shows a significant dichroism (Figure 7.8) indicating that the similar chemistry and structure (c.f. 1-Bromoadamantane-/Thiourea) does indeed correspond to similar transmission properties.

A number of other Thiourea inclusion compounds were investigated including those containing Ferrocine and Benzene Chromium(0) Tricarbonyl (Figure 7.9), both of which showed little dichroism other than in low amplitude effects. One possible explanation is that the thickness of the sample could be too high for these low energies; leading to significant absorption by the Thiourea matrix. Another important factor is that the signal to noise ratio of these results was poor owing to the reduced flux from the beamline at these relatively low energies.

Absorption owing to the host matrix is high for such compounds at the (low) K-edge energies of Fe and Cr leading to high attenuation of any possible dichroic signature. Figure 7.10 shows the broadband

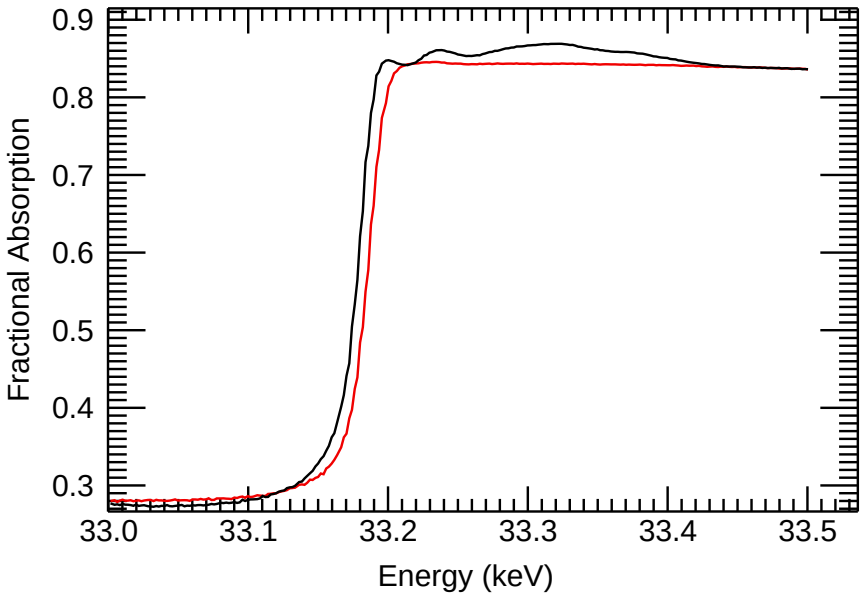

Figure 7.8: Energy spectra for an inclusion compound of a 1-Iodoadamantane guest in a Thiourea host. The curves are as described in Figure 7.5

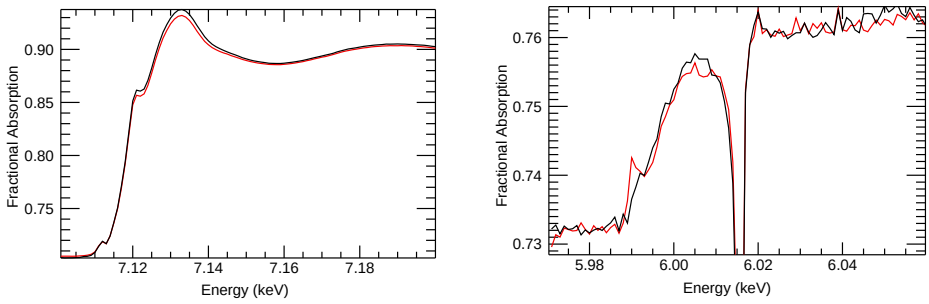

Figure 7.9: Transmission spectra for a Ferrocine/Thiourea inclusion compound (left) and an inclusion compound of benzene chromium(0) Tricarbonyl in Thiourea. The significant dip in the plot for the chromium compound is not real. It is believed to be indicative of a monochromator glitch meaning that data from this compound is not as reliable as for the other materials. This and the poor signal to noise ratio of the data mean that the only realistic conclusion obtainable from this data set is that there is no significant dichroic effect. The curves are as described in Figure 7.5

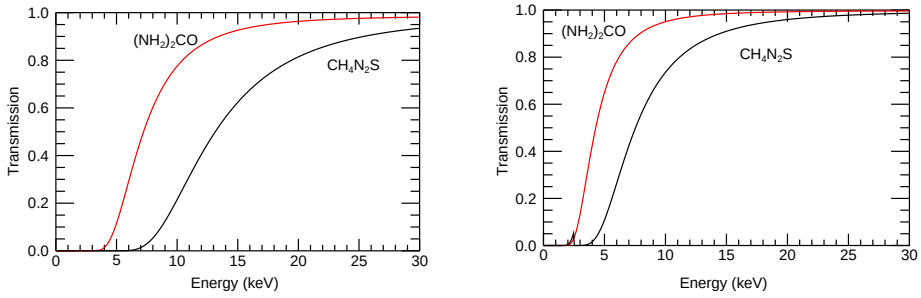

Figure 7.10: Showing the broadband transmission properties (Henke *et. al.* 1993), for Thiourea (black) and urea (red). Left, arbitrary sample thickness = 0.5 mm. Right, sample thickness = 0.1 mm (as for Cr compound).

transmission of Thiourea (black) and urea (red) as a function of energy in the range of interest (0-30 keV). The model assumes a density for both compounds of 1.4 gcm^{-3} and a sample thickness of 0.5 mm (left) and 0.1 mm (right). It is clear that at 6-7 keV the absolute transmission of the host matrix is small, this is supported by Figure 7.9, where the small absolute transmission and shallow edge imply that the majority of the absorption occurs within the Thiourea matrix, diluting the influence of the active element and weakening (or possibly removing) any obvious dichroism. Interestingly, at energies close to the Fe-K and Cr-K edges, the transmission of urea is significantly higher; it would therefore be interesting to investigate whether an appropriate metallic guest could be housed within a urea matrix, where the reduced absorption in the host could lead to increased dichroism even if the bond alignment is reduced as reported for the dibromoalkane/urea inclusion compound (Collins *et al.*, 2002). Unfortunately, at present this is not thought to be possible (Harris, 2007).

The chlorine K-edge is at 2.82 keV, well below the $\sim$ 4 keV low energy cutoff of the beamline. This low energy limit is caused by the presence of a number of beryllium windows and a significant air gap in the light-path. Testing of the chloride analogue of the Bromo/Iodoadamantane inclusion compounds has therefore proved beyond our capabilities to this point. A suitable beamline would need to be found to achieve this with an appropriate rotation stage under vacuum conditions and suitably accurate

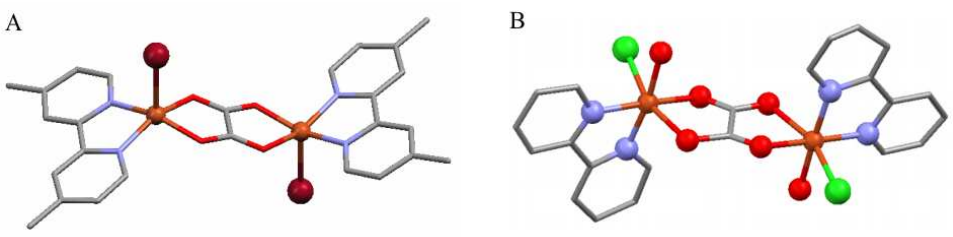

Figure 7.11: Diagrams of the unit cell of the coordination compounds (A) YC19 (B) YC31c. In YC19 the bonds pertinent to dichroism are parallel, for YC31c they are inclined with respect to each other.

monochromator and beam size/morphology. An alternative method for characterising this material is to use a laboratory source and high energy resolution detector (see Section 7.3).

7.4.2 Coordination compounds

Two coordination compounds were also tested, μ-oxolato-bis-[(4,4'-dimethyl-2,2'-dipyridyl)copper bromide] (YC19) and μ-oxolato-bis-[(2,2'-dipyridyl)copper chloride hydrate] (YC31c) – to date, the only two which have grown in needle-like crystals. Other coordination compounds have been produced, however, the lack of symmetry and the block-like nature of the crystals means that a complicated diffraction experiment would be needed to determine the orientation of the bonds for testing. The current experimental arrangement made this difficult and it was therefore decided that this would not be a good use of limited beamtime.

The two usable samples were shown to have different orientation of the pertinent bond with respect to the crystal morphology and were, therefore, expected to show different dichroic behaviour (Figure 7.11). YC19 was shown by single crystal X-ray diffraction to have bonds which were well aligned, whereas YC31c was found to have bonds which were inclined with respect to each other. Figures 7.12 and 7.13 show that this difference translates into a marked difference in observed dichroism.

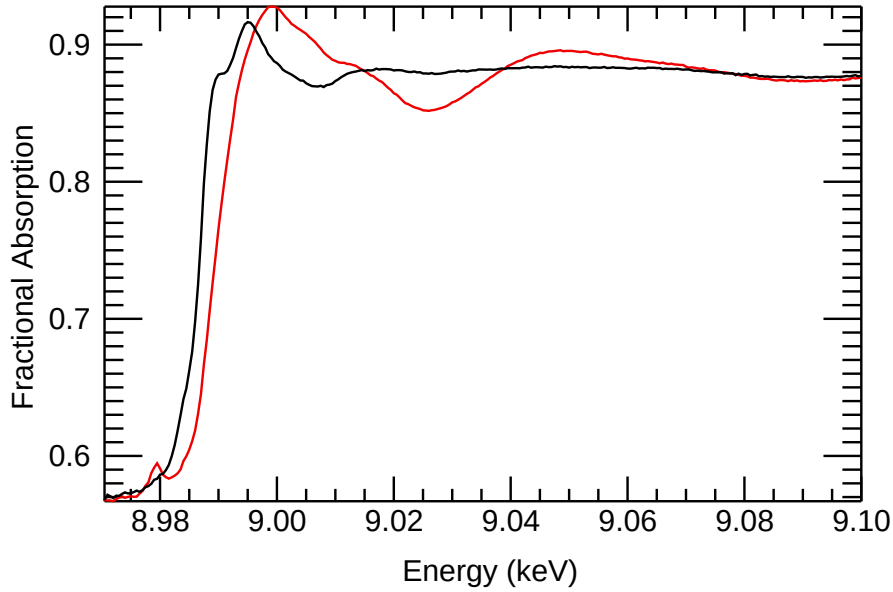

Figure 7.12: Energy spectra for YC19. The curves are as described in Figure 7.5

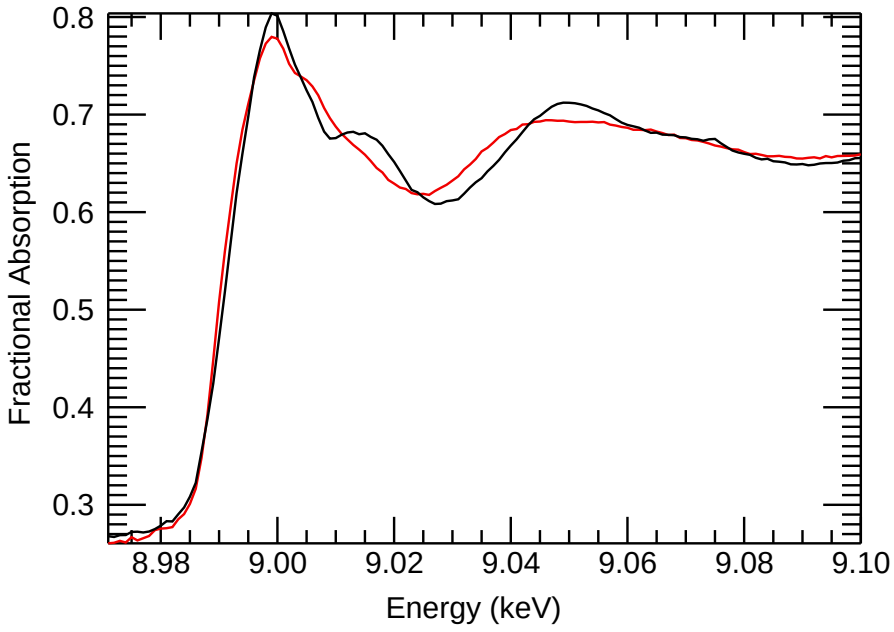

Figure 7.13: Energy spectra for YC31c. The curves are as described in Figure 7.5

7.4.3 Vacuum stability

Subsequent testing at the SRS after vacuum storage showed that while the inclusion compounds survive evacuated conditions well, the copper coordination complexes degenerated into a fine powder. Although the inclusion compounds were shown to have maintained their dichroic properties, there was a certain amount of optical degradation which made the crystals appear more cloudy. Therefore, it is believed that some form of passivation, where the crystals are protected from the vacuum of space will be necessary for a space-based instrument. This could be achieved by coating a flight filter in a thin layer of a material such as polyamide which would be expected to protect the crystal with little absorption added by the passivating layer. This will be discussed further in Section 7.5 where a possible instrument design is considered.

7.5 Prototype Instrument Design

Here I will briefly describe one possible design for a space based instrument and some of the considerations necessary to achieve the deployment of a dichroic filter in this context. The first consideration is the size of the filter. It must cover the whole focal plane, which for the transition edge sensor under consideration for *XEUS* is expected to be less than 10 mm across (Parmar *et al.*, 2006). Hence, a radius of 15 mm is adopted for the filter. This filter must be mechanically uniform with little or no variation in transmission as a function of position, either robust crystal growth strategies or a manufacturing technique capable of co-aligning large numbers of small crystals must be developed. Such manufacturing techniques have all ready been demonstrated for the manufacture of Polaroid J-sheet (Hecht, 1987).

The space environment is hostile for many materials where the thermal and vacuum conditions are detrimental to the integrity of the molecules. Preliminary vacuum exposure studies have shown that

the coordination complexes are not vacuum stable, also the inclusion compounds are known to be highly water soluble, meaning that the environment within the spacecraft would need to be regulated to ensure the survival of such filters during storage in the humid conditions on Earth. As a consequence, the filters are envisaged to incorporate a passivating substance to protect the materials from humid conditions, but more importantly, from the vacuum of space during the lifetime of the mission.

Figure 7.14 shows a possible instrument design, in which a filter wheel would be mounted in front of the cryogenic spectrometer. A stepper motor is used to rotate different filters into the light path, with a second (dormant) motor provided for redundancy. The filters are then mounted onto the wheel in holders which are free to rotate on a bearing about the optical axis of the telescope. This allows the measurement of the number of counts received from the source as a function of angle, allowing measurement of the sin^2 modulation curve and hence, the degree and direction of the polarisation. The individual filters are driven azimuthally by their own motor, again, in order to increase the contingency. This design shows eight filters, each optimised for its own dichroic edge. However, the number of filters would have to be chosen to maximise the scientific output for the minimum instrument mass.

Not shown is a direct transmission path in the filter wheel which is used for observations which do not require the polarimetric capability. Power consumption is expected to be low as only one motor will be in use at any one time (either to rotate the desired filter into the light path or to rotate the filter during measurements).

7.6 Discussion

This work has led to the identification of three compounds which can be used as fixed energy polarisers of X-ray radiation. The results are summarised in Figure 7.15. Each of the three curves shows

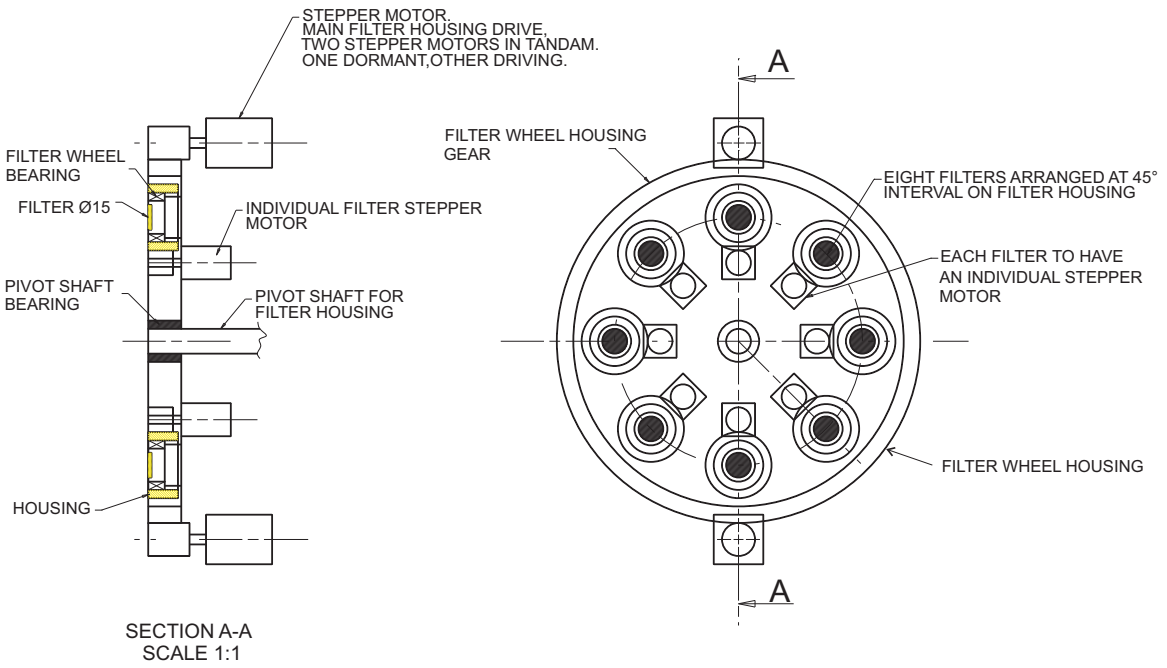

Figure 7.14: Engineering sketch of a potential filter wheel design for the dichroic filter polarimeter (courtesy of Baden Favill, University of Leicester).

the difference between the transmission of a crystal (having Iodine (I-K 33.17 keV), Copper (Cu-K 8.98 keV) or Bromine (Br-K 13.47 keV) as the active element) to X-rays polarised parallel, and perpendicular, to the principal axis of the crystal structure, measured as a function of energy. The x-axis represents the energy with respect to the K-edge in that material, the zero position is the start of the experimental scan except for the case of bromine, which has been shifted by 300 eV so that it is easier to distinguish from the other edges. The apparently modest (15-35%) changes in transmission as a function of polarisation direction are real. However, no attempt to choose an optimised thickness of crystal has been made and a trade off between absolute transmission and the fractional transmission change in the filter is necessary to optimise the response.

7.6.1 Optimisation of the filters

Equations 6.9, 6.10 and 6.11 describe the sensitivity of a polarimeter. Figure 7.16 shows the variation in modulation factor as a function of filter thickness which is calculated using Equation 6.9 by assuming

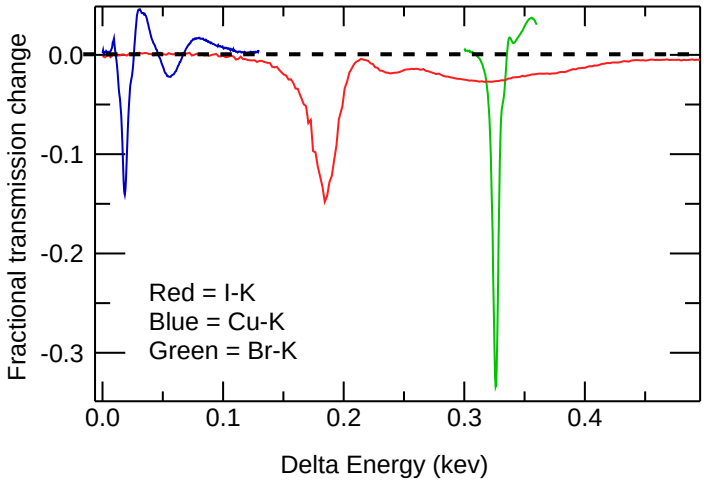

Figure 7.15: Overplot of the difference in transmission change between the two axes of the polariser for all three useful dichroic materials. The results indicate that polarisation information is contained within a bandwidth of a few hundred eV of the absorption edge(I-K 33.17 keV, Br-K 13.47 keV, Cu-K 8.98 keV).

the strength of the dichroism is directly proportional to the depth of the absorption edge. This figure demonstrates that for large filter thicknesses (and therefore low transmission) the modulation factor tends to 1 (i.e. perfect extinction in one axis). While for a terrestrial application where flux is high, this allows a highly efficient polarisation analyser, in a space based context where the measurements are photon limited, the transmission of the filter needs to be high to improve counting statistics. Therefore, a new figure of merit is needed for a dichroic filter polarimeter, allowing the trade off between these opposing requirements.

Equation 6.10 shows that the MDP is proportional to M^{-1} and to $N^{-1/2}$, where N is the count rate experienced by a detector behind the filter. As N is proportional to the filter transmission (T) the appropriate figure of merit, μ, for a dichroic filter can be expressed as,

$$\mu = M\sqrt{T} \propto MDP^{-1}. \tag{7.1}$$

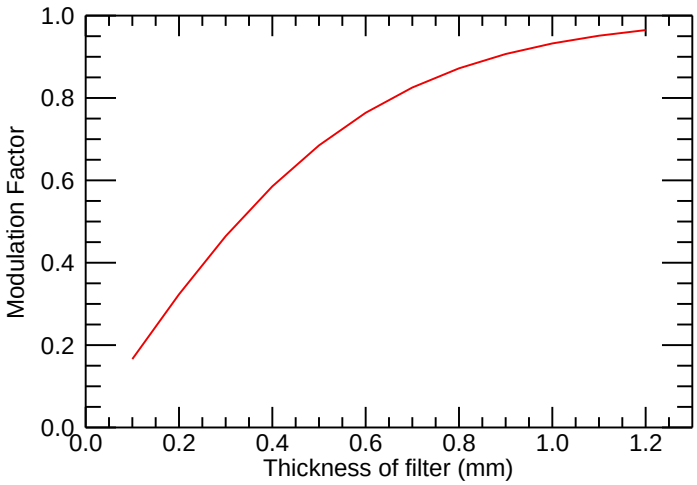

Figure 7.16: The modulation factor plotted as a function of filter thickness for the 1-Bromoadamantane/thiourea inclusion compound.

Figure 7.17 (left) shows μ as a function of filter thickness for the 1-Bromoadamantane/Thiourea inclusion compound. At low thickness, the curve falls (indicating worsening MDP) owing to the low modulation factor at low filter thickness. At higher thicknesses the filter transmission is low, dictating a low count rate on the detector, poor photon statistics and poor MDP. Therefore, the optimum filter thickness lies at the maximum of Figure 7.17 i.e. 0.6 mm. The filters tested herein (Figures 7.5 and 7.6) were of order 0.25 mm in thickness and it is therefore possible that an $\sim 33\%$ improvement in performance (MDP) of the filters could be achieved by optimising the thickness of the filter to maximise μ (or minimise MDP where MDP_{new}=MDP_{old}/1.33). Figure 7.17 (right) shows the same data for YC19 and indicates that only 10% improvement is possible by optimising the thickness of this filter. This is because, fortuitously, we have chosen a crystal with almost optimum thickness (the test sample was 0.22 mm thick with an optimum thicknes of 0.3 mm).

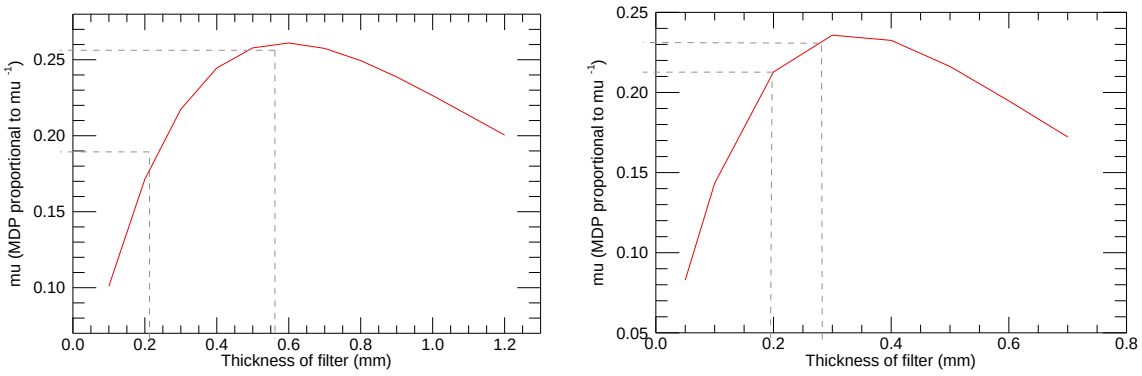

Figure 7.17: The figure of merit μ as a function of filter thickness for the 1-Bromoadamantane/-Thiourea inclusion compound (left) and YC19 (right).

7.6.2 Future experiments

It is expected that the chloride analogue of the inclusion compound should produce a similar dichroic behaviour. However, this has not yet been verified experimentally and a number of physical mechanisms are present which may obscure the dichroic nature of the crystal at the low energy (2.82 keV) of the Cl-K edge. The predominant among these is the broadband absorption in the Thiourea matrix which will be significant at low energies, possibly obscuring the dichroic absorption. This remains to be investigated experimentally. However, Figure 7.10 shows the very high absorption in Thiourea for a low energy edge such a Cl-K. A suitable test setup for low energy edges is a major goal of the next phase of research with the aim of extending the number of compounds in the astrophysically significant $\sim 1 - 10$ keV regime.

Other possible problems exist. These include; sample preparation, where the production of a crystal that is suitably thin but maintains its homogeneity and has a size which is large enough to cover the required focal plane area may prove difficult, and mechanical stability; where the large but thin crystal must be held securely in place without breaking. These difficulties will be addressed in future work after the potential dichroism has been observed or refuted.

7.7 Modeling instrument response

In order to demonstrate the diagnostic power of a dichroic filter polarimeter, a model has been constructed to calculate the response of a dichroic filter and cryogenic focal plane instrument in the context of the *XEUS* observatory. The remainder of this chapter will be concerned with calculating the sensitivity of a dichroic polarimeter to astrophysical sources and assessing the feasibility of such an instrument.

The first element in the instrument response model was a performance specification for the observatory. Knowledge of the effective area as a function of energy was of primary importance, allowing the expected number of photons from a source to be calculated. Given that the sensitivity to polarisation degree and angle is determined statistically, their measurement uncertainties are dictated by counting statistics. Hence, the collecting power (effective area) of the telescope and the brightness of the source dictate the limiting sensitivity of polarisation measurements. The efficiency and resolution of the proposed focal plane instrumentation was then combined with the transmission of the filters (obtained from practical measurements SRS), generating estimates of the sensitivity of the instrument based on experimental data and the published telescope response.

7.7.1 *XEUS*

The X-ray Evolving Universe Spectrometer (*XEUS*) is described in its most recent configuration by Parmar *et al.* (2006) and is scheduled for launch in the time-frame 2015-2025. Its main instruments include a wide field imager based on silicon detectors, a narrow field imager which could either be a transition edge sensor array or one made of superconducting tunnel junctions[1]. It also has ancillary instruments such as a hard X-ray camera, high time resolution spectrometer and imaging polarimeter. It is the successor to XMM-Newton with capabilities which compare favourably to the next generation

[1] It is this narrow field imager which is proposed for use as the detector behind the dichroic filters.

of observatories for other wavelengths (e.g. The James Webb Space Telescope and World Space Observatory). Novel silicon pore optics give 5 m^2 effective area at 1 keV (2 m^2 at 7 kev) and imaging resolution of $\sim 2-5$ arcseconds, which, coupled with the cutting edge focal plane instrumentation give spectral resolving power and timing resolution which are orders of magnitude better than current instrumentation. An imaging polarimeter is included in the definition as a potential additional focal plane instrument.

It is the purpose of the remainder of this chapter to assess the prospects for meeting the science requirement target sensitivity for *XEUS* using a dichroic filter. These state that a polarisation sensitivity of 2% for a 10 mCrab object in a 10 ksec observation must be demonstrated (Parmar *et al.*, 2006). Unfortunately this is a poor measure of sensitivity for a dichroic (narrow band) polarimeter. The "Crab" unit of flux is spectrally sensitive as it assumes a flux given by a cannonical spectrum of the crab nebula (photon index = 2.1, norm = 9.7, absorption = 0.31 $\times 10^{22}$ cm^{-2}) in the 2-10 keV range. The dichroic filters assessed here have an energy at the top of or outside this range, meaning that the efficiency of the filters to polarisation will be highly spectrally sensitive. A source with a harder spectrum than the Crab may be orders of magnitude less bright in terms of the integrated flux from 2 to 10 keV, yet in the few eV energy bandwith pertinent for polarisation measurements with dichroic filters, it may be as bright as or even brighter than the Crab. This is evedent later (in Table 7.3) where the MDP is shown to change drastically depending on the form (spectral index) of the spectrum for Cyg-X1 in its hard and soft states. Rather than addressing the science requirements explicitly, it was decided to assess the minimum detectable polarisation for a number of sources in a realistic (10^5 s) exposure with *XEUS*.

Figure 7.18 shows the effective area of the telescope up to 50 keV assuming a complex multilayer coating which is responsible for the high energy effective area (Lumb *et al.*, 2006) and the current mirror configuration (Willingale, 2007a). The details of the optic configuration and multilayer coating

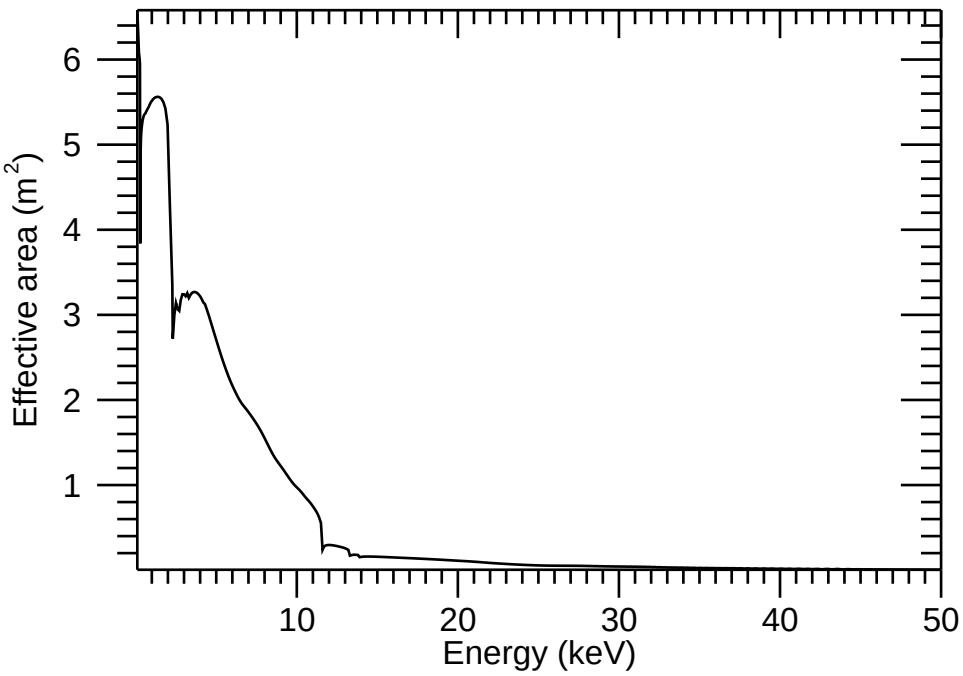

Figure 7.18: The effective area of the *XEUS* mirrors based on the most recent optical configuration (June 2007) with a multilayer coating. No detector efficiency is included in the curve. (Data courtesy of Willingale (2007a))

are omitted and these data should be regarded as indicative because of the rapid evolution of the telescope specification. The curve does not include any detector efficiency or resolution effects, which will be incorporated at a later date.

Although all modeling herein assumes the characteristics of the *XEUS* telescope, it is directly scalable to *Constellation-X* (the U.S. large area X-ray telescope) by changing the effective area and instrumental energy resolution to the appropriate vales.

7.7.2 Detector response

Cryogenically cooled detectors promise unprecedented energy resolution for focal plane instrumentation in future X-ray observatories. The energy resolution of *XMM-Newton* is achieved by using

dispersive reflection gratings which have an intrinsic resolution $E/\Delta E$ of between 150 and 800 in first order between approximately 0.3 and 2.5 keV. For comparison, the *XEUS* specification of 2 eV at 6 keV (Parmar *et al.*, 2006) yields $E/\Delta E$ of 3000 without the need for a reflection grating. It is this energy resolution that allows the use of dichroic filters as astrophysically useful X-ray polarimeters as the region of sensitivity is only ~ 10 eV wide. The quantum efficiency of the detector can be assumed to be equal to the absorption of the 4 μm gold film which acts as the detection medium.

Information is only available for filters with I, Br and Cu as the active (K-shell) absorption edge, yet all lie outside the energy range of the cryogenic spectrometer (0.5-8 keV). The assumption in the model is that for Br-K, and Cu-K the cryogenic spectrometer can be used with an energy resolution of 2 eV. This is not thought to be an unrealistic assumption as the TES is likely to remain in a linear regime at these energies (Kilbourne, 2007), meaning that the energy resolution should remain unchanged as photon energy increases. The lack of effective area and low photon output of most astrophysical sources at $\sim$33 keV means that an iodine based filter is of little astrophysical use and, therefore, suitable detectors will not be considered.

7.7.3 Astrophysical sources

For a Dichroic filter to be a viable astrophysical polarimeter a reasonable MDP must be achieved for a number of astrophysically significant sources. The spectral modeling package XSPEC (version 12.2.1) was used to generate theoretical spectra for sources of interest to use as input for the instrument model. Table 7.2 shows a list of sources that will be considered here and details the XSPEC functions and parameters used to generate them. I will describe the modeling in terms of the Crab Nebula. However, the same process was followed for each of the targets of interest listed in Table 7.2.

	Object				
	Crab [1]	Sco X-1 [2]	Cyg X-1(H) [3]	Cyg X-1(S) [3]	IC4329A [4]
XSPEC Model[a]	pwl×wabs	compTT×wabs	(pwl+BB)×wabs	(pwl+BB)×wabs	cutoffpl×wabs
2-10 keV flux	2.32×10^{-8}	1.32×10^{-7}	8×10^{-9}	1.7×10^{-8}	1.26×10^{-10}
Photon index Γ	2.05	–	1.4	2.7	1.86
Normalisation N_γ	10	–	2.82	10.5	4.16×10^{-2}
Redshift	–	6.6×10^{-7}	–	–	–
T0 (keV)	–	0.36	–	–	–
kT (keV)	–	3.2	0.4	0.4	–
Normalisation N_{kT}	–	24	0.01	0.5	–
τ	–	10	–	–	–
Geometry	–	Spherical	–	–	–
E_{e-fold} (keV)	–	–	–	–	270
N_H (cm^{-2})	3×10^{21}	3×10^{21}	6×10^{21}	6×10^{21}	3.31×10^{21}
References:	[1] Zombeck (1980) [2] Santolamazza *et al.* (2004)				
	[3] Frontera *et al.* (2001) [4] Perola *et al.* (1999)				

Table 7.2: XSPEC parameters used to model the sources considered in this section in order to calculate MDP. The 2-10 keV flux is given in units of erg/cm^2/s with the normalisation values in units of ph/cm^2/s/keV at 1 keV. For Cyg X-1 the labels H and S refer to the hard and soft states respectively. ([a] pwl refers to the XSPEC function "powerlaw".)

7.8 The polarimeter model

The effective area of the telescope (Figure 7.18) was interpolated onto a regular grid of 0.5 eV-wide energy bins, to match the resolution of the SRS measurements of the dichroic filters. The filter transmission data only cover a narrow ($\sim$ 100s of eV) energy range. Therefore, the broadband transmission of the filter cannot be assessed using experimental data. In order to assess the broadband response of the filters, the measured data were fitted to the National Institute of Standards (NIST) online web calculator (Chantler, 1995). The experimental data were then superimposed on the theoretical transmission, replacing the modeled sections with experimental data where it existed. It should be noted that the NIST model is not sophisticated enough to model the polarisation response and it is implicit in the model is that at energies well away from a absorption edge of interest, the transmission is completely non-dichroic.

Figure 7.19 shows the fractional absorption of the 1-Bromoadamantane/Thiourea inclusion compound over the energy range of interest for the *XEUS* telescope. This is used later to define the broadband response of the instrument, in order to determine whether the cryogenic detectors could resolve spectral absorption features *and* polarisation in a single observation.

The next component of the model is the spectrum of the source under investigation. To generate source spectra, a simple model was taken from the literature for each source and plotted using XSPEC. Figure 7.20 shows the model for the Crab Nebula, taken from Zombeck (1980). The absorption features are explained by Schattenburg & Canizares (1986), the largest effect being due to oxygen absorption in the interstellar medium.

These model components were combined with the *XEUS* response, and a simulated spectrum generated (Figure 7.21). The dichroic region of interest is the Br-K edge at 13.5 keV. Therefore, there is a window for simultaneous spectrometry and polarimetry between $\sim$5 and 30 keV. The limiting factor

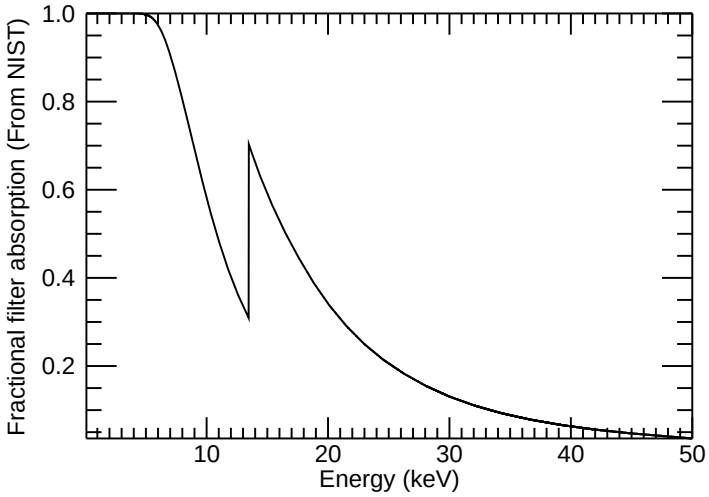

Figure 7.19: Fractional absorption in the filter calculated using the NIST web calculators (Chantler, 1995). The empirical formula for the molecule was used in the calculation and the data fitted to the absorption edge measured at the Daresbury SRS.

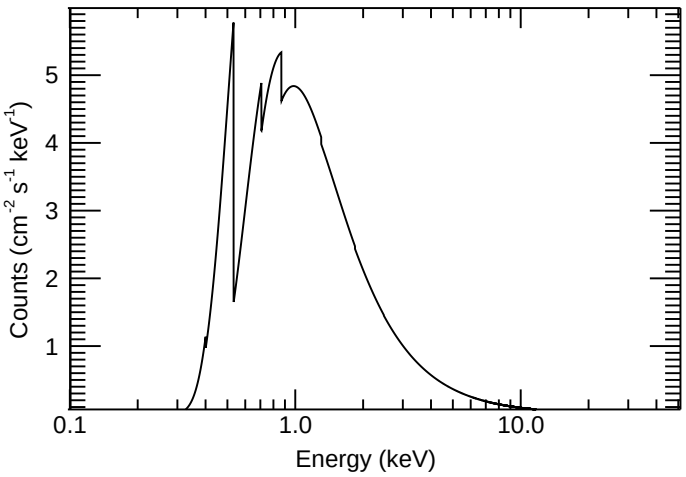

Figure 7.20: Theoretical X-ray spectrum of the crab nebula calculated using the parameters in Table 7.2. The absorption features are explained in Schattenburg & Canizares (1986), where the main feature is oxygen in the interstellar medium. Also present are Nitrogen, Iron, Magnesium and Silicon.

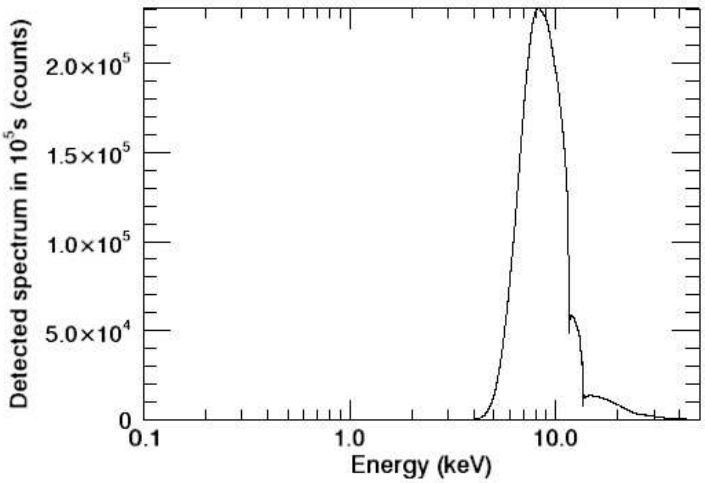

Figure 7.21: The detected spectrum from the Crab nebula assuming the *XEUS* effective area and transmission through a 1-Bromoadamantane/Thiourea inclusion compound filter with transmission given by experiments at the Daresbury SRS. It should be noted that a constant, 100% detector efficiency is assumed over the whole energy range – results should, therefore, be scaled according to detector efficiency.

	Model parameters		MDP (%)				
Line	Energy (keV)	A_{eff} (cm^2)	Crab	Sco X-1	Cyg X-1(H)	Cyg X-1(S)	IC4329A
Br-K	13.5	1800	5.71	3.48	4.62	13.0	70.9
Cu-K	8.9	12500	2.41	1.16	2.22	4.80	36.8

Table 7.3: The performance of a dichroic filter polarimeter based on the *XEUS* telescope parameters and the measured capabilities of bromine and copper based dichroic crystals. The assumed observation time is 10^5 s

will then be the capabilities of the focal plane, where the crogenic detectors are not optimised for such broad band measurements.

7.8.1 Sensitivity predictions

Table 7.3 shows the minimum detectable polarisation of a number of sources assuming that the unoptimised filters tested during this work were flown on the *XEUS* observatory. Values of a few percent are achieved in a 10^5 s observation, demonstrating that although the energy bandwidth

of the effect is small, the polarisation sensitivity remains useful. The goal of future study is to shift the dichroic region of interest to lower energies, where the capabilities of the cryogenic focal plane instruments are more optimised, and the increased effective area of the telescope combined with brighter emission from the source at low energies (c.f. Figure 7.20) promise vastly improved polarimetric response (i.e. a lower MDP). Although it could be argued that Table 7.3 implies that for a source 100 times fainter than the Crab (i.e. 10mCrab) it would take an observation time 100 times longer to achieve the same MDP, this arguments assumes a crab like spectrum and as I have argued in Section 7.7.1, significantly better performance can be achieved than this suggests for harder sources. Description of MDP in terms of Crab units of flux is therefore wholly inappropriated for narrow band dichroic filters and in this context, sources should only be compared in terms of their flux density (counts/cm^2/s/keV) at the dichroic energy of sensitivity.

We can place constraints on the necessary dichroism for a filter to achieve the required 1% MDP in a 10^5 s observation by re-expressing the equation for MDP such that;

$$\mu = \overline{M}\sqrt{T} = \frac{3\sqrt{2}}{MDP \times \sqrt{Spec \times A_{eff} \times \Delta E \times t}}, \tag{7.2}$$

where μ is the figure of merit, $\overline{M}$ the average modulation factor over the energy range ΔE, $Spec$ is the number of counts from the source, A_{eff} is the effective area of the telescope, T is the transmission of the filter and t is the observation time (10^5 s). All parameters are calculated at the edge energy of interest and are assumed to be constant over the range of the EXAFS region (except $\overline{M}$ which is the average over that region of interest).

The calculated values of μ reported in Table 7.4 compare favorably with those measured for the materials studied so far, where for example μ was found to be 0.25 for the 1-Bromoadamantane/Thiourea inclusion compound.

	Model parameters		Constraints on μ to achieve 1% MDP				
Line	Energy (keV)	A_{eff} (cm^2)	Crab	Sco X-1	Cyg X-1(H)	Cyg X-1(S)	IC4329A
I-L	3.9	32400	0.22	0.09	0.26	0.26	3.04
Cl-K	2.8	31800	0.16	0.06	0.22	0.13	2.17
Br-L	1.6	55400	0.07	0.03	0.13	0.05	1.08
Cu-L	0.9	54900	0.06	0.04	0.18	0.06	0.98

Table 7.4: Constraints on the dichroism of filters at lower energy absorption edges necessary to demonstrate 1% MDP in a 10^5 s observation with *XEUS* for each of the astrophysical objects studied. These calculations assume an energy bandwidth of 2 eV can be achieved at each edge. The parameter μ is as described above and is calculated for an average modulation factor over the 2 eV energy range of interest.

7.9 Comparison and complementarity of MPPs and Dichroic filters

In this chapter I have argued the case for Dichroic filters to form part of the *XEUS* mission payload. It must be recognised that a highly capable polarimeter has already been proposed for this mission (the micropatern photoelectric polarimeter) and hence the case for a new technology must be compelling. The data presented here form part of the first ever study of dichroic transmission filters for use in X-ray astronomy and therefore should not be expected to be at the same technology readiness level as the competing technique. However, I have shown that the Dichroic filters have the capability to perform polarimetry at the few percent level.

To predict what impact this kind of polarimeter could have with advances in filter design, it is necessary to assess what properties of the observatory lead to improved MDP. Looking at Equation 6.10 it is clear that increasing the count rate from the source leads to lower MDP and therefore if dichroic absorption edges can be found at lower energies, improved polarisation response can be expected because of the higher effective area of the mirrors and the increased emission from sources at lower energies. Table 7.5 is included by means of a direct comparrison with the MPP assuming dichroic filters with lower energy response can be demonstrated to have similar performance to iodine doped

	Energy		Minimum detectable polarisation (%)				
Line	**keV**	A_{eff} **(cm^2)**	**Crab**	**3C273**	**NGC 4151**	**IC 4329A**	**NGC 5548**
Br(K)	13.5	6000	3.47	37.64	31.78	43.40	70.23
I(L3)	4.6	22000	0.49	7.52	9.31	6.70	11.81
Cl(K)	2.8	30000	0.25	4.32	24.52	3.50	6.25
Br(L3)	1.6	92000	0.09	1.67	-	1.30	2.21
F(K)	0.7	92000	0.07	0.97	-	1.23	1.10
Cl(L3)	0.2	117000	-	0.66	-	-	0.40
MPP[1]	2-10		-	0.9	0.7	0.7	0.8

Table 7.5: The minimum detectable polarisation (MDP) for a range of astronomical X-ray sources in a 10^5 second exposure with XEUS, for an MPP device in the 2-10 keV energy band ([1]data from Table 1 in Costa *et al.*, 2003) and a dichroic filter system based on simulations using data from Collins (1997), Collins *et al.* (2001). The effective area of XEUS at each energy (based on Lumb, 2003) assumed for this work is also provided (It should be noted that this effective area is the XEUS area as of 2003 in order to allow direct comparrison with the MPP instrument). Dichroic filter predictions assume a filter transmission of 30% as reported by Collins, and adopt modulation factors obtained with H-sheet for the currently unmeasured edges (since the structure and chemical composition of H-sheet is not optimised for use as an X-ray dichroic, this is a conservative assumption). These data were reported in Bannister *et al.* (2006) and assume that the dichroic filter is operated with the TES detector currently under consideration for the mission. Note that the poor performance of dichroic filters for the Seyfert galaxy NGC4151 is due to the relatively large neutral hydrogen column density to that object.

H-sheet as demonstrated by Collins (1997).

Table 7.5 demonstrates that the broad energy bandwidth of the MPP instrument makes it a very sensitive polarimeter as it can measure polarisation of photons over the whole energy band. However, at low energies, the dichroic filters appear to perform well, showing rather similar performance despite the 10 eV bandwith of dichroic sensitivity. The dichroic fileters offer a number of advantages, thier self normalisation - enabled by the known bandwidth of the effect, low mass and need for no aditional focal plane area mean that they would be a rather simple device which could be introduced into the light path as needed. An area where dichroic filters are complementary to the MPP is that the photoelectric polarimeter is only sensitive in the energy range ∼2-10 keV, meaning that if extra

diagnostics are needed, a discrete energy polarisation measurement above or below this range could be very useful in analysing astrophysical data.

7.10 Conclusions

Dichroic filters offer a means of constructing a compact, low mass polariser for X-ray radiation. The work reported herein shows that chemical and crystallographic design strategies can be employed to produce efficient polarisers, where the apparent shift in the position of an absorption edge arises because of a polarisation-dependent EXAFS peak which overlaps the edge. A marked change in transmission as a function of the azimuthal orientation of the filter with respect to the polarisation axis of the incident X-rays is observed for such materials. Experimental results and theoretical calculations show that the filters produced to date are not optimised for an astronomical application. This is because of the lack of a large, uniform, plate like crystal and the experimental limitations imposed by the beamline, which did not allow us to test materials with absorption edges in the range $1 - 5$ keV where the main interest lies in the astronomical context.

The lack of a large crystal with which to construct a flight-like filter is unsurprising as it was not one of the goals of the initial study. This work serves as a proof of concept for the technique and has shown that a dichroic filter polarimeter will be feasible with the arrival of the next generation of astrophysical observatories such as *XEUS* and *Constellation-X*. Characterisation of existing filters, and modeling of the behaviour of new dichroic crystal designs has shown the tradeoffs which are necessary to optimise the response of the instrument. This work has also placed constraints on the performance required of future filters in order to meet the goal of 1% MDP in a 10^5 s observation with *XEUS*.

In order to measure the polarisation in a number of sources to better than 1% MDP, the filters must have highly optimised thickness and modulation characteristics. The figure of merit μ must be greater

than 20-30% at a relatively low energy ($\sim$ 1-5 keV) absorption edge in order to meet this goal.

7.11 Summary

Despite the recent and proposed improvements in other areas of instrumentation, astronomical X-ray polarimetry remains in its infancy, despite the first measurement of polarisation in an X-ray source being made over 35 years ago. Costa *et al.* (2001), Bellazzini *et al.* (2003) and Jahoda *et al.* (2007) propose an number of possible polarimeter designs for future X-ray astrophysical observatories. Here I have described a compact and simple, low mass, low power device which could add a polarimetry capability to the high resolution focal plane instruments proposed for these observatories. This concept was first reported in the literature by Bannister *et al.* (2006) and further information is available in Martindale *et al.* (2007a).

Chapter 8

Conclusions

Because of the broad nature of this thesis I will split the conclusions into their three areas. Discussion of each area will begin with an overview of the work undertaken, the reasons for it and end with the outcomes and conclusions.

8.1 Thesis overview

Chapter 1 provided and outline to the subject and scientific and technological areas of astrophysical X-ray instrumentation to which the work in subsequent chapters relates. It began by introducing X-ray astronomy, the mechanisms of X-ray production in an astrophysical context, current and future instruments used to investigate this emission, concluding with discussion of a particular example of such measurements – X-ray polarimetry

8.1.1 Small pore MCP detectors

Chapters 2 and 3 concern the characterisation of new, extremely small pore microchannel plates and the advantages of using MCPs with these smaller pore sizes. First, the context is set by reviewing the use of MCPs as X-ray detectors, they are compared with competing technologies such as CCDs and TESs, where their unmatched ability to provide photon counting operation at high spatial and temporal resloution is used to demonstrated that they still have a niche in the detector parameter space. The progressive reduction in channel size by the manufacturers has resulted in plates with theoretical spatial resolution governed by the MCP pore diameter (3.2 μm for plates tested herein) and temporal resolution of a few 10s of pico seconds.

Experimental results presented here show that the new plates can be operated safely for prolonged periods in hard saturation. The reduction in background noise expected because of the reduced amount of glass (and hence radioisotopes) in the MCPs has not been demonstrated. However, this is thought to be because of increased radioactivity in ceramic components of the detector body as evidenced by a peaked noise pulse height distribution. The limiting temporal resolution measured for these plates was less than 150 ps which is expected to reduce further when a more optimised readout and electronics chain is used.

Despite the astronomical bias of this thesis, the predominant area of exploitation investigated for these MCP detectors was in a terrestrial context, where the extremely high temporal resolution of these devices is to be used to improve detection techniques for the life sciences. The high temporal resolution allows investigation of processes occurring within a living cell and could potentially open up an entirely new area of biological research. The most promising area where these small pore MCPs could be used in an astronomical context is UV and EUV spectroscopy. Here, for a dispersive spectrometer, the high spatial resolution leads to high energy resolution, so long as the efficiency of

the device is high enough to exceed the limitations of photon statistics and the readout technology is capable of matching the improved resolution of the MCP.

8.1.2 MCP optics

Chapters 4 and 5 concern the use of MCPs as X-ray optics. The relevant optic geometries are reviewed along with the state of the art in MCP optic technology before the work reported herein. A terrestrial and two space based applications of these optics are described; an imaging X-ray spectrometer used to measure the elemental compositions of engineering or geological samples. The first space mission which will employ MCP optics technology will be *BepiColombo*, an ESA mission to the planet Mercury. The X-ray telescope will map the elemental composition of the surface in order to determine its mineralogical composition. Second is the *WFT* instrument on *spectrum-RG*, a wide field of view telescope that will cover the whole X-ray sky every 90 minute orbit, allowing the most comprehensive study of X-ray variability to date over the whole sky.

The latest samples of MCP optic material in both the square pore, square pack and radial pack geometries were tested (Chapter 5) and have been shown to be approaching the performance specifications of the missions towards which they are targeted. Indeed, the cartesian packed material is shown to have a limiting resolution of better than 2 arcminutes. This exceeds the performance specifications of *WFT* which needs only 4 arcminutes FWHM in order to meet the requirement of 2 arcminute source position centroiding accuracy on the sky. The radial packed material is shown to have a limiting resolution of better than 8 arcminutes. However, all of the measurements of slumped MCPs reported have been identified to be upper limits because of problems with the detector electronics in the long beamline test facility. It is expected that in the very near future, significantly improved measurements will allow better understanding of the optics and help in the drive towards the first flight of this new optic technology.

8.1.3 X-ray polarimetry

X-ray polarimetry is identified as an area which holds huge promise for the understanding of celestial X-ray sources. Despite this, no progress as been made in X-ray astrophysical polarimetry for over 30 years. This is explained primarily by the lack of suitable instrumentation to exploit it. Chapter 7 describes experiments and design work to produce simple, low mass filters which are sensitive to X-ray polarisation. It shows that the X-ray absorption near edge structure (XANES) in certain, highly ordered materials exhibits a polarisation dependency. Therefore, such materials can be used as simple transmission filters which, if rotated about the optical axis of a telescope, could act as a polarisation analyser. Three materials are identified which exhibit this effect and intensive research is ongoing to push the sensitivity of the filters to lower energies in the astrophysically most significant region of 1-10 keV. The sensitivity of a polarimeter, based on the existing filters, is calculated in terms of a 10^5 s observation with XEUS for a number of objects. This is shown to compare favorably with competing technologies.

The aim of this work is to produce a compact, low mass filter system which could add a polarimetry capability to the next generation of astrophysical observatories for minimal instrument mass and no added complexity to the focal plane. A preliminary engineering sketch of what such a system could look like is shown in Chapter 7.

8.2 Closing remarks

The unifying themes of this thesis are the production and application of space deployable hardware to take scientifically important measurements. MCP detectors have been used extensively in astronomy and the useful application in a space telescope is now questionable, except in certain specialised niches. However, this mature technology is now ripe for exploitation in other scientific fields which

will benefit from the three decades of development work already undertaken to produce a useful detector for astronomy.

Comparing these detectors to MCP optics, it is clear that this new application of microchannel plates is at the beginning of its operational life. The huge effective area per unit mass they offer will open a new window for exploitation of X-ray telescopes in unexplored areas. This is embodied by the *BepiColombo* mission to the planet Mercury which will carry the first ever imaging X-ray telescope for planetary science application. The technology readiness of MCP optics is shown herein to be approaching the acceptance criteria for a flight device and it is highly likely that one will be operational within the next decade.

Finally, dichroic filters for X-ray polarimetry are extremely new. The work reported herein forms part of the first ever investigation of these devices and shows great promise. Much development work is needed to get the devices to a stage where they are ready for application in space. However, the relative simplicity of the technique is in its favour and the maturation towards technology readiness should fit in well with the next gerneration of great astrophysical observatory (XEUS and Con-X) which are scheduled for launch in the timeframe 2015-2025.

Bibliography

Adler, I. & Trombka, J. I. *Physics and Chemistry of Earth*, **10**, 17–43, 1977.

Ambrosi, R. M., Abbey, A. F., Hutchinson, I. B., Willingale, R., Wells, A., Short, A. D. T., Campana, S., Citterio, O., Tagliaferri, G., Burkert, W. & Brauninger, H. *Nuclear Instruments and Methods in Physics Research A*, **488**, 543–554, August 2002.

Angel, J. R. P. *Ap.J.*, **233**, 364–373, October 1979.

Aschenbach, B. *Reports of Progress in Physics*, **48**, 579–629, May 1985.

Auton, J. P. *Applied optics*, **6**, 1023–+, June 1967.

Bannister, N. P., Bunce, E. J., Cowley, S. W. H., Fairbend, R., Fraser, G. W., Hamilton, F. J., Lapington, J. S., Lees, J. E., Lester, M., Milan, S. E., Pearson, J. F., Price, G. J. & Willingale, R. *Annales Geophysicae*, **25**, 519–532, March 2007.

Bannister, N. P. & Fraser, G. W. lobster-ISS science case. http://www.bo.iasf.cnr.it/ResDev/Lobster/lob-lux-ms-008-7.pdf, 2003.

Bannister, N. P., Harris, K. D. M., Collins, S. P., Martindale, A., Monks, P. S., Solan, G. & Fraser, G. W. *Experimental Astronomy*, pages 27–+, September 2006.

Bannister, N. P., Lapington, J. S., Barstow, M. A., Fraser, G. W., Sanderson, B. S., Tandy, J. A., Pearson, J. F. & Spragg, J. E. High-resolution imaging microchannel plate detector for EUV

spectrometry. In Flanagan, K. A. & Siegmund, O. H., editors, *Proc. SPIE Vol. 4140, p. 199-210, X-Ray and Gamma-Ray Instrumentation for Astronomy XI, Kathryn A. Flanagan; Oswald H. Siegmund; Eds.*, pages 199–210, December 2000.

Barstow, M. A., Binette, L., Brosch, N., Cheng, F. Z., Dennefeld, M., Gomez de Castro, A. I., Haubold, H., van der Hucht, K. A., Kappelmann, N., Martinez, P., Moisheev, A., Pagano, I., Ribak, E. N., Sahade, J., Shustov, B. I., Solheim, J.-E., Wamsteker, W., Werner, K., Becker-Ross, H. & Florek, S. The WSO: a world-class observatory for the ultraviolet. In Blades, J. C. & Siegmund, O. H. W., editors, *Future EUV/UV and Visible Space Astrophysics Missions and Instrumentation. Edited by J. Chris Blades, Oswald H. W. Siegmund. Proceedings of the SPIE, Volume 4854, pp. 364-374 (2003).*, volume 4854 of *Presented at the Society of Photo-Optical Instrumentation Engineers (SPIE) Conference*, pages 364–374, February 2003.

Barstow, M. A., Fraser, G. W. & Milward, S. W. *Proc. SPIE*, **597**, 352, 1985a.

Barstow, M. A., Willingale, R., Kent, B. J. & Wells, A. *Optica Acta*, **32**, 197, 1985b.

Bautz, M. W., Pivovaroff, M. J., Kissel, S. E., Prigozhin, G. Y., Isobe, T., Jones, S. E., Ricker, G. R., Thornagel, R., Kraft, S., Scholze, F. & Ulm, G. Absolute calibration of ACIS x-ray CCDs using calculable undispersed synchrotron radiation. In Truemper, J. E. & Aschenbach, B., editors, *Proc. SPIE Vol. 4012, p. 53-67, X-Ray Optics, Instruments, and Missions III, Joachim E. Truemper; Bernd Aschenbach; Eds.*, volume 4012 of *Presented at the Society of Photo-Optical Instrumentation Engineers (SPIE) Conference*, pages 53–67, July 2000.

Bavdaz, M., Lumb, D., Gondoin, P., Lyngvi, A., Rando, N., Peacock, T., van der Laan, T., Wallace, K., Mieremet, A., Oemrawsingh, S., Beijersbergen, M., Collon, M., Kraft, S., Graue, R., Kampf, D. & Freyberg, M. The XEUS x-ray telescope. In Turner, M. J. L. & Hasinger, G., editors, *Space Telescopes and Instrumentation II: Ultraviolet to Gamma Ray. Edited by Turner, Martin J. L.; Hasinger, Günther. Proceedings of the SPIE, Volume 6266, pp. 62661S (2006).*, volume 6266

of *Presented at the Society of Photo-Optical Instrumentation Engineers (SPIE) Conference*, July 2006.

Bellazzini, R., Baldini, L., Bitti, F., Brez, A., Cavalca, F., Latronico, L., Massai, M. M., Omodei, N., Pinchera, M., Sgró, C., Spandre, G., Costa, E., Soffitta, P., Di Persio, G., Feroci, M., Muleri, F., Pacciani, L., Rubini, A., Morelli, E., Matt, G. & Perola, G. C. A photoelectric polarimeter for XEUS: a new window in x-ray sky. In Turner, M. J. L. & Hasinger, G., editors, *Space Telescopes and Instrumentation II: Ultraviolet to Gamma Ray. Edited by Turner, Martin J. L.; Hasinger, Günther. Proceedings of the SPIE, Volume 6266, pp. 62663Z (2006).*, July 2006.

Bellazzini, R., Baldini, L., Brez, A., Costa, E., Latronico, L., Omodei, N., Soffitta, P. & Spandre, G. *Nuclear Instruments and Methods in Physics Research A*, **510**, 176–184, September 2003.

Black, J. K., Brunton, A. N., Bannister, N. P., Deines-Jones, P. & Jahoda, K. *Nuclear Instruments and Methods in Physics Research A*, **513**, 123–126, November 2003.

Blandford, R., Agol, E., Broderick, A., Heyl, J., Koopmans, L. & Lee, H.-W. Compact objects and accretion disks. In Trujillo-Bueno, J., Moreno-Insertis, F. & Sánchez, F., editors, *Astrophysical Spectropolarimetry*, pages 177–223, 2002.

Braga, J., Rothschild, R., Heise, J., Staubert, R., Remillard, R., D'Amico, F., Jablonski, F., Heindl, W., Matteson, J., Kuulkers, E., Wilms, J. & Kendziorra, E. *Advances in Space Research*, **34**, 2657–2661, 2004.

Brown, C. & Yates, H. Summary of images taken using the ME001-8 Micropore Optic Optimisation of Resolution Measurements. Private communication, 2006.

Brunton, A. N., Fraser, G. W., Lees, J. E., Feller, W. B. & White, P. L. X-ray focusing with 11-um square-pore microchannel plates. In Hoover, R. B. & Williams, M. B., editors, *Proc. SPIE*

Vol. 2519, p. 40-49, X-Ray and Ultraviolet Sensors and Applications, Richard B. Hoover; Mark B. Williams; Eds., pages 40–49, June 1995.

Brunton, A. N., Fraser, G. W., Lees, J. E. & Turcu, I. C. E. *Applied optics*, **36**, 5461–5470, August 1997.

Carpenter, J. D. *Microchannel plates in astronomy and planetary science*. PhD thesis, University of Leicester, 2006.

Champouret, Y. Private Communication, 2007.

Chantler, C. T. *Journal of Physical and Chemical Reference Data*, **24**, 71–643, January 1995.

Chao, M. H., Benson, M. K., Harris, K. D. M., Collins, S. P. & Laundy, D. *Angewandte Chemie International Edition*, **42**, 2982–2985, 2003.

Chapman, H. N., Nugent, K. A. & Wilkins, S. W. *Review of Scientific Instruments*, **62**, 1542–1561, June 1991.

Chapman, H. N., Nugent, K. A. & Wilkins, S. W. *Applied Optics*, **32**, 6316–6332, November 1993a.

Chapman, H. N., Rode, A., Nugent, K. A. & Wilkins, S. W. *Applied Optica*, **32**, 6333–6340, November 1993b.

Collins, S. P. *Nuclear Instruments and Methods in Physics Research Section B: Beam Interactions with Materials and Atoms*, **129**, 289–296, July 1997.

Collins, S. P., Cernik, R. J., Fell, B., Tang, C. C., Harris, N. W., Miller, M. C. & Oszlanyi, G. *Journal of Synchrotron Radiation*, **5**(5), 1263–1269, Sep 1998.

Collins, S. P., Laundy, D., Brown, S. D. & Thompson, P. *Nuclear Instruments and Methods in Physics Research A*, **467**, 1034–1036, July 2001.

Collins, S. P., Laundy, D., Harris, K. D. M., Kariuki, B. M., Bauer, C. L., Brown, S. D. & Thompson, P. *Journal of Physics: Condensed Matter*, **14**(1), 123–134, 2002.

Collon, M. J., Günther, R., Kraft, S., Beijersbergen, M. W., Bavdaz, M., Wallace, K., Krumrey, M. & Freyberg, M. Silicon pore optics for astrophysical x-ray missions. In *Optics for EUV, X-Ray, and Gamma-Ray Astronomy III. Edited by O'Dell, Stephen L.; Pareschi, Giovanni. Proceedings of the SPIE, Volume 6688, pp. 668813 (2007).*, volume 6688 of *Presented at the Society of Photo-Optical Instrumentation Engineers (SPIE) Conference*, September 2007.

Connors, P. A., Stark, R. F. & Piran, T. *The Astrophysical Journal*, **235**, 224–244, January 1980.

Costa, E., Bellazzini, R., Soffitta, P., Muleri, F., Feroci, M., Frutti, M., Mastropietro, M., Pacciani, L., Rubini, A., Morelli, E., Baldini, L., Bitti, F., Brez, A., Cavalca, F., Latronico, L., Massai, M. M., Omodei, N., Pinchera, M., Sgró, C., Spandre, G., Matt, G., Perola, G. C., Chincarini, G., Citterio, O., Tagliaferri, G., Pareschi, G. & Cotroneo, V. POLARIX: a small mission of x-ray polarimetry. In Turner, M. J. L. & Hasinger, G., editors, *Space Telescopes and Instrumentation II: Ultraviolet to Gamma Ray. Edited by Turner, Martin J. L.; Hasinger, Günther. Proceedings of the SPIE, Volume 6266, pp. 62660R (2006).*, July 2006.

Costa, E., Bellazzini, R., Tagliaferri, G., Baldini, L., Basso, S., Bregeon, J., Brez, A., Citterio, O., Cotroneo, V., Frontera, F., Frutti, M., Matt, G., Minuti, M., Muleri, F., Pareschi, G., Cesare Perola, G., Rubini, A., Sgro', C., Soffitta, P. & Spandre, G. *ArXiv e-prints*, **709**, September 2007.

Costa, E., Soffitta, P., Bellazzini, R., Brez, A., Lumb, N. & Spandre, G. *Nature*, **411**, 662–665, June 2001.

Costa, E., Soffitta, P., di Persio, G., Feroci, M., Pacciani, L., Rubini, A., Bellazzini, R., Brez, A., Baldini, L., Latronico, L., Omodei, N. & Spandre, G. X-ray Astronomical Polarimetry in the XEUS Era. In Hasinger, G., Boller, T. & Parmer, A. N., editors, *XEUS - studying the evolution of the hot universe*, pages 235–+, 2003.

Cruddace, R. G., Kowalski, M. P., Yentis, D., Brown, C. M., Gursky, H., Barstow, M. A., Bannister, N. P., Fraser, G. W., Spragg, J. E., Lapington, J. S., Tandy, J. A., Sanderson, B., Culhane, J. L., Barbee, T. W., Kordas, J. F., Goldstein, W. & Fritz, G. G. *The Astrophysical Journal*, **565**, L47–L50, January 2002.

Dieters, S. W., Vaughan, B. A., Kuulkers, E., Lamb, F. K. & van der Klis, M. *Astronomy and Astrophysics*, **353**, 203–210, January 2000.

Dolan, J. F. *Space Science Reviews*, **6**, 579–+, 1967.

Fraser, G. W. *X-ray detectors in astronomy.* Cambridge and New York, Cambridge University Press, 1989, 312 p., 1989.

Fraser, G. W. *Nuclear Instruments and Methods in Physics Research A*, **291**, 595–606, June 1990.

Fraser, G. W., Brunton, A. N., Bannister, N. P., Pearson, J. F., Ward, M., Stevenson, T. J., Watson, D. J., Warwick, B., Whitehead, S., O'Brian, P., White, N., Jahoda, K., Black, K., Hunter, S. D., Deines-Jones, P., Priedhorsky, W. C., Brumby, S. P., Borozdin, K. N., Vestrand, T., Fabian, A. C., Nugent, K. A., Peele, A. G., Irving, T. H., , S., Eckersley, S., Renouf, I., Smith, M., Parmar, A. N., McHardy, I. M., Uttley, P. & Lawrence, A. LOBSTER-ISS: an imaging x-ray all-sky monitor for the International Space Station. In Flanagan, K. A. & Siegmund, O. H., editors, *Proc. SPIE Vol. 4497, p. 115-126, X-Ray and Gamma-Ray Instrumentation for Astronomy XII, Kathryn A. Flanagan; Oswald H. Siegmund; Eds.*, pages 115–126, January 2002.

Fraser, G. W., Brunton, A. N., Lees, J. E., Pearson, J. F. & Feller, W. B. *Nuclear Instruments and Methods in Physics Research A*, **324**, 404–407, January 1993.

Fraser, G. W., Lees, J. E., Pearson, J. F. & Barstow, M. A. *Nuclear Instruments and Methods in Physics Research A*, **310**, 292–298, December 1991a.

Fraser, G. W. & Mathieson, E. *Nuclear Instruments and Methods in Physics Research A*, **179**, 591–604, August 1981.

Fraser, G. W., Pain, M. T., Lees, J. E. & Pearson, J. F. *Nuclear Instruments and Methods in Physics Research A*, **306**, 247–260, August 1991b.

Fraser, G. W., Pearson, J. F. & Lees, J. E. *Nuclear Instruments and Methods in Physics Research A*, **254**, 447–462, February 1987.

Fraser, G. W., Pearson, J. F., Lees, J. E. & Feller, W. B. Advances in microchannel plate detectors. In Golub, L., editor, *X-ray instrumentation in astronomy II; Proceedings of the Meeting, San Diego, CA, Aug. 15-17, 1988 (A89-40276 17-35). Bellingham, WA, Society of Photo-Optical Instrumentation Engineers, 1988, p. 98-107. Research supported by the British National Space Centre.*, pages 98–107, 1988.

Friedman, H., Lichtman, S. W. & Byram, E. T. *Physical Review*, **83**, 1025–1030, September 1951.

Frontera, F., Palazzi, E., Zdziarski, A. A., Haardt, F., Perola, G. C., Chiappetti, L., Cusumano, G., Dal Fiume, D., Del Sordo, S., Orlandini, M., Parmar, A. N., Piro, L., Santangelo, A., Segreto, A., Treves, A. & Trifoglio, M. *The Astrophysical Journal*, **546**, 1027–1037, January 2001.

Garcia, M. R., Chappell, J. H., Murray, S. S., Feller, W. B. & Fraser, G. W. Low noise microchannel plate detectors for x-ray astronomy. In Benattar, R., editor, *Proc. SPIE Vol. 1140, p. 101-0, X-Ray Instrumentation in Medicine and Biology, Plasma Physics, Astrophysics, and Synchrotron Radiation, Rene Benattar; Ed.*, pages 101–0, October 1989.

Gehrels, N. & Swift. The Swift Gamma-Ray Burst Mission. In *Bulletin of the American Astronomical Society*, volume 36 of *Bulletin of the American Astronomical Society*, pages 1543–+, December 2004.

Giacconi, R. *Scientific American*, **242**, 80–85, February 1980.

Giacconi, R., Gursky, H., Paolini, F. R. & Rossi, B. B. *Physical Review Letters*, **9**, 439–443, December 1962.

Giacconi, R., Reidy, W. P., Vaiana, G. S., van Speybroeck, L. P. & Zehnpfennig, T. F. *Space Science Reviews*, **9**, 3–+, 1969.

Gómez de Castro, A. I., Lecavelier des Étangs, A. & Reimers, D. Fundamental problems in modern astrophysics requiring access to the ultraviolet range. In Turner, M. J. L. & Hasinger, G., editors, *Space Telescopes and Instrumentation II: Ultraviolet to Gamma Ray. Edited by Turner, Martin J. L.; Hasinger, Günther. Proceedings of the SPIE, Volume 6266, pp. 626608 (2006).*, volume 6266 of *Presented at the Society of Photo-Optical Instrumentation Engineers (SPIE) Conference*, July 2006.

Gowen, R. A., Cooke, B. A., Griffiths, R. E. & Ricketts, M. J. *Monthly notices of the Royal Astronomical Society*, **179**, 303–310, May 1977.

Griffiths, R. E., Cooke, B. A., Peacock, A., Pounds, K. A. & Ricketts, M. J. *MNRAS*, **175**, 449–460, June 1976.

Hamilton, F. J. *A Novel Approach to Ultraviolet Auroral Imaging using Microchannel Plate Technology.* PhD thesis, University of Leicester, 2005.

Harris, K. D. M. Private communication, 2007.

Harrison, F. A., Boggs, S. E., Bolotnikov, A. E., Christensen, F. E., Cook, W. R., Craig, W. W., Hailey, C. J., Jimenez-Garate, M. A., Mao, P. H., Schindler, S. M. & Windt, D. L. Development of the High-Energy Focusing Telescope (HEFT) balloon experiment. In Truemper, J. E. & Aschenbach, B., editors, *Proc. SPIE Vol. 4012, p. 693-699, X-Ray Optics, Instruments, and Missions III, Joachim E. Truemper; Bernd Aschenbach; Eds.*, volume 4012 of *Presented at the Society of Photo-Optical Instrumentation Engineers (SPIE) Conference*, pages 693–699, July 2000.

Hecht, E. *Optics 2nd edition.* Optics 2nd edition by Eugene Hecht Reading, MA: Addison-Wesley Publishing Company, 1987, 1987.

Holland, A. D., Short, A. D. T., Fraser, G. W. & Turner, M. J. L. *Nuclear Instruments and Methods in Physics Research A*, **355**, 526–531, February 1995.

Jahoda, K., Black, K., Deines-Jones, P., Hill, J. E., Kallman, T., Strohmayer, T. & Swank, J. H. *ArXiv Astrophysics e-prints*, January 2007.

Janesick, J. R. *Scientific charge-coupled devices.* Scientific charge-coupled devices, Bellingham, WA: SPIE Optical Engineering Press, 2001, xvi, 906 p. SPIE Press monograph, PM 83. ISBN 0819436984, 2001.

Janson, F. & Murdin, P. *Encyclopedia of Astronomy and Astrophysics*, July 2002.

Kallman, T. *Advances in Space Research*, **34**, 2673–2677, 2004.

Kilbourne, C. Private communication, 2007.

Kirkpatrick, P. & Baez, A. V. *Journal of the Optical Society of America (1917-1983)*, **38**, 766–+, September 1948.

Kitchin, C. R. *Astrophysical techniques.* Bristol, England, Adam Hilger, Ltd., 1984, 451 p., 1984.

Laor, A., Netzer, H. & Piran, T. *Monthly notices of the royal astronomical society*, **242**, 560–569, February 1990.

Lapington, J. S. *Nuclear Instruments and Methods in Physics Research A*, **525**, 361–365, June 2004.

Lapington, J. S., Howorth, J. R. & Milnes, J. S. *Nuclear Instruments and Methods in Physics Research A*, **573**, 243–246, April 2007.

Laprade, B. & Starcher, R. The 2 micron pore microchannel plate. Development of the world's fastest detector, 2001. Burle Electro-Optics, inc. Sturbridge, MA.

Laprade, B. N. & Reinhart, S. T. Recent advances in small pore microchannel plate technology. In Csorba, I. P., editor, *Proc. SPIE Vol. 1072, p. 119, Image Intensification, Illes P. Csorba; Ed.*, pages 119–+, April 1989.

Lees, J. E. *An Investigation of Soft X-ray Imaging and Polarimetry.* PhD thesis, University of Leicester, 1989.

Lees, J. E., Bassford, D., Whitford, C. & Blake, O. *Nuclear Instruments and Methods in Physics Research A*, **537**, 621–625, 2005.

Lees, J. E., Fraser, G. W. & Dinsdale, D. *Nuclear Instruments and Methods in Physics Research A*, **392**, 349–353, February 1997.

Lees, J. E. & Pearson, J. F. *Nuclear Instruments and Methods in Physics Research A*, **384**, 410–424, February 1997.

Lemen, J. R., Chanan, G. A., Hughes, J. P., Laser, M. R., Novick, R., Rochwarger, I. T., Sackson, M. & Tramiel, L. J. *Solar Physics*, **80**, 333–+, October 1982.

Li, T. P., Zhang, S. N., Wang, H. Y., Jiang, L. H., Wu, M., Lu, F. J., Wang, J. M., Song, L. M., Wu, B. B. & Chen, Y. HXMT - A Chinese high energy astrophysics mission. In *36th COSPAR Scientific Assembly*, volume 36 of *COSPAR, Plenary Meeting*, pages 2815–+, 2006.

Long, K. S., Chanan, G. A. & Novick, R. *The Astrophysical Journal*, **238**, 710–716, June 1980.

Lumb, D. The XEUS effective area curve, 2003. ESA - ESTEC.

Lumb, D. H., Bavdaz, M., Christensen, F. E., Dariel, A., Hoghoj, P., Jensen, C. P., Krumrey, M., Madsen, K. K., Ziegler, E., Albertin, B., Hedacq, S., Collon, M. & Buis, E.-J. Multi-layer coating development for XEUS. In Turner, M. J. L. & Hasinger, G., editors, *Space Telescopes and Instrumentation II: Ultraviolet to Gamma Ray. Edited by Turner, Martin J. L.; Hasinger, Günther.*

Proceedings of the SPIE, Volume 6266, pp. 626614 (2006)., volume 6266 of *Presented at the Society of Photo-Optical Instrumentation Engineers (SPIE) Conference*, July 2006.

Martin, A. *MCP optics.* PhD thesis, University of Leicester, 2000.

Martin, A. P., Brunton, A. N. & Fraser, G. W. *Nuclear Instruments and Methods in Physics Research A*, **422**, 567–571, February 1999.

Martin, A. P., Brunton, A. N., Fraser, G. W. & Abbey, A. F. *Nuclear Instruments and Methods in Physics Research A*, **460**, 316–325, March 2001.

Martindale, A., Bannister, N. P., Harris, K. D. M., Solan, G. A., Collins, S. P., Champouret, Y., Muppidi, V. K., Fraser, G. W. & Roy, M. Narrow-band x-ray polarizing filters. volume 6686, page 66860X. SPIE, 2007.

Martindale, A., Lapington, J. S. & Fraser, G. W. *Nuclear Instruments and Methods in Physics Research A*, **573**, 111–114, April 2007.

Martindale, A. & Yates, H. BC-MIX-TN-014 - BepiColombo technical note, 2007. University of Leicester.

Meszaros, P., Novick, R., Szentgyorgyi, A., Chanan, G. A. & Weisskopf, M. C. *The Astrophysical Journal*, **324**, 1056–1067, January 1988.

Michette, A. *X-ray Science and Technology.* IOP publishing Ltd., 1993.

Milnes, J. S. & Howorth, J. Picosecond time response characteristics of microchannel plate PMT detectors. In Paisley, D. L., Kleinfelder, S., Snyder, D. R. & Thompson, B. J., editors, *26th International Congress on High-Speed Photography and Photonics. Edited by Paisley, Dennis L.; Kleinfelder, Stuart; Snyder, Donald R.; Thompson, Brian J. Proceedings of the SPIE, Volume 5580, pp. 730-740 (2005).*, pages 730–740, March 2005.

Mitrofanov, A. V. *Nuclear Instruments and Methods in Physics Research A*, **405**, 286–288, February 1998.

Mushotzky, R. F., Serlemitsos, P. J., Boldt, E. A., Holt, S. S. & Smith, B. W. *The Astrophysical Journal*, **225**, 21–39, October 1978.

Novick, R. Stellar and Solar X-Ray Polarimetry. In Gehrels, T., editor, *IAU Colloq. 23: Planets, Stars, and Nebulae: Studied with Photopolarimetry*, pages 262–+, 1974.

Novick, R. Stellar and solar X-ray polarimetry. In *X-Rays in Space - Cosmic, Solar, and Auroral X-Rays, Volume 1*, pages 435–471, 1975.

Novick, R., Weisskopf, M. C., Berthelsdorf, R., Linke, R. & Wolff, R. S. *The Astrophysical Journal*, **174**, L1+, May 1972.

Novick, R., Weisskopf, M. C., Silver, E. H., Kestenbaum, H. L., Long, K. S. & Wolff, R. S. The OSO-8 Mosaic Graphite Stellar X-Ray Polarimeter. In van der Hucht, K. A. & Vaiana, G., editors, *Advances in Space Exploration*, pages 127–+, 1978.

Nussey, J. P. *Terrestrial and Space Based Applications of Microchannel Plate Optics*. PhD thesis, University of Leicester, 2005.

Owens, A., Bavdaz, M., Beijersbergen, M. W., Brunton, A. N., Fraser, G. W., Martin, D., Nieminen, P., Peacock, A. J. & Pia, M. G. HERMES: an imaging x-ray fluorescence spectrometer for the BepiColombo mission to Mercury. In Tichenor, D. A. & Folta, J. A., editors, *Proc. SPIE Vol. 4506, p. 136-145, Soft X-Ray and EUV Imaging Systems II, Daniel A. Tichenor; James A. Folta; Eds.*, pages 136–145, December 2001.

Pagano, I., Rodonò, M. & WSO Implementation Committee, t. *Chinese Journal of Astronomy and Astrophysics Supplement*, **6**, 377–382, December 2006.

Parmar, A. N., Arnaud, M., Barcons, X., Bleeker, J., Hasinger, G., Kunieda, H., Palumbo, G., Takahashi, T., Turner, M., de Korte, P., Willingale, R., Rando, N., Lyngvi, A., Gondoin, P., Lumb, D., Bavdaz, M. & Verhoeve, P. XEUS: The x-ray evolving universe spectroscopy mission. In Turner, M. J. L. & Hasinger, G., editors, *Space Telescopes and Instrumentation II: Ultraviolet to Gamma Ray. Edited by Turner, Martin J. L.; Hasinger, Günther. Proceedings of the SPIE, Volume 6266, pp. 62661R (2006).*, July 2006.

Pavlinsky, M., Hasinger, G., Parmar, A., Fraser, G., Churazov, E., Gilfanov, M., Sunyaev, R., Vikhlinin, A., Predehl, P., Piro, L., Arefiev, V., Tkachenko, A., Pinchuk, V. & Gorobets, D. Spectrum-RG/eROSITA/Lobster astrophysical mission. In Turner, M. J. L. & Hasinger, G., editors, *Space Telescopes and Instrumentation II: Ultraviolet to Gamma Ray. Edited by Turner, Martin J. L.; Hasinger, Günther. Proceedings of the SPIE, Volume 6266, pp. 62660O (2006).*, volume 6266 of *Presented at the Society of Photo-Optical Instrumentation Engineers (SPIE) Conference*, July 2006.

Peacock, A., Andresen, R. D., Manzo, G., Taylor, B. G., Villa, G., Re, S., Ives, J. C. & Kellock, S. *Space Science Reviews*, **30**, 525–534, March 1981.

Peacock, A., Taylor, B. G., White, N., Courvoisier, T. & Manzo, G. *IEEE Transactions on Nuclear Science*, **32**, 108–111, February 1985.

Pearson, J. F. *Advances in microchannel plate detectors.* PhD thesis, University of Leicester, 1984.

Pearson, J. F. & Martindale, A. Tunnel test facility operating manual, 2007. University of Leicester.

Peele, A. G., Nugent, K. A., Rode, A., Gabel, K., Richardson, M. C., Strack, R. & Seigmund, W. *Nuclear Instruments and Methods in Physics Research A*, **35**, 4420, 1996.

Perola, G. C., Matt, G., Cappi, M., Dal Fiume, D., Fiore, F., Guainazzi, M., Mineo, T., Molendi, S., Nicastro, F., Piro, L. & Stirpe, G. *Astronomy and Astrophysics*, **351**, 937–944, November 1999.

Petre, R., Lehan, J., O'Dell, S., Owens, S., Reid, P. B., Saha, T., Stewart, J., Jones, W. D. & Zhang, W. The Constellation-X Spectroscopy X-ray Telescope: recent technology development. In Turner, M. J. L. & Hasinger, G., editors, *Space Telescopes and Instrumentation II: Ultraviolet to Gamma Ray. Edited by Turner, Martin J. L.; Hasinger, Günther. Proceedings of the SPIE, Volume 6266, pp. 62661Q (2006).*, July 2006.

Pounds, K. A., Allan, D. J., Barber, C., Barstow, M. A., Bertram, D., Branduardi-Raymont, G., Brebner, G. E. C., Buckley, D., Bromage, G. E., Cole, R. E., Courtier, M., Cruise, A. M., Culhane, J. L., Denby, M., Donoghue, D. O., Dunford, E., Georgantopoulos, I., Goodall, C. V., Gondhalekar, P. M., Gourlay, J. A., Harris, A. W., Hassall, B. J. M., Hellier, C., Hodgkin, S., Jeffries, R. D., Kellett, B. J., Kent, B. J., Lieu, R., Lloyd, C., McGale, P., Mason, K. O., Matthews, L., Mittaz, J. P. D., Page, C. G., Pankiewicz, G. S., Pike, C. D., Ponman, T. J., Puchnarewicz, E. M., Pye, J. P., Quenby, J. J., Ricketts, M. J., Rosen, S. R., Sansom, A. E., Sembay, S., Sidher, S., Sims, M. R., Stewart, B. C., Sumner, T. J., Vallance, R. J., Watson, M. G., Warwick, R. S., Wells, A. A., Willingale, R., Willmore, A. P., Willoughby, G. A. & Wonnacott, D. *Monthly Notices of the Royal Astronomical Society*, **260**, 77–102, January 1993.

Price, G. J. *Microchannel Plates in Astronomy.* PhD thesis, University of Leicester, 2001.

Price, G. J., Brunton, A. N., Beijersbergen, M. W., Fraser, G. W., Bavdaz, M., Boutot, J.-P., Fairbend, R., Flyckt, S.-O., Peacock, A. & Tomaselli, E. *Nuclear Instruments and Methods in Physics Research A*, **490**, 276–289, September 2002a.

Price, G. J., Brunton, A. N., Fraser, G. W., Bavdaz, M., Beijersbergen, M. W., Boutot, J.-P., Fairbend, R., Flyckt, S.-O., Peacock, A. & Tomaselli, E. *Nuclear Instruments and Methods in Physics Research A*, **490**, 290–298, September 2002b.

Price, G. J., Fraser, G. W., Pearson, J. F., Nussey, J. P., Hutchinson, I. B., Holland, A. D., Turner, K. & Pullan, D. *Review of Scientific Instruments*, **75**, 2314–2319, July 2004.

Priedhorsky, W. C., Peele, A. G. & Nugent, K. A. *Monthly Notices of the Royal Astronomical Society*, **279**, 733–750, April 1996.

Saab, T., Apodacas, E., Bandler, S. R., Boyce, K., Chervenak, J., Figueroa-Feliciano, E., Finkbeiner, F., Hammock, C., Kelley, R., Lindeman, M., Porter, F. S. & Stahle, C. K. *Nuclear Instruments and Methods in Physics Research A*, **520**, 281–284, March 2004.

Santolamazza, P., Fiore, F., Burderi, L. & di Salvo, T. *Nuclear Physics B Proceedings Supplements*, **132**, 644–647, June 2004.

Schattenburg, M. L. & Canizares, C. R. *The Astrophysical Journal*, **301**, 759–771, February 1986.

Short, A. D. Gaia Astrometric CCDs and Focal Plane. In Turon, C., O'Flaherty, K. S. & Perryman, M. A. C., editors, *ESA SP-576: The Three-Dimensional Universe with Gaia*, pages 343–+, January 2005.

Siegmund, O. H. W., Marsh, D., Stock, J. & Gaines, G. Characteristics of square pore and low noise microchannel plate stacks. In Siegmund, O. H. W., editor, *EUV, X-ray, and gamma-ray instrumentation for astronomy III; Proceedings of the Meeting, San Diego, CA, July 22-24, 1992 (A93-29476 10-35), p. 274-282.*, pages 274–282, October 1992.

Silver, E. H., Weisskopf, M. C., Kestenbaum, H. L., Long, K. S., Novick, R. & Wolff, R. S. *The Astrophysical Journal*, **232**, 248–254, August 1979.

Smith, A., Peacock, A. & Kowalski, T. Z. *IEEE Transactions on Nuclear Science*, **34**, 57–61, February 1987.

Smith, B. W., Mushotzky, R. F. & Serlemitsos, P. J. *The Astrophysical Journal*, **227**, 37–51, January 1979.

Soffitta, P., Baldini, L., Bellazzini, R., Brez, A., Costa, E., di Persio, G., Latronico, L., Omodei, N.,

Pacciani, L. & Spandre, G. *Nuclear Instruments and Methods in Physics Research A*, **510**, 170–175, September 2003.

Soltau, H., Holl, P., Kemmer, J., Krisch, S., Zanthier, C. V., Hauff, D., Richter, R., Bräuninger, H., Hartmann, R., Hartner, G., Krause, N., Meidinger, N., Pfeffermann, E., Reppin, C., Schwaab, G., Strüder, L., Trümper, J., Kendziorra, E. & Krämer, J. *Nuclear Instruments and Methods in Physics Research A*, **377**, 340–345, February 1996.

Stark, R. F. & Connors, P. A. *Nature*, **266**, 429–+, March 1977.

Strüder, L. *Nuclear Instruments and Methods in Physics Research A*, **436**, 53–67, October 1999.

Su, H. *PhD Thesis*. PhD thesis, University of Leicester, in prep.

Swank, J. H., Becker, R. H., Boldt, E. A., Holt, S. S., Pravdo, S. H., Rothschild, R. E. & Serlemitsos, P. J. X-Ray Burst Observations with OSO-8. In *Bulletin of the American Astronomical Society*, volume 8 of *Bulletin of the American Astronomical Society*, pages 364–+, March 1976.

Tananbaum, H. D., White, N. E., Bookbinder, J. A., Marshall, F. E. & Cordova, F. A. Constellation X-ray mission: implementation concept and science overview. In Siegmund, O. H. & Flanagan, K. A., editors, *Proc. SPIE Vol. 3765, p. 62-72, EUV, X-Ray, and Gamma-Ray Instrumentation for Astronomy X, Oswald H. Siegmund; Kathryn A. Flanagan; Eds.*, volume 3765 of *Presented at the Society of Photo-Optical Instrumentation Engineers (SPIE) Conference*, pages 62–72, October 1999.

Tremsin, A. S. & Siegmund, O. H. Polycrystalline diamond films as prospective UV photocathodes. In Fineschi, S., Korendyke, C. M., Siegmund, O. H. & Woodgate, B. E., editors, *Proc. SPIE Vol. 4139, p. 16-24, Instrumentation for UV/EUV Astronomy and Solar Missions, Silvano Fineschi; Clarence M. Korendyke; Oswald H. Siegmund; Bruce E. Woodgate; Eds.*, pages 16–24, December 2000.

Turner, M. J. L. & Hasinger, G. Xeus - physics of the hot evolving universe. www.xray.mpe.mpg.de-/∼xeus/proposal/XEUS_150108.pdf, 2007.

Turner, M. J. L., Smith, A. & Zimmermann, H. U. *Space Science Reviews*, **30**, 513–524, March 1981.

Vidal-Madjar, A., Désert, J.-M., Lecavelier des Etangs, A., Hébrard, G., Ballester, G. E., Ehrenreich, D., Ferlet, R., McConnell, J. C., Mayor, M. & Parkinson, C. D. *The Astrophysical Journal*, **604**, L69–L72, March 2004.

Vidal-Madjar, A., Lecavelier des Etangs, A., Désert, J.-M., Ballester, G. E., Ferlet, R., Hébrard, G. & Mayor, M. *Nature*, **422**, 143–146, March 2003.

Waite, Jr., J. H., Gladstone, G. R., Franke, K., Lewis, W. S., Fabian, A. C., Brandt, W. N., Na, C., Haberl, F., Clarke, J. T., Hurley, K. C., Sommer, M. & Bolton, S. *Science*, **268**, 1598–1601, June 1995.

Weisskopf, M. C., Elsner, R. F., Hanna, D., Kaspi, V. M., O'Dell, S. L., Pavlov, G. G. & Ramsey, B. D. *ArXiv Astrophysics e-prints*, November 2006.

Weisskopf, M. C., Kestenbaum, H. L., Long, K. S., Novick, R. & Silver, E. H. *The Astrophysical Journal - Letters*, **221**, L13–L16, April 1978a.

Weisskopf, M. C., Silver, E. H., Kestenbaum, H. L., Long, K. S. & Novick, R. *The Astophysical Journal*, **220**, L117–L121, March 1978b.

White, N. The Constellation-X Mission. In *High Resolution X-ray Spectroscopy: towards XEUS and Con-X*, August 2006.

Wilken, B., Weiss, W., Stuedemann, W. & Hasebe, N. *Journal of Physics E Scientific Instruments*, **20**, 778–785, June 1987.

Wilkins, S. W., Stevenson, A. W., Nugent, K. A., Chapman, H. & Steenstrup, S. *Review of Scientific Instruments*, **60**, 1026–1036, June 1989.

Willingale, R. Private Communication, 2007.

Willingale, R. http://www.star.le.ac.uk/∼rw/q_v6/srtdoc.html, 2007.

Willingale, R. Xeus mirror technology. XEUS - Physics of the Hot Evolving Universe: Meeting, 2008.

Willingale, R., Fraser, G. W., Brunton, A. N. & Martin, A. P. *Experimental Astronomy*, **8**, 281–296, 1998.

Winkler, C. E., Cumings, N. P., Randolph, J. L. & Talley, D. H. Science instruments for the Advanced X-Ray Astrophysics Facility (AXAF). In Cline, D. B., editor, *Proc. SPIE Vol. 1948, p. 63-74, Astroparticle Physics and Novel Gamma-Ray Telescopes, David B. Cline; Ed.*, volume 1948 of *Presented at the Society of Photo-Optical Instrumentation Engineers (SPIE) Conference*, pages 63–74, October 1993.

Wiza, J. L. *Nuclear Instruments and Methods in Physics Research A*, **162**, 587–601, 1979.

Wolter, H. *Annalen der Physik*, **445**, 94–114, 1952a.

Wolter, H. *Annalen der Physik*, **445**, 286–295, 1952b.

Zombeck, M. V. *SAO Special Report*, **386**, March 1980.